COO-1112-6

THE UNIVERSITY OF MICHIGAN

COLLEGE OF LITERATURE, SCIENCE, AND THE ARTS
Department of Physics

Technical Report

LARGE-ANGLE ANTIPROTON-PROTON ELASTIC SCATTERING

David G. Falconer

ORA Project 04938

under contract with:

U. S. ATOMIC ENERGY COMMISSION
CHICAGO OPERATIONS OFFICE
CONTRACT NO. AT(11-1)-1112
ARGONNE, ILLINOIS

administered through:

OFFICE OF RESEARCH ADMINISTRATION ANN ARBOR

June 1969

TABLE OF CONTENTS

TABLE OF CONTENTS (Cont.)

TABLE OF CONTENTS (Cont.)

LIST OF TABLES

LIST OF TABLES (Cont.)

LIST OF TABLES (Cont.)

LIST OF FIGURES

LIST OF FIGURES (Cont.)

LIST OF FIGURES (Cont.)

ABSTRACT

LARGE-ANGLE ANTIPROTON-PROTON ELASTIC SCATTERING

by

David George Falconer

Chairman: Daniel Sinclair

An experimental and theoretical investigation of the large-angle antiproton-proton cross section indicates that substantial local structure exists both as a function of beam momentum and four-momentum transfer, and that such structure may be attributed, respectively, to the formation of direct-channel boson resonances, and the exchange of meson and nucleon states between the target and projectile. The differential cross-section measurements were made using data from the Argonne thirty-inch MURA chamber at the six beam momenta (invariant masses) 1.63, (2298), 1.77 (2350), 1.83 (2368), 1.88 (2389), 1.95 (2412), and 2.20 GeV/c (2500 MeV), and at momentum-transfers squared greater than $|t| = 0.3$ $(GeV/c)^2$. Off the forward peak the cross section is observed to drop to the familiar minimum at $|t| = 0.4$, rise to a secondary maximum at $|t| = 0.7$, and then form a plateau beginning around $|t| = 1.1$, and extending well into the backward hemisphere. At the very largest scattering angles a sharp, energy-dependent backward peak rises

from the plateau backward of cos θ = -0.9. Interpreted as evidence for a direct-channel boson resonance, the enhancement appears centered at 2345 MeV with a width of 140 MeV, the values quoted by R. Abrams, et al. (1967) for one of their total cross-section structures.

The observed cross sections have been treated analytically by modifying several current theoretical models for application to antiproton-proton elastic scatterings. Starting with the Chou-Yang interaction picture it is shown that a time-independent optical potential governs the interaction between target and projectile, and that for relativistically compressed, gaussian-shaped particles the forward differential cross section depends exponentially on t. In an attempt to account for antishrinking and dip-bump structure, the difference between the P-P, and PBAR-P scattering amplitudes is attributed to an annihilation potential arising from the exchange of a nucleon between the target and projectile. The difference amplitude is then calculated using the Feynman one-particle-exchange mechanism, with absorption corrections deduced from the eikonal picture of R. Glauber. The dip-bump sequence following the forward diffraction peak is credited to interference between the high-energy, and difference amplitudes.

The above processes have also been treated with Regge-cut theory. In this context the forward peak is attributed to the artifice of Pomeranchon exchange, its antishrinking to the exchange of a nucleon-isobar trajectory, and the dip-bump sequence to interference between the Pomeranchon and difference amplitudes. The predicted cross section -- obtained again via the eikonal picture -- is then compared with that produced by reggeizing the multiperipheral contributions from double isobar exchange along the lines suggested by R. Arnold, and conclusions drawn that the two processes are not readily distinguished.

1.0 INTRODUCTION

Before 1960 the antiproton-proton collision served mainly as a tool for investigating the baryonic structure of the nucleon. However, following Chew's (1962a) introduction of the bootstrap hypothesis in 1962, the antiproton-proton collision assumed a new importance based on the distinctly boson character of the PBAR-P system. In particular, the bootstrap hypothesis argued that such a system could be viewed equally well as a massive boson structure, consisting, say, of a collection of pions, or as an anti-bound state of the nucleon and antinucleon. Thus interpreted, the antiproton-proton system could be expected to form boson resonances in the s-channel, exchange light mesons in the t-channel, or dibaryon states in the u-channel. It was therefore not surprising that detailed experimental studies revealed substantially more local structure in the PBAR-P cross section than could be anticipated with the optical models used to analyze the low-energy data.

Unusual fluctuations in the differential cross section were first noted at 1.61 BeV/c by G. Lynch, et al. (1963), when this group observed a sharp diffraction peak followed by a first minimum at $|t|=.44$ $(GeV/c)^2$, and a secondary maximum at $|t|=.74$ $(GeV/c)^2$. Later experiments confirmed

the apparent exponential nature of the forward peak in t, and its tendency to widen (antishrink) with increasing beam momentum (O. Czyzewski, et al. (1965)). Similarly, the first minimum was observed to move toward larger four-momentum transfers with increasing beam energy (W. Katz, et al. (1967)), and seemingly in cadence with the forward peak. More recently, a second minimum was reported by A. Ashmore, et al. (1968) at $|t|=1.8$ $(GeV/c)^2$, very near the momentum-transfer predicted by the simple gray-disc optical model used by W. Katz, et al. (1967).

Local structure has also been observed in the total cross section by R. Abrams, et al. (1967). This study, carried out with counters, measured the PBAR-P and PBAR-D total cross sections between 1.0 and 3.3 GeV/c with a statistical accuracy of 0.1%. Both cross sections contained enhancements on the order of several millibarns at 1.3 and 1.8 GeV/c, and were attributed to either the threshold production of nucleon isobars, or the formation of direct-channel boson resonances. Using the PBAR-D data to separate the isospin states, these experimenters concluded that isospin-one structures were produced at 2190 ±5 MeV (width = 85), and 2345 ±10 MeV (width = 140), and an isospin-zero structure at 2380 ±10 MeV (width = 140).

Similar evidence for I=1, or 2 boson resonances with masses of 2195 ±15 MeV (width < 13), and 2382 ±24 MeV (width < 30) were reported by G. Chikovani, et al. (1966), although the widths observed for these resonances, called the T and U respectively, were much smaller than observed by R. J. Abrams, et al. (1967). More recently, W. A. Cooper, et al. (1968) have measured PBAR-P backward elastic cross section between 1.2 and 1.6 GeV/c, and report a clearly defined peak in the region 1.30 - 1.55 GeV/c. On the other hand, V. Domingo, et al. (1967) found no evidence for a backward peak at 2.7 GeV/c, thus suggesting that the region between the two experiments might contain detectable transition structure.

1.1 Theoretical Background

Theoretical descriptions of the antiproton-proton differential cross section have been highly varied, partially successful, and (with exceptions) essentially parametric. Early treatments of the PBAR-P cross sections were attempted with the relatively sophisticated optical models of Chew and Ball (1958), and Koba and Tokeda (1958). Basically phenomenological, these models incorporated a complex potential (the imaginary part describing a highly absorbing baryon core, and the real part a phase-shifting pion

cloud), and a Fraunhofer-type diffraction integral (evolved from the Schroedinger equation, and Fermi's golden rule) to describe the observed cross sections. More recently, two-parameter gray-disc diffraction models have been fit to the measured cross sections -- mostly by experimentalists -- using the forward scattering amplitude to fix the amplitude transmittance of the disc, and the first minimum its radius. In fact, using this technique W. M. Katz, et al. (1967) succeeded in predicting the position, though not the magnitude, of the second minimum recently observed by A. Ashmore, et al. (1968).

The optical model, though capable of accurate parameterizations of high-energy cross sections provided little insight into the scattering process itself. In an effort to establish a mechanism by which the scattering proceeds, theoreticians hypothesized that (for peripheral collisions at least) the scattering process is mediated by the exchange of a pion, or other meson having the correct quantum numbers. Unfortunately, the unadorned one-particle-exchange model failed to reproduce the experimental cross sections, and K. Gottfried and J. D. Jackson (1964), and M. H. Ross and G. L. Shaw (1964) found it necessary to modify these calculations with absorption corrections. Although these corrections

were soundly motivated, being equivalent in thought and form to the absorptive cores of the early optical models, the technique again obscured the underlying physical mechanisms. Moreover, the model proved less than adequate at large scattering angles, especially with regard to explaining dips, and bumps in the differential cross section. More sophisticated models, involving the exchange of several particles, provided a parametric solution to the difficulty, but tended to be ambiguous, since, for example, a minimum could be attributed to a sharp edge on the absorptive core, the vanishing of a particle exchange term, or interference between several amplitudes.

To some extent the difficulties with the exchange model were alleviated through the efforts of T. Regge (1959, 1960), and the workers that followed him. Noting that partial-wave analysis, which had proved so fruitful in nuclear physics, led to an impossibly large number of partial-waves at high energies, Regge -- following a technique introduced for similar reasons by Nicholson (1910) -- converted the usual partial-wave sum to an integral running parallel to the imaginary axis in the complex angular-momentum plane, plus a set of residues obtained as a result of contour deformation. Further analysis indicated that

these residues looked much like Breit-Wigner forms, and thus were associated with direct-channel resonance formation. In the cross channel these poles actually dominated the scattering amplitude, and one pole in particular, the Pomeranchon, dominated all the others. At high-energies, and small momentum transfers the Pomeranchon predicted that the scattering amplitude in the cross channel should appear exponential in t -- as it does for elastic collisions. Moreover, the Regge theory appeared highly convergent, since, in contrast to partial-wave analysis, the forward peak is completely described by the lowest order term in the expansion, namely, the Pomeranchon.

Given these clues by Regge, other theoreticians began investigating the relativistic Schroedinger equation, determining among other things that ℓ-plane poles in the scattering amplitude correspond physically to the formation of a metastable state between the projectile and target. Interpreted as resonances, these poles could be expected to assume Breit-Wigner forms in the energy, as already observed by Regge. Further analyses indicated that metastable states form whenever the real part of ℓ is integer, and that the mass squared of such states is approximately linear in its spin. Following this lead

Chew and Frautschi (1961, 1962) plotted the known resonances on a graph of spin-versus-mass-squared, and attempted to identify particles falling on a straight line, and possessing identical internal quantum numbers (baryon number, isospin, strangeness, intrinsic parity, etc.). Such trajectories proved immediately useful both in classifying old resonances, and predicting new ones, especially in connection with nucleon-isobar resonances (V. Barger (1968)). In fact, by extrapolating the trajectory into the unphysical region (negative mass squared), and applying crossing symmetry, the amplitude for the corresponding resonance exchange process could be calculated. This technique has also been used to explain the minimum observed in the PBAR-P elastic cross section (S. Frautschi (1966); C. Chiu, et al. (1967)).

Additional work with the Regge calculus indicated that the basic Regge formalism contained no corrections for absorption, and that such corrections were necessary to match theory with experiment. Extending the procedure used for one-particle exchange, R. Arnold (1965) incorporated an absorption correction via the eikonal picture of R. Glauber (1959), while F. Henyey, et al. (1968a) suggested a double-scattering mechanism wherein diffraction scattering is

followed (or led) by Regge-trajectory exchange. In either prescription the Regge-pole amplitudes become Regge-cut contributions owing to the trade-offs possible between momentum transfer associated with absorption, and momentum transfer due to trajectory exchange. In the simplest processes where the strong-interaction conservation laws limit the exchangeable trajectories, the Regge-cut formalism applies readily, as shown for example by F. Henyey, et al. (1968b). On the other hand, elastic antiproton-proton scattering may in principle be mediated by the exchange of any meson trajectory, so that the various Regge-cut contributions become difficult to untangle. One moderately successful treatment, suggested by R. Arnold (1967), reggeizes the multiperipheral diagrams of Amati, Fubini, Stanghellini (1962a, 1962b), and then envokes an eikonal formalism to calculate the amplitude difference between P-P and PBAR-P elastic scattering.

The absorption corrections used in the Regge-cut theory may be derived from the Pomeranchon picture, as suggested by R. Arnold (1967), or obtained from a simple optical model as preferred by F. Henyey, et al. (1968). In either procedure, the beam depletion arising from the production, and/or annihilation processes becomes ever more severe

with decreasing impact parameter, as might be expected on intuitive grounds. In the optical approach the beam depletion obtains by looking for an absorbing potential that reproduces the well-known gaussian behavior of the forward peak. The Pomeranchon technique yields a similar form -- except for some shrinkage of the peak -- so that both methods specify beam depletions that are approximately gaussian in the impact parameter. As noted by many physicists, the similarity of these results suggests that the Pomeranchon is just a Regge-theory technique for describing diffraction scattering, rather than an amplitude arising from the exchange of a legitimate particle trajectory.

The above interpretation also raises the much deeper question as to the roles played by the optical, and exchange models at high energies. Actually, as reflected by the success of the Regge-cut theory, a hybrid model appears correct. At the highest energies elastic scattering becomes purely diffractive, so that the forward amplitude is described by an imaginary optical potential generated by the various annihilation, and production mechanisms. At somewhat lower energies the forward amplitude may be credited in part to diffraction scattering, and in part to, say, rho-trajectory exchange. The scattered field then consists of three parts, namely, a diffracted wave, an

exchange amplitude, and an absorption-correction term. At still lower energies, other trajectories become important, requiring further exchange amplitudes, and correction terms.

As pointed out by Chou and Yang (1966), the imaginary optical potential reflects the spatial structure of the target and projectile, rather than the exchange nature of the collision. At high energies the individual exchange amplitudes all tend to zero, while the spatial structures of the colliding bodies define the zones of annihilation and production, and hence also the diffracted field. At lower energies individual exchange amplitudes become important. The Feynman picture obtains such exchange amplitudes by associating plane waves with the incoming and outgoing particles, and spherical waves with the exchanged ones; consequently, the one-particle-exchange model takes no account of the finite spatial extent of the target, projectile, or exchanged particle -- even if absorption corrections are added. On the other hand, the Regge picture ostensibly accounts for both the finite life-time, and finite spatial extent of the particles making up the exchanged trajectory. That the Regge-exchange formulas also account for the structure of the colliding bodies

remains less clear, although F. Henyey, et al. (1968a, 1968b) argue that this follows from their definition of the exchange amplitude.

If the target consists of several particles, one may expect substantial double scattering within the target region. For a two-particle object like the deuteron the first scatter occurs off the upstream nucleon, and the second off the downstream one. The amplitude for this process apparently interferes with that for single scattering, thereby forming a two-sloped forward peak, as well as a dip-bump sequence near the cross-over point. Similar structure appears with heavier nuclei like helium and carbon, except the multiple scattering amplitudes become difficult to calculate. Thus, one generally uses a net scattering potential that incorporates scattering to all orders implicitly. The dip-bump sequence is then credited to an abrupt edge on this optical potential, rather than an interference mechanism, although the two interpretations must appear equivalent on detailed analysis. On the other hand, a hydrogen target consists of just one nucleon so that double scattering is the sense described above represents a physical impossibility. Dip-bump structure, such as that observed in PBAR-P and PI-P elastic scattering,

must then be attributed to a different interference mechanism, for instance, that occuring between a diffracted field, and a difference amplitude.

1.2 Experimental Background

Following the discovery of the antiproton by Chamberlain, Segre, Wiegand, and Ypsilantis (1955), further experiments were undertaken to measure the antiproton's cross section on bare nucleons, and complex nuclei.† More recently, in an effort to locate fine structure in the antiproton-nucleon cross sections, R. Abrams, et al. (1967) measured the PBAR-P and PBAR-D cross sections to a statistical accuracy of 0.1%. Both cross sections showed statistically significant bumps at 1.3 and 1.8 GeV/c, the latter falling in the range of the present experiment. Having

---

†The antiproton-proton total cross section has been measured at 190, 300, 500, 700 MeV by B. Cork, et al. (1957), at 457 MeV by O. Chamberlain, et al. (1957), at 133; 197, 265, 333 MeV by C. Coombes, et al. (1958), at several energies between 534 and 1068 MeV by T. Elioff, et al. (1959, 1962), at 75-137.5, 137.5-200 MeV by L. Agnew, et al. (1959), at 1.0, 1.25, 2.0 BeV by R. Armenteros, et al. (1960), at several momenta between 3 and 10 GeV/c by G. Von Dardel, et al. (1960), at several momenta between 4 and 20 BeV/c by S. Linderbaum, et al. (1961), at 45, 90, 145, 245, MeV by B. Cork, et al. (1962), at several momenta between 0.575 and 5.35 GeV/c by U. Amaldi, et al. (1964), at 3.3 and 3.7 BeV/c by T. Ferbel, et al. (1965), at several momenta between 6 and 22 GeV/c by W. Galbraith, et al. (1965), at 5.7 GeV/c by K. Bockmann, et al. (1966), and at several momenta between 1.0 and 3.0 GeV/c by R. Abrams, et al. (1967).

measured both the PBAR-P, and PBAR-D cross sections, the collaboration was able to unscramble the I=0, and I=1 isospin states, and thereby observed three new structures in the total cross sections. Two of these structures, at center-of-mass energies 2190 ±5, and 2345 ±10 MeV were found in the isospin-one state, and the other, at 2380 ±10, in the isospin-zero state. As discussed by R. Abrams, et al., these structures can be interpreted either as reflections of nucleon-isobar thresholds, or as evidence for new high-mass boson resonances. The parameters of these antinucleon-nucleon structures are given in Table 1.2-1 below.

Early measurements of the antiproton-proton differential cross section were restricted to low, and intermediate energies owing to limitations imposed by the Bevatron. The first differential cross-section studies were carried out at energies between 45 MeV and 2 BeV using both counters and bubble chambers, and later between 5-60 MeV using nuclear emulsions.† The differential cross sections observed in all these experiments resembled the first quarter cycle

---

†Low-energy cross-section studies have been made at 197, 265, 333 MeV with counters by C. Coombes, et al. (1958), at 75-200 MeV with a propane bubble chamber by L. Agnew et al. (1960), at 1.0, 1.25, 2.0 BeV with counters by R. Armenteros et al. (1960), at 1.61 BeV/c with the 72-inch hydrogen chamber by N. Xuong et al. (1961), at 45, 90, 145, 245 MeV with a 15-inch hydrogen chamber by B. Cork et al. (1962), at 534, 700, 816, 948, 1068 MeV by T. Elioff et al. (1962), and at energies between 5-60 MeV by A. Hossian, et al. (1965).

TABLE 1.2-1

Nucleon-Antinucleon Structure#

ISOSPIN	PLAB	MASS	WIDTH	HEIGHT	(2J+1)K
1	1.32 GeV/c	2190±5 MeV	85 MeV	6 mb	1.6
1	1.76	2345±10	140	3	1.2
0	1.86	2380±10	140	2	0.8

From R. J. Abrams, et al. (1967).

of a cosine wave in the center-of-mass scattering angle, thus making parameterization with any one of several optical models quite feasible, e.g., the black sphere, the gray disc, or the gaussian cloud. More sophisticated models, such as those promoted by Chew and Ball (1958), and Koba and Takeda (1958), incorporated complex interaction potentials with highly absorbing baryonic cores, and phase-shifting pion clouds to simultaneously account for both elastic and inelastic cross sections.

Later in an effort to make precision measurements on the large-angle antiproton-proton differential cross sections, G. Lynch, et al. (1963) rescanned the 1.61 BeV/c Berkeley exposure originally analyzed by N. Xuong, et al. Their log-linear plot of the PBAR-P differential cross section gave the first clear indication that the forward diffraction peak is approximately exponential in the four-momentum transfer squared t. Moreover, in the same plot there appeared a non-statistical first minimum at $|t| = .45$ $(GeV/c)^2$, and a secondary maximum at $|t| = .75$ $(GeV/c)^2$. A result left unquoted in several subsequent studies.[†] After the Cern and Brookhaven proton synchrotrons became operational

---

[†]B. Barish, et al. (1966); V. Domingo, et al. (1967); T. Kitagaki, et al. (1968); S. Frautschi (1966).

additional measurements of the PBAR-P differential cross section were made at higher energies.† These experiments confirmed the exponential dependence of the forward peak in t, and also indicated that the peak tended to widen with increasing beam energy -- a result opposite that for P-P scattering, and in general conflict with single-pole Regge theory. The rate of antishrinking with s, the center-of-mass energy squared, and the slope of the diffraction peak at infinite beam energy were estimated by O. Czyzewski, et al. (1965) by simultaneously fitting the P-P and PBAR-P data available at the time to the convenient form: slope(s) = $A + B/s^{\alpha}$, where A, the slope at infinite energy, was presumed equal in P-P and PBAR-P scattering. According to the fit A = 10.6 ±0.22 $(GeV/c)^{-2}$, indicating a mean interaction radius of 1.28 F, and α = .65 ±.14, suggesting that the diffraction peak antishrinks approximately inversely with the center-of-mass energy.

---

†The high-energy differential cross section has been measured at 3.0 and 3.6 GeV/c by B. Escoubes, et al. (1963), at 7.2, 8.9, 10.0, 12.0 GeV/c by K. Foley, et al. (1963), at 3.28 GeV/c by T. Ferbel, et al. (1965), at 4.0 GeV/c by O. Czyzewski, et al. (1965), at 11.8 and 15.9 GeV/c by K. Foley, et al. (1965), at 5.7 GeV/c by K. Bockmann, et al. (1966), at 1.0, 1.5, 2.0, 2.5 GeV/c by B. Barish, et al. (1966), at 1.18 GeV/c by L. Dobrzynski et al. (1966), at 2.7 GeV/c by V. Domingo, et al. (1967), at 3.66 GeV/c by W. Katz, et al. (1967), at 5.9 GeV/c by A. Ashmore et al. (1968), and at 6.9 GeV/c by T. Kitagaki, et al. (1968).

The first-minimum secondary-maximum sequence, first noted at 1.61 BeV/c by G. Lynch, et al. (1963), also appeared in later experiments at both higher and lower energies.† According to these studies the first minimum bottoms out in the range $0.4 < |t| < 0.6$ $(GeV/c)^2$, while the secondary maximum peaks in the range $0.7 < |t| < 0.9$ $(GeV/c)^2$, both points moving toward larger $|t|$ values with increasing beam momentum. Although hindered by meager statistics, W. Katz, et al. (1967) attempted to parameterize this motion by making a crude fit with the linear form: t(minimum) = A + Bp*, where p* denotes the center-of-mass beam momentum, and obtained (without specifying errors) the values A = 0.3 $(GeV/c)^2$, and B = 0.2 (GeV/c). In the same paper, these authors also noted the suggestion of a second minimum at $|t| = 1.8$ -- a conjecture later verified by A. Ashmore, et al. (1968). As pointed out by W. Katz, et al. (1967) the position of various maxima, and minima (but not their absolute magnitude) are predicted by with a simple back-disc diffraction model with an interaction radius of 1.3 F.

---

†The first-minimum secondary-maximum sequence has been noted explicitly at 1.61 GeV/c by G. Lynch, et al. (1968), at 1.0, 1.5, 2.0, 2.5 GeV/c by B. Barish, et al. (1966), at 1.18 GeV/c by L. Dobrzynski, et al. (1966), at 2.7 GeV/c by V. Domingo, et al. (1967), at 3.66 GeV/c by W. Katz, et al. (1967), at 5.85 GeV/c by A. Ashmore, et al. (1968), and at 6.9 GeV/c by T. Kitagaki, et al. (1968).

More recently, W. Cooper, et al. (1968) have measured the backward elastic cross between 1.2 and 1.6 GeV/c in an effort to ascertain the nature of the bump in the PBAR-P total cross section at 1.3 GeV/c reported by R. Abrams, et al. (1967). By combining the data from all momentum sets these experimenters were able to observe a clearly defined backward peak in the range $-8.0 > \cos\theta > -1.0$. If this enhancement were energy independent, it could be attributed to a u-channel dibaryon exchange, while if it were localized around a particular beam momentum, it could be interpreted as a direct-channel boson resonance, or a nucleon-isobar threshold. By combining all data in the range $-8.0 > \cos\theta > -1.0$ at each momentum set, W. Cooper, et al. (1968) determined that the peak fell roughly between 1.3 and 1.55 GeV/c; however, analysis of the zero, two, four, and six prong events was unable to determine the boson, or threshold character of the enhancement.

Despite the low production cross sections for antiprotons, several crude measurements of the PBAR-P polarization cross section have been carried out by looking for antiprotons showing two successive elastic scatters, and then using the second collision as an analyzer of the first. An early measurement of this kind was made by Button and

Maglic (1962) with the 1.61 BeV/c Berkeley exposure, a study that also demonstrated that the magnetic moment of the antiproton was (very probably) negative, as required by the TCP theorem. Their analysis indicated that for an average center-of-mass scattering angle of 25 degrees the asymmetry parameter was +25 ±10%. In another experiment with data at 3.0 and 3.6 GeV/c, B. Escoubes, et al. (1963) measured an asymmetry parameter of +21 ±13% at an average CM angle of 14 degrees, and a more recent study by L. Dobrzynski, et al. (1966) led to an asymmetry parameter of -13 ±6.5% at an average CM scattering angle of 28 degrees. These results apparently neither support nor contradict the conjecture† that the polarization should execute "anomalous dispersion" in a region of "high-absorbtion" like the first minimum, as is observed, for example, in pion-nucleon scattering.

---

†For a discussion, and illustration of this point, see S. Frautschi (1966).

2.0 RESONANCE AMPLITUDES

Resonances formed through the temporary binding of the target and projectile reveal themselves as enhancements in the differential and total cross sections. Viewed from the center-of-momentum, the resonance phenomenon occurs when the target and projectile approach one another, bind temporarily into a system with well-defined quantum numbers--including mass and width--and break apart again to become free particles. Classically, such a binding is an impossibility. Quantum mechanically, however, the particles have a finite probability for burrowing through the angular momentum barrier, orbiting temporarily about one another, and then tunneling back out to become free particles once again. The amplitudes for these processes may be inferred by studying the nature of the barrier penetration, and applying the known conservation laws to the scattered amplitude.

2.1 Energy Spectrum of the Resonance

Upon penetrating the angular momentum barrier, the reduced-mass particle will shuttle back and forth (in classical fashion) between the origin and the inner wall of the barrier, until on some pass it repenetrates the barrier, and thus destroys the resonant state.

Clearly, if one starts out with N(0) such states at t=0, then the number on decaying between t and t+dt is just

$$dN = -\frac{1}{\tau} N(t)\, dt,$$

where τ is some proportionality constant. Integrating the expression obtains in the usual way the explicit formula

$$N(t) = N(0)\, \exp(-t/\tau) \qquad (t > 0)$$

so that τ really represents the life-time of the state.

According to the above, the temporal portion of the state's (normalized) probability amplitude looks like

$$A(t) = \exp(-i2\pi\nu_o t - t/2\tau)/\sqrt{\tau} \quad (t > 0)$$

where $E_o = \hbar\omega_o = 2\pi\hbar\nu_o$ denotes the nominal energy of the state. As usual, owing to the finite life-time of the resonance, the measured energies will take on a spectrum of values obtained by Fourier analyzing A(t) into its several frequency components:

$$\hat{A}(\nu) = \int_0^\infty A(t)\, \exp(+i2\pi\nu t)\, dt$$

$$= (i/\sqrt{\tau}\,)/[2\pi(\nu-\nu_o) + i/2\tau]$$

The state's energy spectrum must then be the absolute

square of this expression

$$|A(E)|^2 = \frac{|\hat{A}(\nu)|^2}{2\pi\hbar} = \frac{\Gamma/2\pi}{(E-E_o)^2 + (\Gamma/2)^2}$$

This is just a (normalized) Breit-Wigner form, with $\Gamma = \hbar/\tau$, Γ being the full-width at half-maximum of the energy spectrum.

2.2 Quantum Numbers of the Resonance

Resonances always form in states of definite spin J, parity P, isospin I, and--where applicable--definite G-parity, and C-eigenvalue. Moreover, owing to the conservative nature of the strong interaction, any boson resonance necessarily has the same quantum numbers as the partial-waves that formed it, and the partial-waves it decays into. In other words,

$$\vec{J}(\text{INITIAL}) = \vec{J}(\text{RESONANCE}) = \vec{J}(\text{FINAL})$$

$$P(\text{INITIAL}) = P(\text{RESONANCE}) = P(\text{FINAL})$$

$$\vec{I}(\text{INITIAL}) = \vec{I}(\text{RESONANCE}) = \vec{I}(\text{FINAL})$$

$$G(\text{INITIAL}) = G(\text{RESONANCE}) = G(\text{FINAL})$$

$$C(\text{INITIAL}) = C(\text{RESONANCE}) = C(\text{FINAL})$$

The last two relations are useful only if the intermediate state has a well-defined G-parity, and C-eigenvalue.

The system parity associated with the incident L^{th} partial wave follows from the usual definition

$$P(SYSTEM) = P(P)\ P(PBAR)\ P(ORBITAL)$$
$$= (+1)(-1)(-1)^{L}$$

Its C-eigenvalue, on the other hand, obtains from the generalized Pauli principle, and the necessity for Fermi-Dirac statistics among fermions:

$$E(ORBITAL)\ E(SPIN)\ C = -1$$

where the E operators exchange the denoted coordinates. Thus,

$$C = (-1)^{L+S}$$

Combined with the parity result obtained above, this implies that

$$CP = (-1)^{S+1}$$

Thus, since S = 0,1, it is also true that

$$S(INITIAL) = S(RESONANCE) = S(FINAL),$$

as CP is also conserved by the strong interaction.

The allowed values for L, on the other hand, follow from the conservation of total angular momentum

$$\vec{J} = \vec{L} + \vec{S}$$

In other words, if S=0, then L=J, while if S=1, then L = J-1, J, J+1. The quantum numbers associated with these states are listed, respectively, in Tables 2.2-1, 2,3. Note that the set of states

$$J^{PC} = 0^{+-},\ 1^{-+},\ 2^{+-},\ 3^{-+},\ \ldots$$

cannot be attained by the PBAR-P system, and curiously enough no boson resonances with these quantum numbers have been established. This observation lends further credence to the bootstrap picture wherein all boson resonances are viewed as quasi-bound states of the PBAR-P system.

The PBAR-P system has no specific G-parity. Its isospin amplitude can nevertheless be decomposed into eigenstates of G and I, as shown in the Appendix. For these amplitudes

$$G = (-1)^{L+S+I}$$

where L+S+I specifies the even and odd G-parity states. Hence, if the PBAR-P system communicates with a resonance of definite G-parity, then for that portion of the amplitude

$$L(\text{INITIAL}) = L(\text{FINAL}),\ L(\text{FINAL}) \pm 2$$

as S, I, and G are all conserved. The same result, of course, obtains from parity conservation.

2.3 Isospin Spectrum of Resonance

The isospin portion of the incident amplitude consists of a part contributed by the antiproton, and part contributed by the proton

$$|P,PBAR\rangle = |I1,IZ1;I2,IZ2\rangle$$

where I1 = I2 = 1/2, IZ1 = +1/2, IZ2 = -1/2.
It is convenient to decompose this vector into its singlet (I=0), and triplet (I=1) components, as these, rather than the individual states, characterize an s-channel resonance. The decomposition is effected in the usual way by applying the identity

$$1 = \sum_I |I,IZ\rangle\langle I,IZ|$$

To the right-hand side of the above expression

$$|I1,IZ1;I2,IZ2\rangle = \sum_I |I,IZ\rangle\langle I,IZ|I1,IZ1;I2,IZ2\rangle,$$

where, of course, IZ = IZ1 + IZ2 = 0. The Clebsch-Gordon coefficients

$$\langle I,IZ|I1,IZ1;I2,IZ2\rangle = \langle I,0|1/2,+1/2;1/2,-1/2\rangle$$

are given explicitly in Table C.1-2 of the Appendix.

The PBAR-P system can also be decomposed into eigenstates |I,IZ;G> of isospin and G-parity, using the results presented in Table C.3-2 of the Appendix.

$$|P,PBAR> = 1/2|1,0;+> + 1/2|1,0;-> + 1/2|0,0;+> + 1/2|0,0;->$$

Thus if the resonance has both a definite isospin and G-parity, only one-fourth the incident intensity will communicate with it. Similarly, when the resonance decays, it will emit one fourth its intensity into each of the four isospin states

$$|P,PBAR>,\ |PBAR,P>,\ |N,NBAR>,\ |NBAR,N>$$

The first two vectors cannot be distinguished experimentally when in their final-state configuration, so that the decaying resonance will contribute one-half its outgoing intensity to the observed antiproton-proton distributions. Consequently, at most one-eighth the incident PBAR-P intensity may communicate elastically with a resonance of definite isospin and G-parity.

2.4 Resonance Cross Sections

As shown by Blatt and Weiskopf (1952), the

enhancement expected in the elastic cross section due to the formation and decay of a resonance of spin J, and elasticity K is given by the formula:

$$\sigma(\text{resonance}) = (\pi/4k^2)(2J + 1)K^2 \sin^2\delta$$

This formula assumes no interference between the resonance and background amplitudes, and that the intermediate state possesses a definite isospin and G-parity. The quantity δ represents the phase shift associated with the resonance, and depends on the width Γ_o, and mass M_o of resonance according to

$$\sin^2\delta = \frac{(\Gamma_o/2)^2}{(M-M_o)^2 + (\Gamma_o/2)^2}$$

at resonance $M = M_o$, so that $\sin^2\delta = 1$, while if $M-M_o = \Gamma_o/2$, $\sin^2\delta = 1/2$. Thus, Γ_o specifies the full-width at half-maximum for the resonance.

At resonance the enhancement in the total cross section depends linearly on the spin J, and quadratically on its elasticity K. For the energy range covered by the present experiment, the wavenumber k runs from 3.4 to 4.2 inverse fermis, so that the leading factor in σ(resonance) takes the nominal value

$$\pi/4k^2 \simeq 600 \text{ microbarns}$$

This cross section is also the enhancement expected from a spinless resonance with unit elasticity, definite isospin, and definite G-parity. (We still assume no interference between the resonance, and those background amplitudes having the same J,P,C eigenvalues.) More generally, Figure 2.4-1 shows the cross-section enhancement expected for various J and K values, with $k = 3.73\ F^{-1}$--the nominal wavenumber for the present experiment.

2.5 Angular Spectrum of Resonance

As discussed by Blatt and Weiskopf (1952), the angular distribution associated with the formation and decay of a singlet-state resonance of spin J, and elasticity K has the form:

$$d\sigma/d\Omega = (\pi/4k^2)(2J + 1)K^2 |\,|J,0\rangle|^2$$

where $|J,0\rangle$ denotes a normalized spherical harmonic. In other words, in the absence of interference the decay angular distribution follows the square of a zero-order J^{th}-degree Legendre polynomial, as sketched in the Figure 2.5-1. According to these curves the backward cross section for the resonance becomes ever more sharply peaked with increasing J. One measure of this sharpness obtains from the nearness of the minimum to the backward

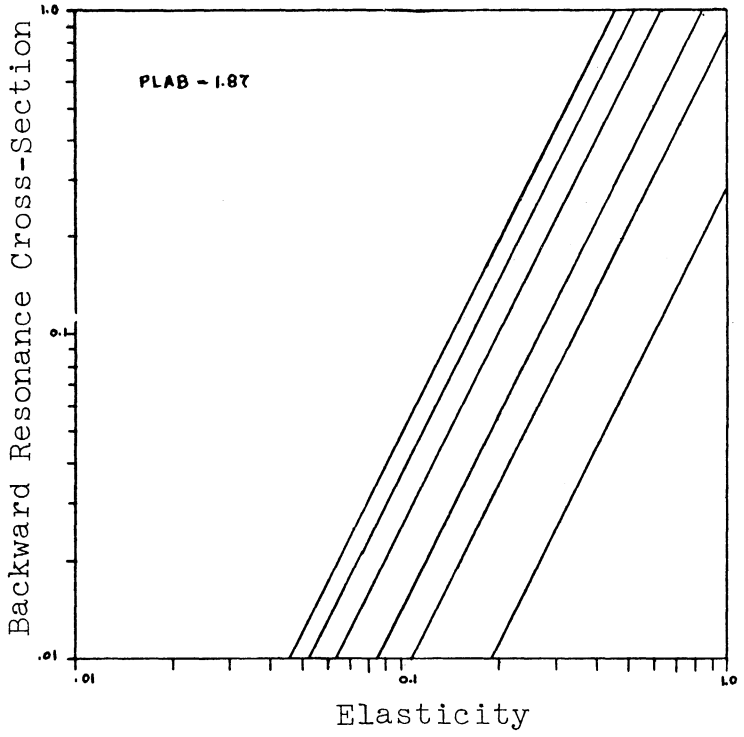

Figure 2.4-1. Resonance Cross-Section Enhancement. Backward hemisphere cross sections shown (from right to left) for J = 0,1,2,4,6,8. These curves assume no interference between the resonance and those background amplitudes having the same J, P, C eigenvalues.

scattering coordinate cos θ = -1.0. For reference these numbers are given in column one of Table 2.5-1.

Scattering via the triplet states leads to more complicated formulas for the decay angular distribution of the resonance. For S=1, and L=J=L', the differential cross section looks like

$$d\sigma/d\Omega = (\pi/4k^2)(2J+1)K^2 \cdot \sum_{\text{spins}} |\langle J,LZ'\rangle\langle J,LZ';1,SZ|J,JZ;J,1\rangle\langle J,JZ;J,1|J,0;1,SZ\rangle|^2,$$

where the Clebsch-Gordon coefficients are defined in Blatt and Weiskopf (1952). As shown in Figure 2.5-2, these curves look much like those for the singlet state, except that the minimum nearest the backward direction does not reach zero. These minima, however, still measure the relative sharpness of the backward peak, and thus are listed in column two of Table 2.5-1.

The remaining triplet states all involve changes in the orbital angular momentum of the system: L=J±1, L'=J±1. As inferred above the angular momentum barrier may be expected to inhibit transitions from the lower to the higher angular momentum states, so that, for example, the process taking the initial orbital state L=J+1 to the final orbital state L'=J-1 likely dominates the reverse case. Under this assumption the decay angular

TABLE 2.5-1

Differential Cross-Section Minima #

	S=0 L=J L'=J	S=1 L=J L'=J	S=1 L=J+1 L'=J-1
J=1	0.0	0.0	NONE
J=2	-0.58	-0.66	-0.46
J=3	-0.77	-0.82	-0.76
J=4	-0.86	-0.89	-0.86
J=5	-0.91	-0.92	-0.91
J=6	-0.93	-0.93	-0.93

Quoted values refer to cos θ; see text for definition of "minima".

distribution to be associated with the resonance takes the form:

$$d\sigma/d\Omega = (\pi/4k^2)\,K^2 \sum_{\text{spins}} \Big| \sum_{L,L'} (2L+1)^{1/2}\, i^{L-L'}\, D(L-L'-2)$$

$$\cdot |L',LZ'\rangle\langle L',LZ';1,SZ'|J,JZ;L',1\rangle\langle J,JZ'L,1|L,0;1,SZ\rangle\Big|^2$$

where D(L-L'-2) denotes a Kronecker delta. The curves associated with this angular distribution are shown in Figure 2.5-3, and indicate that the oscillatory structure noted heretofore appears smoothed owing to the superposition of waves having different relative periods. As a measure of the sharpness of the backward peaks, the half-power points for these curves have been listed in column three of Table 2.5-1.

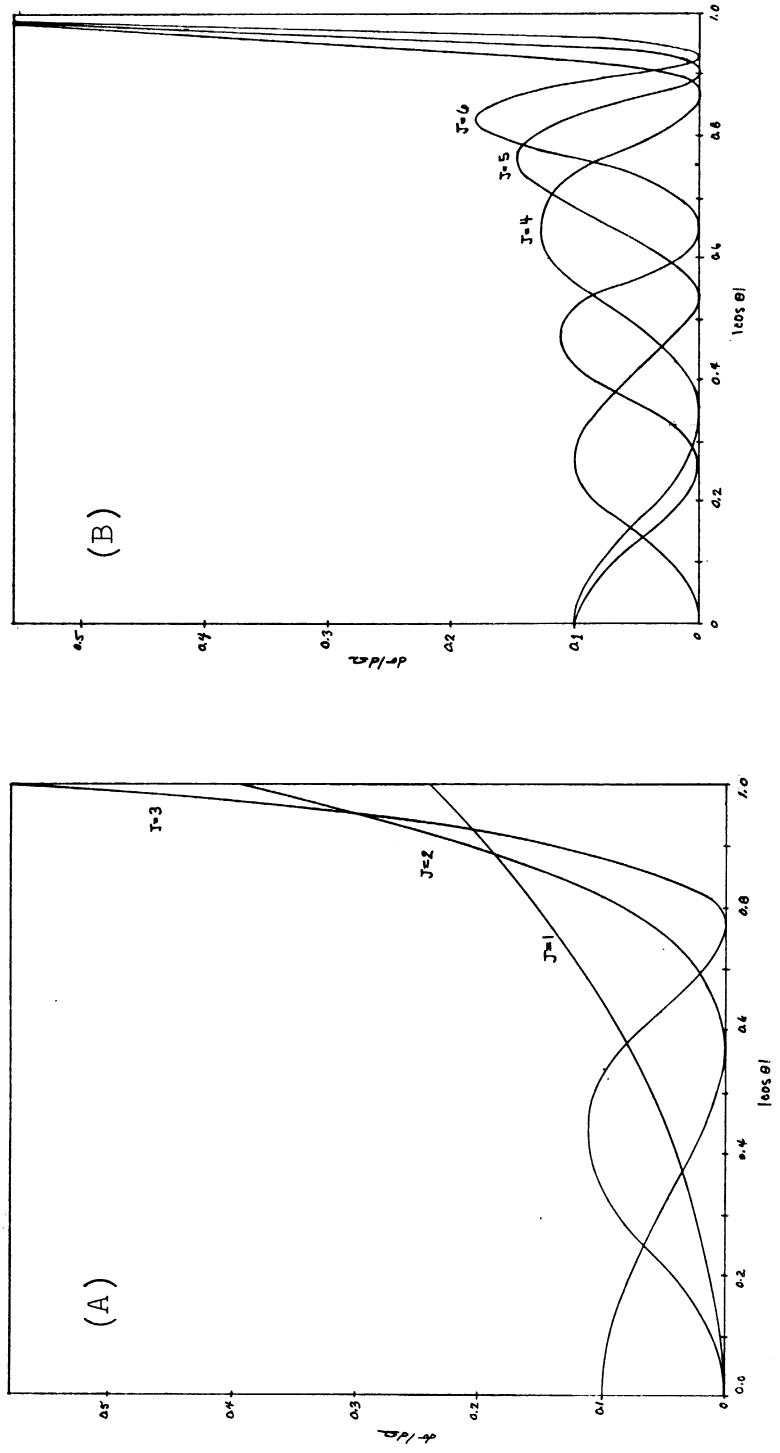

Figure 2.5-1. Decay Angular Distribution for Singlet-State Resonance. (A) J = 1,2,3; (B) J = 4,5,6. (From J. Lys (1968))

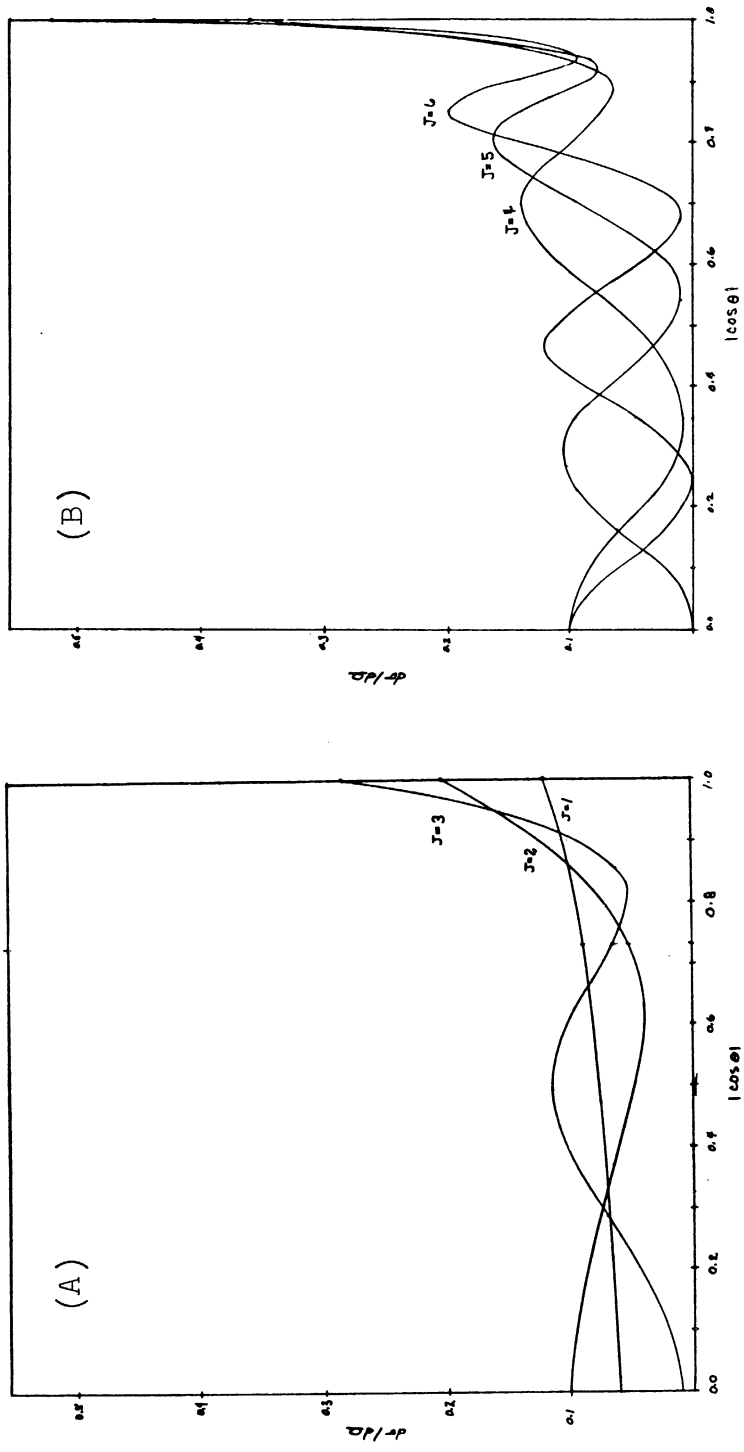

Figure 2.5-2. Decay Angular Distribution for Triplet-State Resonance: I. (A) I=L'=J= 1,2,3; (B) I=L'=J= 4,5,6. (From J. Lys (1968))

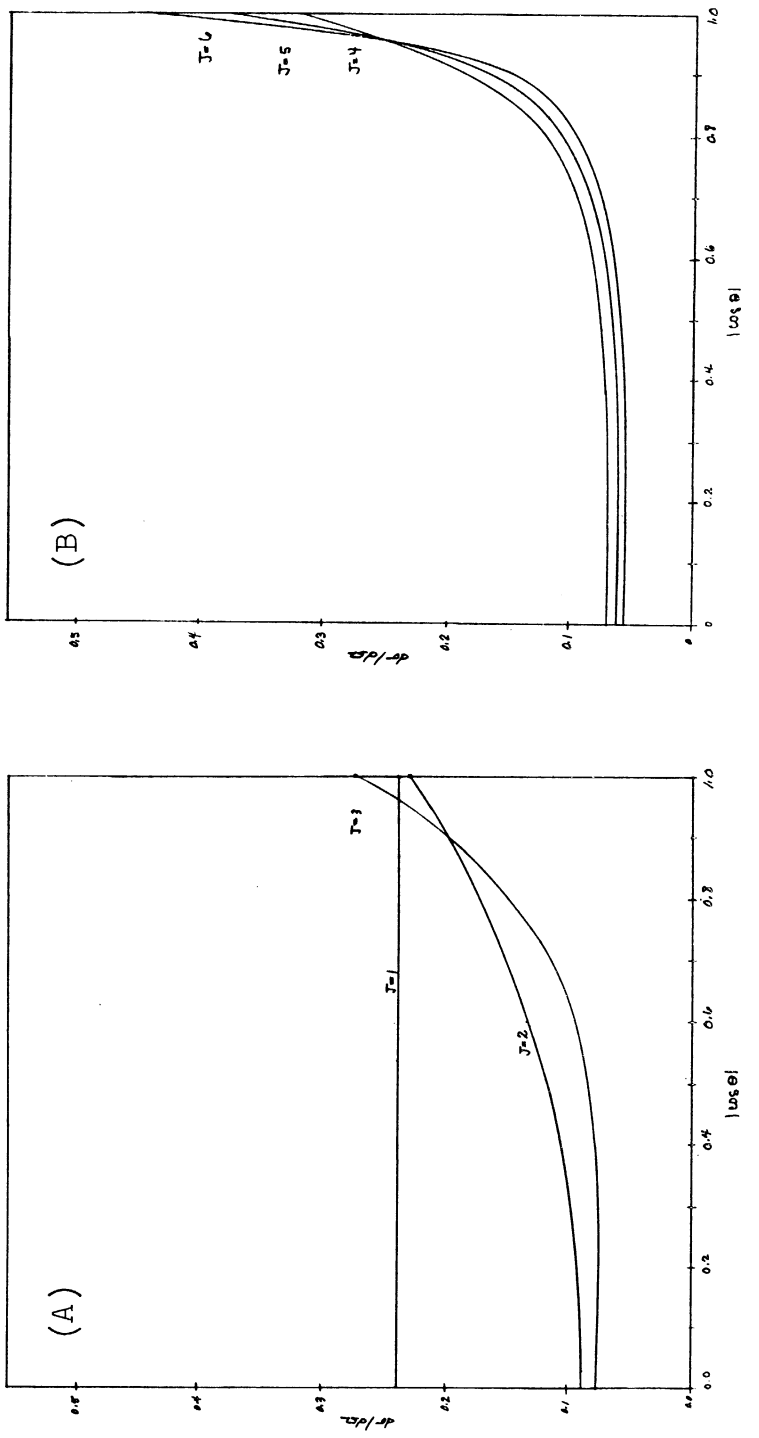

Figure 2.5-3. Decay Angular Distribution for Triplet-State Resonance: II. (A) L-1=L'+1=J= 1,2,3; (B) L-1=L'+1=J= 4,5,6. (From J. Lys (1968))

3.0 THE OPTICAL MODELS

Originally introduced by nuclear physicists, the optical model recognizes the mechanistic, and mathematical similarity between (say) proton scattering by massive nuclei, and optical scattering in a photographic emulsion. The mathematical correspondance (except for phase-space factors) is in fact perfect, the first Born approximation and the Fraunhofer diffraction integral being formally identical. More importantly, however, both processes are inherently statistical, the proton worming its way through the atomic nucleus, and interacting with any one of several nucleons, much as light quanta pass through photographic film, and scatter from the silver gains inbedded in the emulsion. Fortunately, with both phenomena the downstream applitude may be calculated without detailed knowledge of the size or position of the individual nucleons, or silver grains. In particular, the scattered optical amplitude depends only on the shape, and opacity of the developed image, the silver grains playing no essential roll except at large scattering angles.† (See Figure 3.0-1.) Similarly, the nuclear

---

†Unless the wavelength of the incident radiation drops to dimensions comparable to the grain size, the total cross section will remain constant, and differential cross section depend only on the momentum transfer to the photographic emulsion.

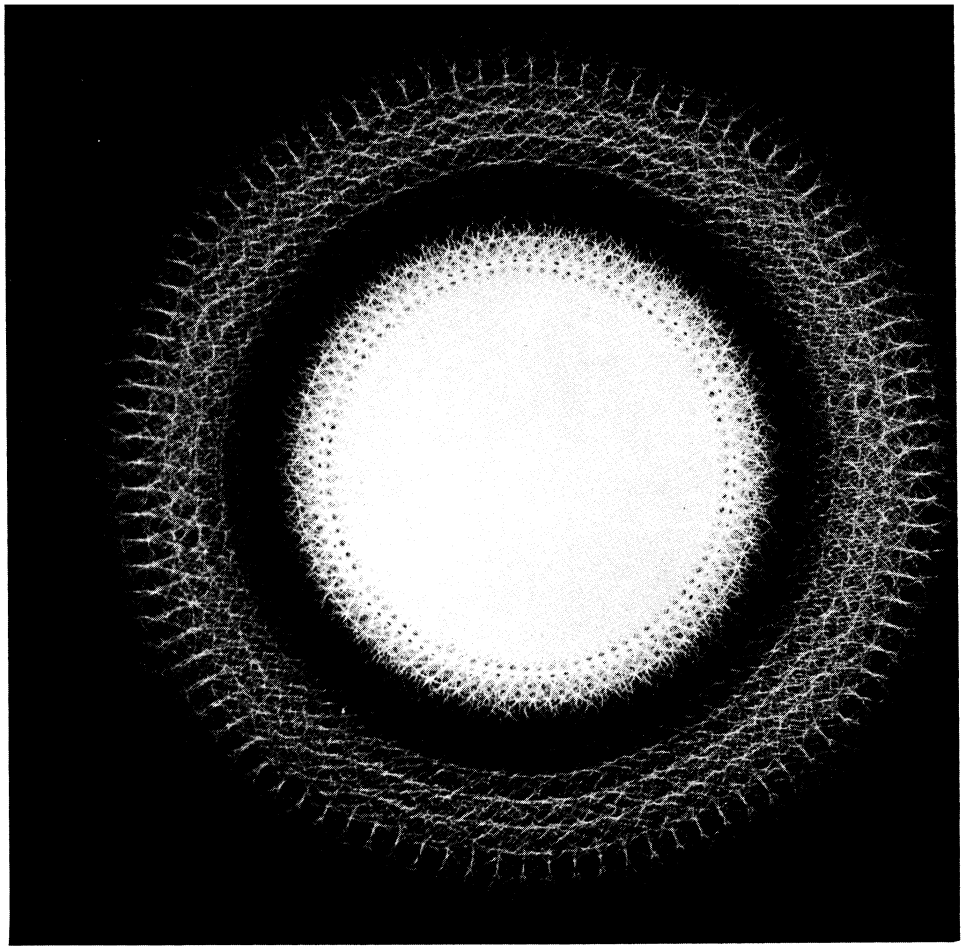

Figure 3.0-1. Optical Scattering. The above diffraction pattern, when viewed in the large, resembles that expected from a circular disc or ring, while in fact it was produced by illuminating an opaque screen containing 96 pinholes located uniformly on the circumference of a circle. If the holes were placed randomly on the circle, the downstream amplitudes from each would be wildly out of phase with the others, thus smoothing the fine structure of the pattern. (See L. Cutrona (1965) for details of the experimental arrangement.)

physicist can argue on the basis of his experimental findings that the downstream proton amplitude depends primarily on the diameter, and density of the atomic nucleus, and not on the positions of the individual nucleons. (The rather obvious similarity between circularly symmetric diffraction fields, and proton-nucleus cross sections lends further credence to the analogy.) Taken together, these factors motivated the introduction, and successful application of the optical model in nuclear physics. (R. Eisberg, p. 576 (1962))

More recently, the optical model, and its various derivatives have gained favor among high-energy physicists, mainly because they lead to accurate fits (and predictions) involving few adjustable parameters. On the other hand, motivation for their use at high energies remains less clear, since the statistical picture invoked by the nuclear physicist holds only for complex nuclei. Nevertheless, high-energy arguments, based on the finite spatial extent of the target and projectile, have recently been put forth by both experimentalists, and theoreticians. These treatments, though varying in detail, picture the elastic collision as a reflection of inelastic processes occuring at impact parameters comparable to the dimensions of the target and projectile. In other words, the interaction potential is

held to have a large imaginary part with a spatial structure describing the zone of inelastic collisions. The coherent-droplet model of Byers and Yang (1964a, 1967b), for example, imagines the target and projectile passing through one another, with strong absorption and phase shifting occuring along the way. Another picture, proposed by A. D. Krisch (1966) (See, also, A. D. Krisch, and J. P. Krisch (1967).) envisions an interaction center -- also called a particle source function -- located midway between the target and projectile,which scatters the incident wave into both the elastic, and inelastic channels. The latter model, in fact, has led to a surprisingly accurate parameterization of the P-P elastic cross section over wide ranges of both s and t (A. D. Krisch (1967)).

3.1 Chou-Yang Interaction Picture

Unlike atomic physics, where, for example, the first Bohr orbit is three to five orders of magnitude larger than the classical radius of the electron, or the measured diameter of the nucleon, strong-interaction physics occurs at ranges comparable to the dimensions of the target, and projectile. From a classical point of view one would expect the physical structure of the particles to play an intimate roll in the collision, much as the hard surface

of a billiard ball introduces constraint equations in Lagrangian mechanics. On the other hand, at the nuclear scale it might be argued that the physical structure, and interaction potential are equivocal concepts -- the potential necessarily assuming the more fundamental role. The latter picture is acceptable, in fact preferable, except that when the constraints imposed by the physical structure are violated, the projectile may be destroyed, a real-life possibility not covered by ordinary potentials, or classical constraint equations. In addition, the nuclear constraints have a typically statistical character, leading in one collision to elastic behavior, and in another to inelastic processes.

Fortunately, the difficulties of inelastic collisions, and statistical-type constraints are well resolved by introducing a complex potential.† The real portion of the potential acts in the usual way, advancing or retarding the phase of the various partial waves, and thereby bending the classical trajectories of the particles. The imaginary part, on the other hand, accounts for inelastic processes, attenuating the lowest order partial waves, and introducing diffraction structure in the elastic cross section. Moreover, as noted

---

†See, for example, S. Fernbach, et al. (1949).

above, the imaginary part of the potential reflects to some degree the structure of the target, and projectile. Taking a cue from the classical picture, Chou and Yang (1968) have conjectured that the potential for collision depends on the degree to which the target and projectile are overlapped. If $P(\vec{x})$ describes the physical density of the projectile, and $T(\vec{x})$ the density of the target, then the integrated overlap is given by the correlation integral (See Figure 3.1-1.)

$$V(\vec{x}) \propto P(2\vec{x}) * T(2\vec{x}) = \int P(2\vec{x} - \vec{x}') \, T(\vec{x}') \, d\vec{x}'$$

Note that the interaction potential $V(\vec{x})$ depends only on the center-to-center separation of the particles, and not explicitly on the time. In the Born approximation the elastic scattering amplitude is proportional to the Fourier transform of the potential $V(\vec{x})$ with respect to the three-momentum transfer $\vec{\Delta}$. In other words,

$$d\sigma/d\Omega \propto |\hat{V}(\vec{\Delta})|^2 \propto |\hat{P}(\vec{\Delta}/2)\hat{T}(\vec{\Delta}/2)|^2,$$

where the circumflex denotes Fourier transformation.[†]

The forward (diffraction) peak, which is generally regarded as a reflection in the elastic channel of the strong absorbtion occuring into the inelastic channels,

---

[†]We have used the convolution theorem $\widehat{A*B} = \hat{A}\hat{B}$.

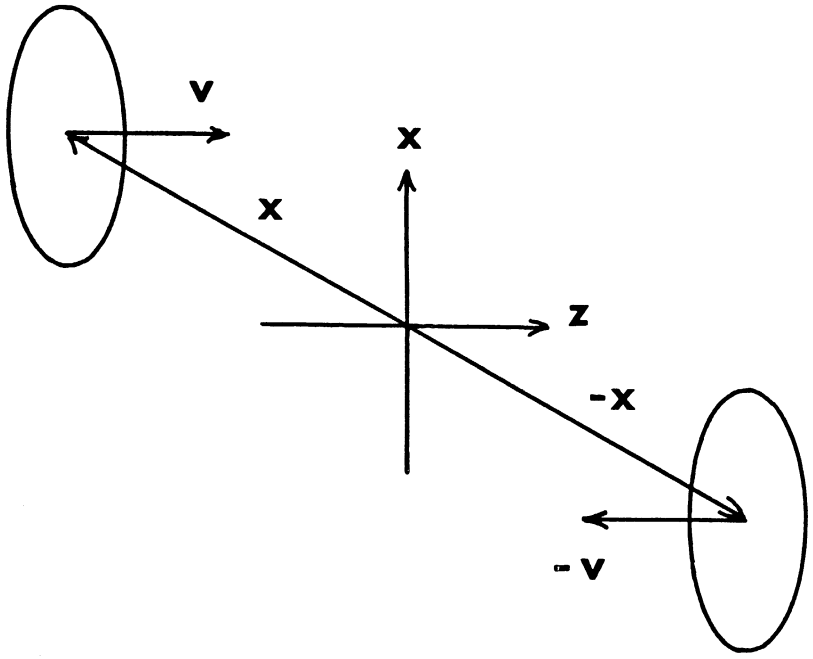

Figure 3.1-1. Chow-Yang Collision Geometry. For equal mass particles the origin of the coordinate system is at the center-of-mass in the center-of-momentum coordinate system.

provides a practical application of the above relations. At high energies the forward peak depends exponentially on the three-momentum transfer squared: $\exp(-2R_o^2\Delta^2)$, with R_o^2 on the order of 5 $(\text{GeV}/c)^{-2}$. In other words,

$$|\hat{P}(\vec{\Delta}/2)\hat{T}(\vec{\Delta}/2)|^2 \propto \exp(-2R_o^2\Delta^2)$$

Assuming the target and projectile have similar distributions, and neglecting possible phase factors obtains

$$\hat{P}(\Delta/2) = \hat{T}(\Delta/2) \propto \exp(-R_o^2\Delta^2/2)$$

or taking the inverse transform

$$P(2r) = T(2r) \propto \exp(-r^2/2R_o^2)$$

where r is the radial coordinate of either particle. According to the present interpretation, therefore, the rms radius of the target and projectile is

$$2\hbar cR_o = 2(.197)\sqrt{5} = .88 \text{ F},$$

a figure not far from the .7 F measured by E. Chambers, and R. Hofstadter (1956) in an electron-proton scattering experiment.†

---

†The present interpretation also provides the convolution description of two-body scattering requested by C. Akerlof, et al. (1966).

3.2 Relativistic Schrodinger Equation

The Klein-Gordon equation provides a relativistically correct description of a spinless particle moving in the vicinity of a scaler potential $V(\vec{x},t)$:

$$[(i\hbar\partial/\partial t - V)^2 - c^2(-i\hbar\nabla)^2 - (mc^2)^2]\ \Psi(\vec{x},t) = 0$$

The equation obtains from first principles by making operator substitutions in the relativistic energy-momentum relation:

$$(E-V)^2 - c^2p^2 - (mc^2)^2 = 0$$

In collision problems $\Psi(\vec{x},t)$ specifies the probability amplitude for locating the particle at $\vec{x}$ and t when subject to an interaction potential $V(\vec{x},t)$ arising from the presence of a target, or the exchange of one or more virtual quanta between the target and projectile. The former view leads, for example, to the optical, and eikonal pictures for high-energy scattering, while the latter, due to Feynman (1948), forms the basis for the one-particle-exchange model.

It is usually argued that the potential V depends only on the vector drawn between the two particles, and not explicitly on the time. In this case, the spatial and temporal portions of the wave-function separate, and it is

possible to write

$$\Psi(\vec{x},t) = \psi(\vec{x}) \exp(-i\omega t)$$

where $E = \hbar\omega$ is the total relativistic energy of the projectile. Substitution then leads to the time-independent Klein-Gordon equation

$$[(E-V)^2 + c^2\hbar^2\vec{\nabla}^2 - (mc^2)^2]\ \psi(\vec{x}) = 0$$

Far from the potential

$$E^2 - (mc^2)^2 = c^2\ p^2 = c^2\ \hbar^2\ k^2,$$

so that we obtain the familiar Schroedinger form:

$$[\nabla^2 + k^2 - U(\vec{x})]\ \psi(\vec{x}) = 0$$

where we have introduced an effective potential $U = (2EV - V^2)/\hbar^2c^2$. Theorists prefer this form of the relativistic wave equation owing to its basic simplicity, and formal similarity with the classical Schroedinger equation. (Note, however, that k denotes the relativistic wavenumber for the incident projectile, and U depends explicitly on its total energy E.)

Before proceding with specific models, it is convenient to write the solution to the relativistic Schroedinger equation as an integral appropriate for the treatment of

scattering problems. Downstream of the potential the probability amplitude necessarily consists of two parts, namely, the unperturbed incident wave exp(ikz), and a spherical wave eminating from the target area. In other words, in the asymptotic limit of laboratory dimensions, the downstream amplitude is

$$\psi_d(x) = \psi_i(x) + \psi_s(x)$$
$$= \exp(ikz) + f(k, \cos\theta)\exp(ikr)/r$$

Note that f(k, cos θ) modulates the outgoing wave with respect to both scattering angle θ, and wavenumber k. To calculate f(k, cos θ) we sum the Huygen spherical wavelets scattered by each element of the potential, a procedure justified by the formal similarity between the relativistic Schroedinger equation, and the static electromagnetic wave equations. The amplitude of the scattered wavelets depends, of course, on the product of the illuminating amplitude, and the strength of the scattering potential. Thus, by adding up contributions from all parts of the potential, we obtain the following integral for the scattered amplitude:

$$\psi_s(\vec{x}) = -\int\psi(\vec{x}')\, U(\vec{x}')\, [\exp(ik|\vec{x}-\vec{x}'|)/4\pi|\vec{x}-\vec{x}'|]\, d\vec{x}'$$

Introducing the notation wave($\vec{x}$) for the Huygen spherical

wavelet:

$$\text{wave}(\vec{x}) = -\exp(ik|\vec{x}|)/4\pi|\vec{x}| = -\exp(ikr)/4\pi r$$

and defining * as the convolution operation leads to the compact form

$$\psi_s(\vec{x}) = [\psi(\vec{x})\ U(\vec{x})] * \text{wave}(\vec{x})$$

which is just Huygen's principle.†

In the far-field approximation the convolution integral for the scattered amplitude simplifies to an ordinary Fourier transformation. In particular, with little error we can replace $|\vec{x} - \vec{x}'|$ by $|\vec{x}| = r$ in the denominator of $\text{wave}(\vec{x})$, and by $r - \vec{x}\cdot\vec{x}'/|\vec{x}|$ in the exponent:

$$\text{wave}(\vec{x}-\vec{x}') \simeq -\exp(ikr - i\vec{k}\cdot\vec{x}')/4\pi r$$

where $\vec{k} = k(\vec{x}/|\vec{x}|)$. Substitution then yields the scattered amplitude in the far-field approximation:

$$\psi_s(\vec{x}) = \text{wave}(\vec{x}) \int \psi(\vec{x}')\ U(\vec{x}')\ \exp(-i\vec{k}\cdot\vec{x}')\ d\vec{x}'.$$

---

†The same procedure can be applied to the time-dependent wave equation, except that the mathematics are more complicated. See, for example, R. P. Feynman, p. 84 (1962), or Chapter 5 below.

Consequently, we can make the following identification:

$$f(k, \cos\theta) = (-1/4\pi) \int \psi(\vec{x}') \, U(\vec{x}') \exp(-i\vec{k}\cdot\vec{x}') \, d\vec{x}',$$

where, of course,

$$d\sigma/d\Omega = |f(k, \cos\theta)|^2.$$

3.3 Optical Model Without Spin

Although details vary among authors, most optical models are equivalent to using a far-field Born approximation to calculate the amplitude scattered by an empirical and/or derived potential U. In general, U may depend both on the spatial coordinate $\vec{x}$, and the projectile energy E; however, even without energy dependence in U, optical models make accurate predictions for the differential cross section over suprisingly wide energy ranges. The Born approximation itself follows from the assumption that even in the immediate vicinity of the potential the total amplitude either 1) differs little from the incident one exp(ikz), or 2) differs by a calculable amount to be included explicitly in $U(\vec{x})$. In either case the integral for $f(k, \cos\theta)$ simplifies to

$$\begin{aligned} f(k, \cos\theta) &= (-1/4\pi) \int \exp(ikz') \, U(\vec{x}') \exp(-i\vec{k}\cdot\vec{x}') \, d\vec{x}' \\ &= (-1/4\pi) \int U(\vec{x}') \exp(i\vec{\Delta}\cdot\vec{x}') \, d\vec{x}' \end{aligned}$$

In other words, the scattering amplitude is just the Fourier

transform of the (perhaps modified) potential $U(\vec{x})$ with respect to the three-momentum transfer $\vec{\Delta}$.

For spherically symmetric potentials, U = U(r), and it is possible to perform the angular integrations immediately

$$f(k, \cos\theta) = -\int_0^\infty U(r') \operatorname{sinc}(\Delta r') \, r'^2 \, dr'$$

where sinc(x) = sin(x)/x. Similarly, if the potential is cylindrically symmetric U = U(ρ,z), and we obtain the form

$$f(k, \cos\theta) = -\frac{1}{2} \int\!\!\!\!\!\!\circ \int_0^\infty U(\rho',z') \, J_o(k\rho' \sin\theta) \cdot \exp[ik(1-\cos\theta)z'] \, \rho' d\rho' dz'$$

where J_o denotes the zero-order Bessel function.

To illustrate the use of these formulas, we consider four examples, each demonstrating a physical or mathematical aspect of the optical model. To remain consistant with the literature we hypothesize forms for $U(\vec{x})$, rather than $V(\vec{x})$.

GAUSSIAN CLOUD: According to the electron-proton scattering studies of E. Chambers, and R. Hofstadter (1956), the nucleon looks approximately gaussian in the radial coordinate, with an rms radius of .72 ±.05 F. A similar result can be inferred from the shape of the forward diffraction peak in P-P elastic scattering, as discussed in Section 3.1.

Thus, we are motivated to consider an imaginary gaussian potential of the form:

$$U(r) = - iU_o \exp(-r^2/4R_o^2)$$

According to the above, the scattered amplitude is

$$f(k, \cos\theta) = + iU_o (4\pi)^{\frac{1}{2}} R_o^3 \exp(-R_o^2\Delta^2)$$

squaring this result for the cross section obtains

$$d\sigma/d\Omega = U_o^2 (4\pi R_o^6) \exp(-2R_o^2\Delta^2)$$

Thus, the differential cross section for this model is exponential in Δ^2. In P-P scattering R_o tends to increase with projectile momentum, while in PBAR-P it tends to decrease, facts clearly not covered by the present form.

YUKAWA POTENTIAL. According to Yukawa theory, the strong force is mediated by pion exchange, and thus should be characterized by an exponentially damped coulomb potential of the form:

$$U(r) = - U_o(R_o/r) \exp(-r/R_o)$$

where R_o is the Compton wavelength of the pion, $\hbar/mc$. The scattering amplitude follows immediately

$$f(k, \cos\theta) = U_o R_o/[\Delta^2 + (1/R_o)^2]$$

Thus, although this potential also predicts a forward peak, its slope is much steeper than observed experimentally. To show this, we convert the cross section to an exponential in (small) Δ^2:

$$d\sigma/d\Omega = U_o^2 R_o^6/[1 + (R_o^2\Delta^2)^2]^2$$
$$\approx U_o^2 R_o^6 \exp(-2R_o^2\Delta^2)$$

But for pions

$$2R_o^2 \approx 100 \text{ (GeV/c)}^{-2}$$

However, the measured value is more like 10 (GeV/c)^{-2}, indicating a sharp discrepency between theory and experiment.

MILKY COIN. The first-minimum secondary-maximum sequence observed in PBAR-P reactions suggests that a target potential with sharper edges might more accurately parameterize the differential cross section. With this in mind, we consider a coin-shaped potential, oriented coaxially with the beam, and characterized by a complex index of refraction n. As the incident wave passes through the region of the potential, it will experience both amplitude attenuation, and phase shifting. In fact, after penetrating the volume

a distance δ, the incident wave exp(ikz) will have been deformed to

$$\exp[ikz + ik(n-1)\delta]$$

The potential U responsible for this deformation obtains as a solution to

$$[\nabla^2 + k^2 n^2]\psi = [\nabla^2 + k^2 - U]\psi$$

In other words, inside the coin $U = (1-n^2)k^2$, and outside $U = 0$. It is necessary, however, to account for the deformation of the incident wave; thus, we instead use an effective potential of the form

$$'U' = (1-n^2)k^2 \exp[ik(n-1)(D+z)]$$

where 2D is the thickness of the coin. Although a general solution is straight forward, it is more interesting to consider the problem where $n \simeq 1 + i\varepsilon$, ε small. Then, $(1-n^2) \simeq -2i\varepsilon$, and the scattered amplitude is:

$$f(k,\cos\theta) = i\varepsilon D R^2 k^2 \frac{2 J_1(kR \sin\theta)}{kR \sin\theta} \frac{\sin(k(1-\cos\theta)D)}{k(1-\cos\theta)D}$$

where R denotes the radius of the coin. For very thin, but highly absorbent coins, D tends to zero, while the product εD becomes the amplitude absorbtance per unit area, say, A;

then,

$$d\sigma/d\Omega = A^2R^4k^4 \quad \frac{2\,J_1(kR\sin\theta)}{kR\sin\theta}$$

a formula often quoted in the literature. Although strictly speaking the optical theorem fails for Born approximated amplitudes, many authors use it to eliminate the parameter A^2 by writing

$$d\sigma/d\Omega = (k\sigma_t/4\pi)^2\ \mathrm{jinc}^2(kR\sin\theta)$$

where $\mathrm{jinc}(x) = 2J_1(x)/x$.

SQUASHED GAUSSIAN. In the center-of-momentum system, both the target and projectile appear relativistically contracted along their directions of motions. If the nucleon looks gaussian in its rest frame, with an rms radius R, then in the CM it will take the form:

$$\exp(-x^2/2R^2 - y^2/2R^2 - \gamma^2z^2/2R^2)$$

where the kinematical factor γ refers to the CM velocity of the particle. Convolving two such nucleons according to the Chou-Yang prescription leads to the following potential

$$U = -iU_o\ \exp[-x^2/4R^2 - y^2/4R^2 - \gamma^2z^2/4R^2]$$

$$= -iU_o\ \exp[-\rho^2/4R^2 - \gamma^2z^2/4R^2]$$

The scattered amplitude follows readily from the cylindrically symmetric transform:

$$f(k, \cos\theta) = \frac{1}{2}\, iU_o\, (2R^2)(4\pi R^2/\gamma^2)^{\frac{1}{2}} \cdot \exp[-R^2k^2\sin^2\theta]\, \exp[-R^2k^2(1-\cos\theta)^2/\gamma^2]$$

Recalling $\Delta^2 = 2k^2\,(1-\cos\theta)$, and defining $\Delta_t = k\sin\theta$ as the transverse component of three-momentum transfer, obtains the simplified form

$$d\sigma/d\Omega = U_o^2\,(4\pi R^2/\gamma^2)\,\exp[-2R^2(\beta^2\Delta_t^2 + \Delta^2/\gamma^2)]$$

For small scattering angles

$$\beta^2\Delta_t^2 + \Delta^2/\gamma^2 \simeq k^2\theta^2 \simeq -t$$

and for large scattering angles

$$\beta^2\Delta_t^2 + \Delta^2/\gamma^2 \simeq 4k^2/\gamma^2 - u(2\beta^2-1)$$

Using three such cores the squashed-guassian theory accurately fits the neutron-proton scattering data of M. Kreisler, et al. (1966) over all CM scattering angles, and over a wide range of beam energies. The model also presumably describes the P-P cross section, except that these particles are indistinguishable. (See Figure 3.3-1.)

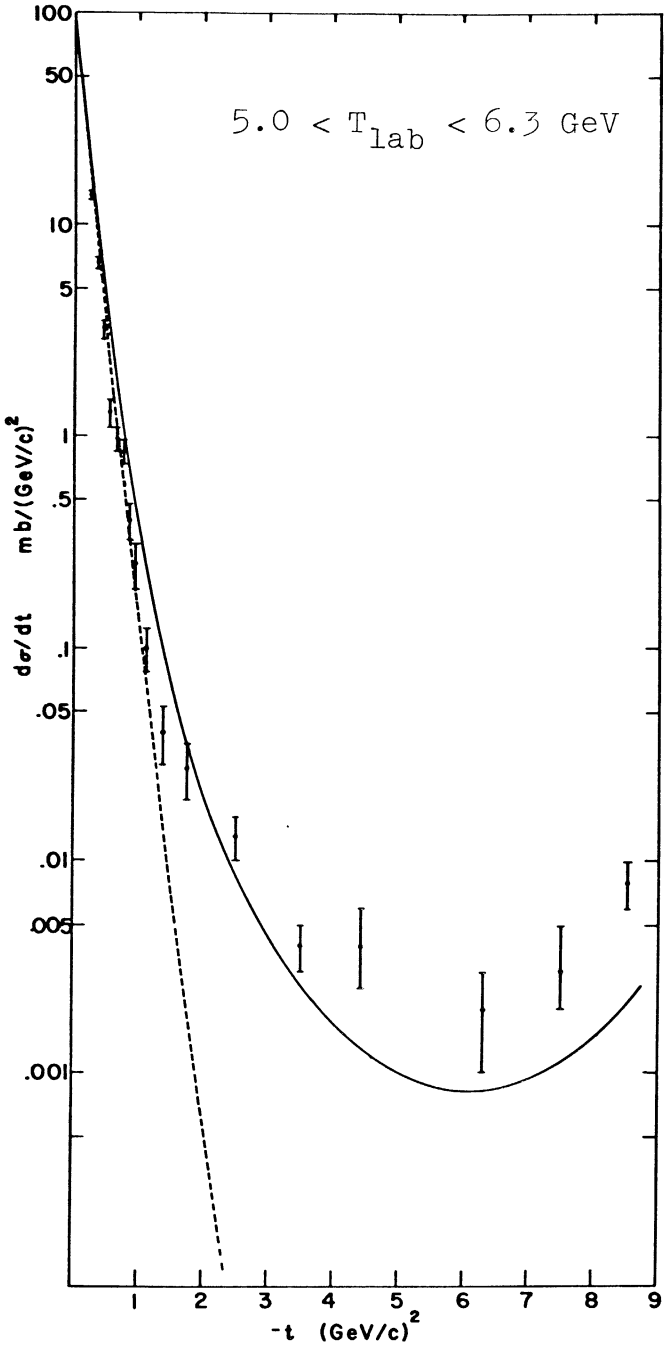

Figure 3.3-1. Squashed-Gaussian Fit to N-P Elastic. The solid line indicates a tri-core fit to the data of Kreisler, et al. (1966). The radii of the cores were taken from Krisch (1967), and the curve normalized with the optical theorem. The dashed curve is a single-core forward-angle fit.

Early antiproton-proton experiments suggested that the PBAR-P interaction potential consists of a small, dense baryon core surrounded by a diffuse meson cloud. At very low energies ($kR << 2\pi$, R = 1 F) the PBAR-P annihilation cross section grows rapidly with decreasing beam momentum, and dominates both the elastic and production cross sections:

$$\sigma_t \simeq \sigma_a >> \sigma_e, \sigma_p$$

(B. Cork, et al. (1962)). The dominance of σ_a over σ_e suggests annihilation off a gray, rather than a black core, at least in a simple optical picture. However, as noted by Feshbach and Weisskopf (1949) the low-energy annihilation cross section associated with a black sphere appears larger than that expected from geometrical optics owing to the wave-mechanical nature of the projectile. In particular,

$$\sigma_a = \pi (a + 1/k)^2$$

where k denotes the CM wave number of the projectile, and a the radius of the baryon core. At very low energies the second term in the parentheses over-rides the first, and the annihilation cross section varies inversely as the square of the projectile velocity -- a result analogous to the one obtained in track-ionization studies for bubble chambers. Accordingly, the elastic diffraction peak generated by the

annihilation channels should shrink rapidly with decreasing beam momentum owing to a corresponding expansion of the scattering region, an effect also observed experimentally by A. Hossian, et al. (1965).

At medium-low energies ($kR < 2\pi$) the elastic and annihilation cross sections have about the same magnitude, both dominating the production cross section (B. Cork, et al. (1962)):

$$\frac{1}{2}\sigma_t \simeq \sigma_e \simeq \sigma_a >> \sigma_p$$

These relations indicate that while the PBAR-P reaction is still dominated by annihilation processes, the effective radius for them is now closer to that of the black sphere since $\sigma_e \simeq \sigma_a$. The marked expansion of the forward peak from the narrow widths measured at very low energies also supports this conclusion.

At medium-high energies ($kR > 2\pi$), on the other hand, the elastic, annihilation, and production cross sections all have about the same magnitude (K. Bockmann, et al. (1966)):

$$\frac{1}{3}\sigma_t \simeq \sigma_e \simeq \sigma_a \simeq \sigma_p$$

These ratios suggest that the various production processes, which heretofore have contributed little to the total cross

section, now match those of annihilation. In addition, since the elastic cross section lies substantially below the inelastic one, and if the baryon core is still presumed black, the production processes must be initiated in a relatively transparent scattering region, namely, the diffuse meson cloud.

At the very highest energies ($kR >> 2\pi$) the PBAR-P total cross section appears to approach that for P-P scattering (C. Czyzewski, et al. (1965)):

$$\sigma_t(pp) \simeq \sigma_t(\bar{p}p) >> \sigma_e(\bar{p}p)$$

The small elastic cross section indicates again that production occurs off a fairly transparent medium, a result also found for P-P scattering. In addition, the width of the forward diffraction peak appears to antishrink toward that characterizing P-P scattering with increasing beam momentum. These results suggest that the meson cloud dominates the high-energy behavior, and that the P-P and PBAR-P processes have the same forward scattering amplitude for $kR >> 2\pi$.

4.0 THE EIKONAL PICTURE

In an effort to bridge the (large) gap between the W.K.B. method and the Born approximation, R. J. Glauber (1955) introduced a calculational technique, first noted by Moliere, which effectively combines the two methods for obtaining the downstream amplitude. The Born approximation, it will be recalled, obtains the scattered amplitude by Fourier transforming the interaction potential, while the W.K.B. method approximates the wave-function via a stationary-phase integral. In contrast, the Glauber technique specifies the downstream wave-function with a hybrid formula that can be interpreted either as a Fourier transform or as a stationary-phase integral, thus giving the Born approximation, and W.K.B. method as appropriate limiting cases. Moreover, the technique produces a forward scattering amplitude that satisfies the optical theorem, a feature not characteristic of the Born approximation.

4.1 The Glauber Picture

Glauber's derivation of the eikonal theory, though rigorous, incorporates more mathematics than appropriate for the present study. Another technique -- a generalization of Huygen's principle -- leads to the same results,

but without a Green's function analysis, and with substantially improved physical insight. In making the Born approximation it will be recalled that the total (scattered plus unscattered) amplitude ψ was replaced by the incident one $\psi_i = \exp(ikz)$, on the argument that only a small portion of ψ_i scatters, and the resulting error should be small. At high-energies, and in the immediate vicinity of the potential, however, the incident amplitude is modified dramatically, its phase and magnitude deviating materially from the form $\exp(ikz)$. A similar problem arises in optics when a plane wave is incident on a highly absorbing, and/or refracting medium, e.g., an industrial-grade diamond. Here, as in strong-interactions, the real local amplitude deviates materially from the incident one at points within the scattering structure. Unfortunately, this is precisely the region where major contributions are made to the Born-approximation integral.

In an effort to keep the Born approximation intact, Glauber decided to modify the incident wave-function to account for distortion, and/or depletion caused by the target potential $U(\vec{x})$. Physically speaking, the modification amounted to assigning a complex refractive index n to the medium, and then calculating the accumulated phase shift, and total attenuation suffered by the incident wave before

reaching the scattering point $\vec{x}$. The refractive index generated by the potential U is determined by solving the defining identity for n:

$$[\nabla^2 + k^2 n^2]\psi = [\nabla^2 + k^2 - U]\psi$$

Thus, within the diffraction region the refractive index varies according to

$$U = k^2 (1-n^2) \simeq 2k^2 (1-n)$$

Consequently, as the incident wave moves through the interaction potential, it will be depleted, and distorted, finally looking like

$$\exp[ikz + ik \int_{-\infty}^{z} (n(x,y,z') - 1)\, dz']$$
$$= \exp\left[ikz - \frac{i}{2k} \int_{-\infty}^{z} U(x,y,z')\, dz'\right]$$

Using this approximation for the incident wave, instead of the unmodified form exp(ikz), leads to the improved Born approximation

$$f(k,\cos\theta) = -\frac{1}{4\pi} \int \exp(ikz') \exp\left[-\frac{i}{2k} \int_{-\infty}^{z'} U(x',y',z'')dz''\right] \cdot U(\vec{x}') \exp(-i\vec{k}\cdot\vec{x}')\, d\vec{x}'$$

a formula originally obtained by Glauber using a Green's function method.

To simplify the above integral, and also improve the approximation, Glauber switched from the usual center-of-momentum coordinate system (projectile incident along z-axis) to the more symmetric brick-wall coordinate system (projectile incident at polar angle $-\theta/2$), as illustrated in Figure 4.1-1. Under this rotation, the exponential factor $\exp(ikz' - i\vec{k}\cdot\vec{x}')$ goes over to

$$\exp[-ik\rho' \, 2 \sin\tfrac{\theta}{2} \cos(\phi - \phi')]$$

where cylindrical coordinates have been used for $\vec{x}'$, and spherical ones for $\vec{k}$. With this change one also obtains, remarkably enough, a perfect differential in z':

$$f(k,\cos\theta) = -\frac{1}{4\pi} \int U(\vec{x}') \exp[-\frac{i}{2k} \int_{-\infty}^{z'} U(\rho',\phi',z'')\, dz''] \cdot \exp[ik\rho' \, 2 \sin\tfrac{\theta}{2} \cos(\phi-\phi')]\, d\vec{x}'$$

Where, being a correction factor itself, the form of the exponentiated integral remains unchanged by the coordinate rotation. Carrying out the z'-integration yields

$$f(k,\cos\theta) = \frac{ik}{2\pi} \int\int \{1 - \exp[-\frac{i}{2k} \int_{-\infty}^{+\infty} U(\rho',\phi',z')\, dz']\} \cdot \exp[-ik\rho' \, 2 \sin\tfrac{\theta}{2} \cos(\phi-\phi')]\, \rho' d\rho' d\phi'$$

The exponentiated integral is just the complex phase shift

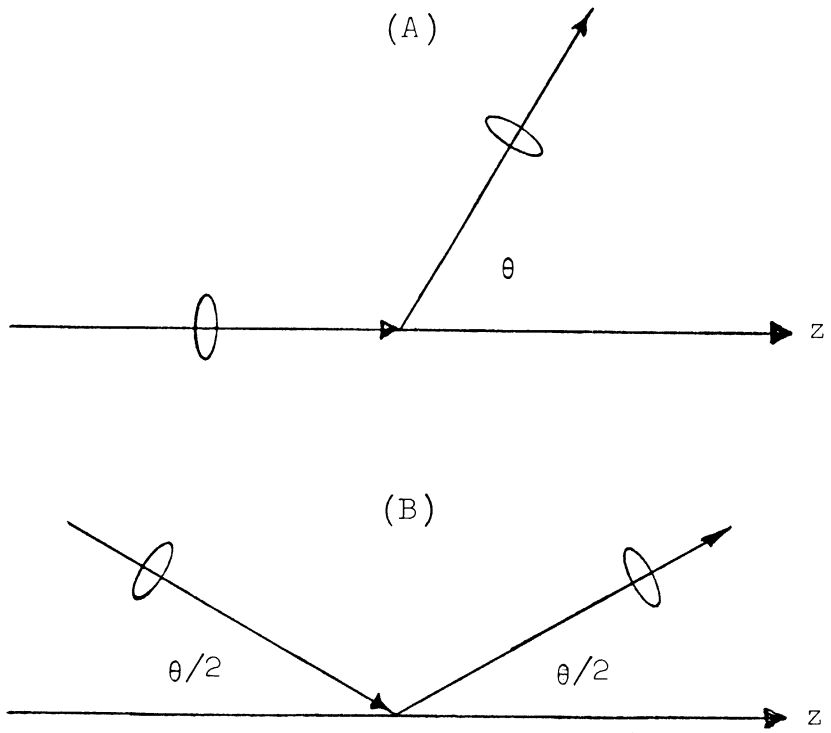

Figure 4.1-1. Breit's Brick-Wall Coordinate System. (A) Conventional System, (B) Breit's System.

suffered by the incident wave on its trip through the region of the potential:

$$\chi(\rho,\phi) = -\frac{1}{2k}\int_{-\infty}^{+\infty} U(\rho',\phi',z')\,dz'$$

The integral $\chi(\rho,\phi)$ is called the optical eikonal function, or "eikonal" for short.

For potentials considered cylindrically symmetric in the brick-wall system, the eikonal approximation becomes

$$f(k,\cos\theta) = ik\int_0^{\infty} \{1 - \exp[i\chi(\rho)]\}\, J_o(k\rho'\ 2\sin\frac{\theta}{2})\rho'd\rho'$$

In the limit of small phase shifts $\chi(\rho')$, the exponential may be expanded to obtain ($\Delta = 2k\sin(\theta/2)$)

$$f(k,\cos\theta) = -\frac{1}{2}\int_0^{\infty} U(\rho',z')\, J_o(\Delta\rho')\,\rho'd\rho'dz'$$

which is just the first Born approximation when computed in the brick-wall frame. In high-energy problems, however, the potential is generally dominated by a large imaginary term $-iU_o$, owing to absorbtion into the inelastic channels, so that such an approximation may not be valid. In these cases it is fruitful to divide the potential U into two parts, namely, $-iU_o$, and a smaller piece δU, representing, for example, the real part of the potential. One can then expand the exponential in δU obtaining

$$f(k,\cos\theta) = ik \int_0^\infty \{1 - (1 + i\delta\chi) \exp(i\chi_o)\} J_o(\Delta\rho') \rho' d\rho'$$

where the eikonals $\chi_o(\rho)$, and $\delta\chi(\rho)$ correspond to the potentials $-iU_o$, and δU, respectively. Consequently, the scattered amplitude can also be written in two parts:

$$f_o(k, \cos\theta) = ik \int_0^\infty \{1 - \exp i\chi_o\} J_o(\Delta\rho') \rho' d\rho'$$

$$\delta f(k, \cos\theta) = k \int_0^\infty \delta\chi \exp i\chi_o J_o(\Delta\rho') \rho' d\rho'$$

where $f_o(\Delta)$ represents the dominant portion of the amplitude, i.e., the diffraction peak, and $\delta f(\Delta)$ a small perturbation term.

The formula for δf looks like a distorted-wave born approximation in the potential $\delta U(x)$, and proves valuable, for example, in the analysis of pion-nucleon charge-exchange scattering (R. C. Arnold (1965)). To show this let $f(k,\cos\theta)$ denote the total (elastic plus charge-exchange) pion-nucleon scattering amplitude, $f_o(k,\cos\theta)$ the elastic protion of the amplitude, and $\delta f(k,\cos\theta)$ the (smaller) charge-exchange amplitude. All experiments indicate that the elastic amplitude is exponential in Δ^2:

$$f_o(k,\cos\theta) = iA_o \exp(-R_o{}^2\Delta^2)$$

so that upon Fourier-Bessel inversion ($b = \rho$)

$$\{ 1 - \exp i\chi_o(b)\} = (A_o/2kR_o^2) \exp(-b^2/4R_o^2)$$

Similarly, it may be argued (albeit aposteriorily) that the charge-exchange amplitude should, in the first approximation, also be exponential in Δ^2:

$$\delta f(k,\cos\theta) = A_1 \exp(-R_1^2 \Delta^2)$$

so that upon inversion

$$\delta\chi(b) = (A_1/2kR_1^2) \exp(-b^2/4R_1^2)$$

Thus, by including the distortion of the incident wave one obtains

$$\delta f(k,\cos\theta) = A_1 \exp(-R_1^2\Delta^2) - A_2 \exp(-R_2^2\Delta^2)$$

where

$$A_2 = A_1A_o/2k(R_1^2 + R_o^2)$$
$$R_2^2 = R_1^2R_o^2/(R_1^2 + R_o^2)$$

Experimentally, $R_1^2 > R_2^2$, and $A_1 > A_2 > 0$, so that the first term dominates at small Δ^2, while the opposite is true at higher Δ^2. The cross-over point according to R. C. Arnold (1965), could explain the minimum observed at $|t| = 0.5$ $(GeV/c)^2$ in the charge-exchange cross section.

4.2 Coherent-Droplet Model

Conceptually similar to the eikonal picture, the coherent droplet model of Byers and Yang (1966) is founded in partial-wave analysis, rather than the Born approximation. As in the eikonal picture, charge-exchange scattering is regarded as part-and-parcel of the elastic scattering amplitude, although the droplet model includes in addition a spin-flip charge-exchange amplitude. The spin-flip amplitude, contrary to one's initial expectation, has a magnitude comparable to that of the non-flip amplitude, even though it would appear that both flipping the spin vector, and exchanging particle charge would amount to a higher order, and hence smaller amplitude process. As pointed out by Byers and Yang, the apparent equal footing for the flip, and nonflip processes "is indicative of the great difficulty in transferring large momenta, but relative ease, to varying degrees, in coherently transferring quantum numbers: charge, spin, strangeness, nucleon number, etc." This feature, although an ad hoc concept in the droplet model, results in a natural way when a spin-flip potential is added to Arnold's eikonal picture.

In the coherent-droplet model, the scattered amplitude obtains by first making partial-wave analyses of the upstream, and downstream solutions to the relativistic Schroedinger

equation. The difference between these sums is then identified as the scattered amplitude, providing there are no incoming spherical wave components. The procedure leads in the usual way to the non-flip amplitude

$$A(k,\cos\ \theta) = \frac{i}{2k} \sum_{\ell=o}^{\infty} (2\ell+1)\ A_\ell\ P_\ell(\cos\ \theta)|T>$$

Here $|T>$ specifies the spin-state of the target, and A_ℓ the quantity $(1-\exp(i\alpha_\ell))$, where $\alpha_\ell/2$ denotes the (complex) non-flip phase shift for the ℓth partial wave. If during collision the projectile flips the spin vector of the target, the incident amplitude $\exp(ikz)|T>$ will be modified by the usual spin-orbit interaction operator, and the incident amplitude will take the distorted form:

$$(i\vec{\sigma}\cdot\vec{n})\ \frac{\partial}{\partial\theta}\ \exp(ikz)|T>$$

In this case the scattered amplitude is still just the difference between the upstream, and downstream solutions. Hence, the spin-flip amplitude is

$$B(k,\cos\ \theta) = (i\sigma\cdot n)\ \frac{\partial}{\partial\theta}\ \frac{i}{2k} \sum_{\ell=o}^{\infty} (2\ell+1)\ B_\ell\ P_\ell(\cos\ \theta)|T>$$

$$= (i\sigma\cdot n)\ \frac{i}{2k} \sum_{\ell=o}^{\infty} (2\ell+1)\ B_\ell\ P_\ell^1(\cos\ \theta)|T>$$

Here B_ℓ denotes the quantity $(1-\exp(i\beta_\ell))$, where $\beta_\ell/2$ is the spin-flip phase shift, and $P_\ell^1(\cos\theta)$ an associated Legendre polynomial of unit order, and degree ℓ. The above forms for $A(k,\cos\theta)$, and $B(k,\cos\theta)$, though accurate, prove inconvenient in an optical-type analysis. Thus, Byers and Yang replaced the awkward sums over ℓ with integrals over the impact parameter b. Using the defining relations

$$\begin{aligned} \Delta &= 2k \sin\frac{\theta}{2} \\ \hbar kb &= \hbar\sqrt{\ell(\ell+1)} \simeq \hbar(\ell+\tfrac{1}{2}) \\ k\,db &= d\ell \end{aligned}$$

and noting the approximations

$$\begin{aligned} P_\ell(\cos\theta) &\simeq J_o((\ell+\tfrac{1}{2})\ 2\sin\tfrac{\theta}{2}) = J_o(\Delta b) \\ -P_\ell^1(\cos\theta) &\simeq (\ell+\tfrac{1}{2})\ J_1((\ell+\tfrac{1}{2})\ 2\sin\tfrac{\theta}{2}) = kb\,J_1(\Delta b) \end{aligned}$$

leads immediately to the formulas

$$\begin{aligned} A(k,\cos\theta) &= ik|T\rangle \int_0^\infty A(b)\ J_o(\Delta b)\ b\,db \\ B(k,\cos\theta) &= ik^2\ (i\vec{\sigma}\cdot\vec{n})|T\rangle \int_0^\infty B(b)\ J_1(\Delta b)\ b^2\,db \end{aligned}$$

Since the amplitudes A(k,cos θ), and B(k,cos θ) are orthogonal by virtue of the orthogonality of $|T\rangle$ and $(i\vec{\sigma}\cdot\vec{n})|T\rangle$, we can suppress these factors, and write instead

$$A(k,\cos\theta) = ik \int_0^\infty \{1 - \exp i\alpha(b)\} J_o(\Delta b)\, bdb$$

$$B(k,\cos\theta) = ik^2 \int_0^\infty \{1 - \exp i\beta(b)\} J_1(\Delta b)\, b^2\, db$$

provided these amplitudes are always added incoherently.

With the scattered amplitudes written as above, the quantities α(b), and β(b) identify immediately as the eikonals for the non-flip, and spin-flip portions of the potential. Thus, following Arnold's technique,† we break α(b), and β(b) into their elastic, and charge-exchange portion of the exponentiated eikonals:

$$\delta A(k,\cos\theta) = k \int_0^\infty \delta\alpha(b) \exp i\alpha_o(b)\, J_o(\Delta b)\, b\, db$$

$$\delta B(k,\cos\theta) = k^2 \int_0^\infty \delta\beta(b) \exp i\beta_o(b)\, J_1(\Delta b)\, b^2\, db$$

Like Arnold, Byers and Yang interpret $\alpha_o(b)$, and $\beta_o(b)$ as the depletors of the incident wave, and as such should be equal with

---

†As discussed in the sequel, Arnold picked his form for α(b) by presuming the charge-exchange porcess is mediated by rho-exchange.

$$\{1 - \exp i\alpha_o(b)\} = \{1 - \exp i\beta_o(b)\} = (A_o/2kR_o^2) \cdot \exp(-b^2/4R_o^2)$$

where the right-hand side is the Fourier-Bessel transform of the experimentally observed distribution $iA_o \exp(-R_o^2\Delta^2)$.

Similarly, the factors $\delta\alpha(b)$, and $\delta\beta(b)$ were interpreted as the charge-exchange amplitude per unit area at the impact parameter b. This amplitude, in turn, was concluded to be proportional to the charge-exchange amplitude per unit volume integrated over a fixed impact-parameter line running parallel to the z-axis. By definition these integrals are just $\alpha_o(b)$, and $\beta_o(b)$, so that

$$\delta\alpha(b) \propto i\alpha_o(b)$$
$$\delta\beta(b) \propto i\beta_o(b)$$

where $\alpha_o(b) = \beta_o(b)$ is given above. Actually, to obtain a good fit to the pion-nucleon charge-exchange data (A. V. Stirling (1965)), Byers and Yang had to insert an <u>ad hoc</u> factor b in the second relation:

$$\delta\beta(b) \propto ib\ \beta_o(b)$$

on the other hand, Arnold took

$$\delta\alpha(b) = (A_1/2kR_1^2)\exp(-b^2/4R_1^2)$$

so that the two treatments used slightly different parameterizations.

5.0 PARTICLE EXCHANGE, AND ABSORPTION

The outstanding success of the one-particle-exchange picture in quantum electrodynamics led Feynman (1961b), and others[†] to use the same picture for strong interactions, with the mediating photon replaced by Yukawa's finite-mass pion. Unfortunately, even after proper formulation of the interaction Lagrangians, and phase-space factors, the adopted theory failed to match with the experimental cross sections. In forward nucleon-nucleon scattering, for example, where one-pion exchange was expected to dominate the amplitude, the observed forward peak appeared much wider than the theoretically predicted one. To alleviate this difficulty, and also account for the large inelastic cross sections at high-energies, theoreticians introduced absorption factors into the one-particle-exchange picture via Glauber's eikonal model. With these factors included, and spin properly accounted for, the predicted elastic, and inelastic cross sections fell into line with the experimental data.

[†]The one-particle-exchange picture has been discussed by R. P. Feynman (1949a, 1949b), Chew and Low (1959), S. D. Drell (1960, 1961), Salzman and Salzman (1960, 1961), A. S. Goldhaber (1964), Gottfried and Jackson (1964), and J. D. Jackson (1965a, 1965b).

5.1 One-Particle Exchange

According to Feynman (1961b) collisions on the atomic and nuclear scale are mediated by the exchange of virtual quanta between the target, and projectile. Lacking an exact classical analog, the exchange mechanism may nevertheless be visualized by considering a center-of-momentum collision with an impact parameter b too large for ordinary surface-contact collision. If, prior to passing by one another, the projectile ejects a lighter particle toward the target, and the target in turn captures it, the motion of both target and projectile will be altered, thus signalling the occurance of a collision. Such collisions will appear elastic providing the mass, and energy of the target, and projectile remain the same before and after collision. In other words, the exchange particle must carry no net energy between the target, and projectile, so that while traversing the space between the colliding bodies the particle's energy must equal zero: $E^2 = p^2 + m^2 = 0$. But $p^2 > 0$ for any physical process, so that the exchange appears kinematically disallowed.

In the atomic and nuclear domain, however, one may expect the constraints of classical mechanics to appear violated within the bounds set by the uncertainty principle. In particular, the energy of the exchanged particle may

deviate by as much as ΔE from its classical value, providing it does so for a time no longer than Δt, where $\Delta E \cdot \Delta t > \hbar$. In other words, if the exchange (ejection plus capture) occurs within a time Δt, the energy-momentum relation may still be satisfied according to

$$\Delta E^2 = p^2 + m^2$$

The characteristic collision time must then be on the order of

$$\Delta t = \hbar/\Delta E = \hbar/mc^2 = 10^{-23} \text{ sec}$$

and the characteristic interaction length something like

$$\Delta \ell = c\Delta t = \hbar c/mc^2 = 10^{-13} \text{ cm}$$

where the numerical values refer to exchanged pions.

Unlike the optical and eikonal models described above, exchange scattering requires a time-dependent formalism to properly account for the time-lag between ejection by the projectile, and capture by the target. The incident amplitude is easily made time-dependent by affixing a factor $\exp(-i\omega t)$ to the static amplitude:

$$\psi_i(x,t) = \exp(ikz - i\omega t)$$

If this amplitude illuminates the static unit potential $\delta(\vec{x})$,

it will scatter a Huygen's wavelet of the form

$$- \exp(ikr - i\omega t)/4\pi r$$

since $\exp(ikz - i\omega t)\ \delta(\vec{x}) = \delta(\vec{x})\ \exp(-i\omega t)$. More generally, if $\psi_i(\vec{x},t)$ illuminates a momentary, and unit potential $\delta(\vec{x})\ \delta(t)$, the product satisfies

$$\exp(ikz - i\omega t)\ \delta(\vec{x})\ \delta(t) = \delta(\vec{x})\ \delta(t)$$
$$= \delta(\vec{x}) \int_{\omega} \exp(-i\omega t)\ d\omega/2\pi$$

and hence the scattered field will contain equal portions of all frequency components:

$$\text{wave}(\vec{x},t) = - \int[\exp(ikr - i\omega t)/4\pi r]\ d\omega/2\pi$$

where $\omega^2 = k^2 + m^2$ during integration.† This function specifies the field scattered by the momentary, and unit potential $\delta(\vec{x})\ \delta(t)$, and thus defines the time-dependent Huygen spherical wavelet. Consequently, for time-dependent potentials $U(\vec{x},t)$ the Huygen principle becomes:

$$\psi_s(\vec{x},t) = [\psi_i(\vec{x},t)\ U(\vec{x},t)] * \text{wave}(\vec{x},t)$$

where * denotes four-convolution with respect to the variables $\vec{x}$ and t.

---

†Here and in the sequel we set $\hbar = c = 1$.

In the center-of-momentum system the projectile, and target enter the interaction region as plane waves:

$$\exp(i\vec{k}_1\cdot\vec{x} - i\omega_1 t) = \exp(-i\tilde{k}_1\cdot\tilde{x})$$
$$\exp(i\vec{k}_2\cdot\vec{x} - i\omega_2 t) = \exp(-i\tilde{k}_2\cdot\tilde{x})$$

Here $\tilde{k}_1$ denotes the incident four-momentum of the projectile, and $\tilde{k}_2$ that for the target. At some space-time point $\tilde{x}_1 = (\vec{x}_1, t_1)$ the projectile may emit a particle of mass m, and then recoil as shown in Figure 5.1-1A. Since the direction cosines of the ejected particle are random, the emitted wave will appear to radiate from $\tilde{x}_1$ as a time-dependent Huygen spherical wavelet, producing a field at $\tilde{x}_2$ of the form

$$\text{wave}(\vec{x}_2 - \vec{x}_1, t_2 - t_1) = \text{wave}(\tilde{x}_2 - \tilde{x}_1)$$

as illustrated in Figure 5.1-1B. In an elastic collision, the energy and mass of the projectile remain constant during collision, so that the field scattered to the point $\tilde{x}_3$ must look like ($k_3 = k_1$, $\omega_3 = \omega_1$)

$$\exp[ik_3\,|\vec{x}_3 - \vec{x}_1| - i\omega_3(t_3 - t_1)]/4\pi\,|\vec{x}_3 - \vec{x}_1|$$
$$= \exp(ik_3 r_3 - i\omega_3 t_3 + i\tilde{k}_3\cdot\tilde{x}_1)/4\pi r_3$$

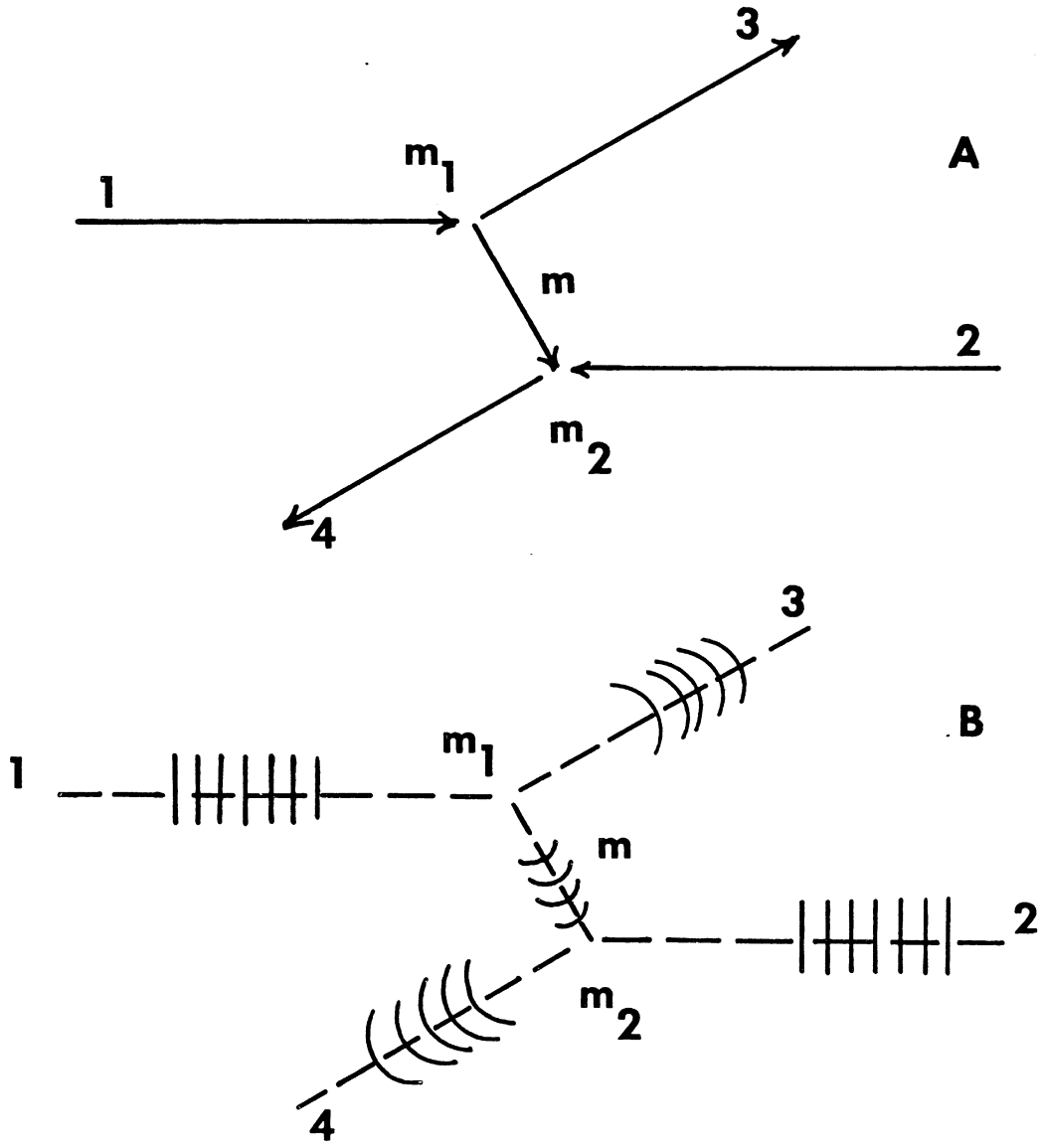

Figure 5.1-1. One-Particle-Exchange Scattering.
(A) classical picture, (B) wave-mechanical picture.

where we have made the usual far-field approximation. Similarly, on capturing the exchange particle, the recoiling target will give rise to an amplitude of the form:

$$\exp(ik_4 r_4 - i\omega_4 t_4 + i\tilde{k}_4 \cdot \tilde{x}_2)/4\pi r_4$$

where, of course, $k_4 = k_2$, $\omega_4 = \omega_2$.

The probability amplitude for having all five processes -- projectile incident with momentum $\tilde{k}_1$, target incident with $\tilde{k}_2$, particle exchange between $\tilde{x}_1$ and $\tilde{x}_2$, projectile scattered to $\tilde{x}_3$, and target recoil to $\tilde{x}_4$ -- must, according to the usual rules of quantum mechanics, be proportional to the product of the individual amplitudes:

$$\begin{aligned}
&[\exp(-i\tilde{k}_1 \cdot \tilde{x}_1)\ \exp(ik_3 r_3 - i\omega_3 t_3 + i\tilde{k}_3 \cdot \tilde{x}_1)/4\pi r_3 \\
&\qquad \cdot \text{wave}(\tilde{x}_2 - \tilde{x}_1) \cdot \\
&[\exp(-i\tilde{k}_2 \cdot \tilde{x}_2)\ \exp(ik_4 r_4 - i\omega_4 t_4 + i\tilde{k}_4 \cdot \tilde{x}_2)/4\pi r_4
\end{aligned}$$

The "usual rule" invoked here really derives from Huygen's principle, or the first Born approximation. For if one interprets the first two lines of the expression as a scattering potential $U(\vec{x}_2, t_2)$, then the last one states that the amplitude observed at $\tilde{x}_4$ owing to scattering at $\tilde{x}_2$ is just the product of the incident target amplitude,

the potential U, and a far-field Huygen wavelet. If $t_1 > t_2$, the exchanged particle must instead travel from $\tilde{x}_2$ to $\tilde{x}_1$, and the last two lines become the potential that scatters the projectile at $\vec{x}_1$ to the observation point $\vec{x}_3$. Thus, according to this view, the above expression is valid for all t_1 and t_2.

Since the Huygen spherical wavelet damps out exponentially for space-like four-distances, exchange may in principle occur between any two space-time coordinates $\tilde{x}_1$ and $\tilde{x}_2$. For a given event, however, the points $\tilde{x}_1$ and $\tilde{x}_2$ cannot be experimentally determined, so that it is necessary to average over the ejection coordinate, and sum over the capture coordinate to obtain the observed amplitude. Letting

$$C = (A_1 A_2/4\pi r_3 4\pi r_4) \exp(ik_3 r_3 - i\omega_3 t_3) \exp(ik_4 r_4 - i\omega_4 t_4)$$

and delaying momentarily the averaging, leads to the following matrix element between the initial, and final states

$$M = C \iint \exp[i(\tilde{k}_3 - \tilde{k}_1)\cdot\tilde{x}_1] \, \text{wave}(\tilde{x}_2 - \tilde{x}_1) \cdot \exp[i(\tilde{k}_4 - \tilde{k}_2)\cdot\tilde{x}_2] \, d\tilde{x}_1 \, d\tilde{x}_2$$

The integrals evaluate readily with the following momentum-space representation for the Huygen wavelet:

$$\text{wave}(\tilde{x}) = \int [\exp(-i\tilde{q}\cdot\tilde{x})/(\tilde{q}^2 - m^2)]\, d\tilde{q}$$

Substitution lead immediately to

$$M = C\,(2\pi)^4\,\delta(\tilde{k}_1 - \tilde{k}_3 + \tilde{k}_2 - \tilde{k}_4)/[(\tilde{k}_1 - \tilde{k}_3)^2 - m^2]$$

The four-dimensional delta function -- which becomes a Kronecker delta on averaging -- insures that energy and momentum are conserved, while the term in the denominator indicates that the amplitude depends on the four-momentum transfer squared t. Thus, according to the above, the differential cross section associated with one particle exchange is of the form

$$d\sigma/dt \propto 1/|t-m^2|^2$$

where for simplicity we have omitted all flux and phase-space factors.

5.2 s,t,u Channel Scattering

In addition to the one-particle-exchange mechanisms considered above, the scattering may also proceed through the formation of a metastable bound state, or the exchange of some particle with quantum numbers that effectively convert the target into the projectile, and the projectile into the target. In antiproton-proton scattering the metastable state has the quantum numbers appropriate for a high-

mass boson resonance, and the identity-converting exchange particle the character of a dibaryon state. These collision mechanisms, together with the one analyzed above, are illustrated schematically in Figure 5.2-1. Called, respectively, s-channel t-channel, and u-channel processes, these mechanisms are, of course, indistinguishable experimentally, so that each contributes to the observed cross section. The nature of the contribution follows from the amplitudes for each:

$$M(s) \propto 1/(s - m^2)$$
$$M(t) \propto 1/(t - m^2)$$
$$M(u) \propto 1/(u - m^2)$$

These formulas follow immediately from the t-channel amplitude derived above, and diagrams of Figure 5.2-1. The kinematical quantities s,t,u are defined in the usual way

$$s = (\tilde{k}_1 + \tilde{k}_2)^2 = 4(k^2 + m^2)$$
$$t = (\tilde{k}_1 - \tilde{k}_2)^2 = -2k^2(1 - \cos\theta)$$
$$u = (\tilde{k}_1 - \tilde{k}_4)^2 = -2k^2(1 + \cos\theta)$$

where the right hand formulas hold only in the center-of-mementum for equal mass particles of three-momentum k, and scattering angle θ.

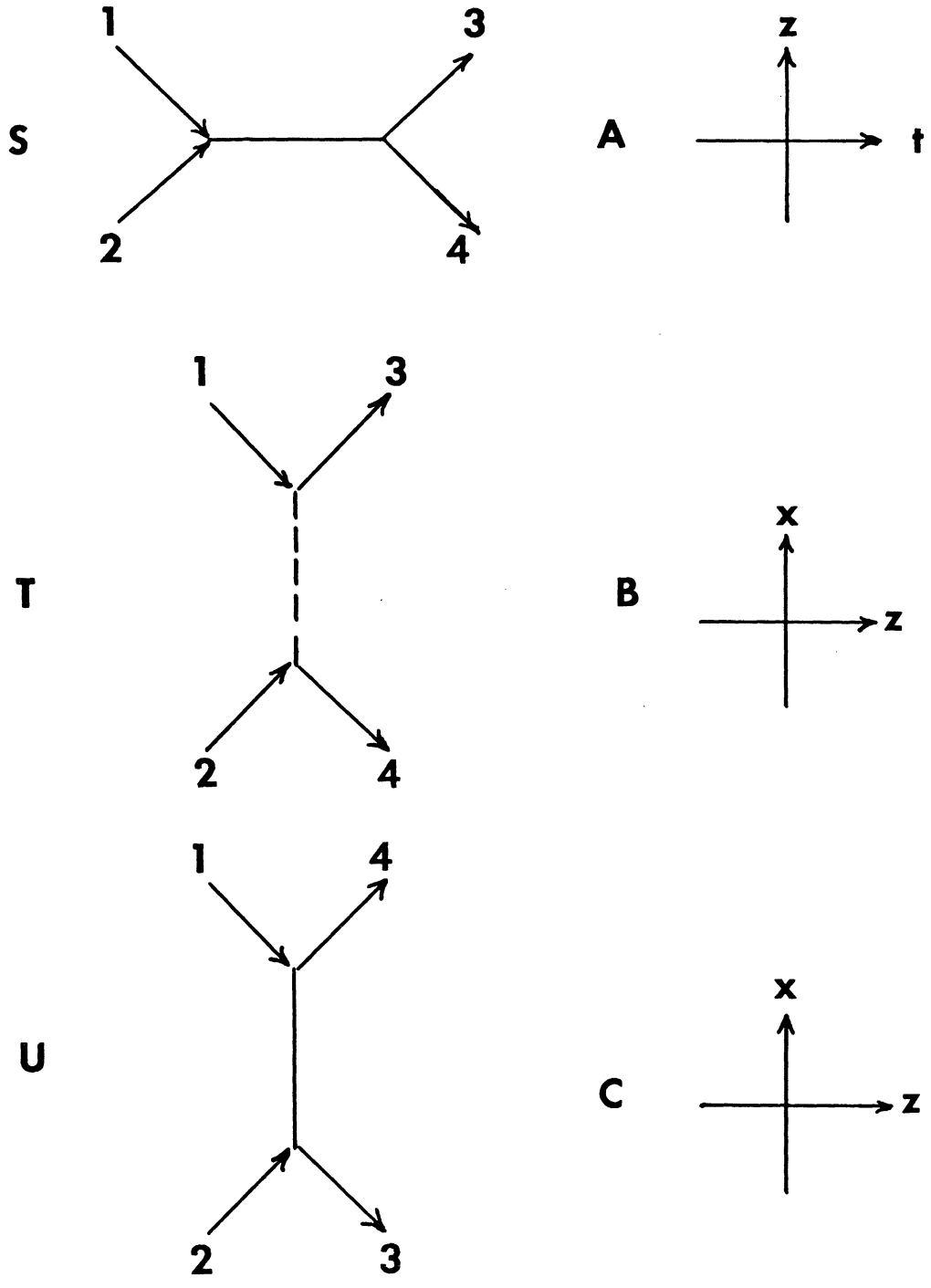

Figure 5.2-1. s-, t-, u-Channel Scattering. For PBAR-P scattering (A) is an s-channel process mediated by heavy meson formation, (B) a t-channel process mediated by light meson exchange, and (C) a u-channel process mediated by heavy dibaryon exchange.

5.3 Absorption Corrections

As noted in the discussion of the optical model, the amplitude $1/(t - m^2)$, which is just the Fourier transform of the Yukawa potential, fails to describe the forward nucleon-nucleon cross section when m is taken as the pion mass. To account for the descrepency Gottfried and Jackson (1964), and Ross and Shaw (1964) argued that the cross section is dominated by absorption into the inelastic channels, rather than simple one-particle exchange. To account for the absorption, Glauber's eikonal picture was invoked, and the scattered amplitude written as

$$f(\Delta) = ik \int_0^\infty \{1 - \exp i\chi(b)\} \; J_o(\Delta b) \; b \; db$$

a formula derived earlier. Gottfried and Jackson then imagined that the eikonal χ consists of two parts, namely, a large imaginary term $\chi_o(b)$ describing the absorption by the inelastic channels, and a smaller real term $\delta\chi(b)$ corresponding to particle exchange. By expanding the exponential in $\delta\chi$, and keeping only the largest term, the above scattering integral becomes

$$f_o(\Delta) = ik \int_0^\infty \{1 - \exp i\chi_o(b)\} \; J_o(\Delta b) \; b \; db$$

Thus, to first order the exchange mechanism makes no contribution to the scattering amplitude. According to all the experimental data, the forward nucleon-nucleon cross section is gaussian in the three-momentum transfer so that as

before

$$f_o(\Delta) = ikA_o \exp(-R_o^2\Delta^2)$$

Inverting the Fourier-Bessel transform above then leads to

$$\{1 - \exp i\chi_o(b)\} = (A_o/2R_o^2) \exp(-b^2/4R_o^2)$$

which, of course, defines the eikonal $\chi_o(b)$.

The same formalism may be applied to inelastic processes such as

$$\pi p \rightarrow \rho p$$

In this case $f(\Delta)$ describes both the usual elastic amplitude, and a pseudo-elastic amplitude associated with the above process, while $\chi(b)$ represents the eikonal generated by the elastic, pseudo-elastic, and inelastic portion of the potential U. Thus, $\chi(b)$ may be divided into three parts, namely, a large imaginary term χ_o describing the absorption by inelastic channels other then rho-p, a small real part $\delta\chi$ arising from the various elastic scattering processes, and another small real part $\delta\chi'$ corresponding to the one-pion-exchange mechanism mediating the above reaction. By expanding the resulting exponentials in $\delta\chi$ and $\delta\chi'$, and looking for the pseudo-elastic terms, one obtains the following amplitude for the rho-p final state:

$$\delta f' = k \int_0^\infty \delta\chi'(b) \exp i\chi_o(b)\, J_o(\Delta b)\, b\, db$$

The Yukawa potential presumably describes the pion exchange, so that the associated (covariant) eikonal looks like:

$$\delta\chi' = (+U_o/2k) \int_{-\infty}^{\infty} [\exp(-mr)/mr]\, dz$$

where $r^2 = b^2 + z^2$, and U_o is a constant. Integrating the expression, and making a large impact-parameter approximation ($mb >> 1$) leads to

$$\delta\chi' = (+U_o/km)\, K_o(mb)$$
$$\simeq (+U_o/2km) \exp(-m^2b^2/4)$$

where K_o denotes the zero-order modified Bessel function of the second kind. Similarly, according to the elastic-scattering results:

$$\exp i\chi_o(b) = 1 - (A/2R_o^2) \exp(-b^2/2R_o^2)$$

Consequently, $\delta\chi'$ suppresses the high-b contributions to $\delta f'$, while χ_o suppresses the low-b ones.

6.0 REGGE THEORY

At high energies many partial waves are required for an accurate description of a forward diffraction peak. In an effort to find a more convergent representation for the scattering amplitude, T. Regge (1959, 1960) converted the usual partial-wave expansion to a contour integral, deformed the path of integration, and then showed that the resulting residues--called Regge poles--looked much like Breit-Wigner resonance forms. The same technique was earlier applied by A. Sommerfeld (1949) to ascertain the tendency of radio waves to propagate beyond the earth's horizon, a process not unlike the tunneling of a projectile through the angular momentum barrier. Subsequent studies[†] of the positive energy solutions to the Schroedinger equation indicated that should a projectile tunnel through an angular momentum barrier, and form a metastable state, a corresponding Regge pole should appear in the scattering amplitude. However, the numerical results of these analyses proved disappointing, presumably because both the true force field, and relativistic nature of the problem were little understood. Consequently, a more empirical approach to

---

[†]See, for example, T. Regge (1959, 1960), M. Froissart (1961), G. Chew, and S. Frautschi (1961, 1962), Chew et al. (1962), S. Frautschi et al. (1962).

the Regge concept evolved, and the residues postulated directly from the experimental observation of resonances.

6.1 Regge-Pole Theory

It is well known that with or without absorption, and regardless of the underlying dynamical mechanism, the field scattered by a spinless interaction may always be written as a sum of partial waves:

$$f(k,\cos\theta) = \sum_{\ell=0}^{\infty} F(k,\ell)\, P_\ell(\cos\theta)$$

where $d\sigma/d\Omega = |f|^2$. To improve the convergence, T. Regge (1959, 1960) decided to analytically continue the coefficients $F(k,\ell)$ into the complex ℓ-plane by replacing the partial-wave sum with a Sommerfeld-Watson transform:

$$f(k,\cos\theta) = -\frac{1}{2\pi i}\int_C \frac{\pi F(k,\alpha)\, P_\alpha(-\cos\theta)}{\sin\pi\alpha}\, d\alpha$$

where the integration contour surrounds (in the clockwise direction) the poles created along the real α-axis by the zeros in $\sin\pi\alpha$. The validity of the transformation follows from the Cauchy residue theorem, and the behavior of the integrand when α approaches an integer value n, that is, $\alpha = n + \delta$, with δ small:

$$\frac{\pi F(k,\alpha)\ \exp(-i\pi\alpha)\ P_\alpha(\cos\ \theta)}{\cos\ \pi n\ \sin\ \pi\delta} \simeq \frac{\pi F(k,n)(-1)^n\ P_n(\cos\ \theta)}{(-1)^n \pi\delta}$$

Thus, the poles in the integrand reproduce the partial-wave analysis term-by-term.

Following Sommerfeld, Regge then deformed the integration contour around the real α-axis, and formed a new straight-line path running parallel to, and one-half unit to the left of the imaginary ℓ-axis, as shown in Figure 6.1-1. In addition, for a wide range of Yukawa-type potentials Regge demonstrated that the only singularities to be expected while deforming the contour were the upper-half plane poles in $F(k,\alpha)$--now known as Regge poles. Thus, according to Cauchy's theorem, the amplitude also has the form:

$$f(k,\cos\ \theta) = -\frac{1}{2\pi i} \int \frac{F(k,\alpha)\ P_\alpha(-\cos\ \theta)}{\sin\ \pi\alpha}\, d\alpha$$

$$+ \sum_j \beta_j\ P_{\alpha_j}(-\cos\ \theta)/\sin\ \pi\alpha_j$$

where $\alpha_j(k)$ denotes the complex-plane location of the j^{th} pole, and $\beta_j(k)$ the residue associated with $F(k,\alpha_j)$. The above formula, called the Regge representation of the scattered amplitude, is valid for all $\cos\ \theta$, namely, also for the unphysical region $\cos\ \theta > 1$.

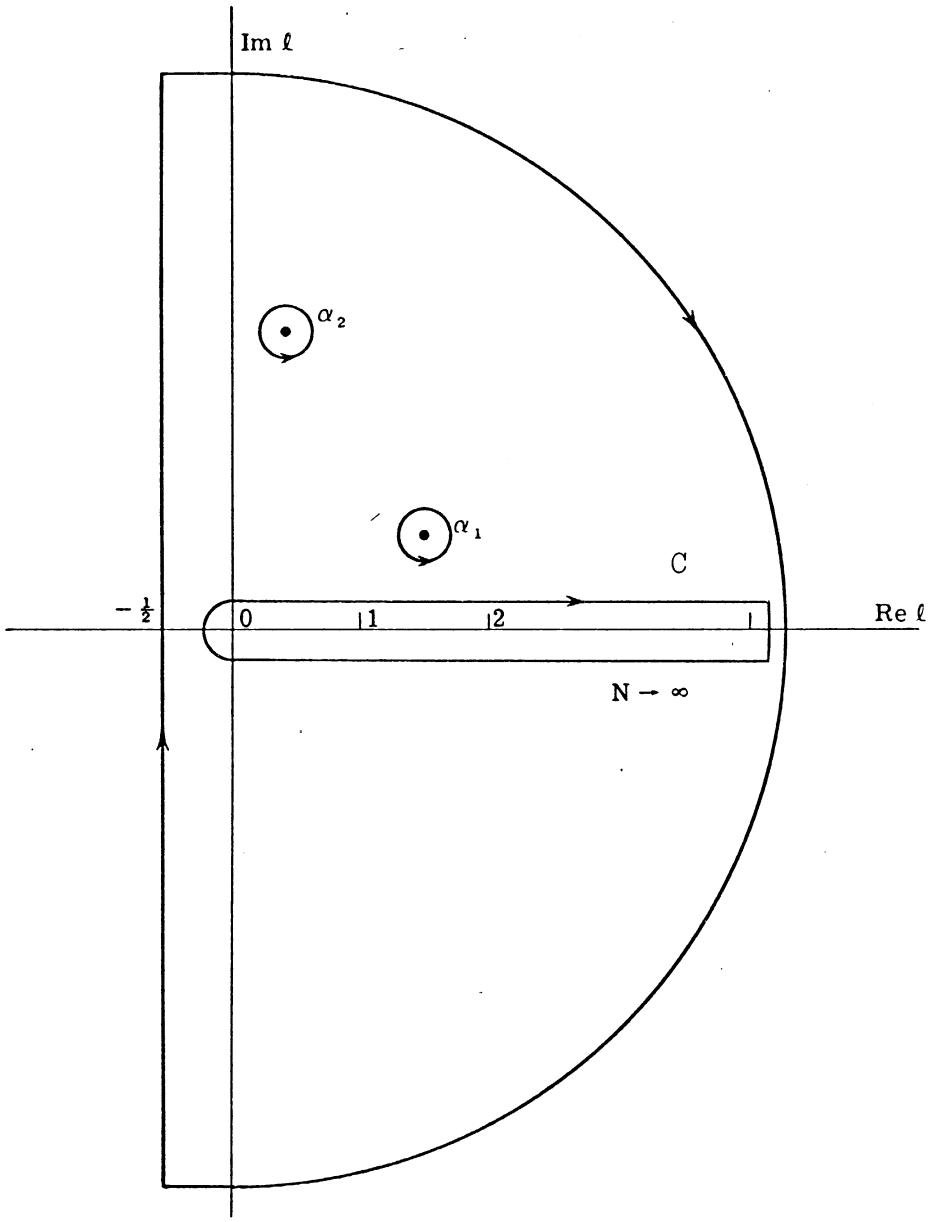

Figure 6.1-1. Regge Contours. Regge deformed the conventional Sommerfeld-Watson contour (C) past the poles α_1, α_2, ... to a new location defined by $\ell = -1/2$.

The physical contribution made by the j^{th} pole is seen by expanding the j^{th} term in the Regge sum into a series of partial waves:

$$f_j(E,\cos\theta) = \sum_{\ell=o}^{\infty} F_j(E,\ell)\, P_\ell(\cos\theta)$$

where k has been replaced by the total CM energy E to simplify the physical interpretation. The coefficients $F_j(E,\ell)$ obtain in the usual way:

$$F_j(E,\ell) = \frac{(2\ell+1)}{2} \int_{-1}^{+1} \frac{\beta\, P_\alpha(-z)}{\sin \pi\alpha} P_\ell(z)\, dz$$

$$= \frac{(2\ell+1)\,\beta}{\pi(\alpha-\ell)(\alpha+\ell+1)}$$

where we have dropped the subscripts j on the right-hand side for simplicity. To interpret $F_j(E,\ell)$ we suppose for some special energy E_o that the Regge pole $\alpha_j(E)$ approaches the integer ℓ; then, we may expand $\alpha_j(E)$ about $(E-E_o)$ to obtain

$$\alpha_j(E) \simeq \ell + a(E - E_o) + ib$$

where, of course,

$$a = \mathrm{Re}\,[\partial\alpha_j(E_o)/\partial E\,], \quad b = \mathrm{Im}\,\alpha(E_o)$$

Substitution of this linearized form into the formula for $F_j(E,\ell)$ yields for the ℓ^{th} term of the partial-wave expansion:

$$F_j(E,\ell)\ P_\ell(\cos\ \theta) = \frac{\beta(E)\ P_\ell(\cos\ \theta)}{\pi a(E-E_o+ib/a)}$$

This is recognized as the well-known Breit-Wigner formula for a resonant amplitude of mass E_o, spin ℓ, and width Γ, $\Gamma/2 = b/a$.

The above suggests that we may associate Regge poles with the formation of resonant states in the amplitude. Should, moreover, $\alpha_j(E)$ approach several different integers ℓ_1, ℓ_2, ... at several different energies E_1, E_2, ... the same Regge pole will generate resonance structure at different projectile energies, and in different angular-momentum states. In fact, the path $\alpha_j(E)$ generated in the complex ℓ-plane by varying the CM energy E--with the resonance points $\alpha_j(E_1)$, $\alpha_j(E_2)$, ... clearly demarked--is called a Regge trajectory. That more than one resonance should appear on a Regge trajectory appears reasonable if one considers a radial potential U(r) that generates a well-defined angular momentum barrier, such as a square-well potential of radius R and depth U_o. In this case the radial portion of the relativistic Schroedinger equation,

$$[\frac{1}{r^2}\frac{d}{dr}(\frac{1}{r^2}\frac{d}{dr}) + k^2 - \frac{\ell(\ell+1)}{r^2} - U(r)]\psi(r) = 0$$

allows one to speak of an effective potential 'U' consisting of the square-well, and a centrifugal term:

$$'U' = U(r) + \frac{\ell(\ell+1)}{r^2}$$

as sketched in Figure 6.1-2. Viewed as a one-dimensional problem, the projectile on encountering the angular momentum barrier will either be reflected back from it, or burrow through to the valley formed between the origin and the radius r = R. While in this region the projectile will shuttle back and forth on the valley slopes until it penetrates the barrier to escape once again as a free particle. Should such temporary bending occur at a specific energy E_o, then resonance like structure would be expected in the ℓ^{th} partial wave in the scattered amplitude. Similarly, the system may also evidence structure for other values of the angular momentum ℓ_1, ℓ_2, ... at the energies E_1, E_2, ...

As noted by Frautschi, et al. (1962), the potential binding the resonating particles generally depends on the orbital parity of the state. The exchange forces giving rise to such potentials tend to raise or lower the energy of the observed resonances as ℓ is even or odd. Viewed as a perturbation, such exchange forces lead to an

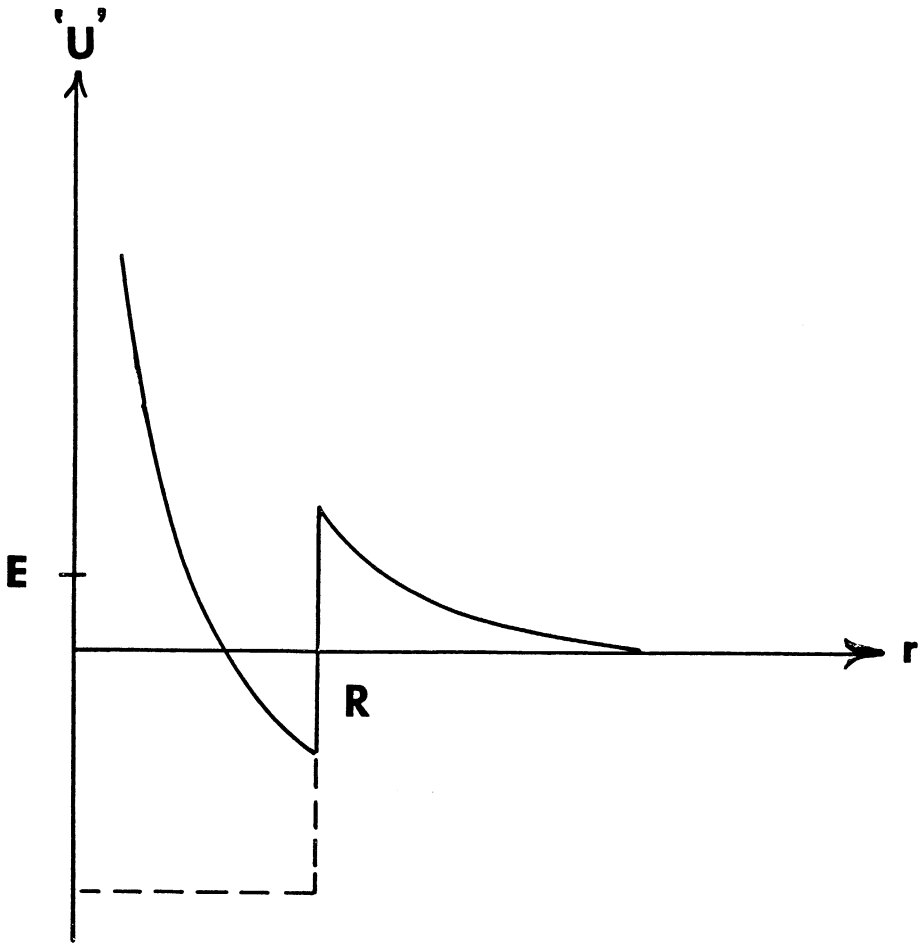

Figure 6.1-2. Angular-Momentum Barrier. The effective potential 'U' consists of a square-well part, and a centrifugal term. Projectiles with $\ell(\ell+1)/R^2 > k^2 > 0$ may penetrate the cusp of the angular-momentum barrier, and enter the valley to the left of r = R. The dotted line indicates the shape of the square-well.

interaction potential containing two parts:

$$U(\vec{x}) = U_o(\vec{x}) + (-1)^{\ell} U_e(\vec{x})$$

where $U_o(\vec{x})$ specifies the dominant portion of the potential, $U_e(\vec{x})$ denotes the exchange-force part, and $(-1)^{\ell}$ describes the direction of the mass splitting. For similar reasons, the resonance masses predicted by the Regge residues are expected to be lower or higher as ℓ is even or odd. In fact, it is customary to note this possibility explicitly by separating the even and odd parts in the residue:

$$\beta\, P_\alpha(-\cos\theta)/\sin\pi\alpha = \beta/2[P_\alpha(-\cos\theta) + P_\alpha(+\cos\theta)]/\sin\pi\alpha + \beta/2[P_\alpha(-\cos\theta) - P_\alpha(+\cos\theta)]/\sin\pi\alpha$$

The two terms are then considered separate trajectories, and given a separate quantum number, called the "signature," to distinguish them. Using the identity:

$$P_\alpha(z) = \exp(i\pi\alpha)\, P_\alpha(-z)$$

The even and odd trajectories take the useful form:

$$\text{Even} = \beta/2[1 + \exp(i\pi\alpha)]\, P_\alpha(-\cos\theta)/\sin\pi\alpha$$

$$\text{Odd} = \beta/2[1 - \exp(i\pi\alpha)]\, P_\alpha(-\cos\theta)/\sin\rho\alpha$$

In the direct or resonance forming channel, the

Regge trajectory serves both as a classification device for studied particles, and a predictive technique for the masses and spins of the unobserved ones. In practice, only the real part of $\alpha(E)$--the spin of the resonance--can be measured directly, so that one normally uses a Chew-Frautschi (1962) plot of spin versus mass-squared as a classification device. Such plots then link particles with the same internal quantum numbers (baryon number, strangeness, isospin, intrinsic parity, etc.), but with different signatures and spins. Joined with SU(3) symmetry, which classifies particles having equal spins, but different isospin and strangeness, the two schemes allow one to step among resonance states having different signature, spin, isospin, and strangeness. According to R. Arnold (1965), in a bootstrap picture where meson resonances are viewed as (physical or unphysical) bound states of the antinucleon-nucleon system, one expects little in the way of exchange splitting as this would necessarily entail the exchange of a relatively massive dibaryon state. On the other hand, V. Barger (1968) observes that exchange splitting for pion-nucleon resonances tends to be large--about 250 MeV --ostensibly because in a bootstrap picture the relatively light excited-nucleon states mediate the exchange process.

When applied to the reaction in the crossed, or particle exchange channel, Regge theory serves as a method for examining the asymptotic behavior of the forward differential cross section. The amplitude generated in the crossed channel by a Regge trajectory in the direct channel obtains, basically, by writing the residue as a function of the invariants s and t, and then exchanging them in the resulting expression. For elastic scattering in the direct channel

$$-\cos(s,t) = \frac{2t}{4m^2 - s} - 1$$

so that at high ($2s >> 4m^2 - t$) energies in the crossed channel this argument becomes

$$-\cos(t,s) = \frac{2s}{4m^2 - t}$$

The Legendre polynomials which appear both in the residues and the background integral, grow geometrically for large arguments z:

$$P_\alpha(z) \sim \frac{(2\alpha)!}{2^\alpha\ \alpha!\ \alpha!}\ z^\alpha$$

where the gamma function $\Gamma(x) = (x-1)!$ defines the factorial for non-integer values of x. Thus, for large s

in the cross channel, the background integral falls off as $s^{-1/2}$, and the amplitude is dominated by the trajectory having the largest Re α. Dropping the signature factor, we write this residue as ($s_o = 4m^2$)

$$\frac{\sqrt{t}\ \beta\ (2\alpha)!}{\sin \pi\alpha\ 2^{\alpha}\alpha!\alpha!}\left(\frac{s}{4m^2 - t}\right)^{\alpha} = A(t)\,(s/s_o)^{\alpha(t)}$$

(The square root of t appears because crossing symmetry applies only to the covariant portion of the direct channel amplitude, namely, $\sqrt{s}\ f(s,t)$ which on crossing becomes $\sqrt{t}\ f(t,s)$.) The differential cross section associated with this amplitude is then

$$d\sigma/d\Omega = (1/s)\left|A(t)\,(s/s_o)^{\alpha(t)}\right|^2$$

or equivalently

$$d\sigma/dt = (\pi/p^2)\ d\sigma/d\Omega \simeq (4\pi/s)\ d\sigma/d\Omega$$
$$= 4\pi\left|A(t)\right|^2 \exp\{[2\alpha(t)-2]\ln(s/s_o)\}$$

since $s = 4(p^2 + m^2) = 4p^2$ at high energies.

The high-energy proton-proton scattering data indicates that 1) at t=0 $d\sigma/dt$ tends to a constant, 2) the diffraction peak is exponential in t, and shrinks with increasing s, 3) the forward scattering amplitude is mostly imaginary, 4) the total cross section tends

to a constant with large s. According to the above formula for $d\sigma/dt$, the differential cross section will appear constant at t = 0 if

$$\alpha(0) = 1.0$$

Exponentiality in t obtains if to first order

$$\alpha(t) = 1 + 10t$$

and (decreasing) shrinkage results directly from the $\ln(s/s_o)$ in the exponent. The forward cross section will appear mostly imaginary if the signature of the leading trajectory is even, since 1) according to R. Arnold (1966) $\alpha(t)$ and $\beta(t)$ are real for negative t, and 2) for any even signature trajectory near t=0:

$$[1 + \exp(i\pi\alpha)]/\sin \pi\alpha \simeq i/2$$

Moreover, according to the optical theorem

$$\sigma_t(s) = 4\pi[A(0)(s/s_o)^{\alpha(0)}]/kM$$

$$\simeq 4\pi A(0)(s/s_o)^{\alpha(0)-1}$$

so that the total cross section tends to a constant with increasing s if $\alpha(0) = 1$, a requirement consistent with, but independent of the one obtained above.

Known as the Pomeranchan, or vacuum trajectory,

the pole is also credited with mediating pion-nucleon collisions, and thus assigned zero baryon number, zero strangeness, zero isospin. (The well-established $f^{o}(1250)$ with $J^{P}I^{G} = 0^{+}2^{+}$ likely represents the exchange-degenerate J=2 entry on this trajectory. (R. Arnold [1965])

6.2 Application of Regge-Pole Theory

At non-asymptotic energies other direct channel residues may contribute to the cross channel amplitude. In fact, the charge-exchange collision

$$\pi^{-}p \rightarrow \pi^{o}n$$

forbids Pomeranchon exchange altogether, and thus must be mediated by some other trajectory. The allowed exchange particles clearly must have non-zero isospin, and positive G-parity, and in coupling to the pi-pi system conserve parity

$$P(\pi^{-}\pi^{o}) = (-1)^{J}$$

In addition, Bose statistics, as imposed through the generalized Pauli principle, restrict the exchange particle to negative signatures:

$$\text{signature} = (-1)^{J} = (-1)^{I}$$

since no mesons with I > 1 are currently known. Taken together the last two conditions imply that the exchange trajectory must have $J^P = 1^-, 3^- \ldots$ the only established mesons satisfying all these restrictions are the $\rho(760; 1^-, 1^+)$, and $\rho(1620; 3^-, 1^+)$.

The amplitude mediating the pion-nucleon charge-exchange process contains, of course, both non-flip and spin-flip parts. The Regge residue associated with the spin-flip processes obtains in the usual way by applying a Sommerfeld-Watson transform to the partial-wave analysis of the direct-channel spin-flip amplitude:

$$\gamma(s)\ P_\alpha^1(-\cos\theta)$$

where, like $\beta(s)$, $\gamma(s)$ is the residue associated with the pole. For large z the first order Legendre polynomial grows as

$$P_\alpha^1(z) \sim \frac{-i(2\alpha)!\ \alpha}{2^\alpha \alpha!\ \alpha!}\, z^{\alpha-1}$$

Thus, in the cross channel the spin-flip Regge amplitude takes the form:

$$\frac{-i\sqrt{t}\ \gamma\ (2\alpha)!\ \alpha}{\sin\pi\alpha\ 2^\alpha \alpha!\ \alpha!}\left(\frac{2s}{4m^2-t}\right)^{\alpha-1} = B(t)\ \alpha(t)\,(s/s_o)^{\alpha(t)-1}$$

The latter form is also valid for collisions between particles of unequal mass.

Several measurements of the pion-nucleon charge-exchange cross section exist in the range 6-18 GeV/c. At each energy the differential cross section appears to first rise from its $|t|=0$ value to an absolute maximum in the general vicinity of $|t|=.05$ $(GeV/c)^{+2}$, and then drop exponentially until $|t|=0.5$ $(GeV/c)^{+2}$, where a distinct dip-bump sequence commences. (See Figure 6.2-1a.) A linear best-fit by Hohler et al. (1966a) to the exponential portion of the forward peak indicates that $\alpha(t) = .57 + .91t$. Extrapolated back into the direct channel ($s>0$), this trajectory passes close to the $\rho(760)$ pole as shown in Figure 6.2-1b, thus reaffirming the earlier conclusion that the charge-exchange process is mediated by rho-exchange. The peculiar dip in the cross section near $t=0$ is usually credited to a spin-flip amplitude vanishing in the forward direction. Moreover, the spin-flip amplitude in the cross channel vanishes when $\alpha(t)$ vanishes, namely at $|t|=0.6$ $(GeV/c)^{+2}$, thus generating a dip-bump sequence in the differential cross section, and presumably also

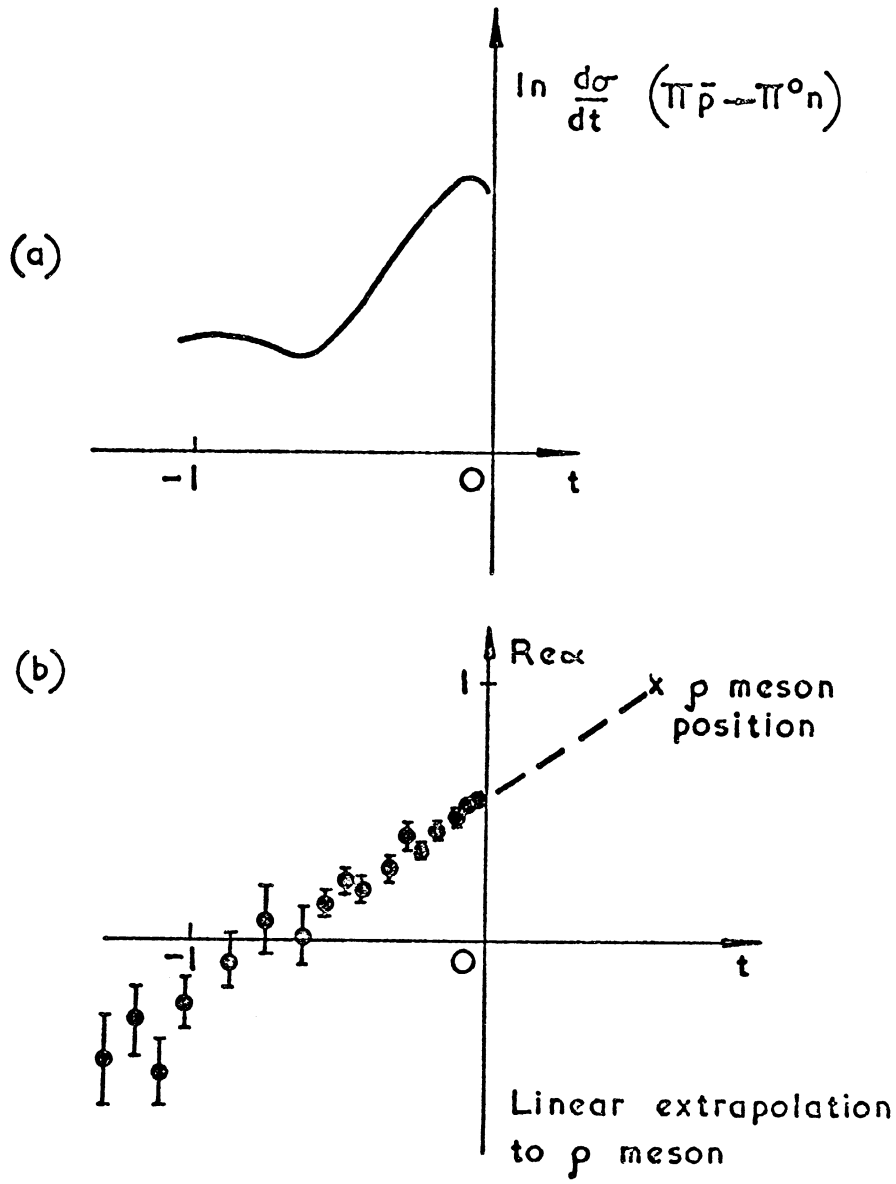

Figure 6.2-1. Rho-Trajectory and Charge-Exchange Scattering. Here (b) shows a Chew-Frautchi plot of the $\rho(760)$ trajectory in both the direct channel ($t > 0$), and the cross channel ($t < 0$) regions, and (a) a sketch of the pion-nucleon charge-exchange data, as taken from R.N. Phillips (1966).

a one-cycle oscillation in the polarization, as observed in elastic pion-nucleon scattering (S. Suwa, et al. [1965, 1966]).

In P-P and PBAR-P elastic scattering, any or all of the leading trajectories may contribute to the scattering amplitude, thus making these processes difficult to analyze quantitatively, although some qualitative remarks are possible. Experimentally, the PBAR-P forward peak antishrinks with increasing s, in direct contrast to the P-P scattering results, and the predictions of Pomeranchon exchange. In addition, the PBAR-P cross section contains a pronounced dip-bump sequence around $|t|=0.5$ $(GeV/c)^{+2}$, while the P-P cross section appears quiet in this region, but shows some dipping at $|t|=3.0$ $(GeV/c)^{2}$ (C. Akerlof, et al. [1967]), and substantial polarization activity around $|t|=0.3$ $(GeV/c)^{+2}$ (P. Grannis, et al. [1966]). With respect to PBAR-P data, it is tempting to interpret the dip-bump structure at $|t|=0.6$ $(GeV/c)^{+2}$ as the vanishing of a spin-flip amplitude associated with the rho-trajectory. If this interpretation is correct, then according to Frautschi (1966) one expects 1) the dip-bump sequence (being associated with a secondary trajectory) to go away with increasing s, as it does, for example, in pion-nucleon scattering

(C. Coffin, et al. [1966]), and 2) the polarization should fluctuate substantially in the general vicinity of the minimum, also as in pion-nucleon scattering (S. Suwa, et al. [1965, 1966]). However, as noted by W. M. Katz, et al. (1967), the ratio of the differential cross section at the secondary maximum to that at the first minimum remains fairly constant in s, a result also confirmed at higher energies by T. Kitagaki, et al. (1968), and A. Ashmore, et al. (1968). Similarly, recent polarization measurements by C. Daum, et al. (1968) show no regular oscillatory structure in the region of the first minimum.

In an effort to explain the antishrinking observed in the PBAR-P forward peak, Frautschi (1966) has also argued that secondary trajectories of opposite signature, and C-eigenvalue tend to cancel in P-P scattering, and add in PBAR-P. For definiteness in discussing this argument we suppose both scattering processes are dominated by a purely imaginary, signatureless Pomeranchon trajectory, but are also modified by the exchange of the $\rho(760)$ trajectory with its negative signature, and negative C-eigenvalue, and by the exchange of the $A_2(1300)$ trajectory with its positive signature

and positive C-eigenvalue. The amplitudes for the PBAR-P, and P-P exchange processes are not independent, but linked by crossing symmetry, and crossing symmetry plus charge-conjugation, respectively, to the direct-channel PBAR-P amplitude, as shown in Figure 6.2-2. According to rough plots by Arnold (1965) in the direct channel ($s>0$), and by Frautschi (1966) in the cross channel ($s<0$), the trajectories for the ρ and A_2 both have $\alpha(t) = 1/2 + \alpha_1 t$, while for the Pomeranchon $\alpha(t) = 1 + \alpha_1 t$. In the direct channel the reality of $\beta(t)$, the presence of two identical interaction vertices, and the optical theorem combine to guarantee that all three amplitudes have a positive imaginary part at $t=0$. Thus, the (covariant) scattering amplitude in the cross channel near $t=0$ assumes the basic form:

$$iA(P)(s/s_o) \pm 1/2[1 - \exp(i\pi/2)]\, A(\rho)(s/s_o)^{1/2} + 1/2[1 + \exp(i\pi/2)]\, A(A_2)(s/s_o)^{1/2}$$

where the plus (minus) sign refers to P-P (PBAR-P) elastic scattering, and $A(P) >> A(\rho) \simeq A(A_2) > 0$. Even for $A(\rho) = A(A_2)$, the ρ and A_2 amplitudes fail to cancel as they are 90 degrees out of phase. However, their (much larger) cross terms with the Pomeranchon amplitude are seen to cancel for P-P, and add for PBAR-P, as asserted by Frautschi.

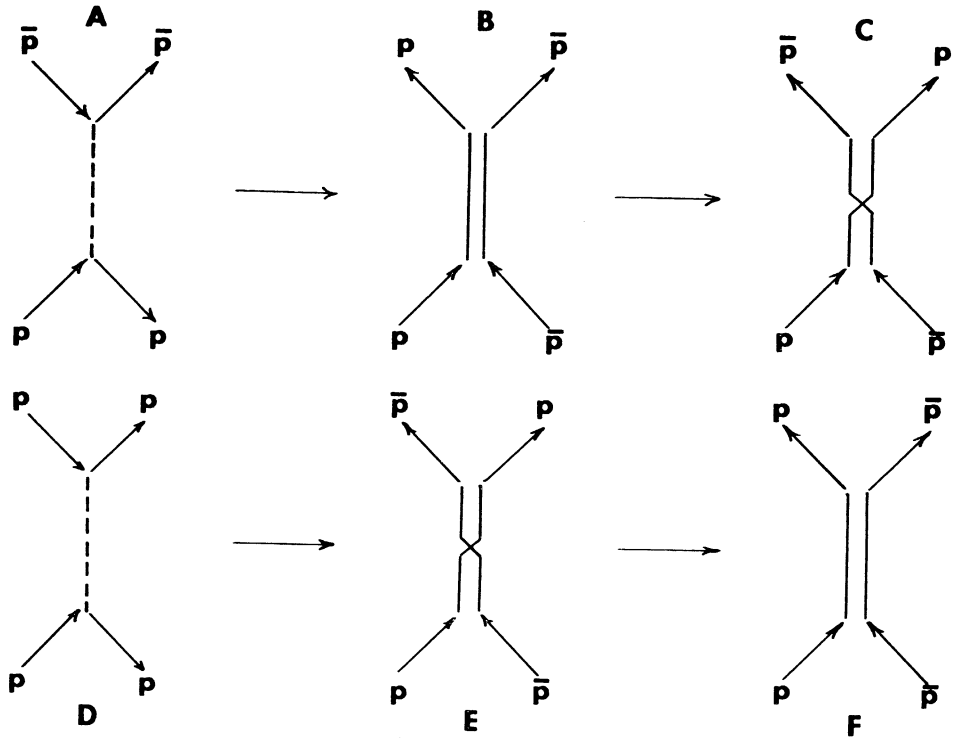

Figure 6.2-2. Crossing Symmetry and Charge Conjugation. Crossing symmetry sends (A) to (B), and (D) to (E). Charge conjugation applied to the mediating meson sends (B) to (C), and multiplies the amplitude by the C-eigenvalue of the meson. Charge-conjugation applied to the P-PBAR final state of (E) sends it to the PBAR-P state of (F), and multiplies the amplitude by the C-eigenvalue of the mediating meson, since C is conserved at strong-decay vertices.

6.3 Regge-Cut Theory

As noted above, by exchanging a ρ-trajectory between the projectile and target one is able to fit both the small forward dip, and pronounced first minimum in pion-nucleon charge-exchange scattering. However, in an earlier calculation it was found that the ρ-production process $\pi p \to \rho n$ could be treated with a one-pion exchange model only if substantial absorption were applied to the incident, and scattered waves. These results then raise the question as to whether absorption corrections are part-and-parcel of the Regge-pole theory, or should be added to the various Regge-exchange amplitudes by methods similar to those used to embellish the one-particle-exchange model. Actually, as clarified by Arnold (1965) either position is tenable, depending on whether one treats absorption as an *ad hoc* phenomenon in all channels, or regards all channels as connected (by unitarity) to the elastic one, and hence subject to the same absorption as described by the Pomeranchon trajectory. In either case, recent papers[†] make it clear that unadorned Regge-exchange amplitudes, like their

---

[†] See, for example, R. Arnold (1965, 1967), G. Cohen-Tannoudji, *et al.* (1967), E. J. Squires (1968), J.N.J. White (1968), F. Henney, *et al.* (1968a, 1968b).

one-particle-exchange counter-parts, require corrections for absorption losses. In this connection, one then regards the absorption as reflecting the physical structure of the colliding bodies, and the basic Regge amplitude $A(t)(s/s_o)^{\alpha(t)}$ as describing the reoccurrence, and metastable nature of the exchanged resonances.

Absorption may be incorporated into a Regge-exchange model by either extending--as we do here--the eikonal picture presented earlier, or invoking the covariant S-matrix formulas of N. Sopkovich (1962). The eikonal treatment proceeds from Arnold's conjecture (1965) "that at energies above a few BeV, the effective optical potential is to be given by (the Fourier-Bessel transform) of the leading Regge poles." This argument follows in a natural way from the eikonal approximation for the elastic scattering amplitude:

$$f_o(s,\Delta) = ik \int_0^\infty [1 - \exp i\chi_o(b)]\, J_o(\Delta b)\, b\, db$$

$$\simeq k \int_0^\infty \chi_o(b)\, J_o(\Delta b)\, b\, db$$

According to Arnold's conjecture, then, the eikonal $\chi_P(\Delta)$ to be associated with the Pomeranchon amplitude $A_P(\Delta)(s/s_o)^{\alpha_P(t)}$ is specified by inverting the above transform:

$$kM\ \chi_P(b) = \int_0^\infty A_P(\Delta)\ (s/s_o)^{\alpha_P(\Delta)}\ J_o(\Delta b)\ b\ db$$

where M makes both sides covariant. It is also possible to specify the forward elastic pion-nucleon scattering amplitude phenomenologically. In this case one notes that the forward amplitude is mostly imaginary, decreases exponentially with t, and evidences little, if any, shrinkage:

$$ikM[1 - \exp i\chi_o(b)]$$

$$= \int_0^\infty ikMA_o \exp(-R_o^2\Delta^2)\ J_o(\Delta b)\ \Delta\ d\Delta$$

$$= (ikMA_o/2R_o^2)\ \exp(-b^2/4R_o^2)$$

as already noted in Section 4.1 above.

Similarly, according to Arnold's conjecture, the eikonal χ_ρ for the charge-exchange process is just the Fourier-Bessel transform of the ρ-trajectory amplitude:

$$kM\ \chi_\rho(b) = \int_0^\infty A_\rho(\Delta)\ (s/s_o)^{\alpha_\rho(\Delta)}\ J_o(\Delta b)\ b\ db$$

As discussed earlier, $A_\rho(\Delta)$ varies little with Δ, and $\alpha_\rho(\Delta)$ appears linear in Δ^2:

$$A_\rho(\Delta) = \text{constant} = \sqrt{s_o}\ A_1$$

$$\alpha_\rho(\Delta) = 1/2 - R_1^2\Delta^2$$

Substitution in the integral formula for χ_ρ then yields

$$kM\,\chi_\rho(b) = \int_0^\infty MA_1 \exp[-R_1^2\,\Delta^2\,\ln(s/s_o)]\,J_o(\Delta b)\,\Delta\,d\Delta$$

$$= [MA_1/2R_1^2\,\ln(s/s_o)]\exp[-b^2/4R_1^2\,\ln(s/s_o)]$$

The absorption-corrected Regge-exchange amplitude for charge-exchange scattering then follows from the usual eikonal perturbation formula:

$$f_\rho(s,\Delta) = k\int_0^\infty \chi_\rho(b)\,\exp i\chi_o(b)\,J_o(\Delta b)\,b\,db$$

$$= A_1\exp[-R_1^2\,\Delta^2\,\ln(s/s_o)]$$

$$- A_2\exp[-R_2^2\,\Delta^2]$$

where

$$A_2 = A_oA_1/2[R_o^2 + R_1^2\,\ln(s/s_o)]$$

$$R_2 = R_o^2R_1^2\,\ln(s/s_o)/[R_o^2 + R_1^2\,\ln(s/s_o)]$$

so that the second term vanishes at high energies. According to R. Arnold (1965) the dip observed at $|t|=0.6$ $(GeV/c)^2$ in charge-exchange scattering arises from destructive interference between these two terms.

The first term in the expression for $f_\rho(s,\Delta)$ is just the Regge-pole amplitude associated with ρ-exchange. The second term is more subtle, but may be viewed as

arising from a Regge-cut, rather than a Regge pole. To show this we consider the identity†

$$A_2 \exp(-R_2^2\Delta^2) = 2\pi \int_0^\infty A_o \exp[-R_o^2(\vec{\Delta}-\vec{\Delta}')^2] \cdot A_1 \exp[-R_1^2\vec{\Delta}'^2 \ln(s/s_o)]\, d\vec{\Delta}'$$

Looking at just the covariant portion of the expression, and defining a weighting function:

$$W(\vec{\Delta}) = A_o \exp(-R_o^2\Delta^2)$$

leads to the recognizable form:

$$(s/s_o)^{1/2} A_2 \exp(-R_2^2\Delta^2) = 2\pi \int W(\vec{\Delta}-\vec{\Delta}')\, A_\rho (s/s_o)^{\alpha_\rho(\vec{\Delta}')}\, d\vec{\Delta}'$$

where A_ρ and α_ρ are defined above. Written in this form the amplitude appears generated by Regge cut, i.e., a superposition, or continuum of Regge poles, each weighted according to $W(\vec{\Delta})$. As pointed out by F. Henyey, et al. (1968A) such Regge cuts may be interpreted as a double scattering mechanism, where the absorption represents one scatter, and the Regge-trajectory exchange the other.

---

†The expression is generally valid:

$$\int_0^\infty A(b)\, B(b)\, J_o(\Delta b)\, b\, db = 2\pi \hat{A}(\vec{\Delta}) * \hat{B}(\vec{\Delta}),$$

where the circumflex denotes Fourier-Bessel transformation, and the asterisk two-dimension convolution.

It is also possible to rework Frautschi's (1962) arguments in a Regge-cut picture. In this case the dip observed at $|t| = 0.5$ in PBAR-P elastic scattering is credited to destructive interference between the Pomeranchon and Regge-cut amplitudes, while its anti-shrinking results because secondary trajectories of opposite signature, and C-eigenvalue cancel in P-P, but add in PBAR-P scattering. That the Regge-cut amplitude looks like a double scattering mechanism follows from the double-exchange diagram of Figure 6.3-1. The first exchange, denoted with D, represents momentum transferred through ordinary diffraction scattering, and thus gives rise to an amplitude

$$A_o \exp(-R_o^2 \Delta^2)$$

The second exchange, denoted with an R, represents, for example, the exchange of a ρ-trajectory, and thus contributes an amplitude

$$A_\rho (s/s_o)^{\alpha_\rho(\Delta)}$$

The amplitude for both processes obtains by averaging over all momentum transfer combinations; that is,

$$2\pi A_o \exp(-R_o^2 \vec{\Delta}^2) * A_\rho (s/s_o)^{\alpha_\rho(\vec{\Delta})}$$

$$= (s/s_o)^{1/2} A_2 \exp(-R_2^2 \vec{\Delta}^2)$$

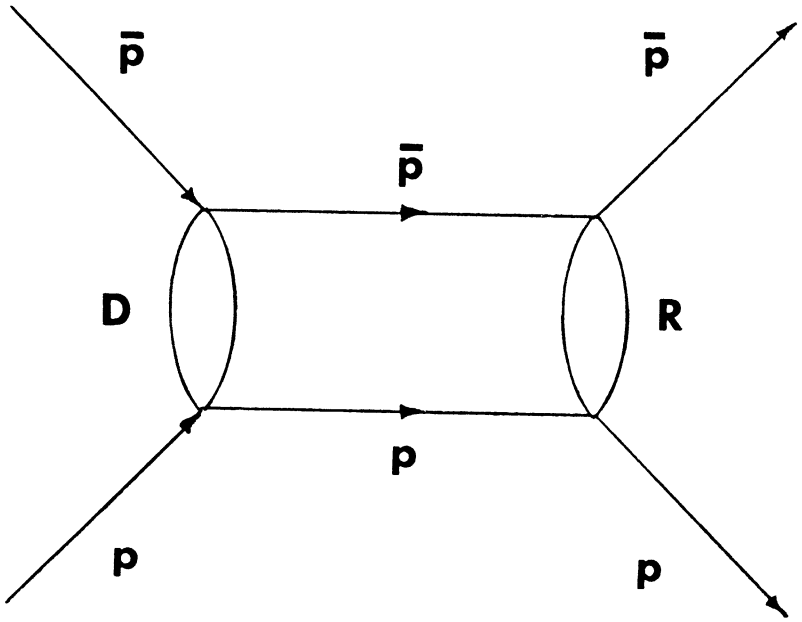

Figure 6.3-1. Regge-Cut Diagram. The first exchange, denoted by D, represents momentum transfered by diffraction scattering, and the second, denoted by R, shows momentum transferred through Regge-trajectory exchange.

Since this is just the Regge-cut amplitude written convolution notation, the double-scattering concept is seen to be equivalent to the eikonal picture used heretofore.

6.4 Application of Regge-Cut Theory

As noted earlier the one-nucleon-exchange picture fails to describe the forward PBAR-P elastic cross section. Similar difficulties arise when the exchanged nucleon is replaced by a nucleon-isobar trajectory. On the other hand, one moderately successful picture originally suggested by R. Arnold (1967), but modified here, credits the difference between P-P and PBAR-P scattering to double baryon exchange. The double baryon exchange is in turn derived by approximating the multiperipheral diagram of Figure 6.4-1A with the simpler diagram of Figure 6.4-1B. An amplitude for the latter process obtains by averaging momentum transfered through the first exchange, and momentum transfered by the second. Assuming the exchange of a nucleon-isobar trajectory then leads to the convolution integral

$$2\pi \int A_1(s/s_o)^{\alpha_1(\vec{\Delta}-\vec{\Delta}')}\ A_1(s/s_o)^{\alpha_1(\vec{\Delta}')}\ d\vec{\Delta}'$$

The trajectory $\alpha_1(t)$ is presumably the same one that mediates backward pion-nucleon elastic scattering, and

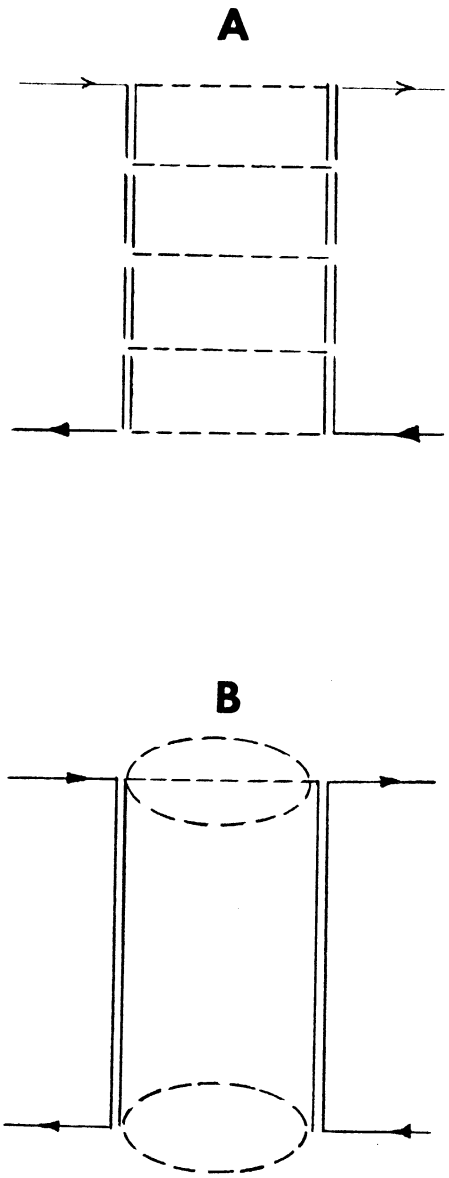

Figure 6.4-1. Baryonic Multiperipheral Diagram. (A) The vertical legs of the diagram indicate nucleon-isobar trajectories, and the horizontal rungs meson trajectories. (B) Here the various rungs have been grouped into two meson-trajectory fireballs.

as such has the linear form:

$$\alpha_1(\Delta) = \alpha_o - R_1^2\Delta^2$$

$$\alpha_o = .15,\ R_1^2 \simeq R_o^2 = 5.0\ (\text{GeV/c})^{-2}$$

That is, the slope of the pion-nucleon backward peak resembles that for forward P-P scattering.

The eikonal to be associated with double baryon exchange obtains through Fourier-Bessel transformation:

$$\chi(k,b) = i(1/kM)^2 A_1^2 (s/s_o)^{2\alpha_o} \exp(-b^2/2R_o^2)/(2R_o^2)^2$$

where the extra factor (1/kM) is the intermediate phase-space factor quoted by Arnold (1967). At low energies the amplitude corresponding to this eikonal may be expected to dominate the usual high-energy one:

$$f_o(k,\Delta) = i(k\sigma_t/4\pi)\ \exp(-R_o^2\Delta^2)$$

In particular, the amplitude will look like

$$f(k,\Delta) = ik \int_0^\infty \{1 - \exp i\chi(k,b)\}\ J_o(b\Delta)\ b\ db$$

where $\chi(k,b)$ is given above.

The exponent in the braces, which defines the radius of the interaction, and hence the slope of the forward peak, drops to 1/e of its maximum value when

$$(1/kM)^2 A_1^2 \ (s/s_o)^{2\alpha_o} = (2R_o^2)^2 \exp(+\ b^2/2R_o^2)$$

At low energies, or small k the left-hand side is large, so that a relatively large value of b is needed to satisfy the inequality

$$b^2 >> 2R_o^2$$

while at higher energies the opposite is true:

$$b^2 << 2R_o^2$$

This indicates that where the formula for $f(k,\Delta)$ holds the PBAR-P cross section will evidence material anti-shrinking. In addition, when the factor enclosed by the braces vanishes, the incident amplitude will be striking an opaque scattering structure, and σ(elastic)/σ(total) = 1/2, as observed experimentally around 1 GeV/c.

At higher energies the term in braces can be expanded to first order in the eikonal

$$f(k,\Delta) = ik(1/kM)^2 A_1^2 \ (s/s_o)^{2\alpha_o} \exp(-R_o^2\Delta^2/2)/2(2R_o^2)$$

The forward peak defined by this formula is twice as wide as the high-energy one, so that the form appears inconsistent with experiment. However, Arnold (1967) argues that before this expansion is valid, the high-

energy amplitude quoted above becomes operational, and dominates the forward scattering amplitude.

The low-energy amplitude may also be credited to absorption from nucleon-isobar exchange:

$$\chi(k,b) = (i/kM)\ A_1\ (s/s_o)^{\alpha_o}\ \exp(-b^2/4R_1^2)/(2R_o^2)$$

and antishrinking appears as before. At higher energies where the exponent in the braces can be expanded to first order in this eikonal, the amplitude looks like

$$f(k,\Delta) = iA_1(s/s_o)^{\alpha_o}\ \exp(-R_o^2\Delta^2)/M$$

Here the width of the forward peak approximates that expected at high-energies, so that a smooth transition between low and high energy behavior obtains. Although nucleon-isobar exchange, being the lower order process, seems more attractive than the double baryon exchange suggested by Arnold (1967), the two mechanisms remain indistinguishable with present experimental and theoretical knowledge.

7.0 NATURE OF THE EXPERIMENT

The present experiment was conceived largely as an exploratory search for non-strange boson resonances. Consequently, large-angle scattering was considered of special interest, since the low background present at these scattering angles make it particularly sensitive area for detecting direct-channel resonances. In fact, assuming no interference develops with the background, the enhancement expected in the elastic cross section due to the formation and decay a resonance of spin J, and elasticity K is given by

$$\sigma(\text{resonance}) = (\pi/4k^2)(2J + 1)K^2$$

(This formula, which is derived in Chapter 2, presumes an intermediate state of definite isospin , and thus differs by one-fourth from the formula usually quoted.) The heights of the two structures observed, for example, by R. J. Abrams, et al. (1967) in their PBAR-P, and PBAR-D total cross-sections suggest values of 1.2 and 0.8 for (2J+1)K for their 2345 and 2380 MeV enhancements, respectively. Taking (2J+1)K = 1.0 as a nominal value, and using the above formula indicates that the (minimum) expected enhancement from these structures decreases from .120 mb at J=2 to .046 mb at J=6. These figures are

comparable to the elastic cross section in the backward direction (about 10 microbarns/steradian), and suggest that (even without constructive interference) such resonances might be detectable as backward peaks. At the time of the experiment the (speculative) U-meson of G. Chikovani, et al. (1966) was considered worth searching for, especially since, in principle, all its quantum numbers could be determined via a PBAR-P experiment (G. Kane [1967]). As a result the momentum range was adjusted to detect this particularly narrow (width < 30 MeV), but massive (2382 ± 24 MeV) boson structure.

7.1 Argonne Seven-Degree Beam

The general layout of the Argonne seven-degree beam, as it evolved up to the time of the present experiment, is shown schematically in Figure 7.1-1. The antiprotons were obtained by directing a portion of the ZGS spill onto a copper target attached to a movable platform located inside the ring of the accelerator. The target was fifteen mills high, and one-quarter inch wide, with magnets and separators allowing a vertical full-aperture of two milliradians, and a horizontal full-aperture of twenty milliradians. Particles emitted from this target were collimated by the quadrupole pair Q1 and Q2 whenever they were emitted at the desired momentum

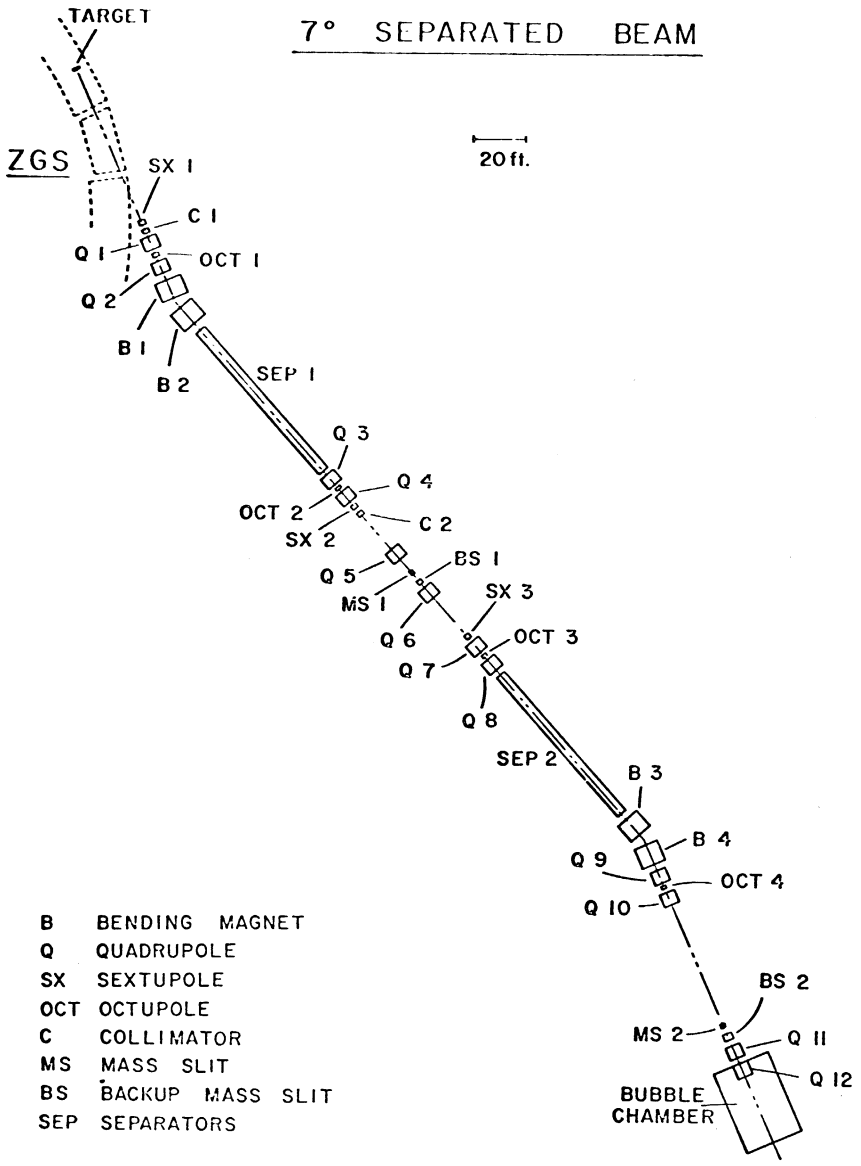

Figure 7.1-1. Argonne Seven-Degree Beam

into the acceptance solid angle defined by the collimator C1. (Off momentum rays remained uncollimated, eventually either leaving the beam line, or striking one of the system elements.) The two bending magnets B1 and B2--the electromagnetic equivalent of the optical prism--served both to direct the beam into the desired area of the building, and fan the particle trajectories in the horizontal direction so that the momentum bite could be controlled by the horizontal collimator C2. On leaving the bending magnets the beam entered the first separator SEP1, where a set of crossed electric and magnetic fields imparted a vertical velocity to any particle not satisfying cE=vB. (The separator thus acted as a mass selector, since the collimated rays all had approximately equal momentum.) The quadrupoles Q3 and Q4 following the separator then focussed the beam in the horizontal direction at the momentum collimator C2, and in the vertical direction at the first mass slit MS1. Particles not having the desired momentum were thus stopped by the collimator C2, and those not having the antiproton mass absorbed in the upper and lower faces of the mass slit MS1.

The second stage of the transport system, beginning at the downstream side of the first mass slit MS1,

served to bring the particles to the bubble-chamber entry port, as well as perform additional mass separation on the beam. This stage being essentially a mirror image of the first, recollimated the beam in the vertical direction with the quadrupole pair Q7 and Q8, and refocused it (just forward of sextupole SX3) in the horizontal direction with the quadrupole Q6. The beam next passed through the second separator, and then into the field of the bending magnets B1 and B2, where the particle trajectories were turned toward the bubble-chamber entry port. Finally, quadrupoles Q9 and Q10 focused the beam (in both the horizontal and vertical direction) to the point normally occupied by mass slit MS2. (Mass slit MS2 was removed for the present run in order to obtain a maximum antiproton beam intensity.) After passing through the double focal point at MS2, the beam again diverged until reaching quadrupole Q11, whereupon it was abruptly rotated about its longitudinal axis owing to a similar rotation of Q11 from the usual quadrupole position. Quadrupole Q12, which was positioned slightly off-axis but not rotated azimuthally like Q11, completed the particle motion by rotating the beam another 45 degrees, and pitching it vertically to offset the action of the fringe field of the bubble-chamber. The net action of Q11 and Q12 was thus to bring

the beam to a double focus in the vicinity of the beam-entry port, with its longest dimension rotated into a vertical position, thereby causing the particles to enter the chamber as a sheet perpendicular to the optical axes of the cameras.

The bubble chamber following the last quadrupole was a thirty-inch hydrogen-filled device, designed and built by the Midwestern Universities Research Association. Its expansion, and recompression cycles were controlled automatically using timing signals sent out from the ZGS control room during the preparation, and acceleration of each batch of protons. Prior to beam entry, the hydrogen was brought into a sensitive, or superheated condition by a rapid drop in chamber pressure. Hydrogen molecules lying along the trajectory of the antiproton (or one of its reaction products) were then ionized through low-energy collisions with these particles, and bubbles formed in the fluid from the resulting thermal motions of the ions. After these bubbles had grown to dimensions sufficient for good photography (about 35 microns), the light rings at the far end of the chamber were flashed, and four stereoscopic pictures taken of the bubble-chamber tracks. Approximately midway between the time of beam entry, and film exposure

the chamber decompression cycle was terminated, and the recompression cycle begun to prepare the chamber for the next batch of antiprotons.†

The remaining (undescribed) elements of the beam-transport system, namely, the octupoles, sextupoles, and backup mass slits, served mainly to refine the operation of the system by allowing larger momentum bites, and acceptance of solid angles at the target. In particular, the sextupoles SX1, SX2, SX3 corrected for the chromatic aberration associated with those particles having momenta slightly off the nominal. Similarly, the octupoles OCT1, OCT2, OCT3, OCT4, all located between a pair of focusing quadrupoles, corrected for the octupole moments not eliminated in the design of the quadrupoles. Finally, the backup mass slits BS1 and BS2 provided a backstop for those particles not completely stopped by the first mass slit, or whose trajectories may have carried them over these slits.

7.2 Large-Angle Scan

As the forward diffraction peak was considered well studied, the large-angle scan rules were designed to measure the antiproton-proton elastic differential

---

†Actually, the MURA chamber was double-pulsed during most of the exposure.

cross section backward of $|t| = 0.6$ $(GeV/c)^2$ with negligible scan-rule bias, and in the range $0.3 < |t| < 0.6$ $(GeV/c)^2$ with some correctable bias, while heavily suppressing events in the forward peak. After the film arrived in Ann Arbor, studies were made to determine methods for separating the large-angle events from the copiously produced forward scatters, and the topology-simulating inelastic collisions. In this connection, suggested scan rules were formulated analytically, and then applied to a set of computer simulated events to determine their effectiveness in suppressing forward scatters, and inelastic contaminants--both as a function of vertex location, and aximuthal position about the beam. Promising rules were then applied to several hundred real events whose elasticity, and four-momentum transfer were already known from direct measurement, and fitting. The surviving rules were then weighted according to their effectiveness in deleting forward scatters and inelastic events, their ease of application at the scanning screen, their susceptibility to misinterpretation by scanners, and their overlap with other rules, and a final set of rules decided upon,

As a result of these studies the scanners were asked to look for all two-prong events produced in the

fiducial volume by a legitimate beam track, and which satisfied the following six criteria:

1. "The positive track leaves the chamber." (This rule, derived from range-energy formulas, eliminated the great majority of forward elastic scatters.)

2. "The positive and negative tracks start out from opposite sides of the beam track in all four views." (This rule, obtained from transverse-momentum conservation, was designed to suppress events with an inelastic topology.)

3. "The angle between the positive, and negative track is less than 95 degrees in all four views." (This rule was designed to eliminate events with an inelastic topology, and was based on the kinematical fact that the angle between the outgoing tracks must be less than 90 degrees for equal-mass particles--the extra 5 degrees arising from the projective geometry of the camera lenses.)

4. "The negative track falls in the Nth negative-track bin on the fan template, and the positive track falls in the first, second, third,..., or Nth positive-track bin in View 2 or View 4." (This rule was designed to suppress forward scatters, and insured that the angles

between the beam, and the outgoing tracks were consistent with large-angle scattering; the fan-template, shown in Figure 7.2-1, enforced this criterion as a function of azimuthal position about the beam by means of the corresponding bin requirement.)

5. "The positive-track curvature is less than or equal to that of the curvature template (39 cm) in View 2 or View 4." (This rule, which required that the proton have a minimum momentum after collision, was also designed to eliminate forward scatters.)

6. "The vertex-zone bubble-density of any outgoing track that curves more than the line on the curvature template in View 2 and View 4 exceeds that of the beam track in its lightest view." (This rule, also designed to suppress inelastic contamination, made use of the fact that below a certain projected curvature the bubble-density of protons and antiprotons must exceed that of the beam, a statement not necessarily true for pion events.)

After selection of a final set of scan rules, additional scanners were assigned to the experiment, and the scanning effort brought up to the desired level. To expedite the bookkeeping task, the scanners were

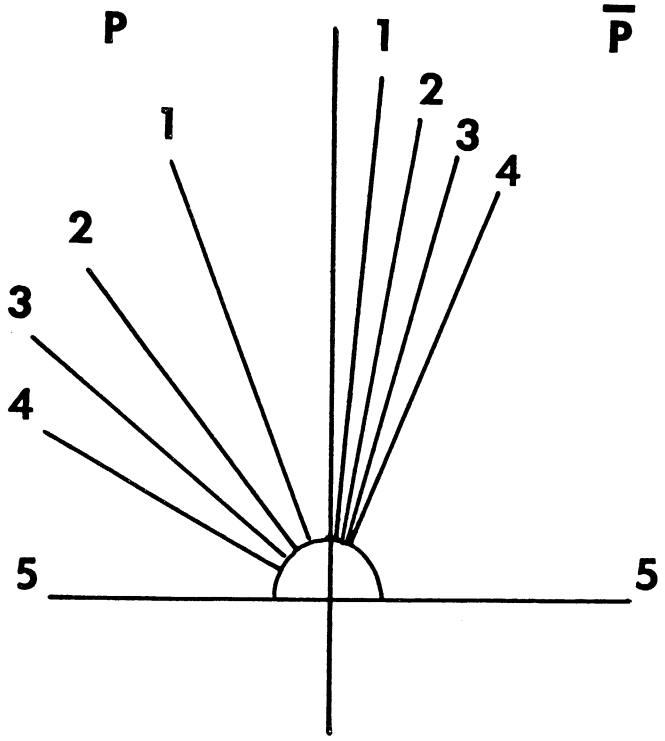

Figure 7.2-1. The Fan Template

asked to fill out one computer data card for each event found on the film; these cards contained such information as the roll and frame number of the event, the general location of the event vertex, and the approximate bubble density of the outgoing tracks. The cards were then run through a commercial device that read the pencil marks photoelectrically, and punched a set of (binary-coded-decimal) holes in the card containing the pencilled information. The punched cards were then processed with a Michigan computer program called SCAN[†] which compared the results reported by the first and second scanners, and prepared (among other things) a list of those events not found by both scanners, or found by both scanners, but given different vertex locations. This list, called a disagreement sheet, was then given to one of the more experienced scanners who went to the scanning machine to resolve the disagreements on an individual basis. The mark-sense cards obtained from the disagreement scan were then combined with those from the two regular scans, and the whole reprocessed with the program SCAN. On this pass the program calculated the scanning efficiency for each scanner, as well as his "extraneity," or tendency to pick up events failing one

---

[†]The program SCAN was designed and written by M. Church.

or more of the scan rules. The program then listed the events found by each scanner, those they disagreed upon, and finally those that were to be measured.

7.3 Square-Hit Scan

During the course of the large-angle scan it became apparent that the scanners were picking up the very backward scatters at a markedly lower efficiency than, say, those in the vicinity of $|t| = 1.0$ $(GeV/c)^2$. A study of this problem indicated that the efficiency drop could be associated with an abrupt change in the event topology. In particular, the efficiency remained high so long as the outgoing antiproton exited the chamber, but dropped rapidly when it annihilated anywhere in the fiducial volume. Moreover, it was concluded following a study of the problem that the rarity of the backward scatters (about one per 400 frames as compared with 40 per 400 frames for the large-angle scatters) was responsible for the unavoidably low scanning efficiency.

Since the square-hit events[†] represented the

[†]A square-hit event was defined as one in which the outgoing antiproton annihilated in the chamber. Similarly, a large-angle event was taken as one passing the large-angle scan rules, but whose outgoing antiproton exited the chamber.

most interesting part of the study from the standpoint of detecting direct-channel resonances, it was decided to rescan the film for just these events using a new set of scan rules. These rules differed from the large-angle ones in that the last three rules were replaced by the requirements that the antiproton annihilate in the chamber, and that the positive track move away from the interaction vertex with at a kinematically allowed angle. In particular, the square-hit scanners were asked to look for all two-prong events produced in the fiducial volume, and satisfying the following criteria:

1. "The positive particle exited the chamber."

2. "The angle between the positive, and negative track is less than 95 degrees in View 2 or View 4."

3. "The positive, and negative tracks start out from opposite sides of the beam track in all four views."

4. "The positive track makes an angle of less than 15 degrees with the beam track in all four views."

5. "The negative track is very dark (continuous), and annihilates into two, four, or six pions before leaving the chamber."

As in the large-angle scan, the square-hit

scanners were instructed to double scan† the film, and make out one data card per event. The disagreement scans were carried out by physicists, as the number of events was comparatively small (about 500), and good feedback was desired between scanner and physicist. Events of an ambiguous or dubious nature were always recorded under the premise that it would be easier to measure and fit than to correct for scanning biases. Finally, scanner attentiveness was maintained by a financial reward in proportion to the difficulty of the event.

7.4 Event Measurement

Event measurement was begun on a full-scale basis soon after the scanning operation became routine. The measuring personnel were obtained (primarily) by retraining the better scanners in the use of the rear-screen measuring machine currently in use at the University of Michigan.§ After retraining, the measurers were given a list of about 40 events (one roll), and

---

†Actually, owing to a commitment to the 1968 Vienna Conference, it was possible to double scan only 80% of the film.

§Since processing the present film, J. Chapman has brought two computer-linked image-plane digitizers into operation.

instructed to proceed slowly at first, increasing their speed as dexterity permitted. The measured coordinates, and control information--recorded by the measurers on punched data cards--were given to an "expeditor" who transferred the data to magnetic tape, and then mailed the tapes to New York University for further processing. Events failing the checking program CAST were remeasured and sent back to New York for reprocessing. Those events not passing the remeasure were deemed unmeasurable, and a correction introduced for them as described in Section 10.1.

The rear-screen measuring machines used in the present experiment were designed, and assembled at the University of Michigan. The bubble-chamber film was mounted horizontally on a movable stage, and imaged to the back side of an upright viewing screen with a system of lenses and mirrors. The position of the image relative to the center of the screen was controlled manually with a pair of electrically actuated motors that drove the film stage to the right and left, and backward and forward. Track coordinates were recorded by placing a bubble under a cross-hair attached at eye level to the front side of the viewing screen. The position of the image relative to the cross-hair was monitored by scaling

impulses from an angular-disc-encoder (or Moire fringe counter) mechanically connected to the stage. The bubble coordinates were recorded when the measurer depressed a floor peddle that caused the scaler to place the contents of its two registers into temporary storage buffers. Following this operation the measurer was free to move onto another bubble, while the buffered data was automatically punched onto data cards with a commercial key-punch unit. With this system the better operators were able to measure on the order of ten events per hour.

The checking program CAST[†] began its editing task by looking for illegal, illogical, and missing data in the control information, and filing the track and fiducial measurements into convenient storage arrays. The program then inspected the data for the proper number of tracks and interaction vertices, ascertained the origin and termination of tracks, and deduced the position of any unmeasured vertex points. A sliding circle fit was then carried out on each track in each camera view measured to detect badly measured points, as well as determine the rms measuring error for the event. A special policing subroutine MCFUZZ[§] then graded the

---

[†]The Michigan checking program CAST was written by B. Bell, under the direction of T. Murphy and B. Roe.

[§]The policing subroutine MCFUZZ was written by T. Murphy.

quality of the measurement by examining the measurer's adherence to the scan rules, his tendency toward carelessness, and his rms measuring error. The average score for each measurer was then compared with those of other measurers, and personnel experiencing difficulty given extra training.

7.5 Reconstruction and Fitting

After checking by CAST, the measured events were reconstructed in the three-view hydrogen geometry program TVGP.† The reconstruction was begun by transforming the measured coordinates to a set of idealized film planes, where corresponding fiducial lines were made parallel, and camera dip and tilt suppressed. Sliding circle fits were then made on the measured coordinates in each view, and the three camera axes joined by perpendicular reference lines. To determine the chamber coordinates of bubbles, lines parallel to the reference lines were drawn from the measured film points to the sliding circle of the next view, the intersection defining a so-called corresponding point in the new

---

†The geometry program TVGP was written by T. Day at Lawrence Radiation Laboratory in early 1965, and introduced to the Michigan Bubble-Chamber Group by J. Chapman in 1967. See, also, T. Day (1967).

view. The measured point, and the corresponding point were then projected into the chamber as optical rays, and the point of closest approach of these rays taken as the first approximation to the coordinates of the bubbles. To check the accuracy of the determination a third ray was drawn from the bubble back toward the sliding circle. If this ray missed the sliding circle, another corresponding point was defined, and the procedure repeated until the chamber coordinates of the bubble were considered well defined. After locating the chamber coordinates of each measured bubble, the program then fitted a helical spiral through the bubbles, thereby obtaining a first approximation for the particle trajectory in the chamber. The fit was then improved by assuming that the fitted parameters of the spiral, and fitted coordinates for the bubbles were only nominal values, and subject to first order (linear) corrections. To make these corrections the fitted bubble coordinates were projected back to their respective film planes, and the first order corrections determined by making a least-squares fit in the plane of the film. Having determined the best fit to the measured coordinates, TVGP then calculated the momentum, dip and azimuth for the track at the event vertex, assigning errors to these quantities from the error matrix obtained during fitting.

Finally, the measured range of the track was compared with that predicted by range-energy tables, and incompatible mass hypotheses flagged.

Following reconstruction, the events were subjected to kinematical analysis in TVGP's companion program SQUAW.† This analysis determined, using the constraints of energy and momentum conservation, whether the measured event represented an elastic or inelastic collision. As an aid SQUAW was given a list of energetically possible reactions, called mass hypotheses, and instructed to proceed through the list determining whether one or more of the hypotheses was consistent within statistical error with the measured angles and curvatures. The determination was carried out by assigning the outgoing tracks the mass presumed under the hypothesis, and then adjusting the measured values within their errors so as to best satisfy energy and momentum conservation. In particular, the adjusted or fitted values were obtained by minimizing the chi-square error between the measured and fitted values under the (mathematical) constraints of energy, and momentum

---

†Like TVGP, the kinematics program SQUAW was written by T. Day at Berkley in late 1965, and introduced to the Michigan Bubble-Chamber Group by J. Chapman in early 1967.

conservation. Besides allowing for larger adjustments on poorly measured quantities, this technique had the advantage--over, say, making joint cuts on missing mass, and non-coplanarity--of producing a single number, namely, the minimized chi-square, that was a measure of the consistency of the hypothesis with the data as a whole. Owing to the constraint equations, the minimization was carried out via the method of Lagrange multipliers, using a cut-and-try technique to locate the minimum.

The reconstruction, and fitting information put into storage by SQUAW was abstracted, and placed on magnetic tape with a specially written subroutine called ARROW. The ARROW tape was then merged event-by-event with another tape containing the results of the scanning effort, i.e., whether the event was found by one out of two scanners, two out of three, etc., and the result placed on a preliminary summary tape. This summary tape was then purged of all double, and triply measured events, as well as the zero, one, and two-constraint fits, and the result copied to a final summary tape containing 6601 three- and four-constraint events. The Berkley program SUMX (L. Champomier [1963]), converted for use at Michigan by G. Benson (1966), read the final

summary tape, and made the histograms, ideograms, etc. necessary for the data analysis. When the University of Michigan replaced its IBM 7090 computer with an IBM 360/67 time-sharing and terminal system, SUMX was converted to Fortran IV, and its machine language and Boolean-algebra statements removed, thus making it a universally compatible program.

7.6 Beam-Momentum Distributions

After the film arrived in Ann Arbor approximately fifty long beam tracks from each of the six momentum sets were measured using the rear-screen measuring machines. These tracks were processed with the Michigan heavy-liquid program SHAPE, and again at New York University with the hydrogen geometry program TVGP. The two programs yielded substantially the same results for the center-of-chamber momenta, namely, the following: 2.224, 1.956, 1.888, 1.840, 1.782, and 1.630 GeV/c, all with a spread of 1%. (Here a spread of 1% means that two thirds of the measured beam tracks had momenta lying within 1% of the nominal values quoted above.) All the elastic events were fit with these momenta, using an assigned error of ±1.4% as input to the fitting program SQUAW.

Histograms of the beam-momentum stretch variable

for good elastic events (3C and 4C fits with chi-square < 36) suggested that the nominal momenta quoted above were systematically high by about 3/4%. In particular, these histograms all peaked at the stretch-variable value .55, indicating that the fitted momenta were systematically lower than the inputted values quoted above by approximately this amount times the assigned error of 1.4%, or about .77%.† In general, such an error can arise either from an inaccurate beam-momentum determination, or improper magnetic-field values. Since elastic events remain relatively insensitive to small changes in the magnetic field, that is, the angle and mass constraints dominate those of curvature during fitting, it was concluded that the nominal beam momenta were all set too high in SQUAW. Thus, before processing the V-events, new beam momenta were determined by looking at the good elastic events refitted with an unknown beam momenta

---

†The stretch-variable for a quantity x is defined as

[x(unfitted) - x(fitted)]/|error(unfitted) - error(fitted)|

A histogram of stretch-variables should typically have a gaussian shape, with zero mean and unit standard deviation, provided the errors have been properly assessed. In the present case error(unfitted) was set at 1.4%, and was generally very much larger than error(fitted). Thus, the beam-momentum stretch-variables had the approximate form:

[x(unfitted) - x(fitted)]/error(unfitted).

(giving 3C fits). The resulting spectra verified the setting error, and led to the new nominal momenta used to fit the V-events: 2.205, 1.944, 1.883, 1.823, 1.763, and 1.624 GeV/c, again with a spread of ±1%.†

---

†The V-events were measured, and processed by M. Church, and H. Ring.

8.0 EVENT FITTING AND IDENTIFICATION

The measured events were fit to the elastic hypothesis in SQUAW, and the good elastic events identified by means of the chi-square error in their highest constraint fit. Sample purity was ascertained by checking bubble-density consistency, and missing-mass distributions. The misassignment of measuring error, and consequences of systematic error were determined by comparing the experimental missing-energy, and chi-square distributions with the theoretical ones.

8.1 Elastic Fitting Procedure

The measured events were fit to the elastic hypothesis in SQUAW using four independent fitting techniques. These procedures--called respectively Mark 1, Mark 8, Mark 9, and Mark 10 fits--were written into the fitting program in an effort to pass both the normal elastic events, and those suffering such difficulties as an off-momentum beam track, or small-angle scatter in an outgoing track.

MARK 1 FIT. The Mark 1 fit always attempted an elastic fit using the maximum number of enforceable constraints, producing thereby 4C-fits to the majority of the genuine

elastic events. In cases where the measured length of one or both of the outgoing tracks was too short for good momentum determination, SQUAW dropped the uncertain momenta, and tried instead a 3C- or 2C-fit to the elastic hypothesis. Similarly, if the geometry program TVPG sensed that one of the outgoing tracks was not a baryon (because its measured range exceeded that predicted by the range-energy tables by several standard deviations), or deduced that it was too poorly measured for reliable fitting, the angles and curvature of that track were dropped, and a 1C-fit to the elastic hypothesis tried.

MARK 8 FIT. The Mark 8 fits always dropped the beam momentum, and then tried an elastic fit using the remaining enforceable constraints, producing thereby a 3C-fit to the majority of the genuine elastic events. (Dropping the beam momentum allowed those events that failed Mark 1 fit because of an unusually high or low beam momentum, to still pass the elastic hypothesis.) In the case where the measured length of one or both of the outgoing tracks was too short for good momentum determination, SQUAW dropped the uncertain momenta, and attempted instead a 2C- or 1C-fit to the elastic hypothesis. However, if the geometry program sensed that one of the outgoing tracks was not a baryon, or very poorly measured, the angles and

curvature of that track were dropped, and a simple 0C-fit to the elastic hypothesis carried out.

MARK 9 FIT. The Mark 9 fit always dropped the momenta of the two outgoing tracks, and then tried an elastic fit using the remaining enforceable constraints, producing thereby a 2C-fit to the majority of the genuine elastic events. (Dropping the outgoing momenta allowed those events that failed the Mark 1 fit because of a small-angle scatter in an outgoing track to still pass the elastic hypothesis.) If, however, the geometry program sensed that one of the outgoing tracks was not a baryon, or very poorly measured, the angles and curvature of that track were dropped, and a simple 0C-fit to the elastic hypothesis carried out.

MARK 10 FIT. The Mark 10 fit always presumed that an unmeasured, neutrally charged particle (or particles) was produced during collision, and thus tried a 0C-fit to this inelastic hypothesis. This fit determined the missing mass, missing energy, and missing momentum for the interaction from the unfitted angles, and curvatures.

8.2 Inelastic Fitting Procedures

The measured events were also fit to several inelastic hypotheses to determine, as a function of the permitted chi-square error, the number of events that had both good elastic, and inelastic fits. The inelastic hypotheses tried were those considered most likely to contaminate an elastic sample, either because their cross-section was large, or because their kinematics resembled those for the elastic collision.

MARK 12 FIT. The Mark 12 fit hypothesized that the two outgoing tracks were pions, and then attempted a fit to this hypothesis using the maximum number of enforceable constraints. (This fit was thus analogous to the Mark 1 fit for the elastic hypothesis.) If one or both of the outgoing tracks was short, SQUAW dropped their momenta, and tried instead a 3C- or 4C-fit to the hypothesis. Similarly, if the geometry program sensed that one of the outgoing tracks was not a pion, or very poorly measured, the angles and curvature of that track were dropped, and a 1C-fit to the hypothesis tried instead. If more than three constraints had to be dropped no Mark 12 fit was attempted.

MARK 11 FIT. The Mark 11 fit hypothesized that the two outgoing tracks represented pions, and that an unmeasured missing neutral was produced in collision. In this case SQUAW made a 0C-fit to this hypothesis, and obtained the missing mass, missing energy, and missing momentum associated with the hypothesis.

MARK 21 FIT. The Mark 21 fit hypothesized that the two outgoing tracks were kaons. This fit was otherwise identical to the Mark 12 fit.

MARK 20 FIT. The Mark 20 fit hypothesized that the two outgoing tracks were kaons, and that an unmeasured missing neutral was produced in collision. This fit was otherwise identical to the Mark 11 fit.

MARK 4 FIT. The Mark 4 fit hypothesized that the two outgoing tracks were an antiproton, and proton, and that an unmeasured pi-zero was produced during collision. In this case SQUAW made a 1C-fit to the hypothesis, unless one of the outgoing tracks was short, in which case its momentum was dropped, and a 0C-fit carried out.

MARK 2 FIT. The Mark 2 fit hypothesized that the two outgoing tracks were a pi-minus and proton, and that an

unmeasured antineutron was produced during collision. This fit was otherwise identical to the Mark 4 fit.

MARK 3 FIT. The Mark 3 fit hypothesized that the two outgoing tracks were an antiproton and pi-plus, and that an unmeasured missing neutron was produced during collision. This fit was otherwise identical to the Mark 11 fit.

8.3 Good-Elastic Events

The confidence-level range for the present experiment was established by looking at the size of the elastic sample, and the percentage of inelastic contamination associated with various lower limits for the confidence level. The final cut-off setting of one chance per million was obtained by increasing the confidence-level range until a 4C elastic event with less than even betting odds against a constrained inelastic hypothesis entered the sample of good-elastic events. The sample-size attenuation corresponding to this limit was then estimated, and found to be negligible (actually about 1/5%, as discussed in Section 8.6 below). The confidence-level limit in SQUAW was thus set at one part per million for all elastic-fit classes, with the proviso that the 3C, 2C, and 1C contaminations would be studied

separately.

8.4 Sample Purity

The distribution of passing elastic events (confidence level greater than one part per million) among the various fit classes is shown in Table 8.4-1. These events were placed in the table according to the constraint level of their most restrictive fit, the Mark 1 fit being more difficult than the Mark 8, and the Mark 8 more difficult than the Mark 9, in general. As expected the majority of passing elastics fell into 4C Mark 1 classification, indicating the basic correctness of our measurement and fitting procedures. Because the 4C-hypothesis is difficult to fake, most of the events in this classification are believed to be genuine elastic events. The 2C and 3C Mark 1 fits, and the 2C Mark 8 and Mark 9 fits, on the other hand, likely contain serious contamination owing to the reduced constraint level of the fits. The 1C Mark 1 fits, and the 0C Mark 8 and Mark 9 fits resulted when the geometry program TVGP sensed a non-baryonic, or miss-measured outgoing track, so that these events can be either elastic or inelastic in general.

To estimate the sample purity for the various

fit classes, the author went to the scanning machines, and looked at 25% of the events entered in the middle three columns of Table 8.4-1, and a small sample of those in the last column. The elastic events were discriminated from the inelastic ones primarily on the basis of ionization, although some subjective judgement was used to delete obviously inelastic events. (For instance, no baryon can orbit through 90 degrees in the MURA chamber, and no elastic collision can have a V-decay with it.) The results of this survey are shown in Table 8.4-2. The various entries represent, respectively, the percentage of events that were determined to be definitely elastic, definitely inelastic, and ambiguous. (Note that as expected none of the 4C Mark 1 fits were consistent with inelastic.) The errors shown were assigned using the usual square-root-of-the-sample-size formula.

To check that the fitting program did not fail an anomalously large number of genuine elastic events, a missing-mass histogram was made of those events failing all elastic fit attempts. This plot, which is shown in Figure 8.4-3, shows no tendency for events to cluster around MM=0, indicating that SQUAW was not failing events with an elastic topology in substantial numbers. Further confidence in the fitting technique evolved from the

TABLE 8.4-1

Distribution of Events Among Fit Classes[#]

MARK	0C	1C	2C	3C	4C	TOTALS
1	3	79	1	63	3211	3357
8	177	0	9	19	0	205
9	9	0	34	0	0	43
TOTALS	189	79	44	82	3211	3605

[#]The table contains a total of 3605 entries taken from a sample of 9185 measured events, of which 5580 had no Mark 1, 8, or 9 fit to the elastic hypothesis.

TABLE 8.4-2

Sample Purity From Bubble Density[#]

Mark	Constraint	Elastic	Inelastic	Ambiguous
1	1	52±13%	41±12%	7±5%
1	2[@]	-	-	-
1	3	65±18%	25±13%	10±7%
1	4	100%	0%	0%
8	2	0%	100%	0%
8	3	100%	0%	0%
9	2	29±20%	71±32%	0%

[#]Errors quoted are purely statistical.

[@]No events of this type were examined.

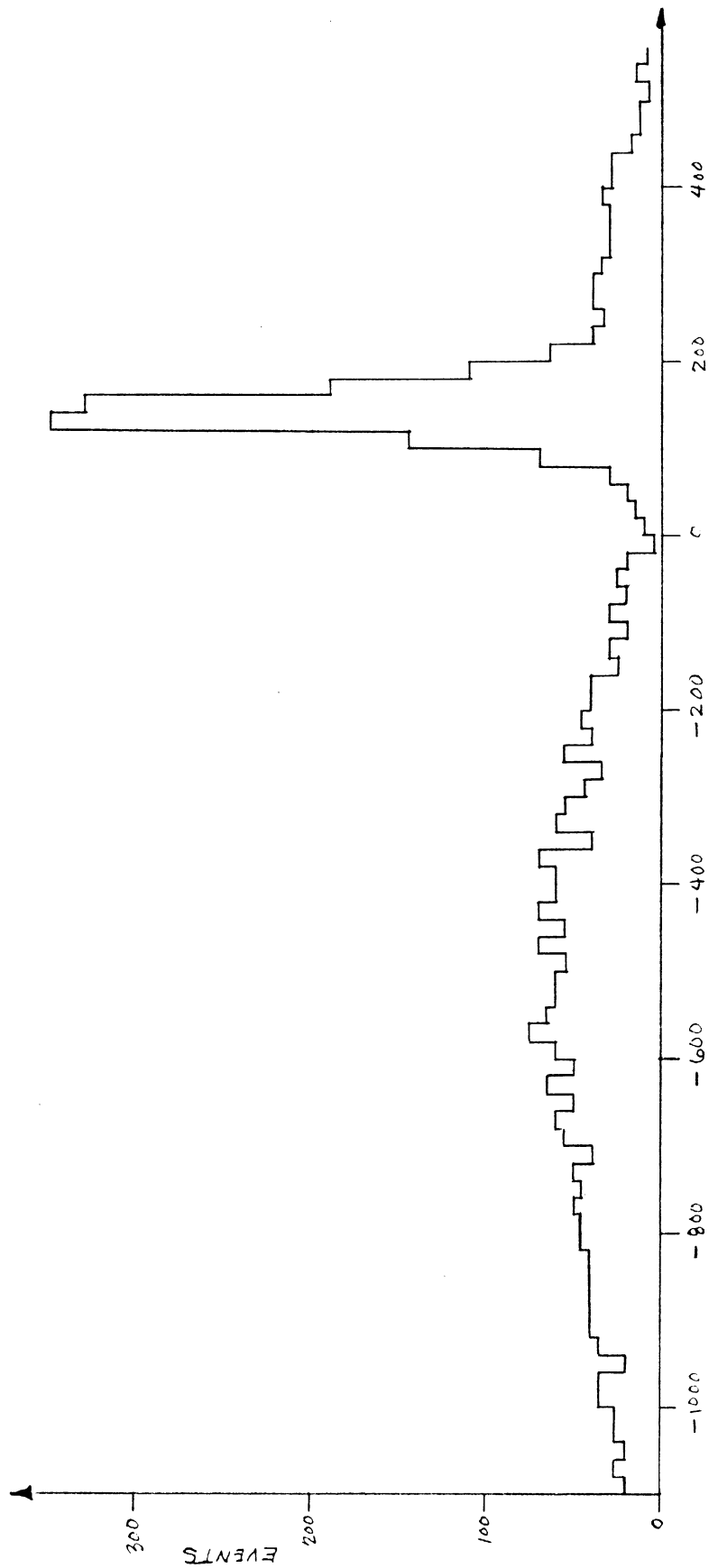

Figure 8.4-1. Missing-Mass Distribution for Non-Elastic Events. The histogram, which contains a total of 4187 events, peaks sharply around the neutral pion mass (135 MeV), and dips to zero at MM=0. However, the width of the peak exceeds that of the pion mass (.014 MeV) by orders of magnitude, the difference in these values reflecting the finite-mass resolution of the experiment.

strong concentration of events around the pion mass (135 MeV) in this plot, and the absence of the same in the missing mass-histogram for the 4C Mark 1 fits of Figure 8.6-1 below. From these observations it was concluded that the fitting program had no tendency to fail good elastic events, and was able to differentiate final states such as PBAR-P-PIZERO from the elastic one.

As another check on the fitting procedure, a two-dimensional histogram of missing-mass squared versus missing-energy squared was prepared using those events failing both the 3C, and 4C elastic-fit attempts. This histogram, which is shown in Table 8.4-3, also has a pion peak at MM= 135 GeV, while the dip observed in the missing-mass distribution at MM=0 appears lost in the coarse resolution of the histogram. The missing-energy squared also appears peaked, but at a higher energy, namely, around 200 MeV, since the missing energy is the sum of the rest and kinetic energy of the missing particle. The slight (100 event) rise in the missing energy distribution at ME=0 represents those events whose measured angles were in error, as a result, for example, of a single scatter in an outgoing track. With these facts in mind, the histogram is seen to contain no anomalously large concentration of events about MM=0=ME, as

TABLE 8.4-3

Missing-Mass Squared v. Missing-Energy Squared[#@]

MP/MM	-.12	-.10	-.08	-.06	-.04	-.02	.00	+.02	+.04	+.06	+.08	+.10	TOT
+.240	2	0	1	1	2	1	10	23	6	1	3	2	52
+.220	2	1	0	4	2	4	8	28	3	1	0	2	55
+.200	1	1	0	2	3	2	5	42	2	1	2	0	61
+.180	0	2	2	0	4	5	6	31	8	5	4	0	67
+.160	1	2	3	3	5	0	9	45	12	6	4	3	93
+.140	2	3	1	4	3	3	12	49	10	22	2	3	94
+.120	0	2	5	2	4	3	13	60	15	6	3	5	118
+.100	2	3	0	2	1	6	17	64	22	8	9	2	136
+.080	2	6	1	2	4	4	23	94	29	12	6	0	183
+.060	3	6	1	10	4	4	21	127	53	9	0	0	238
+.040	5	5	6	4	4	8	43	143	28	0	0	0	283
+.020	4	6	11	9	11	16	44	35	0	0	0	0	136
.000	18	28	16	13	16	16	46	0	0	0	0	0	153
-.020	1	4	3	2	8	7	6	1	0	0	0	0	32
-.040	4	2	2	6	5	4	5	3	0	0	0	0	31
-.060	1	2	3	4	2	3	4	2	1	0	0	0	22
-.080	0	2	0	1	2	1	1	2	2	0	0	0	11
-.100	0	1	1	0	0	0	0	0	2	4	0	1	9
-.120	0	0	0	0	1	0	1	1	1	3	2	1	10
TOTALS	48	76	56	69	81	87	275	787	195	59	36	20	

[#]Table consists of 1789 events having no 3C or 4C fit to the elastic hypothesis.

[@]Missing-mass squared (in GeV^2) increases from left to right; missing-energy squared (in GeV^2) increases from bottom to top.

would be expected if elastic events were failing the fitting program in significant numbers.

To eliminate the anomalies that might otherwise arise from the inclusion of poorly fitted events in the sample, only the 3C and 4C events were used to determine cross sections, angular distributions, etc. The cut was made at the 3C, rather than the 4C level, so as to include in the sample of good elastic events those that had a short outgoing track. This insured that the square-hit events, to which much of the experimental effort was devoted, would not receive negative bias when the antiproton stopped and/or annihilated in the chamber. The sample-size correction necessitated by the deletion of the 1C and 2C events was determined from Tables 8.4-1 and 8.4-2 above.

8.5 Missing Mass, Energy, Momentum Distributions

The distributions of missing mass MM, missing energy ME, and missing momentum MP provide insight into the quality of measurement, the misassignment of random errors, the consequences of systematic error, and the degree of inelastic contamination. Although only two of the three quantities can be mathematically independent, each is useful in its own right owing to its ready

physical interpretation. The definitions adopted for these quantities are the following more or less conventional ones:

$$
\begin{aligned}
ME^2 &= (E_{in} - E_{out})^2 \\
ME &= E_{in} - E_{out} \\
MP^2 &= |\vec{P}_{in} - \vec{P}_{out}|^2 \\
MP &= |\vec{P}_{in} - \vec{P}_{out}| \\
MM^2 &= (E_{in} - E_{out})^2 - (\vec{P}_{in} - \vec{P}_{out})^2 \\
MM &= \text{sign}(MM^2)\ |MM^2|^{1/2}
\end{aligned}
$$

where sign x = +1 if x > 0, and -1 if x < 0. The energies, and momenta referred to here are the unfitted ones obtained from the geometry program TVGP. Definitions for missing mass, energy, and momentum squared are included for completeness, but are not used in the sequel.

The missing mass, energy, and momentum distributions for the 4C Mark 1 fits are shown in Figure 8.5-1,2,3. As expected, the missing mass distribution appears heavily concentrated at the negative MM values, dropping toward zero for MM > 0. The negativeness of the distribution results because small errors in angle or curvature measurements--whether positive or negative--invariably lead to negative MM values. The handful of events with positive MM likely represent those cases where the error in curvature was large and positive. Since none of the 4C elastics

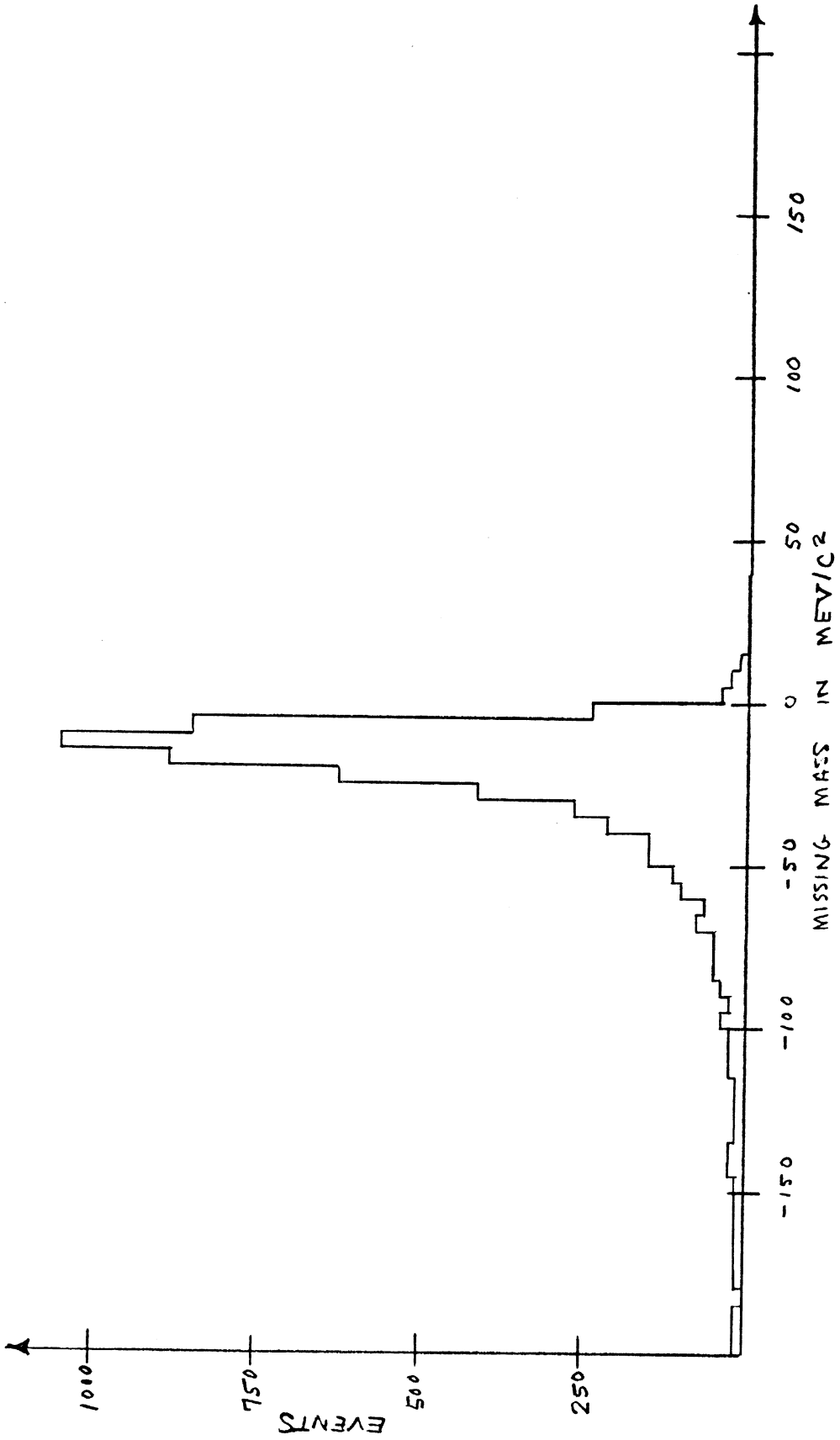

Figure 8.5-1. Missing-Mass Distribution for 4C Events. The histogram contains 5790 events.

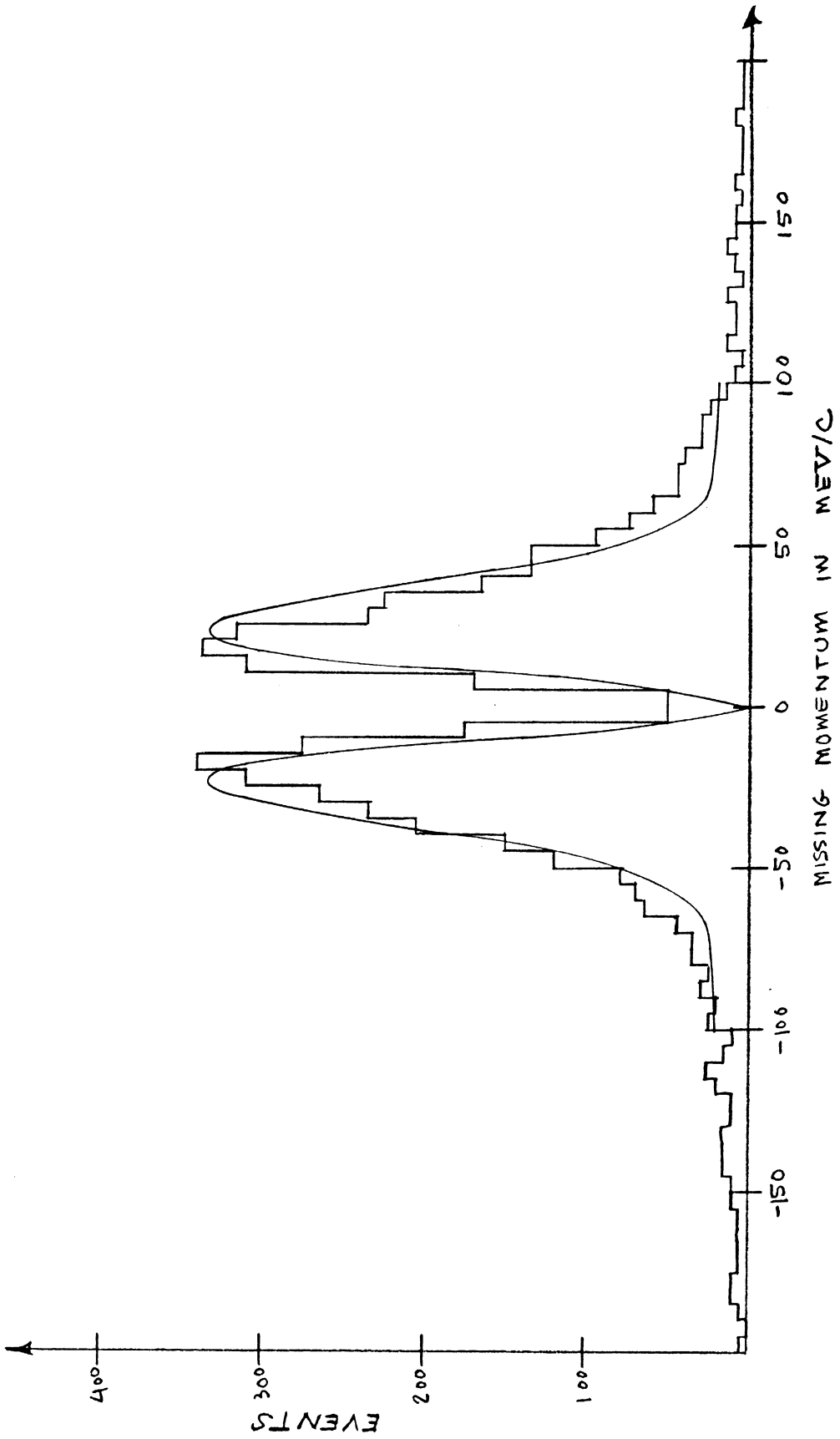

Figure 8.5-2. Missing-Momentum Distribution for 4C Events. The histogram contains 5571 events.

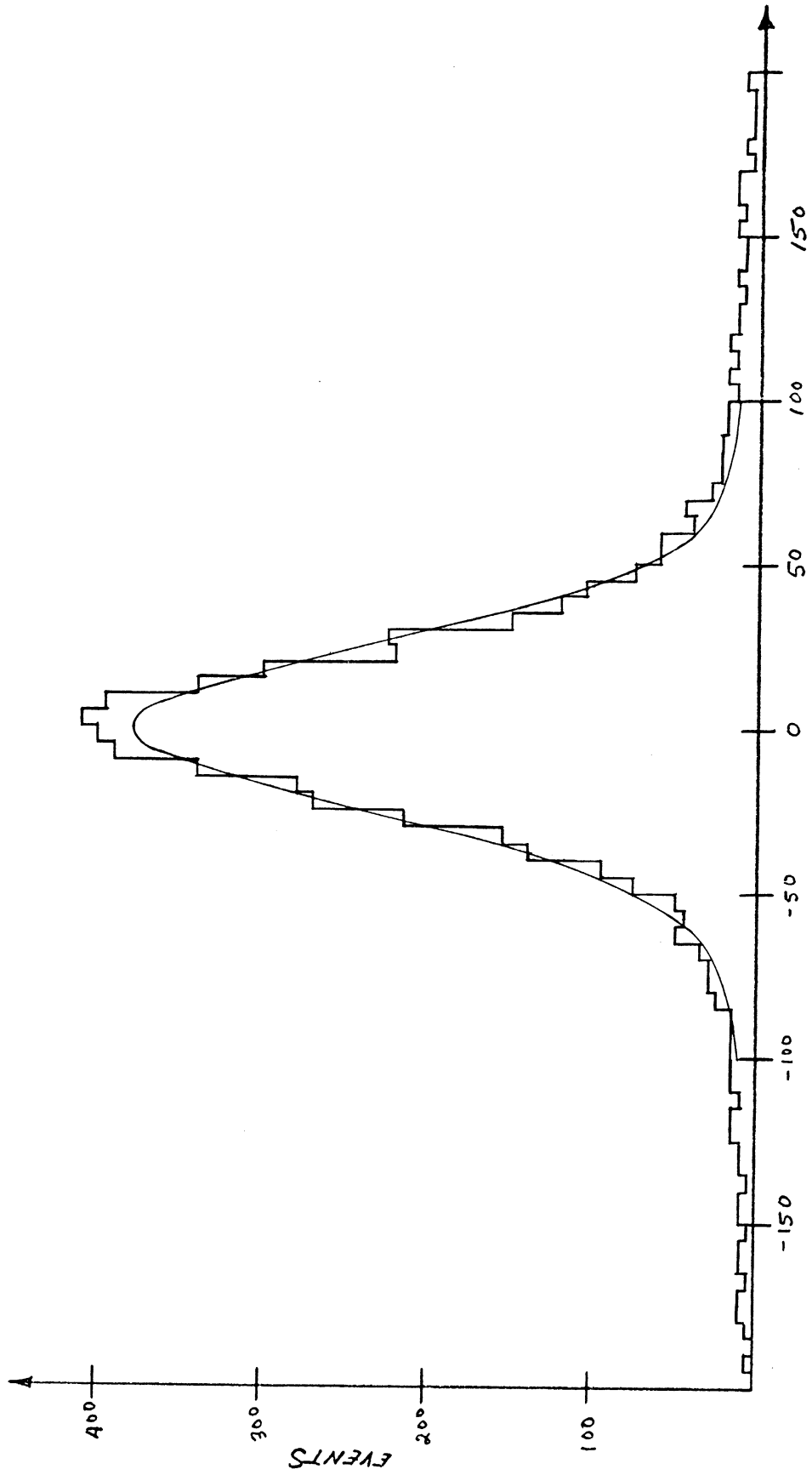

Figure 8.5-3. Missing-Energy Distribution for 4C Events. The histogram contains 5777 events.

had MM greater than 75 MeV/c, it was concluded that the sample contained negligible inelastic contamination of the form PBAR-P-PIZERO. A similar plot for the 3C events, also contained no events with MM > 75 MeV/c, indicating a similar purity for this sample.

The missing momentum distribution, on the other hand, appears more or less symmetric about MP=0. The dip at the origin results, as in the case of missing mass, from the dependence of MP on more than one random variable, namely, the three components of missing momentum. The situation arising here is reminiscent of Maxwell-Boltzmann theory, wherein each of the three molecular velocity components is presumed distributed like a gaussian random variable.† The probability that the molecular velocity v lies between v and v+dv is then given by the celebrated Maxwell-Boltzmann distribution $v^2\exp(-v^2/2v_o^2)$. The factor v^2 leading the exponent arises from the phase-space volume element $v^2\ dv\ d\Omega$, and causes the distribution to drop to zero at v=0. The same argument holds if we replace v by MP, and presume the errors in the missing momentum components are gaussian random variables. In fact, the solid curve of Figure 8.5-2

---

†Alternatively, one can use the Central-Limit Theorem to establish the gaussian character of the velocity components.

was obtained by fitting a biased Maxwell-Boltzmann distribution to the experimental data. The bias was added to compensate for the long tails that exist in data, presumably a result of systematic errors.

The missing energy distribution, like the missing momentum distribution appears centered about the origin, and would have the conventional gaussian form, except that its tails are too high, and its peak too narrow. If the measurement errors were truly gaussian, and the systematic errors negligible, the ME distribution would also have a gaussian structure, at least to first order. The clearly non-gaussian behavior of the experimental distribution indicates that one or both the above assumptions is false, and suggests that the distribution should be parameterized differently. In an earlier thesis G. Benson (1966) proposed that a Breit-Wigner form might be a more realistic fitting function, since its peak is narrower, and its tails higher than those of the gaussian form. Alternatively, J. Chapman (1965) has suggested that the ME distribution might be the sum of a widely dispersed base arising from the systematic errors, and an ordinary gaussian distribution produced by the measurement errors. To check these ideas, and also obtain an estimate of the rms width of the ME dis-

tribution, the data were fit with both a Breit-Wigner function, and a biased gaussian form. The chi-square errors associated with these fits were, respectively, 103 and 113, indicating the superiority of the form suggested by Benson. The results of the fitting, which are shown in Figure 8.5-3, give a full-width at half-maximum of 58.1 MeV to Breit-Wigner fit and an rms width of 35.0 MeV to the gaussian portion of the Chapman form.

When the measurement errors have been properly assessed, both as to magnitude and form, the rms width of the missing-energy distribution should equal that of the resolution function formed from the errors in missing energy, as propagated from those in the track measurements. If properly assessed as to form, but not magnitude, the two widths will differ by the error in the error assignments. According to the above we expect that the measurement errors are approximately gaussian distributed, so that a gaussian resolution function should be formed of the errors. Such a resolution function was made, and is shown in Figure 8.5-4. The rms width of the distribution is 29.2 MeV, indicating that the errors assigned in TVGP were under estimated by about $(35.0 - 29.2)/35.0 = +16.6\%$, apparently because both the assigned errors and the resolution function ignored the

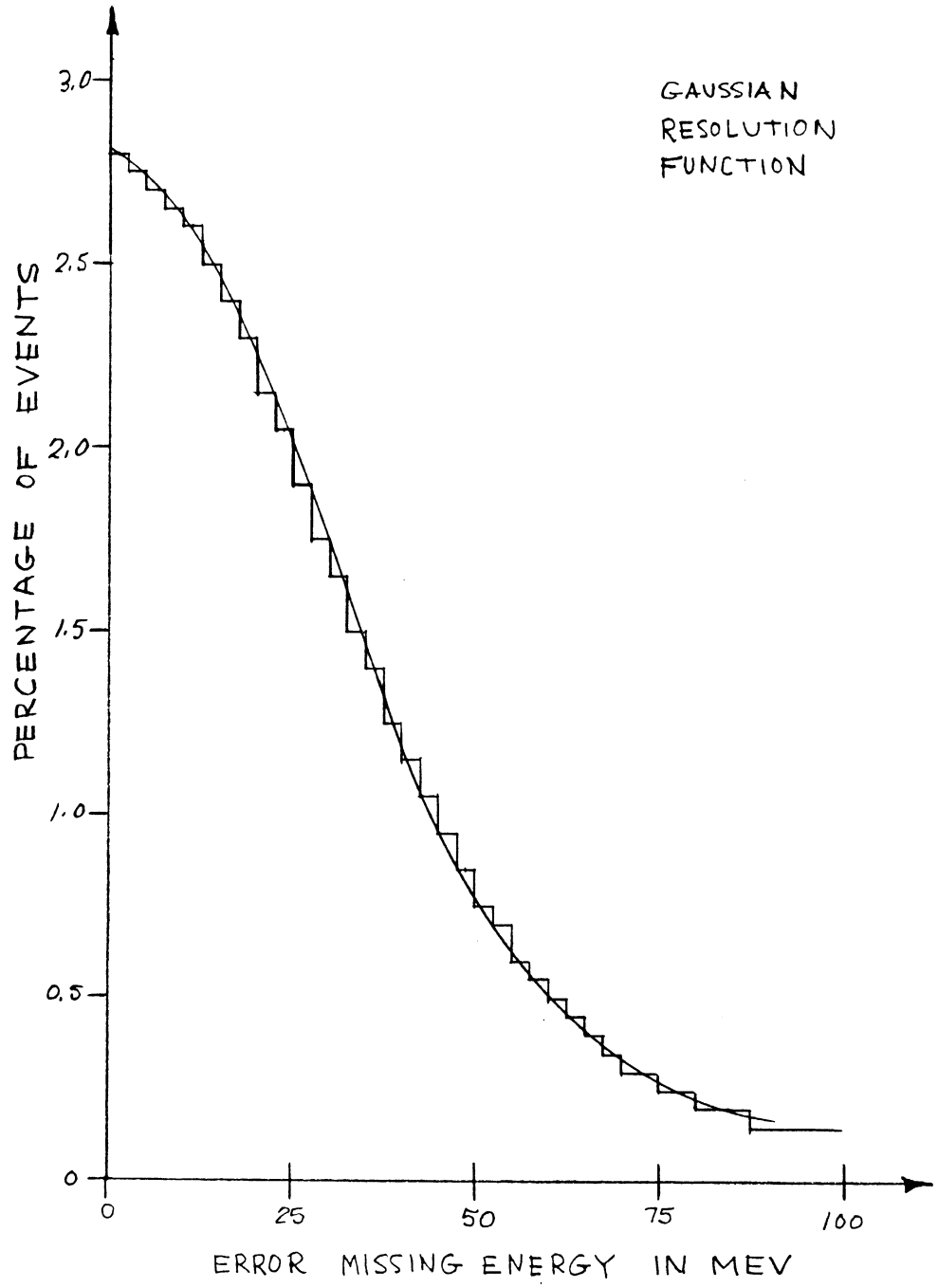

Figure 8.5-4. Gaussian Resolution Function. This resolution function consists of 6115 uniformly weighted gaussian forms, each of width equal to the error in missing energy, as assigned to 6115 events in SQUAW.

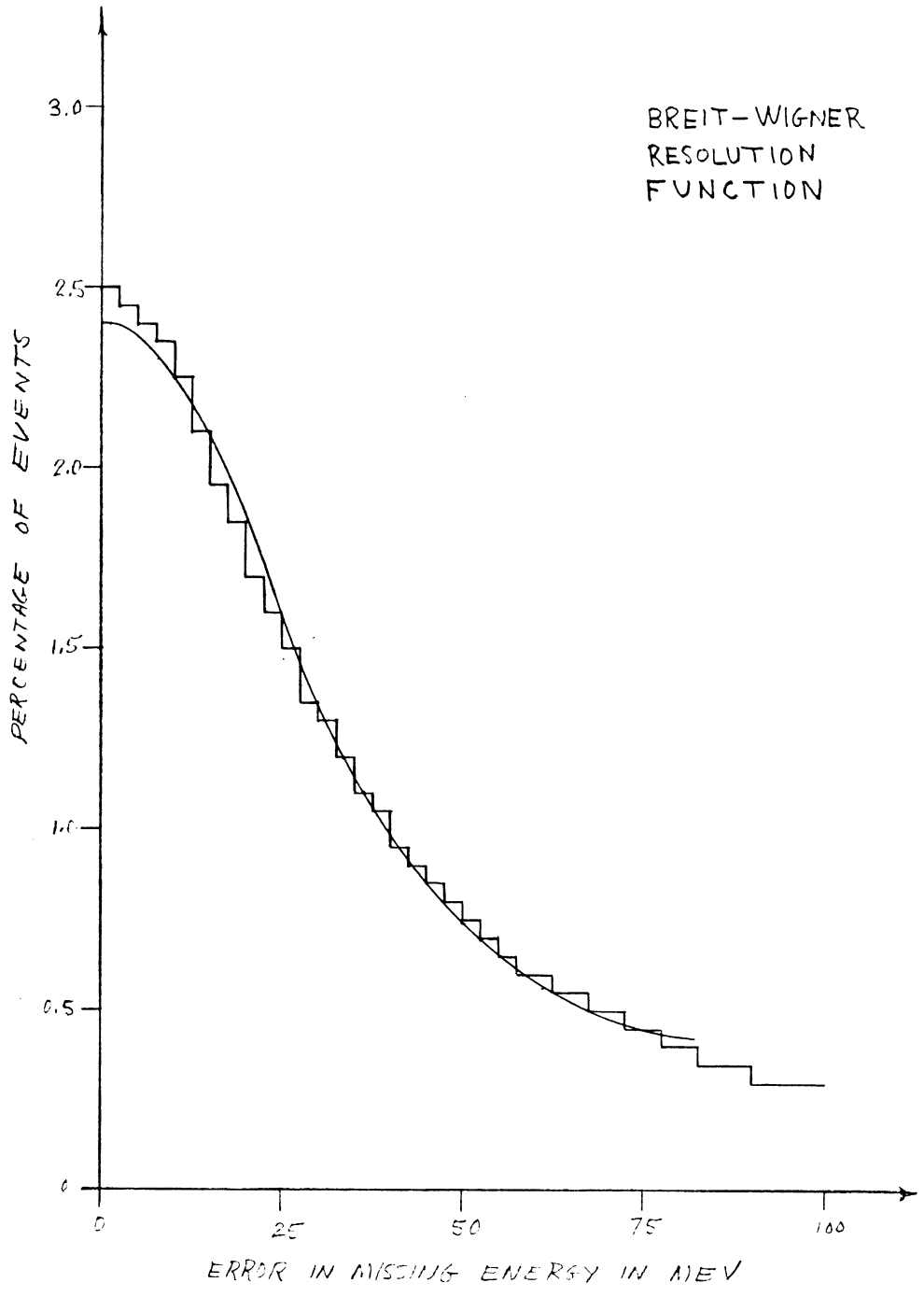

Figure 8.5-5. Breit-Wigner Resolution Function. The resolution function consists of 6115 uniformly weighted Breit-Wigner forms, each of full-width at half-maximum equal to the error in missing energy as assigned to 6115 events in SQUAW.

possibility of systematic error. For comparison a Breit-Wigner resolution function was also constructed, and is shown in Figure 8.5-5. Its full-width a half-maximum is 48.2 MeV, thus suggesting that the errors in TVGP were under estimated by (58.1 - 48.2)/58.1 = +17.0%, consistent with the gaussian result above.

8.6 Scatter Plots with MM, ME, MP

The two-dimensional histograms shown in Tables 8.6-1,2,3 were formed from the missing masses, energies, and momenta associated with the events having a 4C Mark 1 fit. These plots provided additional insight into the measurement, and fitting process, as described below:

MP vs ME. This plot has a strong concentration of events along† the diagonal line ME=MP, and a lesser concentration along the missing momentum axis ME=0. The diagonal concentration results (presumably) from errors in curvature measurement, as these reflect themselves approximately equally in ME and MP. The axial clustering, on the other

---

†Actually, the distribution lies somewhat below the diagonal line for MP > 0 and somewhat above for MP < 0. This results because an error δP in the momentum generates a corresponding error δE in the energy given by $\delta E = (P/E)\ \delta P$, where $P < E$. Similar effects can be found in the MM vs ME, and MM vs MP plots.

TABLE 8.6-1

Missing Momentum vs. Missing Energy[#]

ME/MP	-.24	-.20	-.16	-.12	-.08	-.04	.00	+.04	+.08	+.12	+.16	+.20	+.24
+.280	0	0	0	0	0	0	0	0	0	0	0	0	0
+.240	0	0	0	0	0	0	0	0	0	0	0	0	4
+.200	0	0	0	0	0	0	0	0	0	0	0	13	23
+.160	0	0	0	0	0	0	0	0	0	0	29	42	6
+.120	0	0	0	0	0	0	0	0	0	74	48	5	2
+.080	0	0	0	0	0	0	0	0	164	68	6	2	0
+.040	0	0	0	0	0	0	2	890	144	6	2	4	5
-.000	14	8	4	4	14	566	1820	547	12	9	4	3	5
-.040	4	3	2	11	122	1024	3	0	0	0	0	0	0
-.080	1	2	5	45	176	1	0	0	0	0	0	0	0
-.120	0	2	33	63	0	0	0	0	0	0	0	0	0
-.160	0	2	33	28	0	0	0	0	0	0	0	0	0
-.200	21	11	0	0	0	0	0	0	0	0	0	0	0
-.240	3	1	0	0	0	0	0	0	0	0	0	0	0
-.280	0	0	0	0	0	0	0	0	0	0	0	0	0

[#]Missing momentum (in GeV/c) increases from left to right; missing energy (in GeV) increases from bottom to top.

TABLE 8.6-2

Missing Mass vs. Missing Energy#

ME/MM	-.24	-.20	-.16	-.12	-.08	-.04	.00	+.04	+.08	+.12	+.16	+.20	+.24
+.280	0	4	6	4	0	0	0	0	0	0	0	0	0
+.240	0	3	10	6	4	0	1	0	0	0	0	0	0
+.200	0	2	10	14	13	0	1	0	0	0	0	0	0
+.160	1	1	10	21	41	4	0	0	0	0	0	0	0
+.120	2	2	4	9	68	46	0	0	0	0	0	0	0
+.080	0	1	3	7	50	169	9	1	0	0	0	0	0
+.040	5	3	2	4	31	537	471	0	0	0	0	0	0
.000	19	11	8	13	23	704	2232	0	0	0	0	0	0
-.040	4	3	2	10	23	513	615	0	0	0	0	0	0
-.080	3	1	2	7	30	168	21	0	0	0	0	0	0
-.120	0	0	1	4	42	49	2	0	0	0	0	0	0
-.160	1	1	6	16	30	11	0	2	0	0	0	0	0
-.200	0	2	5	12	14	2	0	0	0	0	0	0	0
-.240	0	1	8	11	0	0	1	1	0	0	0	0	0
-.280	1	4	8	5	1	0	0	0	0	0	0	0	0

#Missing mass (in GeV/c^2) increases from left to right; missing energy (in GeV) increases from bottom to top.

TABLE 8.6-3

Missing Mass vs. Missing Momentum#

MP/MM	-.24	-.20	-.16	-.12	-.08	-.04	.00	+.04	+.08	+.12	+.16	+.20	+.24
+.280	3	2	11	6	3	0	0	0	0	0	0	0	0
+.240	10	3	13	15	3	0	1	0	0	0	0	0	0
+.200	0	7	11	22	28	0	1	0	0	0	0	0	0
+.160	0	0	7	14	61	7	0	0	0	0	0	0	0
+.120	0	0	0	15	78	64	0	0	0	0	0	0	0
+.080	0	0	0	0	44	265	10	1	0	0	0	0	0
+.040	0	0	0	0	0	772	665	0	0	0	0	0	0
.000	0	0	0	0	0	0	1825	0	0	0	0	0	0
-.040	0	0	0	0	0	768	823	0	0	0	0	0	0
-.080	0	0	0	0	43	244	25	0	0	0	0	0	0
-.120	0	0	0	16	41	64	2	0	0	0	0	0	0
-.160	0	0	6	10	41	13	0	2	0	0	0	0	0
-.200	0	11	6	15	21	6	0	1	0	0	0	0	0
-.240	18	2	7	14	6	0	1	0	0	0	0	0	0
-.280	3	2	9	12	1	0	0	0	1	0	0	0	0

#Missing mass (in GeV/c^2) increases from left to right; missing momentum (in GeV/c) increases from bottom to top.

hand, represents those events having angular measurement errors since the latter are manifested in the missing momentum, but not the missing energy.

MM vs ME. This plot has a strong concentration of events along the diagonal rays $|ME| = MM < 0$, and a lesser concentration results from errors in curvature measurements, while the axial clustering arises from errors in angle measurements.

MM vs MP. This plot has a strong concentration of events along the diagonal rays $|ME| = MM < 0$, but shows no events along the missing mass axis. The diagonal concentration results again from errors in curvature measurements, as well as those in the angle measurements. No axial clustering is expected, since MM and MP depend equally, but oppositely on the angular errors.

8.7 Chi-Square Errors

The distribution of chi-square errors for events passing the 4C elastic hypothesis is shown in Figure 8.7-1. Note that as with missing momentum the distribution dips toward zero at the origin, rises to a maximum around chi-square equal to two, and then drops exponentially until it reaches a plateau that extends out to chi-square values

on the order of thirty. In theory, the chi-square distribution should follow a four-dimensional Maxwell-Boltzmann distribution. In other words, the probability that the chi-square error for a given event will lie between χ^2 and $\chi^2 + d\chi^2$ is proportional to

$$2 \exp(-\chi^2/2)\ \chi^3\ d\chi = \chi^2 \exp(-\chi^2/2)\ d\chi^2$$

providing the measurement errors are gaussian, and the systematic errors negligible. If, however, the measurement errors have been miss-assigned by a factor Q in TVGP, the chi-square distribution will be magnified according to the formula

$$(Q\chi)^2 \exp(-Q^2\chi^2/2)$$

The factor Q can be ascertained by fitting the experimental chi-square distribution under various magnifications until a best value for Q is obtained. On the other hand, if systematic errors cause some of the track measurements to be inaccurate, the functional form of the chi-square distribution will be altered. Following the interpretation for systematic errors used in the study of missing energy, we presume that such errors produce only a simple bias to the normal Maxwell-Boltzmann distribution. The solid curve in Figure 8.7-1 shows the result of a biased, and magnified Maxwell-Boltzmann fit to the

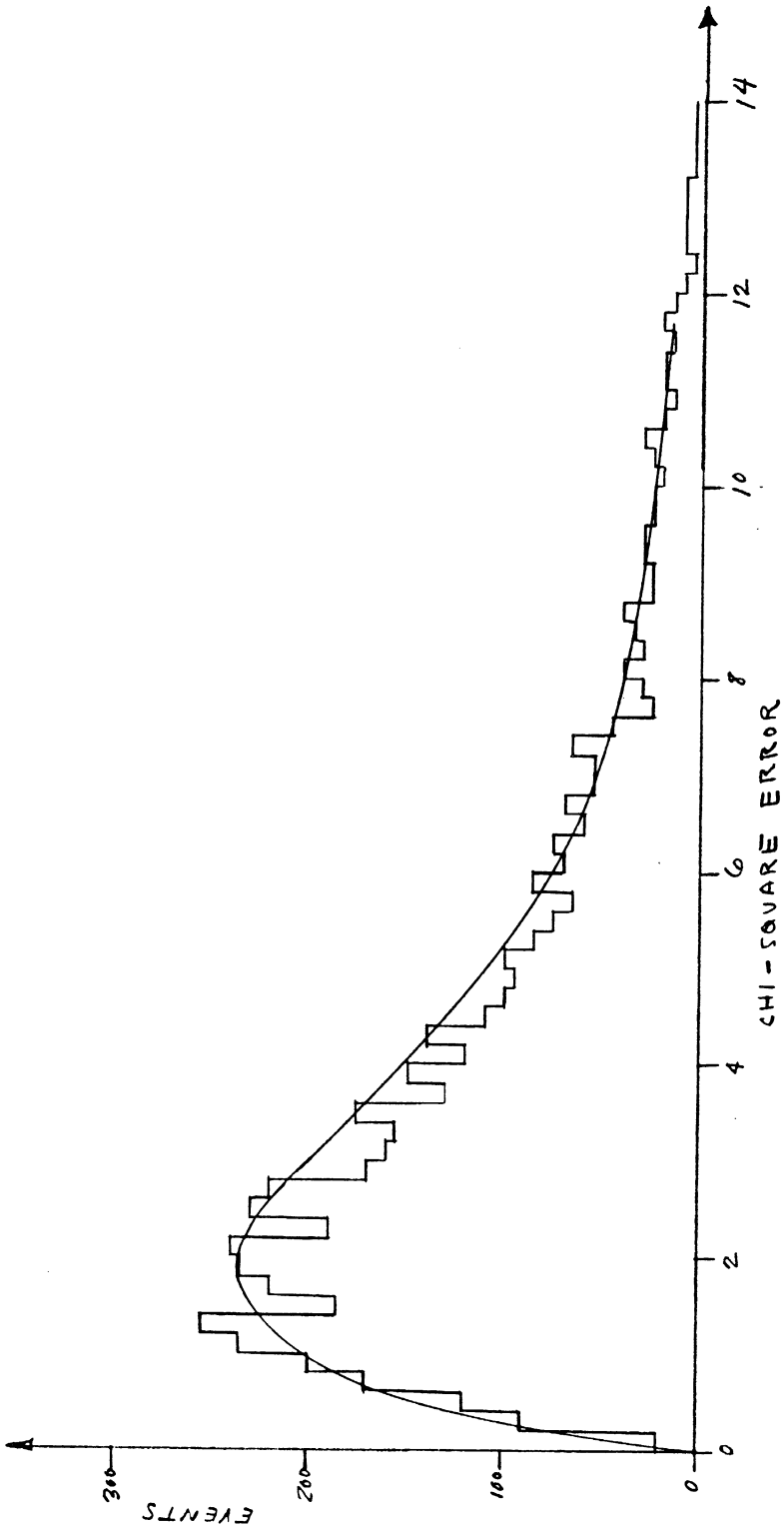

Figure 8.7-1. Chi-Square Errors for Elastic Events. The plot contains 5677 elastic events.

experimental data.[†] According to the fitting program a best fit obtained at a magnification given by Q = 1.06, and with a bias level of 7.5 events per bin. This indicates that the measurement errors were over-estimated by 6.0 percent, and that about 14 percent of the 4C fits suffered from systematic error.[§]

The chi-square probability distribution for events passing the 4C elastic hypothesis is shown in Figure 8.7-2. Note that the distribution appears sharply peaked near the origin, drops to a minimum in the intermediate probability range, and then rises slowly to another maximum at unit probability. When the measurement errors have been properly assessed in magnitude and form, and systematic errors negligible, the chi-square probability distribution should appear flat. The sharp peaking at the low confidence levels is a reflection of the systematic errors that generated the plateau in the chi-square error distribution from which the peak

---

[†]To ensure equivalent treatments of the error-assignment problem, the fits to the missing-energy, and chi-square distributions were applied to data samples having the same dynamic range, namely, 16 decibels.

[§]The 14 percent figure was obtained by multiplying the number of bins in the chi-square-error range zero to 16 by 7.5, adding the number of 4C events in the unfitted range between 16 and 34, and then dividing the result by the total number of 4C fits.

derives. The slight tilting of the remaining distribution results from our over-estimate of the measuring errors, since the latter tends to lower the chi-square errors, and hence increase the confidence level. No attempt was made to fit the probability distribution, however, as this would amount to a repetition of our analysis of the chi-square error distributions presented above.

The chi-square probability distribution for a sample of 144 events passing the 3C Mark 1, and 3C Mark 8 fits is shown in Figure 8.7-3. Since the sample contains so few events, a Maxwell-Boltzmann analysis was not considered worthwhile, and thus was omitted. Instead, we note (qualitatively) that the events appear concentrated at the expected confidence levels, namely, zero and one, as in the 4C fits. This suggests that SQUAW correctly analyzed the failure of the 4C fit attempt, and remedied the situation by dropping the proper constraint.

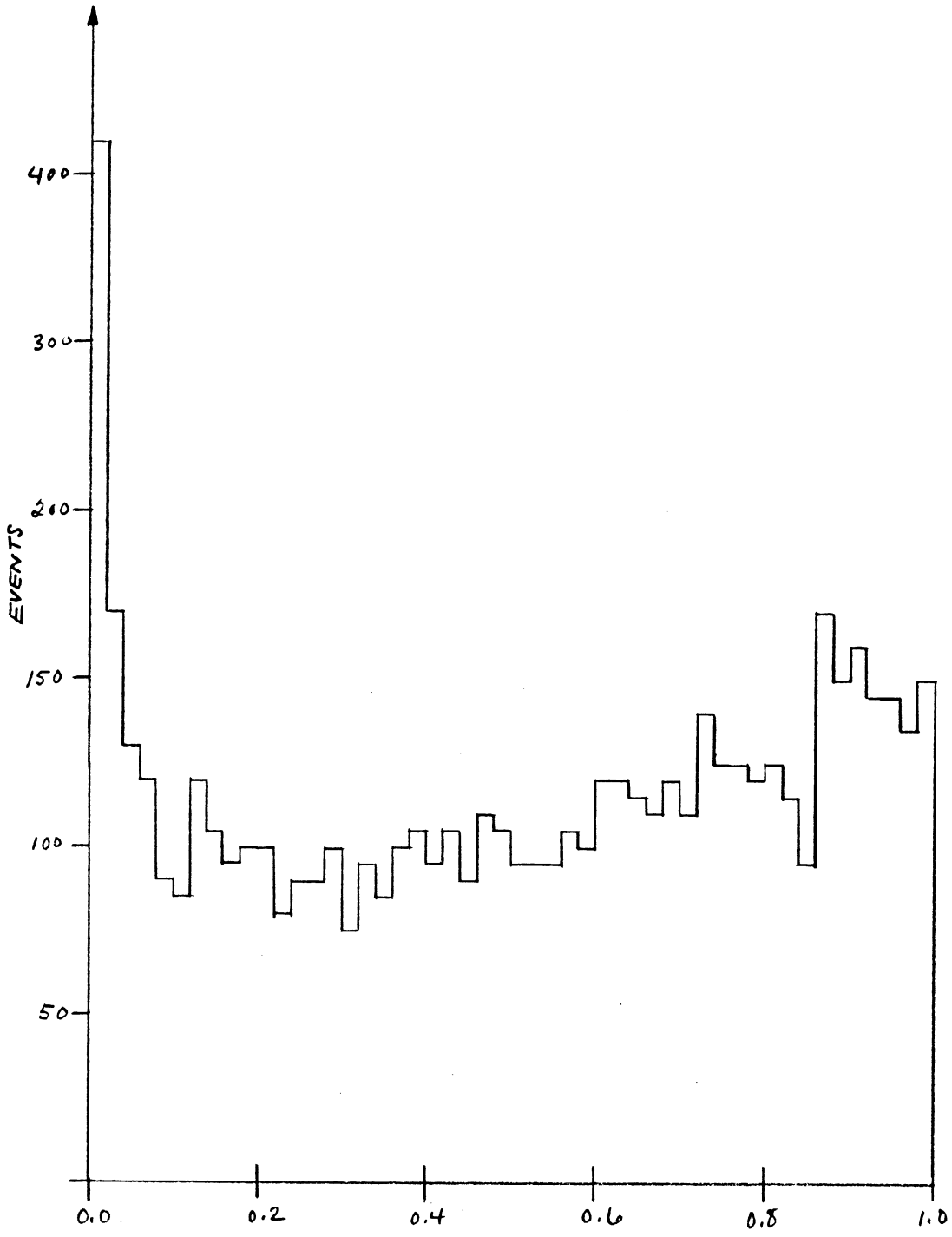

Figure 8.7-2. Chi-Square Probability for 4C Events. The histogram contains 5964 4C Mark 1 events; note the scale change for the ordinate above 200 events.

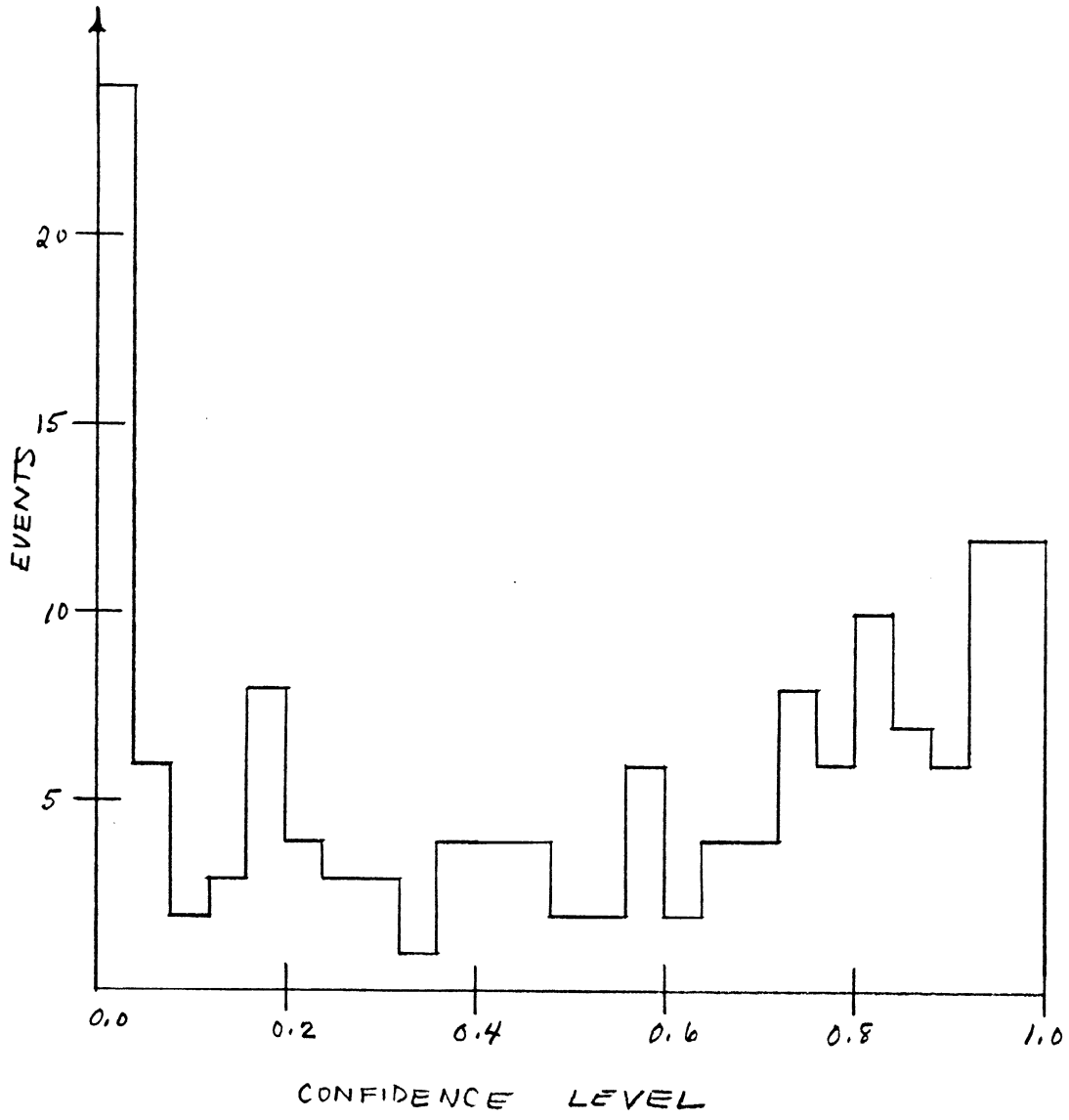

Figure 8.7-3. Chi-Square Probability for 3C Events. The histogram 144 3C Mark 8 and Mark 9 events.

9.0 ABSOLUTE CROSS SECTION DETERMINATION

This chapter presents the details of our absolute cross section determination. Since no attempt was made to tabulate the total number of PBAR-P interactions produced at each momentum set, the data could not be normalized to the accurate total cross section measurements of R. Abrams, et al. (1967). Instead, the absolute cross sections were deduced from the total beam-track length scanned at each momentum set. The scanned beam-track length was in turn determined by examining the geometry, and optics of the MURA chamber.

9.1 Geometry and Optics of MURA Chamber

The usable volume of the MURA chamber resembled a right circular cylinder approximately 30 inches (76.2 cm) in diameter, and 15 inches (38.1 cm) in height. The top and bottom faces of the cylinder were covered with glass plates having fiducial marks engraved on their inner surfaces. The chamber was illuminated through the bottom glass, and photographed through the top glass. The nominal plane of the beam tracks was also approximately the median plane of the chamber. The magnetic field ran approximately parallel to the axis of the chamber, and caused undipped 1 GeV/c tracks to arc with 101.3 cm radius

of curvature. The chamber coordinate system had its z-axis running along the chamber axis, and its origin centered on the inside surface of the window nearest the camera. (See Figure 9.1-1.)

Chamber illumination was provided by four circularly shaped xenon flash rings centered on the corners of a square positioned parallel to, and approximately 218 cm below the median plane, and having a diagonal dimension of 71.7 cm. A condensing doublet set adjacent to the bottom window directed light from the four flash rings diagonally through the chamber, and onto an image plane that coincided roughly with the front nodal plane of the four camera lenses in the unfolded optical system. The lenses were also effectively centered on the corners of a square running parallel to, and located an optical distance of 152.6 cm above the median plane, and having a diagonal dimension of 67.5 cm. (Table 9.1-1 gives the quadrant, and coordinates of the unfolded camera axes.) The chamber optics were designed so that the four flash-ring images would lie concentrically about the diagonally opposite camera lenses. With this geometry very little unscattered light reached the cameras, and the system appeared to have dark-field illumination. On the other hand, a large fraction of the scattered light reached the

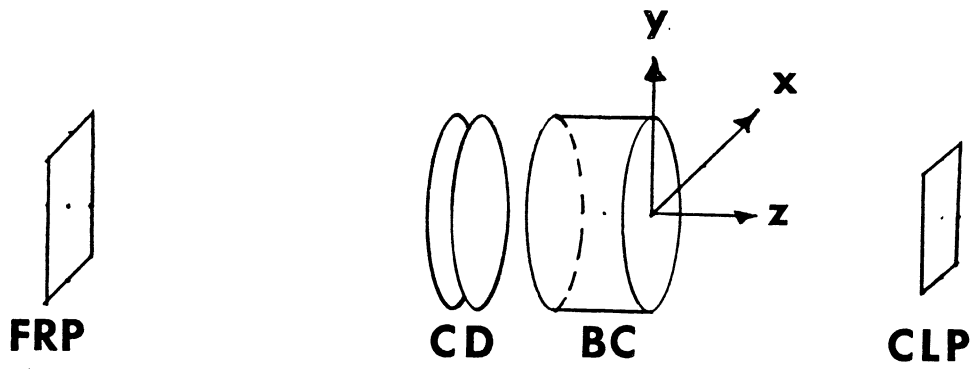

Figure 9.1-1. MURA Chamber Geometry. Here BC denotes the bubble chamber, FRP the plane of the xenon flash rings, CLP the plane of the camera lens, and CD the condensing doublet. (The figure is drawn approximately to scale.)

TABLE 9.1-1

Quadrant and Coordinates of Camera Axes

Camera Number	x-Coordinate	y-Coordinate	Quadrant
1	-23.35 cm	+23.35 cm	2
2	-23.35	-23.35	3
3	+23.35	-23.35	4
4	+23.35	+23.35	1

camera lenses, since (as in high-energy elastic scattering) most of the radiation was concentrated in the forward direction where the cameras were located.

The four camera lenses were Carl Meyer (Burke and James, Inc.) Videostigmats having an f/4 aperture, and a 125 mm focal length. These lenses were chosen to minimize off-axis aberrations, mainly coma and astigmatism, with flatness of field and uniformity of focal length of secondary importance. During exposure the lenses were closed down to f/16 or f/22 to insure good depth-of-field, and focused approximately one-inch beyond the median plane to obtain good magnification on bubbles nearest the camera. The film planes were located about 13.8 cm behind the back nodal plane of the lenses, producing a nominal chamber-to-film minification of 11.2.

The chamber illumination system, rather than the Videostigmats, determined the field-of-view of the camera at the median plane of the chamber. A ray trace provided by Argonne (J. A. Froehlich [1965]) of the extreme rays from the flash rings indicated that the illuminated area for each camera was approximately a circle of radius 33.2 cm, displaced approximately 3.7 cm from the chamber axis in the direction of the optical axis of the camera lens. The maximum fiducial volume for event vertices was

thus the (mathematical) union of these areas. To speed the scanning, and also provide adequate track length for measurement, the scanners were instructed to record only those events whose vertex appeared in all four camera views. In terms of the chamber optics, this rule generated a vertex fiducial volume for the experiment that was the (mathematical) intersection of the four circles of illumination. The intersected region of Figure 9.1-2 indicates that this area was roughly circular with a maximum radius of 30.6 cm, and a minimum radius of 29.5 cm. Since the beam tracks entered the chamber from the lower left-hand quadrant, and exited through the upper right-hand quadrant, the minimum radius effectively defined the vertex fiducial volume. The edges of the circles, however, were not always sharp when observed on film, so that a margin of safety was included, and the optical fiducial volume defined to be a circle lying in the median plane, having a radius of 29.0 cm, and centered on the chamber axis.

When the fitted elastic events became available, checks were made on the above determination by looking at histograms, and scatter-plots of the vertex coordinates. The scatter plot shown in Figure 9.1-3, for example, gives the xy-distribution of event vertices for 6601 good elastic

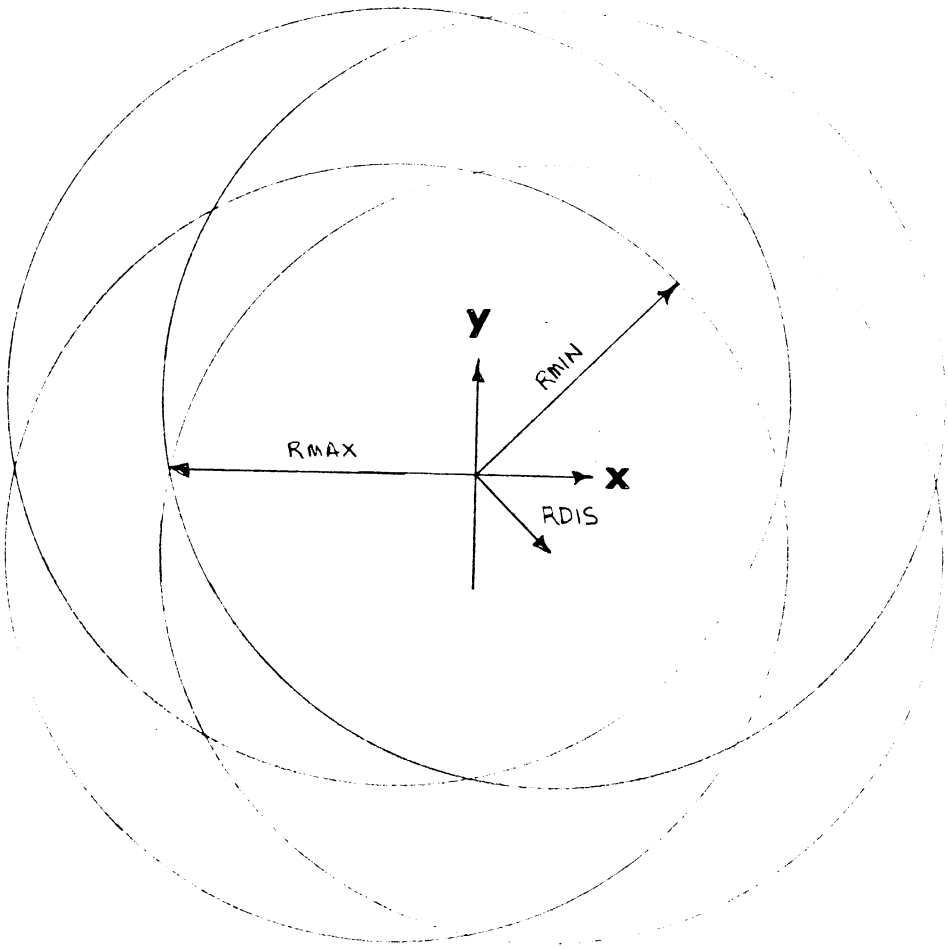

Figure 9.1-2. Vertex Fiducial Volume. The vertex-fiducial volume, as defined by the scan rules, was the (mathematical) intersection of the four eccentric circles of illumination. Since each circle was displaced diagonally from the center by a distance RDIS = 3.7 cm, the length of the minimum radius vector RMIN = 29.5 cm, while that of the maximum radius vector RMAX = 30.6 cm. (The figure is highly exaggerated.)

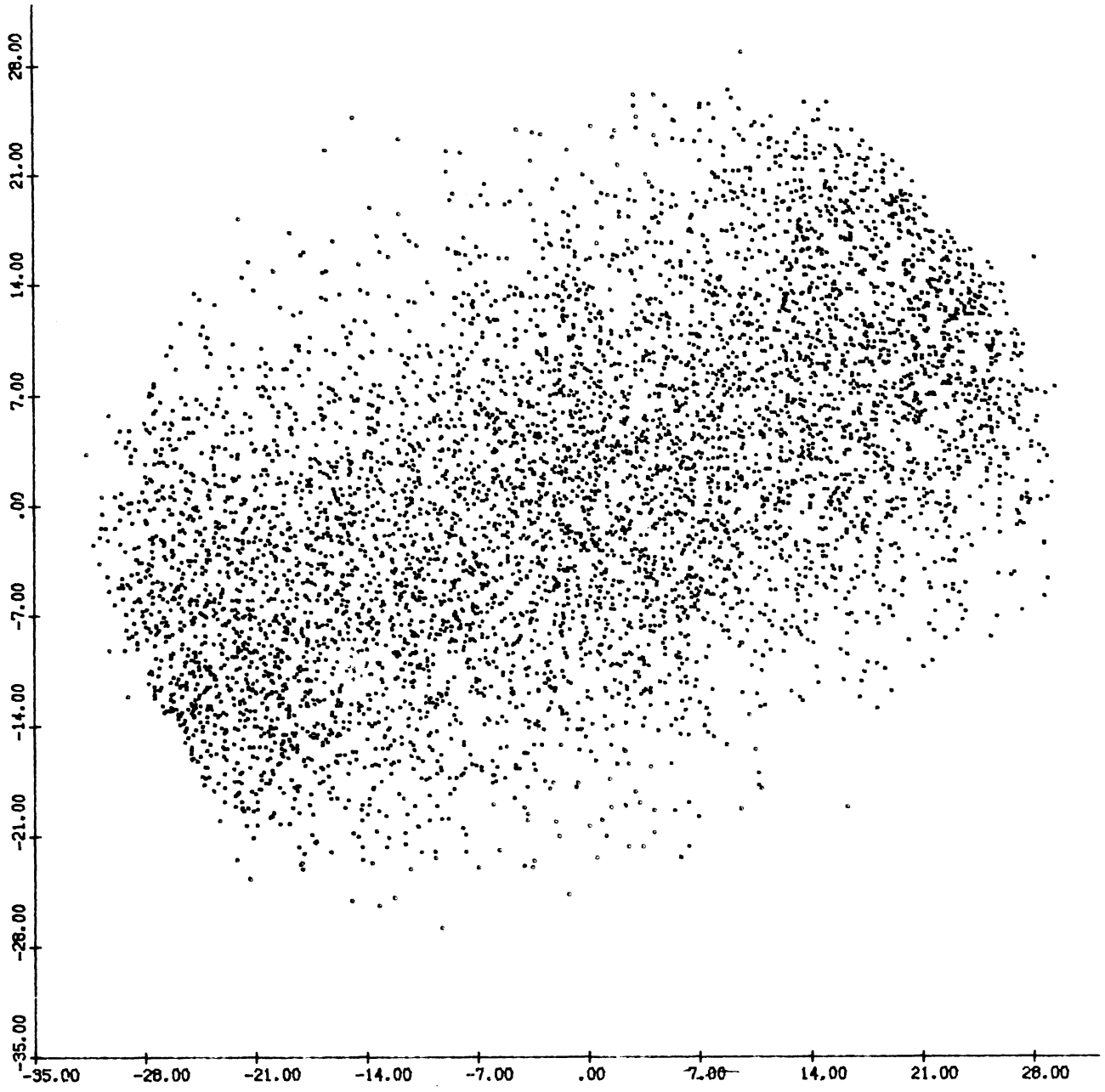

Figure 9.1-3. Event-Vertex Distribution.

events. A histogram of the radial coordinate of the good elastic events, shown in Figure 9.1-4, indicates in addition that the event distribution drops rapidly between 28 and 30 cm radius. This two centimeter uncertainty in radius likely results from a similar uncertainty in the illuminated edge on the bubble-chamber photographs. To eliminate any inaccuracies that might arise from this effect a new vertex fiducial volume was defined with a radius of 28 cm, also centered on the bubble-chamber axis.

9.2 Beam-Track Count

The average number of beam tracks per frame at each of the six momentum sets was determined by counting the number of tracks entering the vertex fiducial volume on every twentieth frame. Tracks were called qualifying beam tracks, and included in the count only if they passed between two selected points on camera view two, and deviated by less than one part in fifteen from the nominal direction of the beam. The line segment connecting the points ran perpendicular to the general direction of the beam, and was called the (gross) count line. The position of this line in the vertex fiducial volume was ascertained by noting its position relative to several fiducial marks, and then projecting it through the camera lenses onto the

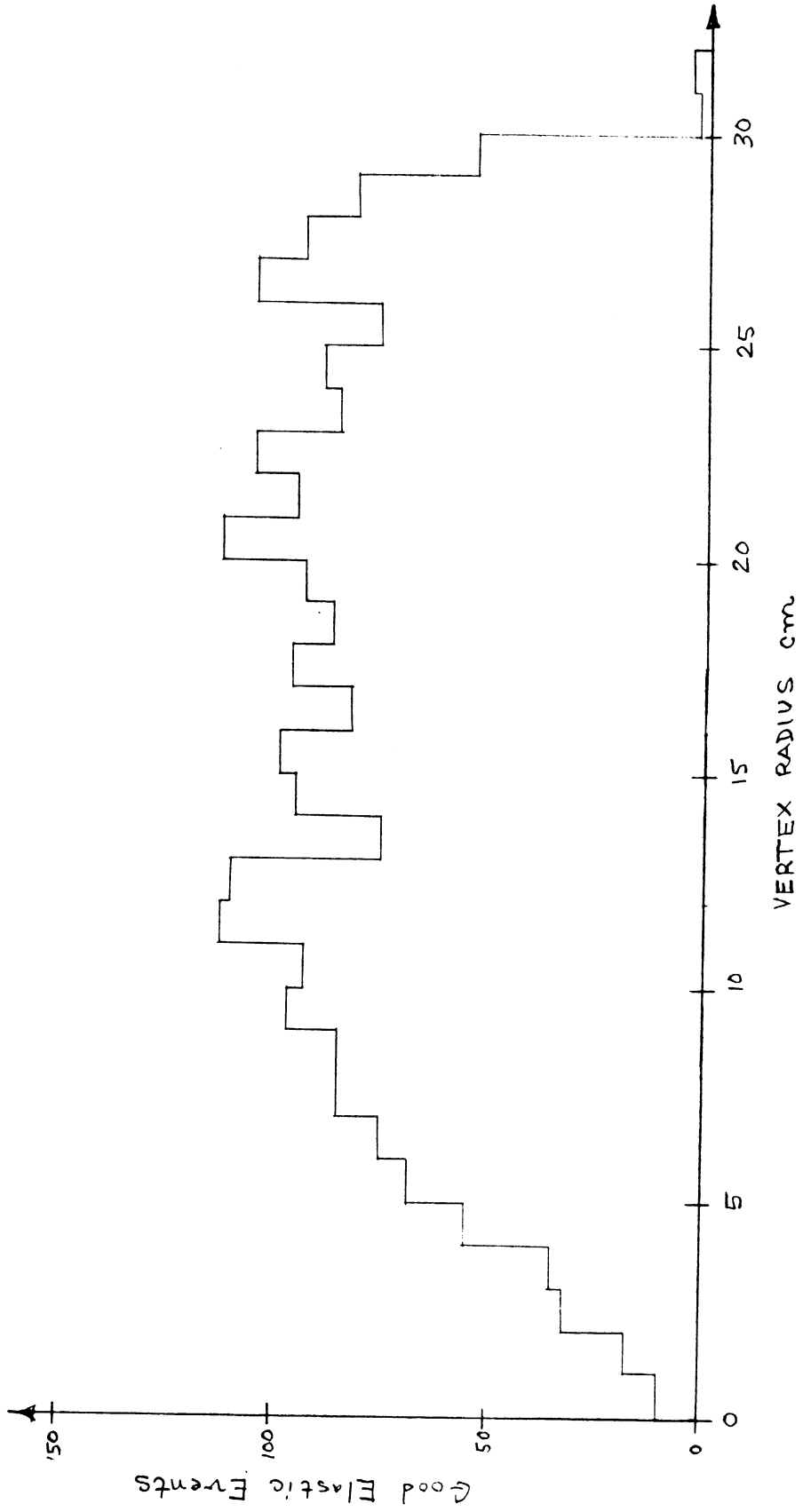

Figure 9.1-4. Radial-Coordinate Distribution. Note that the distribution drops rapidly between 28 and 30 cm radius.

median plane of the chamber.† In terms of the chamber coordinates, the count-line projection is described by equation:

$$y = -3.76x - 122,$$

where x and y are dimensioned in centimeters. (See Figure 9.2-1.)

During the beam count careful note was also made of missing rolls, missing frames, blank frames, and underexposed or overexposed section of film. These notes were compared with those made by the scanners on their pass through the film, and differences resolved on an individual basis. Table 9.2-1 contains the results of the beam and frame counts at each of the six momentum sets. These figures do not include a small correction (less than 2%) for the beam tracks passing above or below the (gross) count line.

9.3 Beam-Track Profiles

The beam-track profile, as seen by the scanners, was determined by partitioning the count line into twenty-five appropriate sized bins, and then counting the relative

---

†The author is indebted to C. Dyer for determining the position of the count line in the fiducial volume.

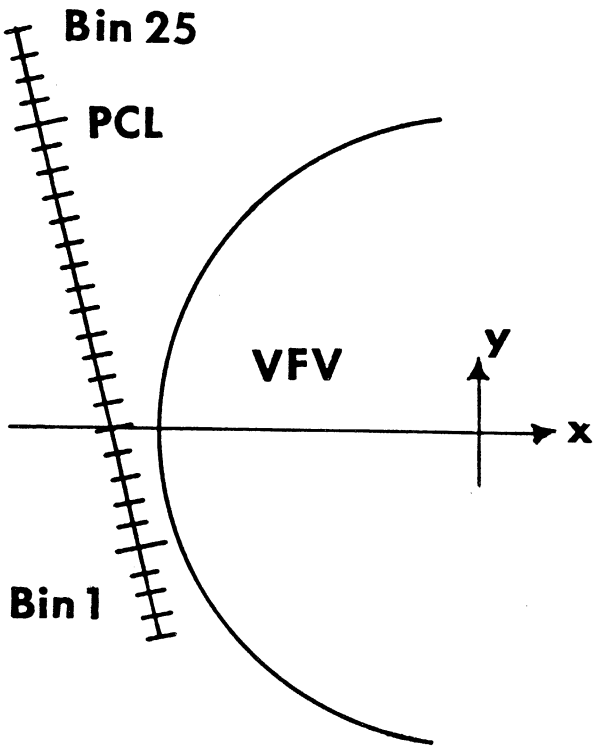

Figure 9.2-1. Count-Line Geometry. The elongated marks on the partitioned count line PCL denote the bins spanned by the gross count line. The beam profile was determined using all twenty-five bins. The circular segment denotes the upstream edge of the (28 cm) vertex fiducial volume VFV.

TABLE 9.2-1

Tracks and Frames Scanned

Beam Momentum	Frames Scanned	Qualifying Beam Tracks Scanned[#]
2.20 GeV/c	23,034	310,148 ±.80%[@]
1.95	23,136	323,504 ±.78%
1.87	26,747	388,548 ±.71%
1.83	24,710	319,522 ±.79%
1.75	24,634	316,156 ±.79%
1.63	24,078	281,765 ±.84%

[#]Includes only beam tracks that crossed the (gross) count line, and deviated by less than one part in fifteen from the nominal direction of the beam.

[@]Includes a one-percent correction for misexposed frames.

number of beam tracks that crossed each bin at each momentum set. Bin number one was located in the third quadrant of the vertex fiducial volume near the optical axis of camera two, and bin twenty-five in the second quadrant near camera axis one. Bins five through twenty-one spanned the (gross) count line used to determine beam-track density. Approximately 800 tracks at each momentum set were classified into the twenty-five bins, except at the first set (2.20 GeV/c) where about 1200 tracks were studied. Roughly half the tracks were taken from the beginning of the respective exposures, and half from the end, in an effort to average over any changes in beam position arising from current fluctuations in the beam-transport magnets.

The beam distribution along the count line was determined by histogramming the good elastic events at each momentum set. According to these plots the beam was centered in the general vicinity of bin eleven, and skewed slightly upward in the direction of camera four, with a nominal full-width at half-maximum of ten bins. (When used below to calculate average track lengths these distributions are normalized, and denoted for the i^{th} momentum set by $p_i(j)$, $j=1,25$.)

The profile of the beam in the depth coordinate z

was obtained by histogramming the vertex coordinate of good elastic events from all momentum sets. The resulting distribution was centered about the plane z = -18.5 cm, and had a full-width at half-maximum of approximately 1.5 cm. This indicated that the beam was confined to a coin-shaped region located a half-centimeter above the median plane, and having a nominal height of 1.5 cm.

The dip of the beam relative to the median plane was also investigated using the good elastic events. As indicated by histograms the beam dipped away from the cameras by something less than one-tenth of one degree. Dips of this magnitude increase the track length in the fiducial volume by a negligible amount (a few microns), and were thus neglected in determining absolute cross sections.

9.4 Beam Variation Along Count Line

The last quadrapole in the beam line, Q12, focused the beam in the z-direction, and dispersed it in the y-direction, thus causing the beam to enter the chamber port in a form convenient for scanning. As a result of this operation the pitch θ of the beam relative to the x-axis varied from bin-to-bin along the count line, with tracks in the higher numbered bins having the greatest average

pitch. The distribution of pitches at each bin, and at each momentum set was determined by making two-dimensional histograms of the good elastic events. These distributions, together with the beam-track profiles, were then used to determine the average beam-track length in the chamber. (When used below to calculate average track lengths, these distributions are normalized and, denoted by $p_{ij}(\theta)$, where the subscripts refer to the j^{th} bin of the ith momentum set.)

A check for similar fluctuations in the momentum distribution of the beam indicated that significant, but irregular variations were also present in these distributions. For completeness these results were also tabulated, and incorporated into the track-length determination described below. (When used below to calculate average track lengths, these distributions are normalized, and denoted for the i^{th} momentum set, and j^{th} bin by $p_{ij}(P)$, where P is the laboratory momentum of the beam.)

9.5 Average Beam-Track Length

The average beam-track length at each momentum set was computed by averaging over the beam profile, pitch, and momentum distributions described above. The computation was carried out by first determining the fiducial-volume track length for a beam track crossing the count

line at bin j, with a pitch θ, and momentum P. This length was then weighted according to the probability distributions for the variables j, θ, and P. In particular, the average track length, assuming none of the anti-protons interacted in the chamber, was obtained via the formula:

$$\bar{\ell}_i = \sum_{j=1}^{25} \iint \ell(j,\theta,P) \exp[\rho\sigma_t \Delta(j,\theta,P)]$$

$$P_i(j)\ P_{ij}(\theta)\ p(P)\ d\theta\ dP$$

To facilitate the calculation the two-integrals were also reduced to sums, and the whole carried out on a digital computer.

The exponential factor in the integrand compensates for tracks that were not counted because they interacted before reaching the count line ($\Delta>0$), or that were counted but failed to reach the fiducial volume ($\Delta<0$). The quantity $\Delta(j,\theta,P)$ is the orbital distance between the edge of the fiducial volume when the track passes through bin j with momentum P, and pitch θ, and is taken positive (negative) if bin j lies inside (outside) the fiducial volume. The product $\rho\sigma_t$, which specifies the beam depletion per unit length, was obtained by taking the density of hydrogen as .0622 g/cc, and using the

PBAR-P total cross section measurements of R. J. Abrams, et al. (1967).

Table 9.5-1 gives the average beam-track length at each momentum set, assuming no interactions occur in the fiducial volume. The assigned errors are purely statistical, and based on the number of good elastic events available at each momentum set for the determination of the profile, pitch, and momentum distributions, as well as on the systematic and statistical errors associated with the PBAR-P total cross section measurements. (See Section 9.8 below.) The right-hand column of Table 9.5-1 specifies the efficiency of the beam-count described above. These numbers are simply the ratio of the number of qualifying beam tracks crossing the gross count line (bins five through twenty-one) to the total number of beam-tracks crossing the profile count line (bins one through twenty-five). Their errors were assigned with the usual square-root-of-the-sample-size formula.

9.6 Beam Contamination

Even before the experimental run little beam contamination was expected owing to the relatively low beam momenta, and relatively large mass difference between the antiproton, and its possible muon, pion, and kaon

TABLE 9.5-1

Average Beam-Track Length in Vertex Fiducial Volume[#]

Beam Momentum	Ave. Track Length	Statistical Uncertainty	Systematic Uncertainty	Beam-Count Efficiency[@]
2.205	52.48 cm	±.08 cm	±.05 cm	99.4 ±0.2%
1.944	52.41	±.08	±.05	99.9 ±0.29%
1.883	52.59	±.08	±.05	99.6 ±0.2%
1.823	52.17	±.08	±.05	99.7 ±0.2%
1.763	52.09	±.08	±.05	99.6 ±0.2%
1.624	52.70	±.08	±.05	99.8 ±0.2%

[#]For 28 cm vertex fiducial volume.

[@]See text for definition of beam-count efficiency.

contaminants. The possibility of contamination was reduced further by the length of the Argonne seven-degree beam (about 490 feet), and its two stages of separation (both operated at less than peak efficiency to prevent separated contaminants from orbiting over the mass slits, and perhaps entering the chamber). Further precaution was taken by mounting a pion-sensitive Cherenkov counter upstream of the second mass slit to monitor high-velocity particles. This counter was reset after each reel (1200 frames) was exposed, and its operation checked occasionally by sweeping the beam across the mass slit with the separators. During the course of the run the author noted only one count in a series of random checks that included about one-fourth the film.

A substantial portion of the beam was scattered, however, by an aluminum cover plate, and the stainless-steel beam-entry port, and by the liquid hydrogen situated between the port, and the vertex fiducial volume. The aluminum cover plate was approximately .64 cm thick, and presented about 5.42×10^{23} (effective) targets/cc, while the stainless-steel port was about .27 cm thick, and presented about 1.23×10^{24} (effective) targets/cc. The distance between the port, and the fiducial volume was about 15.2 cm, with the liquid hydrogen presenting about

3.7×10^{22} targets/cc.[†] The percentage of the beam scattered into the inelastic channels by these two media (using a total inelastic cross section of 60 mb) amounted to 7.5%. Only a fraction of these scatters produced a negative track with a direction and momentum capable of simulating a qualifying beam track. An accurate calculation of this fraction was difficult, however, since neither the total or differential cross sections for the various inelastic channels are currently known. In lieu of this calculation the author went to the scanning machines, and looked at 157 obviously inelastic collisions. Only six events in this sample produced a negative track that could be construed as a qualifying beam track. Thus, it was concluded from this study that the fiducial-volume beam contamination was .3 ±.2%.

Another estimate of beam contamination was obtained by measuring the lengths of delta-rays produced a sample of 9800 qualifying beam tracks.[§] Only one of these had a range greater than that which could arise in an antiproton-electron collision at our energies. Since the pion-

---

[†]The author is indebted to F. Schweingruber for furnishing these numbers.

[§]This study was carried out by R. Kiang under the direction of J. Lys.

electron cross section for producing delta rays longer than that obtainable in an antiproton-electron collision represents about one-fortieth the total pion-electron cross section, it was concluded that approximately 40 of the 9800 tracks were actually pions. This indicated that the pion contamination in the fiducial volume was .4 ±.3%.

9.7 Cross-Section Per Event

The cross section per event at each momentum set was determined from 1) the number of antiprotons entering the vertex fiducial volume, 2) the average beam-track length in this volume, 3) the density of targets, and 4) PBAR-P total cross section. The beam contamination, and beam-count efficiency were also incorporated into the determination, but not the scanning, measuring, book-keeping, reconstruction, or fitting losses, as these are channel dependent in general. The number of targets presented per unit volume by the liquid hydrogen was deduced from the thermal conditions of the chamber. According to vapor pressure measurements taken during exposure, the temperature, and density of the liquid hydrogen target were, respectively, $26.4^{\circ} \pm 0.2^{\circ}$ K, and 62.2 ±0.4 mg/cc.[†]

[†]The temperature and density of the hydrogen were obtained in the usual way using the average metered vapor pressure, and the National Bureau of Standards Cryogenic

Consequently, the number of proton targets present per unit volume was

$$\rho = (2 \text{ targets/molecule})(6.025 \times 10^{23} \text{ molecules/mole})$$
$$\cdot(1/2.016 \text{ moles/g})(.0662 \pm .0004 \text{ g/cc})$$
$$= 3.717 \pm .022 \times 10^{22} \text{ targets/cc}$$

In making the above calculation, we have noted that hydrogen contains two atoms per molecule.

Tables 9.7-1 through 9.7-3 list the various parameters and correction factors used to determine the cross section per event at each momentum set. The total cross section values shown in Table 9.7-1 were obtained at Brookhaven National Laboratory, and incidentally indicate the existence of a two millibarn bump around 1.8 GeV/c (R. J. Abrams, et al. [1967]). The right-hand column of Table 9.7-3 contains the cross section per event at each of the momentum sets. The uncertainties assigned to these (important) quantities were obtained by combining statistical errors orthogonally, and systematic errors linearly.

Tables. A thermodynamic study of the MURA chamber, carried out at Argonne National Laboratory, indicates that such average values yield substantially correct target densities at beam-entry time. (F. Schweingruber, private communication.)

TABLE 9.7-1

Antiproton-Proton Total Cross Sections[#]

Beam Momentum	Cross Section	Statistical Uncertainty	Systematic Uncertainty[@]
2.205 GeV/c	86.31 MB	±.06 MB	±1/2%
1.944	91.36	±.06	±1/2%
1.883	92.75	±.06	±1/2%
1.823	94.14	±.06	±1/2%
1.763	95.32	±.06	±1/2%
1.624	97.57	±.06	±1/2%

[#]Deduced from R. J. Abrams, et al. (1967).

[@]Includes momentum-dependent uncertainties.

TABLE 9.7-2

Scanned Beam Tracks

Beam Momentum (GeV/c)	Scanned Beam Tracks (Uncorrected)#	Beam Count Efficiency	Scanned Beam Tracks (Corrected)#
2.205	310,148 ±.80%	99.4 ±.2%	311,084 ±.83%
1.944	323,504 ±.78%	99.4 ±.2%	324,480 ±.81%
1.883	388,548 ±.71%	99.5 ±.2%	389,329 ±.79%
1.823	319,522 ±.79%	99.7 ±.2%	319,522 ±.82%
1.763	316,159 ±.79%	99.6 ±.2%	316,473 ±.82%
1.624	281,765 ±.84%	98.7 ±.3%	284,045 ±.86%

#Quoted error purely statistical.

TABLE 9.7-3

Cross Sections Per Event[#]

Beam Momentum (GeV/c)	Beam-Track Length (Centimeters)	Target Density/cc ($\times 10^{22}$)	Cross Section Per Event (Microbarns)
2.205	52.48 ±.02[$]	3.717 ±.012[$] ±.010[@]	1.793 ±.015[$] ±.006[@]
1.944	52.41 ±.02	3.717 ±.012 ±.010	1.728 ±.014 ±.006
1.833	52.59 ±.02	3.717 ±.012 ±.010	1.437 ±.012 ±.005
1.823	52.17 ±.02	3.717 ±.012 ±.010	1.766 ±.015 ±.006
1.763	52.09 ±.02	3.717 ±.012 ±.010	1.787 ±.015 ±.006
1.624	50.72 ±.02	3.717 ±.012 ±.010	2.044 ±.018 ±.007

[#]Fiducial volume radius = 28.0 cm.

[@]Quoted error reflects systematic uncertainties.

[$]Quoted error includes both statistical and momentum-dependent uncertainties.

10.0 EXPERIMENTAL FINDINGS

In this chapter we present the differential cross sections obtained via the large-angle, and square-hit scans. The raw data is first corrected for omission and duplication in the bookkeeping system, and scanning efficiency and scan-rule bias as a function of the center-of-momentum scattering angle. The modified distributions are analyzed for maxima and minima in the differential cross section, and dips and bumps in the backward cross section in the next chapter.

10.1 Bookkeeping and Processing Corrections

Problems of omission and duplication in the bookkeeping system were minimized by using a digital computer, rather than human help, to tabulate the results of scanning and measuring. Errors originating in the processing system, particularly at the measuring machine, proved more difficult to control, and a significant number of the scanned events were either lost or duplicated in processing. Event duplication resulted primarily from the inadvertent remeasure of an already measured event, although a small fraction were intentionally doubly measured to verify the soundness of the scan rules. Events were omitted from the summary tape either because the

measurer forgot, or decided not to measure an event, or because the event failed the monitoring program CAST, or the geometry program TVGP.

The event duplication problem was handled by purging the sample of good elastic events of all duplicate events. The procedure used was the following: the roll, frame, and four-momentum transfer in (GeV/c) associated with each event were first abstracted from the summary tape, and stored in the memory of the digital computer according to their roll, and frame number. Events with the same roll, and frame numbers were then compared with one another to determine if any pair had the same four-momentum transfer to two decimal places. When a pair of matching events was found, the first event read from the summary tape was declared the duplicate, and deleted from the list in the memory. Using the purged list, a new summary tape was derived containing only non-duplicate events. To check that the above procedure was effective in detecting doubly measured events, the author personally checked the results of the purge for several rolls that had been mistakenly doubly measured, and found that all such duplicates had been deleted from the new summary tape. To determine if any non-duplicate events were deleted in the processing, the

probability that two events would have the same roll, frame, and four-momentum transfer to two decimal places was computed, and indicated that less than 1/10% of the events could have deleted by the purge, a figure negligible in the present study.

Events were omitted from the summary tape, on the other hand, either as the result of an error or decision by the measurers, or because the event failed to pass the monitoring and reconstruction programs CAST-TVGP. With regard to the former the action taken by the measurer fell into three categories: 1) he inadvertently skipped the event during measurement of the roll, 2) he decided the event could not be measured under the existing measuring rules, 3) he concluded that the event was in flagrant violation of a scan rule, and hence should not be measured. To keep the measurers from falling back on 2) and 3) whenever a difficult event was encountered, and also to obtain a list of intentionally omitted events, the measurers were instructed to write out in long-hand the reason for passing over the event.† The list obtained with this procedure then provided a means for determining the fraction of unmeasured events

---

†The author is indebted to C. T. Murphy for pointing out this effective, but convenient enforcement technique.

that should in fact have been subjected to measurement.

The number of good elastic events lost through errors or omissions by the measurers, or failures in the monitoring and reconstruction programs CAST-TVGP were determined by collating the events on the general summary tape (which contained the results of all measurements, including the CAST-TVGP fails) with events found by the scanners.† New lists were then made on the unscanned events, the unmeasured events, and the CAST and TVGP fails. An event was declared unmeasured (unscanned) if no event with same roll, and frame numbers appeared on the general summary tape (scanned event list); an event was considered a permanent CAST (TVGP) fail if its best measurement led to a CAST (TVGP) fail. The list of unmeasured events was then compared with the list of events overtly deleted by the measurers, and the fraction accidentally left unmeasured thereby determined. The fraction of good elastic events among the permanent CAST fails, the permanent TVGP fails, and the accidentally unmeasured events was then presumed equal to fraction of good elastic events appearing among the scanned events,

---

†The collating, and bookkeeping program referred to here was written, prepared, and run by L. Peterson.

TABLE 10.1-1

Bookkeeping and Processing Losses

PLAB (GeV/c)	Loss (Percent)	Statistical Error	Systematic Error
1.63	8.3%	0.5%	1.0%
1.77	5.4%	0.5%	1.0%
1.83	4.7%	0.5%	1.0%
1.88	8.2%	0.5%	1.0%
1.95	5.7%	0.5%	1.0%
2.20	4.9%	0.5%	1.0%

when the latter were successfully measured, that is, passed both CAST and TVGP.†

10.2 Large-Angle Scan-Rule Bias

As discussed in Section 7.4 above, the large-angle scan rules were designed to detect all events with $0.6 < |t|$ $(GeV/c)^2$, have a good probability for picking up events in the range $0.3 < |t| < 0.6$, and heavily suppress events in the well-studied forward diffraction peak $0.0 < |t| < 0.3$. Since the scan rules proved wholly efficient in none of these regions, it was necessary to determine the exact scan-rule bias at each momentum set, and in each t interval using digital-computer simulation techniques. The simulation was carried out by determining the center-of-momentum energy from the nominal beam momenta, and the scattering angles of the tracks from t. The angles, and momenta of the outgoing tracks were then Lorentz transformed to the laboratory system, and the event vertex centered on one of the twenty-five laterally positioned bins used to determine the beam-track

---

†This procedure, though less than appealing, seems conventional, and appears the only method, short of a detailed (and prohibitively difficult) study of each event, for determining the number of good elastic events among the CAST-TVGP fails.

profile.† The vertex was then stepped upstream, and downstream by following the path of a hypothetical beam track passing through the center of the profile bin. (This procedure, though more complicated than a Monte-Carlo technique, allowed the various event vertices to be weighted according to the beam-track density at the interaction point.) After the vertex coordinates were picked, a check was made that the coordinates lay in the illuminated portion of the fiducial volume. On passing this test, the antiproton's momentum vector was rotated into coincidence with the beam direction at the vertex point. A second rotation then put the event topology in the desired azimuthal position about the beam. Finally, the angles, curvature, and bubble density of each track on each camera view were calculated using the formulas given in the Appendix, and the mathematical equivalent of the scan rules applied on the various camera views.

To ensure that accurate results were obtained the simulation procedure was repeated using beam momenta spread above and below the nominal one. The pass-fail results for each momentum hypothesis were then weighted

---

†This set of bins, called the projected count line in Section 9.2, partitioned a line (y=-3.76x-122) in the median plane of the chamber that ran approximately at right angles to the nominal direction of the beam.

according to the normalized beam-momentum distributions $p_{ij}(P)$ for i^{th} momentum set, and j^{th} profile bin.† The simulation procedure was similarly embellished by varying the pitch θ of the beam at the profile bins, instead of the momentum P, with the pass-fail results being weighted to the beam-pitch distributions. An additional simulation was also carried out with both the momentum and pitch varying to determine if the two had any tendency to concatenate their effects on the pass-fail distributions. The results of these three studies indicated that the average values for P and θ yielded substantially correct results, the largest pass-fail variance amounting to less than 1%. Moreover, since the digital-computer time required for the simulation increased from minutes to hours when these variations were included, it was decided in the interest of economy to use the mean values for the balance of the study.

The mathematical formulation of the scan rules proved straight forward in principle, but vexing in practice. Actually, only the fan-template rule (4), and the positive-track curvature rule (5) were effective in failing elastic events with $|t| > 0.3$, since the other rules

---

†See, also, Section 9.4 above.

were designed either to attenuate the forward diffraction peak, or suppress the background of inelastic events. The more arduous phase of the formulation arose in attempting to ascertain the rules actually employed by the scanners, rather than the ones they were instructed to use. The rule on positive-track curvature, for example, was somewhat unclear, since curvature may be determined either globally or locally with the same template. The global determination amounts to a comparison of the sagitta of the template with that of the track, a technique that tends to be ambiguous when the track is long, and inaccurate when it is short.† On the other hand, the local determination is equivalent to a comparison of the rate-of-change of the template tangent with that of the track in the immediate neighborhood of the event vertex. The technique thus depends on the accuracy with which the tangents can be aligned at the vertex, but is otherwise unambiguous. Although the author trained the scanners in the tangent technique, and also prepared a special section in the scan rules describing the procedure, the scanners still gravitated to the sagitta technique,

---

†When the track is long, the radius of curvature decreases with the range of the particle, but increases with its distance from the optical axis; when the track is short, the length of the sagitta (and hence the accuracy of the determination) varies quadratically with the track length.

since the latter was slightly easier to apply. In spite of this, and because it could be unambiguously defined, the vertex-zone curvature was used throughout the simulation. As a check on the soundness of this procedure, the radius of the positive track in View 2 or View 4, whichever was greater, was histogrammed using the good elastic events, and is shown in Figure 10.2-1. Note that the distribution drops sharply at 40 cm radius, but that a significant number of events with a smaller radius still slipped by the scanners. The latter, of course, could have resulted either from use of the sagitta technique, or from uncertainties arising when the positive track was short.

The fan-template rule also proved somewhat difficult to formulate, mainly because of the template design. As shown in Figure 7.2-1, the template rays terminated a quarter inch from the template origin, thus forcing the scanners to make their bin determinations at this distance from the event vertex. As a result, some tracks were able to curve out of their original bin, and into an adjacent one prior to point where the scanners made their bin determination.† To determine the sig-

---

†This possibility was brought to the author's attention by D. Sinclair.

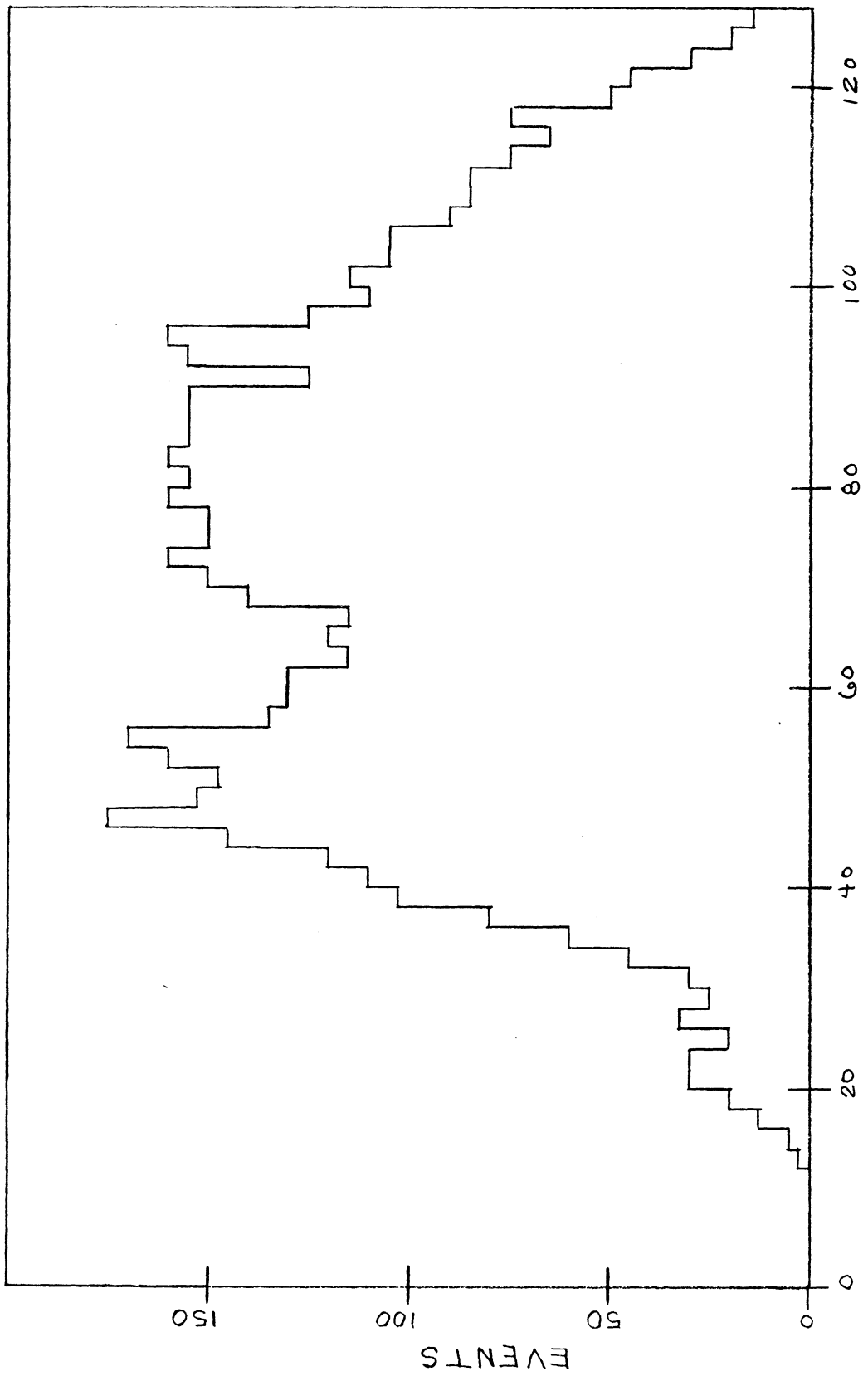

Figure 10.2-1. Positive-Track Radius on Viewing Screen. The histogram contains 6214 good elastic events.

nificance of this effect the full set of scan rules were applied both to the good elastic events, and the computer simulated ones, assuming first that the bin determinations were made at the origin, and then at one quarter inch from the event vertex. When applied to the real events the first set of scan rules deleted a total of 1013 events from the original sample of 6214 good elastic events, while the latter deleted only 995 events. As a result it was concluded that the scanners tended to make their bin judgements at some--perhaps variable--distance downstream. Owing to the subjectivity of the effect and its tendency to occur at the lower momentum transfers, no attempt was made to parameterize it directly. Instead, it was presumed both for the purpose of simulation, and initial sample cutting that all bin determinations were made exactly one-quarter inch downstream.

As a check on the soundness of the simulation technique, the azimuthal distributions predicted by the simulation program were compared with those for the good elastic events.† In particular, two-dimensional histograms of t versus azimuth were prepared at each momentum set using both the good elastic events (with the scan

---

†This verification technique was suggested by J. Vander Velde.

rules in force), and the computer simulated ones.[†] The resulting distributions for all six momentum sets, and the momentum-transfer range $0.5 < |t| < 0.6$ are shown, respectively, in Tables 10.2-2 and 10.2-3. Within statistics--unfortunately rather poor owing to the cuts on both projectile energy and four-momentum transfer--the two distributions appear in good agreement.[§] As a result it was concluded that the simulation technique accurately portrayed the event distributions in the chamber, as well as the scanners' notion of the scan rules.

To guarantee accurate corrections for scan-rule bias, a new set of scan rules was formulated that were more restrictive than the ones used by the scanners. These rules were then applied to both the good-elastic events, and the computer-simulated ones to determine if the original simulation was sound. The argument advanced here presumes that, except for increased statistical fluctuations, the experimental results should remain invariant under transition to a more restrictive set of

---

[†]Here $-\pi < \psi < +\pi$ is the azimuthal position about the beam track, taken positive when the antiproton scattered toward the cameras, and zero when it scattered without dip in the positive y direction.

[§]Note the natural asymmetrical bias between events with the antiproton scattered upwards, and those with it scattered downwards.

TABLE 10.2-2

Experimental Azimuthal Event Distributions#

Azimuth Degrees	1.63 (GeV/c)	1.77 (GeV/c)	1.83 (GeV/c)	1.88 (GeV/c)	1.95 (GeV/c)	2.20 (GeV/c)
10	2	0	0	0	0	0
30	4	1	0	0	0	0
50	0	0	1	1	0	0
70	1	4	1	1	0	0
90	1	6	4	1	0	4
110	1	3	4	0	0	1
130	1	0	0	0	0	0
150	3	0	2	0	1	0
170	0	0	0	0	0	0
190	3	1	4	0	0	0
210	4	5	3	6	5	0
230	4	5	4	5	6	0
250	6	6	6	2	9	2
270	4	2	1	5	3	2
290	4	8	6	5	6	2
310	7	3	3	6	6	4
330	8	3	7	6	6	0
350	3	1	3	2	1	0

#Table includes good elastic events with $0.3 < |t| < 0.4$, and passing a (10% restricted) set of computer-applied scan rules.

TABLE 10.2-3

Simulated Azimuthal Event Distributions#

Azimuth (Degrees)	1.63 (GeV/c)	1.77 (GeV/c)	1.83 (GeV/c)	1.88 (GeV/c)	1.95 (GeV/c)	2.20 (GeV/c)
10	100%	30%	0%	0%	0%	0%
30	49%	0%	0%	0%	0%	0%
50	43%	28%	5%	2%	0%	0%
70	49%	12%	5%	4%	1%	0%
90	90%	80%	71%	71%	65%	51%
110	83%	53%	45%	27%	26%	10%
130	36%	19%	5%	4%	2%	0%
150	37%	12%	2%	0%	0%	0%
170	100%	0%	0%	0%	0%	0%
190	100%	99%	0%	0%	0%	0%
210	100%	69%	56%	53%	51%	37%
230	82%	82%	74%	65%	56%	41%
250	65%	65%	65%	65%	65%	61%
270	48%	48%	50%	52%	52%	63%
290	48%	48%	50%	49%	50%	48%
310	86%	84%	78%	81%	81%	58%
330	100%	100%	99%	94%	90%	13%
350	100%	12%	0%	0%	0%	0%

#The quoted percentages represent the scan-rule efficiency at each momentum set, and each azimuthal angle as determined from a sample of simulated events with $|t|=.35$.

rules.† Toward this end the fan-template angles for the positive track, and maximum allowed curvature for the positive track were both reduced by a fixed amount, namely, first by 10%, then by 20%. These changes made the new rules a subset of the original ones in the sense that events picked up by the second set were necessarily also picked up by the first. The invariance of the experimental results was then checked by applying the two sets of restricted rules to both the good elastic events, and the computer simulated ones. The scan-rule bias for each momentum set, each four-momentum transfer, and each set of scan rules was then determined from the pass-fail ratio for the simulated events. The passing good elastic events were then weighted inversely as the scan-rule bias associated with each event, and the result histogrammed against t. As shown in Tables 10.2-4 through 10.2-6, the results for the two restricted cases agree within statistics, while there appears some discrepancy between the non-restricted and 10% restricted case. This indicated that by applying the 10% restricted scan rules to both the good elastic events, and the computer simulated ones that accurate corrections for scan-rule bias could be obtained.

---

†The technique for verifying the soundness of the simulation technique was suggested by C. Murphy.

TABLE 10.2-4

Debiased Event Distributions (Non-Restricted Scan Rules)

$\|t\|$ $(GeV/c)^2$	1.63 (GeV/c)	1.77 (GeV/c)	1.83 (GeV/c)	1.88 (GeV/c)	1.95 (GeV/c)	2.20 (GeV/c)
0.25	163.6	274.3	302.6	306.9	317.9	464.1
0.35	47.7	72.2	68.4	67.0	74.3	56.7
0.45	48.0	60.9	61.5	51.3	60.4	33.9
0.55	111.0	107.0	100.0	111.5	89.1	58.0
0.65	135.0	119.0	114.0	135.0	104.0	92.0
0.75	128.0	135.0	98.0	128.0	110.0	102.0
0.85	108.0	57.0	70.0	84.0	60.0	93.0

TABLE 10.2-5

Debiased Event Distributions (10% Restricted Scan Rules)

$\|t\|$ $(GeV/c)^2$	1.63 (GeV/c)	1.77 (GeV/c)	1.83 (GeV/c)	1.88 (GeV/c)	1.95 (GeV/c)	2.20 (GeV/c)
0.25	679.8	439.0	434.3	518.9	388.7	326.7
0.35	48.4	73.1	81.8	88.2	93.9	78.0
0.45	49.3	54.3	57.1	45.1	50.6	29.7
0.55	105.0	100.0	97.4	103.8	79.2	46.9
0.65	106.0	119.0	114.0	134.0	102.2	86.4
0.75	95.0	135.0	95.0	128.0	110.0	102.0
0.85	63.0	82.0	77.0	108.0	83.0	93.0

TABLE 10.2-6

Debiased Event Distributions (20% Restricted Scan Rules)

$\|t\|$ $(GeV/c)^2$	1.63 (GeV/c)	1.77 (GeV/c)	1.83 (GeV/c)	1.88 (GeV/c)	1.95 (GeV/c)	2.20 (GeV/c)
0.25	895.0	666.6	473.9	613.0	483.5	337.8
0.35	42.8	80.2	84.9	114.8	101.3	74.4
0.45	47.6	53.4	50.7	44.3	58.2	37.5
0.55	100.4	89.3	98.9	105.0	73.8	31.5
0.65	106.0	116.0	110.0	121.6	92.8	72.4
0.75	95.0	135.0	98.0	128.0	110.0	97.9
0.85	63.0	82.0	77.0	108.0	83.0	90.9

TABLE 10.2-7

Large-Angle Scan-Rule Efficiency (10% Restricted Scan Rules)

$\|t\|$ $(GeV/c)^2$	1.63 (GeV/c)	1.77 (GeV/c)	1.83 (GeV/c)	1.88 (GeV/c)	1.95 (GeV/c)	2.20 (GeV/c)
.25	11.6%	11.2%	9.2%	7.9%	7.5%	7.0%
.35	72.3	49.2	33.0	30.6	28.7	19.2
.45	97.3	92.0	82.3	77.7	69.2	40.8
.55	100.0	100.0	98.6	97.3	94.7	70.4
.65	100.0	100.0	100.0	100.0	99.8	92.6
.75	100.0	100.0	100.0	100.0	100.0	99.0
.85	100.0	100.0	100.0	100.0	100.0	100.0

Having established the soundness of the debiasing procedure, the simulation program was rerun at all momentum sets, and narrow t intervals in an effort to obtain accurate curves for the scan-rule bias. The results of these runs are shown in Table 10.2-7, where the scan-rule bias is listed against t for each momentum set. Note that at the highest momentum set the bias disappears beyond $|t|=0.85$, while at the lowest momentum set this happens at $|t|=0.55$. The corrections required in the region of the first minimum range vary from 10 to 50%. Finally, in the region of the forward peak the statistics are poor, and the correction severe, as expected from the design of the scan rules.

10.3 Square-Hit Scan-Rule Bias

The working rule for the square-hit scan required that the scattered antiproton annihilate into charged particles before leaving the chamber. As a result, the events picked up on the square-hit scan, and those picked up on the large-angle scan formed substantially disjoint sets. On the other hand, while neither scan was particularly efficient about the cross-over point $|u| = 0.1$, the union of the two scans covered all angles in this region with both high scanning efficiency, and low scan-

rule bias. This suggested that by lumping the good elastic events from both scans together, and purging any duplicate events from the combined sample, the experiment could be effectively reduced to one involving a single double scan.† Owing to the simplifications introduced with this point of view, it was decided to combine the two sets of events, and treat the combination for the balance of the study as arising from a single ficticious double scan.

The more difficult aspect of the square-hit scan resulted from the undesired, but unfortunately unavoidable, tendency for the scanners to miss highly dipped events with a short (< 1 cm) antiproton track. The region of this bias was determined using the good elastic events by making a histogram of the antiproton track length in View 2 or View 4, whichever was greater. As shown in Table 10.3-1 the distribution drops sharply between three and four millimeters track length, indicating that the scanners may have been missing events in this region. To verify this possibility the azimuthal distribution of events with short (few cm in chamber) antiproton tracks was histogrammed using all the good

---

†This possibility was first suggested and verified by J. Lys.

TABLE 10.3-1

Projected Antiproton Track Length

Number Events	0	0	0	6	1	5
Track Length (cm)	0.05	0.15	0.25	0.35	0.45	0.55

TABLE 10.3-2

Experimental Azimuthal Distributions[#]

Azimuth[@] (Degrees)	.005 $(GeV/c)^2$	.015 $(GeV/c)^2$	.025 $(GeV/c)^2$	.035 $(GeV/c)^2$	.045 $(GeV/c)^2$	.055 $(GeV/c)^2$
5	0	2	2	1	2	4
15	0	2	1	2	1	1
25	0	4	5	0	0	2
35	0	1	1	2	4	2
45	0	0	2	2	2	2
55	0	0	1	0	1	2
65	0	0	3	0	3	4
75	0	0	2	2	4	0
85	0	0	0	0	2	2

[#]Here $|u|$ increases from left to right.

[@]The azimuthal distribution has been twice-folded: once about 180 degrees, and again about 90 degrees.

elastic events, and the result presented in Table 10.3-2. Note that the distribution drops sharply for highly dipped events, indicating that strong azimuthal bias was present at the very backward scattering angles ($.00 < |u| < .02$).

To determine the magnitude of the bias, the simulated events were subjected to a linearly increasing bias whenever the projected antiproton track length dropped below a specific value P, and to a 100% bias whenever its projected length dropped below a second value Q. The best values for P and Q were ascertained by running simulations at various P and Q values until a good fit to the experimental distributions of Tables 10.3-1 and 10.3-2 were obtained. This study indicated that the nominal cut-off length was Q = 3 mm, and that the linear bias affected tracks shorter than P = 1 cm. As shown in Table 10.3-3, the simulated result agrees within statistics with the experimental one, suggesting that the source of the azimuthal bias has been properly assessed.

To obtain the square-hit scan-rule bias the simulation program was run at each projectile momentum, and at appropriate u intervals in the range $0.0 < |u| < 0.1$. The results of the simulation, which are shown in Table

TABLE 10.3-3

Simulated Azimuthal Distributions[#]

Azimuth (Degrees)	.005 $(GeV/c)^2$	.015 $(GeV/c)^2$	.025 $(GeV/c)^2$	.035 $(GeV/c)^2$	.045 $(GeV/c)^2$	.055 $(GeV/c)^2$
5	0.0%	51.5%	100.0%	100.0%	100.0%	100.0%
15	0.0	50.8	100.0	100.0	100.0	100.0
25	0.0	48.5	100.0	100.0	100.0	100.0
35	0.0	45.0	100.0	100.0	100.0	100.0
45	0.0	40.0	96.5	100.0	100.0	100.0
55	0.0	33.5	83.7	100.0	100.0	100.0
65	0.0	7.0	68.8	100.0	100.0	100.0
75	0.0	5.0	54.7	94.0	100.0	100.0
85	0.0	0.0	44.0	83.0	99.0	100.0

[#]The distributions have been twice folded as in Table 10.3-2 above.

TABLE 10.3-4

Square-Hit Scan-Rule Efficiency

u $(GeV/c)^2$	.005	.015	.025	.035	.045	.055
Efficiency[#]	0.0%	68.0%	99.0%	100.0%	100.0%	100.0%
Efficiency[@]	0.0%	31.1%	83.1%	97.1%	99.9%	99.0%

[#]With sharp cut-off at 3 mm projected track length, but no linear bias.

[@]With 3 mm cut-off, and linear bias below 1 cm projected track length.

10.3-4, indicate that scan-rule bias became severe backward of $|u|=.02$.

10.4 Large-Angle Scanning Efficiency

The scanning efficiency for the large-angle scan was determined with the correlated-miss model described in the Appendix. This model incorporates the view that each event may be assigned an event difficulty D, and that relatively few events prove either extremely difficult ($D >> 1$) or extremely easy ($D << 1$) for scanners, but that the great majority are of some intermediate difficulty. In addition, it is presumed that scanners find events with an efficiency e(D) that decreases steadily with increasing D, thus introducing a tendency for events missed by one scanner to also be missed by a second. A concrete example of the latter effect arises in connection with the present experiment if one compares the (large-angle) scanning efficiency--calculated with any reasonable model--at moderate scattering angles ($0.5 > \cos\theta > -0.5$) with that in the backward direction

---

Event difficulty D--always a positive number--corresponds roughly to one's intuitive notion for such a variable. However, like ordinary probability, it eludes precise verbal definition, although (also like probability) it can be defined operationally, as shown in the Appendix.

($-0.9 > \cos\theta > -1.0$). In the first region, where events had the typical topology, and were prolifically produced, the overall efficiency was high . . . better than 99%, while in the second, where the topology was atypical, and rarely produced, the efficiency dropped below the 50% mark, indicating a strong correlation between events missed by the first scanner, namely the backward scatters, and those missed by the second, also the backward scatters.

Similar effects are observed even when $\cos\theta$ is fixed. For example, the scanning efficiency tends to decrease with increasing dip angle, as might be expected on intuitive grounds. This effect is shown clearly in Table 10.4-1, where the random-miss scanning efficiency for the good elastic events in the range[†] $0.4 > \cos\theta > 0.3$ has been tabulated against the azimuthal angle ψ. This cutting, and searching process could, in principle, be continued to look for other factors--such as event position in chamber--that might cause missed events to appear correlated. The method proves impossible in practice, however, since each cut reduces the events available for the next determination. Worse, the technique is unconvincing, since one has no assurance that all such effects have

---

[†]The total scan-rule bias in the range $0.4 > \cos\theta > 0.3$ amounted to less than 0.1%.

TABLE 10.4-1

Scanning Efficiency Versus Azimuth[#]

Azimuth (Degrees)	Single-Scan Efficiency	Double-Scan Efficiency	Double-Scan Error
10	97.1%	99.9%	0.1%
30	94.7	99.7	0.3
50	94.5	99.7	0.3
70	93.6	99.6	0.5
90	86.6	98.2	1.2
110	88.9	98.8	1.0
130	96.9	99.9	0.1
150	93.6	99.6	0.5
170	94.1	99.7	0.3
190	91.4	99.3	0.6
210	89.7	98.9	0.9
230	95.1	99.8	0.3
250	97.2	99.9	0.1
270	86.4	98.1	1.5
290	92.5	99.4	0.5
310	98.0	99.9	0.1
330	94.6	99.7	0.3
350	96.0	99.8	0.2

[#]Calculated with the random-miss model using good elastic events from the range $0.4 > \cos\theta > 0.3$.

been listed, and accounted for. In addition, bias other than the ones mentioned above tend to be quite subtle and virtually impossible to treat analytically.

The correlated-miss model represents a workable alternative to the cut, and search technique outlined above. Unlike the latter the correlated-miss technique is both convincing and precise, since, on the one hand, the model accounts for all sources of correlation among missed events, and on the other, does not subject the events to a concatenation of ever finer cuts. The procedure is workable in the sense that all factors correlating the missed events are summarily lumped, and a net correction to the random-miss formulas determined from the number of events observed by the scanners. The correction factor is obtained by developing reasonable forms for the event distribution, and scanning efficiency as a function of the event difficulty D.[†] For doubly scanned rolls the model involves only one parameter D_o, the event difficulty at which the scanning efficiency of the average scanner drops to 1/e of its best value, namely, 100% at D=0. This parameter, in fact, replaces

---

[†]Although any parameterization is open to debate, for reasons given in the Appendix the event distribution $\rho(D)$, and the scanning efficiency $e(D)$ were parameterized with $2D \exp(-D^2)$, and $e_o \exp(-D^2/D_o^2)$, respectively.

the average scanning efficiency $\bar{e}$ used in the random-miss model. (If a portion of the film has been triply scanned, as for example, in the present experiment, additional information becomes available, and a second parameter e_o, the average scanning efficiency for zero difficulty events, can be defined.)

To account for correlation among missed events, and the attendent loss in overall scan efficiency, the correlated-miss model adds a (usually) small correction to the basic random-miss efficiency formulas. As shown in the Appendix, for doubly scanned events the overall efficiencies associated with the two models are, respectively,

$$E_2(\text{random}) = 2N_oN_2/(N_o + N_2)^2$$
$$E_2(\text{correlated}) = 2N_oN_2[1 - (N_1/2N_2)^2]/(N_o + N_2)^2$$

where N_1 is the number of events found by just one scanner, N_2 the number found by both scanners, and $N_o = N_1 + N_2$ the number observed by either or both scanners. Note that the bracketed quantity modifies the basic random-miss formula, and that if $N_2 >> N_1$ --the case of high individual scan efficiencies--the two forms become identical. On the other hand, if $N_1 > 2N_2$--the case of very low individual efficiencies--the correlated-miss model

fails, at least as we have parameterized it. Since the existence of correlation has already been demonstrated among the good elastic events (cf. Table 10.4-1), and because the models are both one-parameter theories, the correlated-miss interpretation was chosen for the balance of the study.

In an effort to obtain better statistics at each plotting interval, the numbers N_1, N_2, E(random), E(correlated) were histogrammed against the variable cos θ using the large-angle scan data from all six momentum sets. Since the scanning efficiency varies slowly with cos θ, and because cos θ represents the most appropriate variable when considering both forward and backward scattering, this variable was chosen over the other two possibilities t, and u. As shown in Table 10.4-2, the numbers N_1 increase markedly relative to N_2 in both the forward and backward directions, indicating that the scanning efficiency was dropping rapidly in these regions. The drop at forward scattering angles is credited both to the severe scan-rule bias at small momentum transfers, and small scan-rule variations among the individual scanners, in this especially sensitive region. The drop at the backward scattering angles, on the other hand, reflects a poor detection efficiency for these square-

TABLE 10.4-2

Large-Angle Scanning Efficiency for Double Scans[#]

cos θ	N_1	N_2	E(ran)	E(cor)	Error
+.95	5	2	-	-	-
+.85	69	37	76.7%	10.0%	4.9%
+.75	75	130	95.0	87.1	1.1
+.65	38	136	98.5	96.6	0.5
+.55	41	268	99.5	98.9	0.2
+.45	83	442	99.3	98.4	0.2
+.35	71	520	99.6	99.1	0.1
+.25	64	462	99.6	99.1	0.1
+.15	49	319	99.5	98.9	0.1
+.05	38	230	99.4	98.7	0.2
-.05	21	134	99.5	98.9	0.2
-.15	17	97	99.4	98.6	0.3
-.25	13	65	99.2	98.2	0.5
-.35	14	96	99.5	99.0	0.2
-.45	11	59	99.3	98.4	0.4
-.55	15	74	99.2	98.1	0.4
-.65	13	53	98.8	98.1	0.7
-.75	28	45	94.4	85.2	2.1
-.85	32	39	91.5	76.1	2.9
-.95	53	58	90.2	71.3	2.9

[#]Includes only events passing computer-applied 10% restricted scan rules.

hit events having a very short antiproton track length. These effects also reflect themselves as differences between E(random), and E(correlated), indicating that the random-miss model is correcting for the tendency of events missed by the first scanner to also be missed by the second.

Triple scans were carried out on approximately 13% of the film, primarily to increase the overall scanning efficiency on those rolls where one or both of the double scanners had low individual efficiencies. As a result the average scanning efficiency for the triple scanners fell below that for the double scanners, thus necessitating a correction to the usual formulas for triple-scan efficiency. When statistics are plentiful, as, for example, when all the film has been triple scanned, such effects are properly accounted for by introducing a second parameter, e_o, in the correlated-miss model, and using the three numbers N_1, N_2, N_3 (the number of events found by one, two, and three scanners, respectively) to ascertain e_o, D_o, and E_3(correlated). Unfortunately, in the present experiment the numbers N_1 are generally too small for accurate determination of these parameters, and an alternate procedure had to be used. In particular, the main parameter D_o was taken directly from the double-scan results, and the modifying parameter e_o, as well as

the overall efficiency E(correlated), determined from the two larger numbers N_2, and N_3.† (The D_o values, as obtained from the double scans, are given in Table 10.4-3.)

To determine E(random) and E(correlated) for the triple scans, the numbers N_2 and N_3 were histogrammed against the angular variable cos θ, and the results presented, along with the two efficiencies, in Table 10.4-4. Note that the scanning efficiency according to either model drops rapidly in both the forward and backward directions, similar to that observed for the double scans, and ostensibly for the same reasons. Since the large-angle scan involved a mixture of both doubly and triply scanned events, an average overall scanning efficiency, good for either model, was defined with the formula:

$$E(\text{average}) = [N_o(\text{double}) + N_o(\text{triple})] / [N_t(\text{double}) + N_t(\text{triple})]$$

where N_t equals the total number of events, seen and unseen, passing the large-angle scan rules for the respective scans.

---

†Although the difference between a good scanner and an average one results primarily from a decrease in D_o, the difference between the average scanner and a poor one obtains mostly from a change in e_o.

TABLE 10.4-3

Nominal Event Difficulty From Double Scans

cos θ	D_o	cos θ	D_o
+.85	.27	-.05	3.43
+.25	1.57	-.15	3.23
+.65	2.48	-.25	3.00
+.55	3.47	-.35	3.57
+.45	3.11	-.45	3.12
+.35	3.70	-.55	2.98
+.25	3.67	-.65	2.67
+.15	3.46	-.75	1.49
+.05	3.33	-.85	1.20

TABLE 10.4-4

Large-Angle Scanning Efficiency For Triple Scans#

cos θ	N_2	N_3	E(ran)	E(cor)	Error
+.90	10	2	75.6%	-	25.6%
+.70	19	16	97.7	94.7%	4.1
+.50	35	102	99.9	99.6	0.3
+.30	20	127	99.9	98.8	0.1
+.10	20	74	99.9	99.7	0.2
-.10	7	32	99.9	99.7	0.2
-.30	6	23	99.9	99.7	0.4
-.50	4	17	99.9	99.6	0.3
-.70	8	7	97.9	95.3	5.6
-.90	6	3	93.6	75.0	13.4

#Includes only events passing computer-applied (10% restricted) scan rules.

10.5 Square-Hit Scanning Efficiency

In the interest of expediancy, and economy, second scans were omitted for a significant portion of the square-hit scan. As a result, the scanning efficiency for the average scanner was first determined from the doubly scanned events, and then presumed the same for singly scanned events. Since the single scans were carried out by the same people, and at the same time as the double scans, this supposition is believed sound. The results from the double scans are presented in Table 10.5-1, and indicate that the total scanning efficiency remained high (about 90%) out to $|u|=.01$. The single scan results, which are shown in Table 10.5-2, suggest that the square-hit scan was particularly sensitive to the very backward scatters.

10.6 The Corrected Data

The distribution of events among the several momentum sets, and over the various center-of-momentum scattering angles are presented in Figures 10.6-1 through 10.6-10. In particular, the histograms of Figures 10.6-7,8,9 give the distribution of all events from all momentum sets as a function of the three kinematic variables $\cos\theta$, t, u, while Figures 10.6-1 through 10.6-6 show the same distributions for the individual momentum

TABLE 10.5-1

Square-Hit Scan Efficiency for Double Scans

$\|u\|$	N_1	N_2	Effy	Error
.005	0	0	0%	0%
.015	1	8	99%	1%
.025	7	7	89%	8%
.035	5	4	85%	12%
.045	11	4	66%	17%
.055	5	11	97%	3%
.065	7	6	86%	10%
.075	4	7	95%	5%
.085	6	5	86%	11%
.095	7	3	71%	19%

TABLE 10.5-2

Single-Finds Versus u

$\|u\|$	N_o	$\|u\|$	N_o
.010	1	.110	1
.030	3	.130	0
.050	4	.150	0
.070	1	.170	0
.090	0	.190	0

sets. Finally, the histogram of Figure 10.6-10 shows the backward elastic cross section as a function of energy for the four angular regions $-0.9 > \cos\theta > -1.0$, $-0.8 > \cos\theta > -1.0$, $-0.6 > \cos\theta > -0.8$, and $0.0 > \cos\theta > -1.0$.

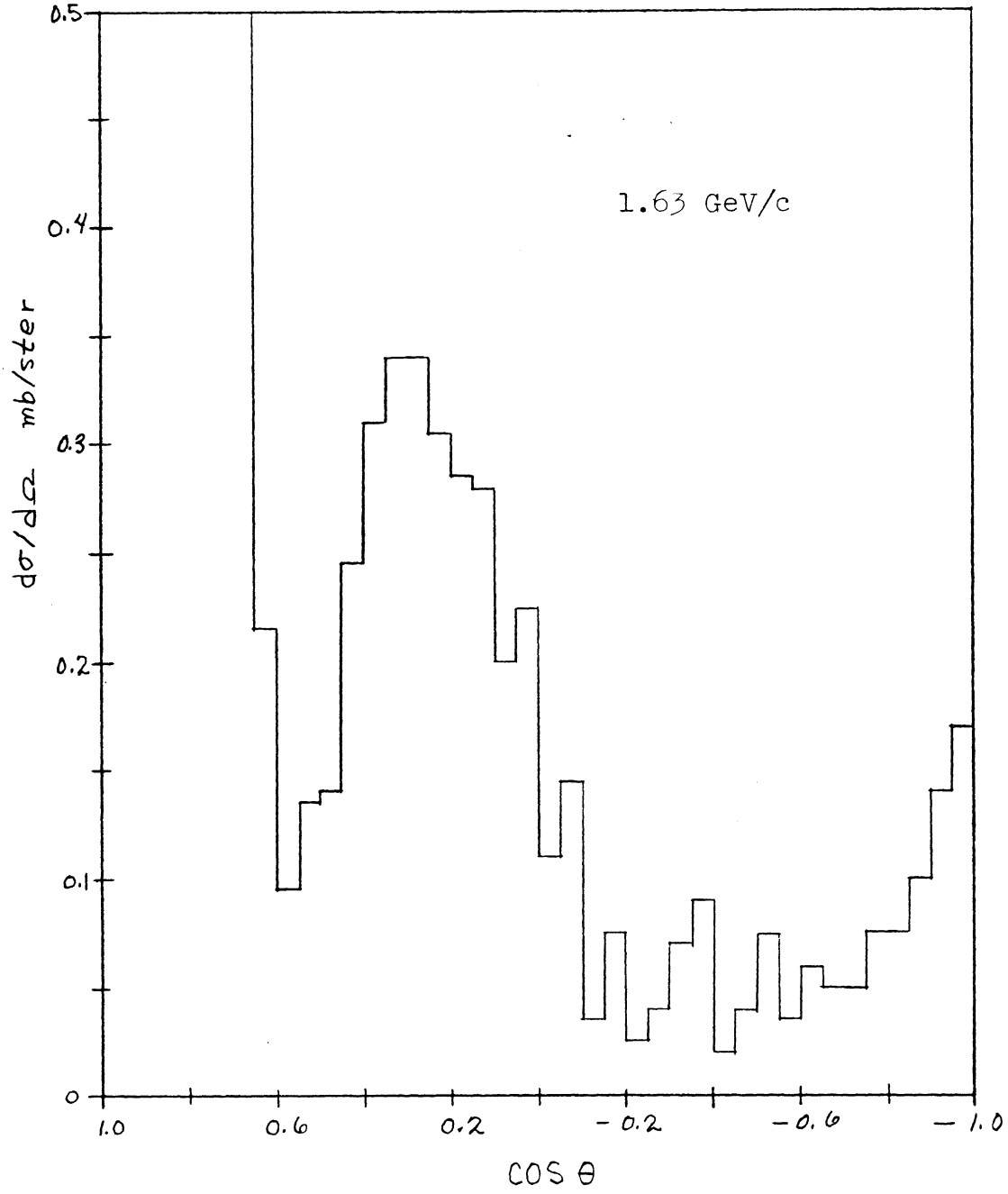

Figure 10.6-1. Differential Cross Section at 1.63.

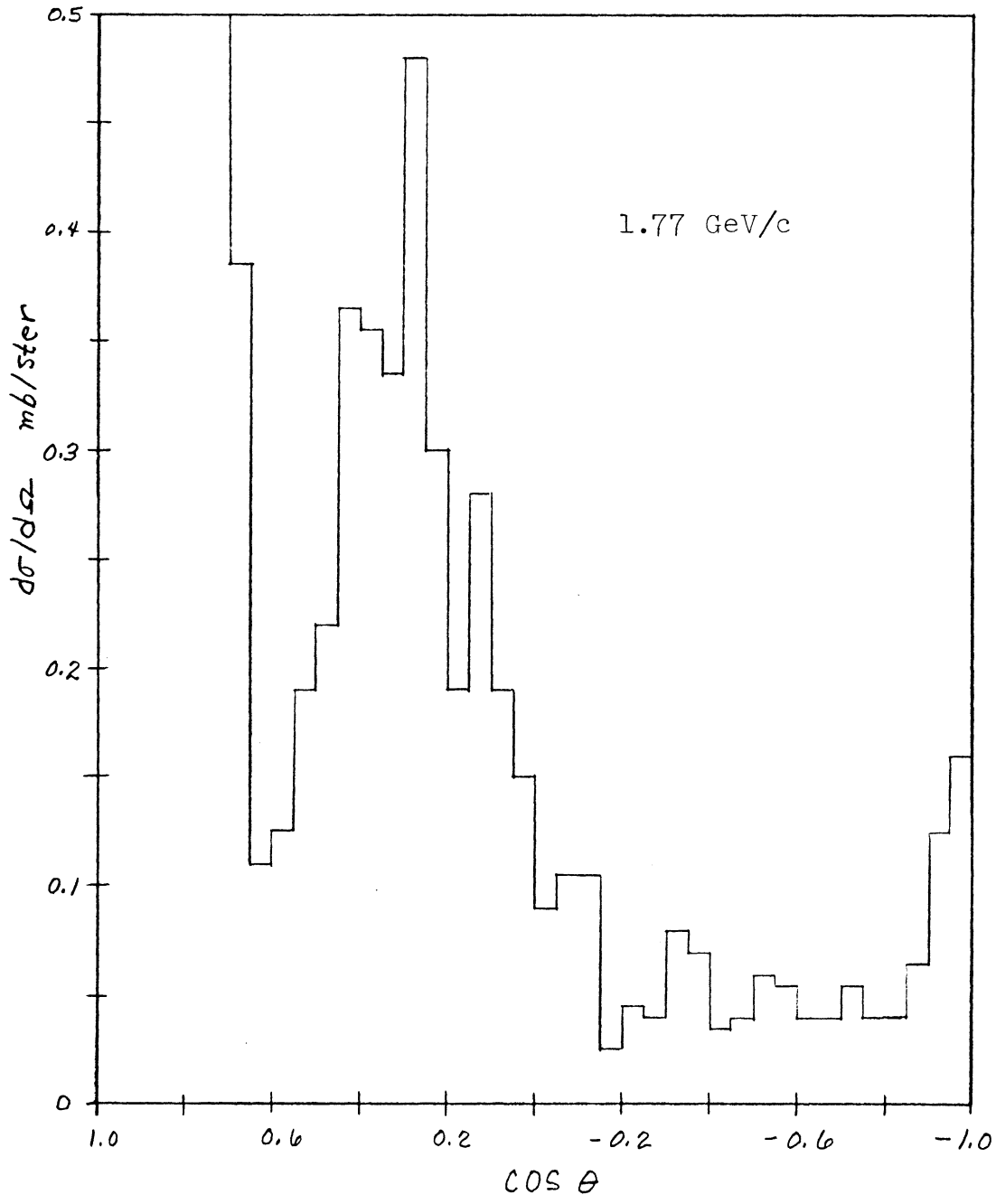

Figure 10.6-2. Differential Cross Section at 1.77.

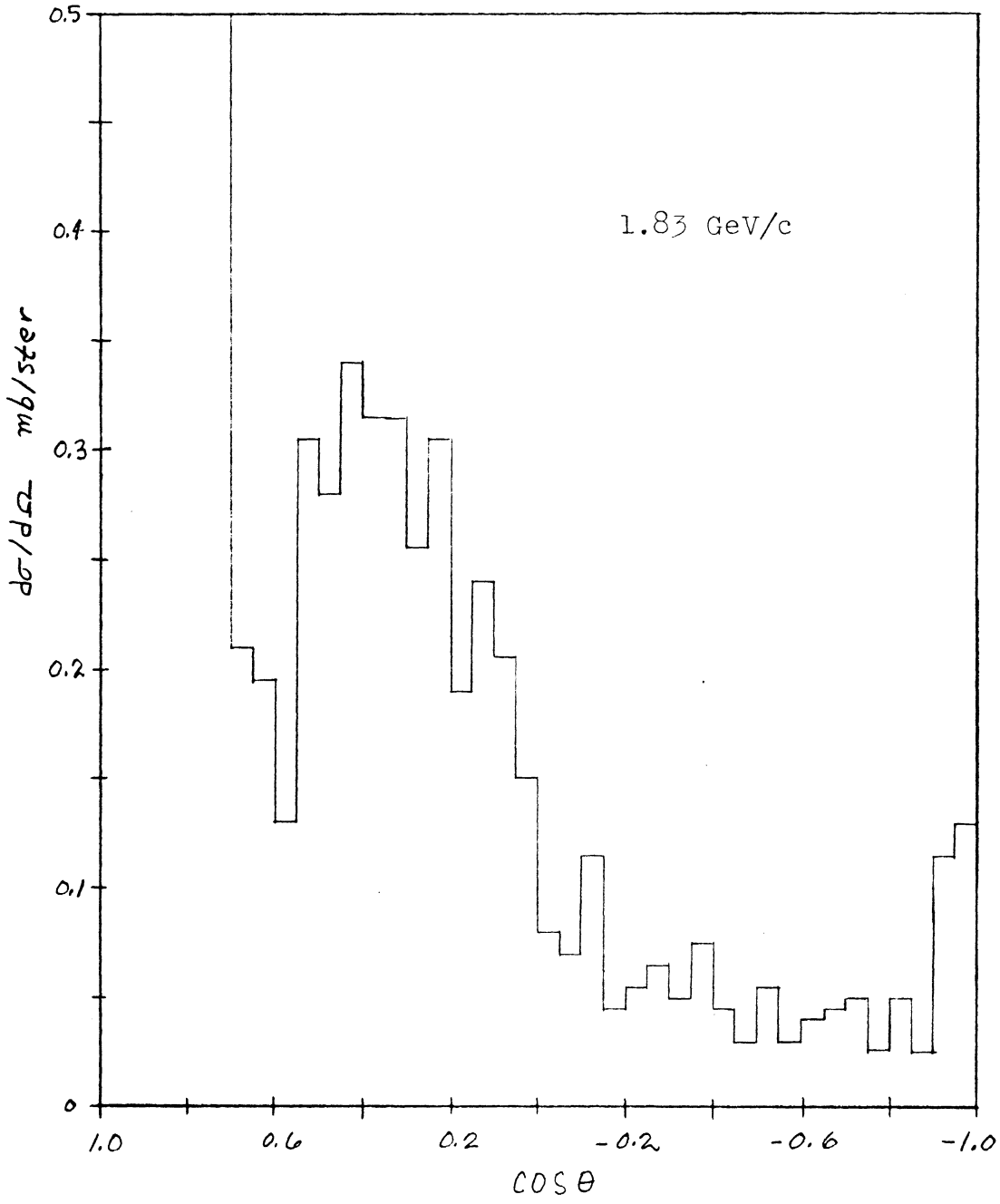

Figure 10.6-3. Differential Cross Section at 1.83.

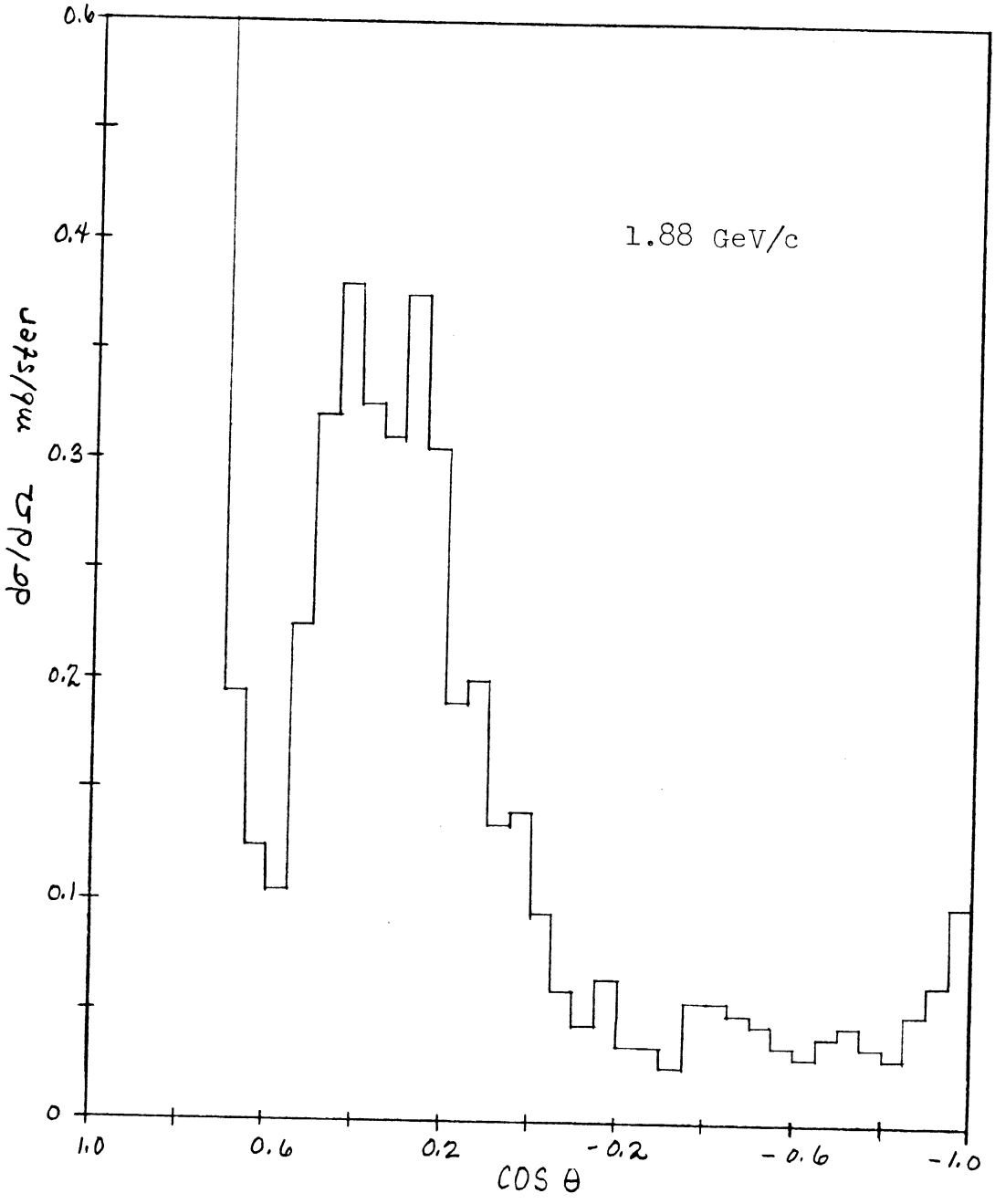

Figure 10.6-4. Differential Cross Section at 1.88.

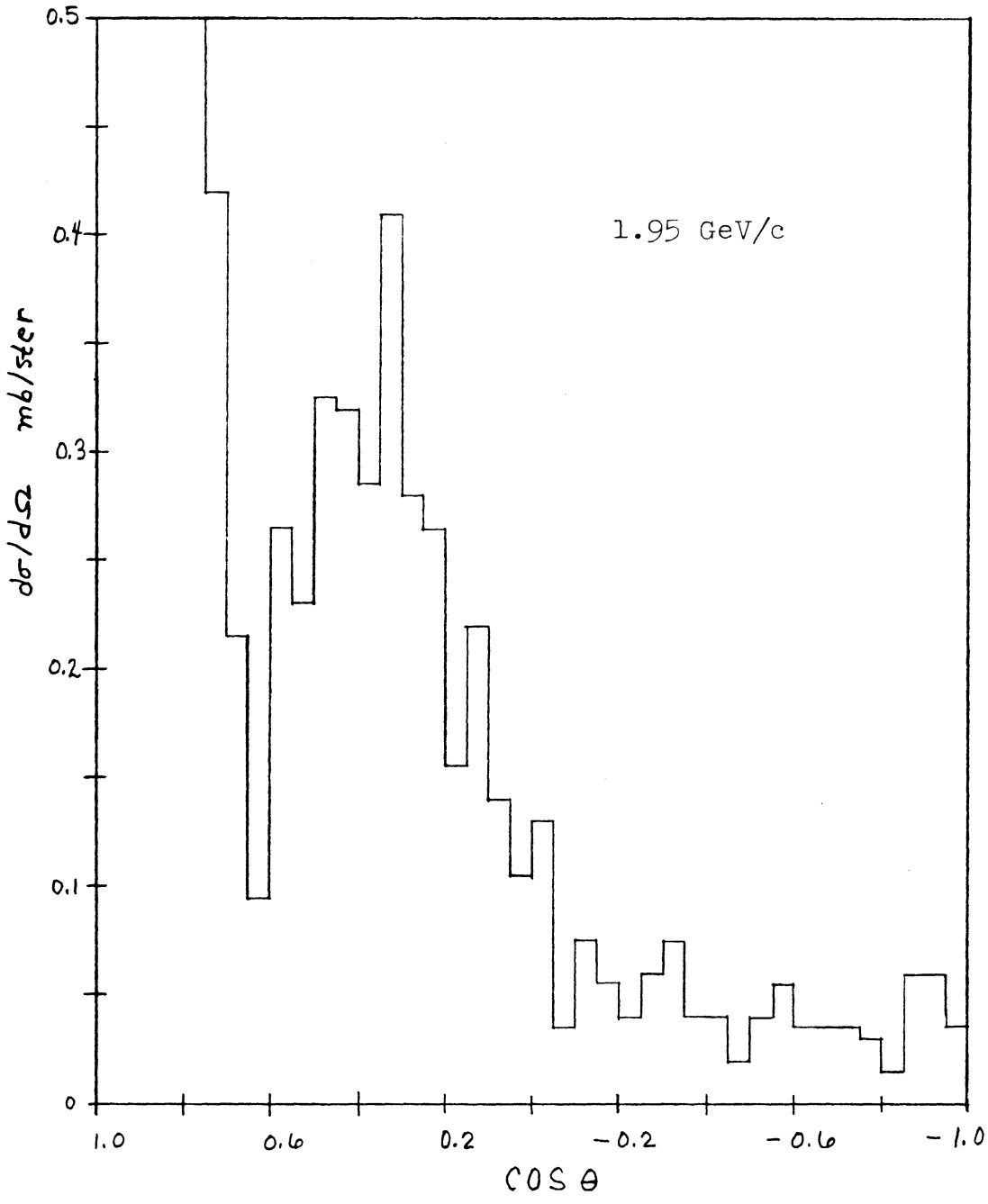

Figure 10.6-5. Differential Cross Section at 1.95.

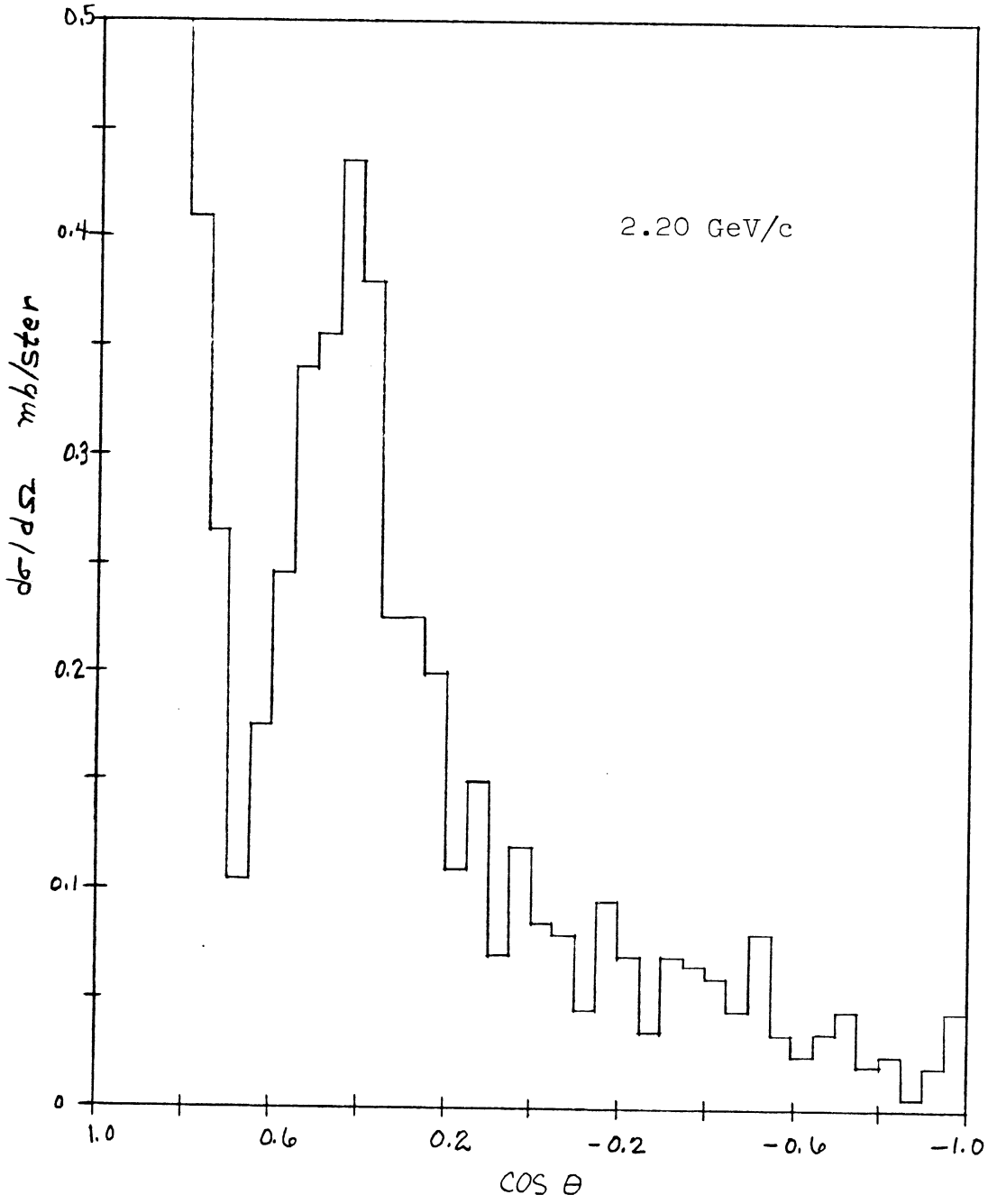

Figure 10.6-6. Differential Cross Section at 2.20.

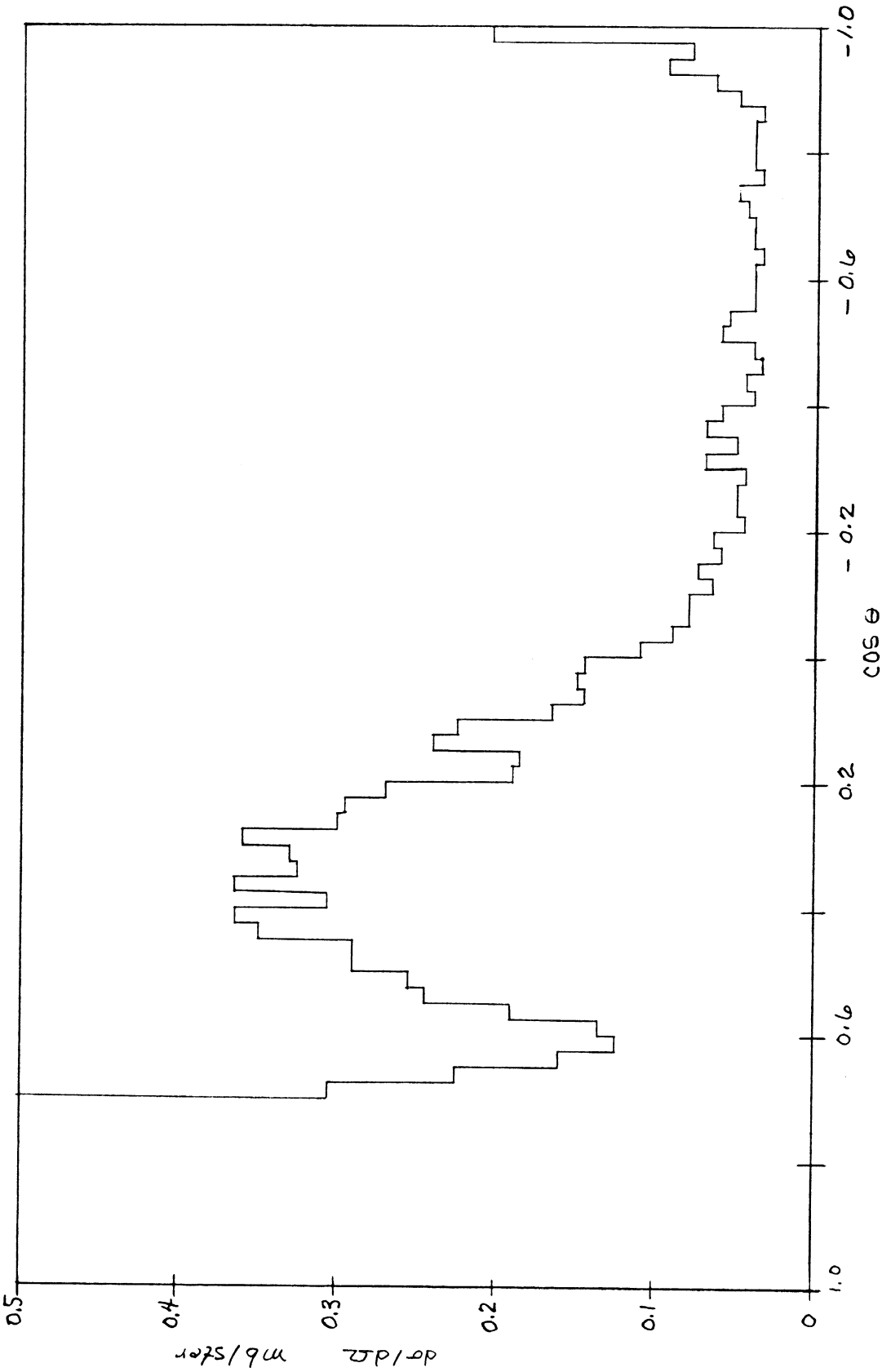

Figure 10.6-7. Differential Cross Section in cos θ.

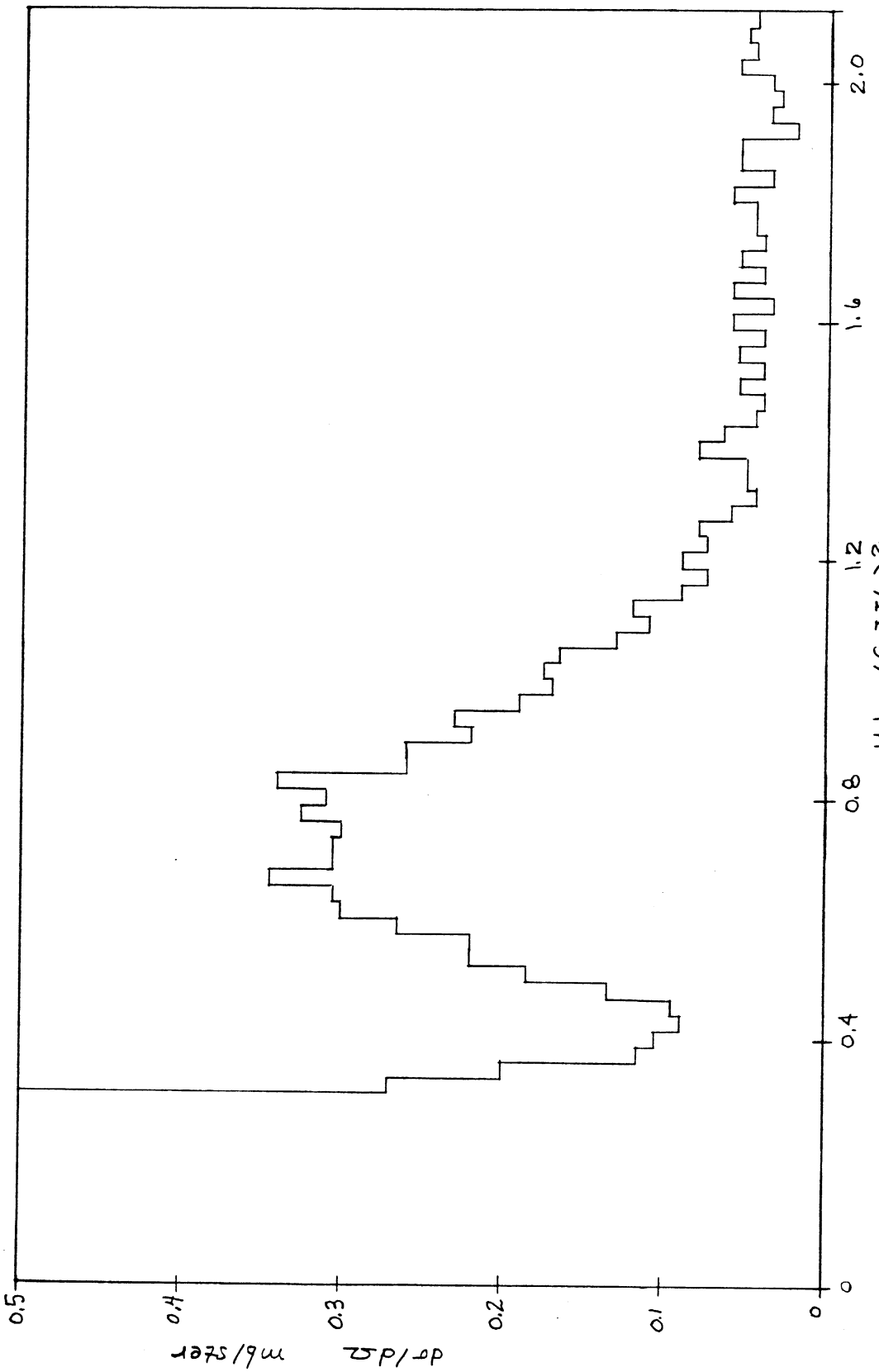

Figure 10.6-8. Differential Cross Section in t.

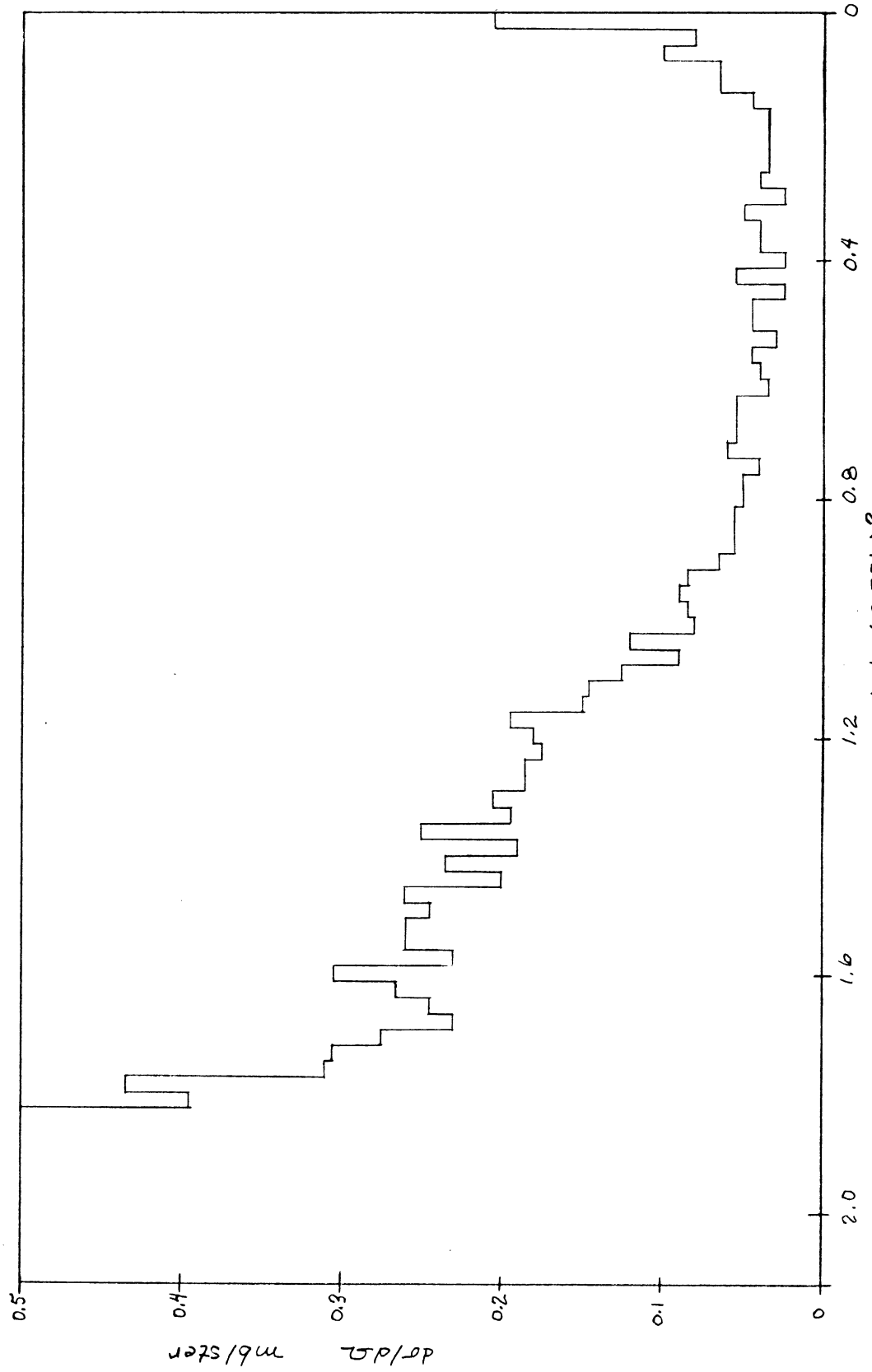

Figure 10.6-9. Differential Cross Section in u.

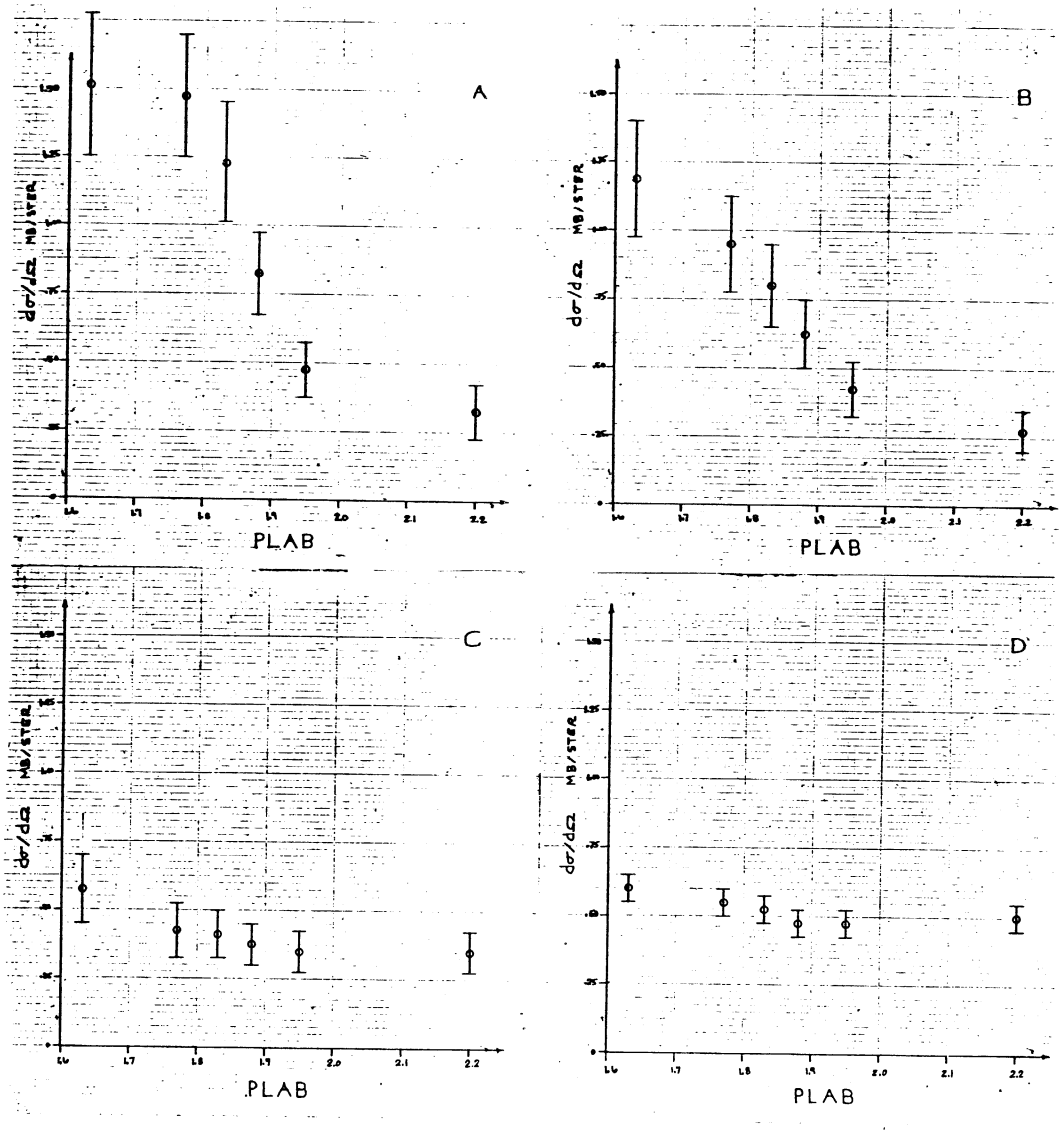

Figure 10.6-10. Backward Elastic Cross Sections.
(A) $-0.9 > \cos\theta > -1.0$, (B) $-0.8 > \cos\theta > -1.0$,
(C) $-0.6 > \cos\theta > -0.8$, (D) $0.0 > \cos\theta > -1.0$.

11.0 RESULTS AND CONCLUSIONS

This chapter presents the results and conclusions drawn from the experimental findings presented in Chapter 10 above. The collected data is first viewed as a differential cross section measurement, and appropriate parameterizations applied to the observed structure. The angular distributions are then compared with those predicted by the four theoretical models for scattering discussed earlier, and conclusions drawn that our Regge picture more closely represents the observed PBAR-P cross section than the absorption-corrected exchange model. The data is next studied for its energy-dependent structure, and evidence for a non-statistical backward peak cited. Finally, the results of the present experiment are compared with those obtained in other studies, and conclusions drawn that a high-spin s-channel resonance may form, and decay at our energies.

11.1 Large-Angle Cross Section

The angular distributions of Figures 10.6-1 through 10.6-9 appear highly structured relative to, say, the P-P differential cross section. In Figure 10.6-7, for example, the forward diffraction peak dominates the cross section forward of $\cos\theta = 0.3$, while at $\cos\theta = 0.6$

the distribution drops to a (first) minimum, consistent with the findings of other experimenters (Chapter 1.2). Following this valley the cross section rises again to a (secondary) maximum at cos θ = .35, and then drops again to a plateau beginning around cos θ = 0.0, and extending out to the backward peak observed beyond cos θ = -0.9. The break defining the intersection of the secondary maximum and the plateau is difficult to interpret as a second minimum, since on the one hand no third maximum appears in the data, and on the other the distinct second minimum observed by A. Ashmore, et al. (1968) at 5.9 GeV/c lies at a much higher four-momentum transfer, namely, $|t|$ = 1.8 $(GeV/c)^2$. Thus the plateau suggests the presence of an s-wave (or s-wave like) background, below which the forward diffraction field drops at $|t|$ = 1.1. At higher energies, the plateau apparently disappears, leaving visible the second minimum measured by A. Ashmore, et al. (1968).

The distribution of events in t, the square of the four-momentum transferred from the projectile to the target, is shown in Figure 10.6-8. Note that the distribution follows the same general behavior as the cos θ histogram in the forward direction, but appears to tail-off, rather than plateau, in the backward direction. The forward behavior is expected since forward elastic cross sections are known to depend primarily on t, and,

hence for small changes in the projectile momentum, also primarily on cos θ. The backward behavior, on the other hand, results mostly from the kinematical fact that the maximum four-momentum transfer increases with projectile momentum, so that the lower momentum sets are expected to stop contributing events to the histogram before the higher ones do, causing the data to tail-off at the higher |t| values. For completeness we also note that the first minimum appears around |t| = 0.4, the maximum peaks around |t| = 0.7, and the plateau initiates around |t| = 1.1, although these numbers will be given more precisely in the sequel.

The distribution of events in u, the complement of the four-momentum transfer squared, is given in Figure 10.6-9. Note that the distribution follows the same general behavior as the cos θ histogram in the backward direction, but shows a materially different structure in the forward direction, including the destruction of the (first) minimum. The backward behavior is expected on the grounds that backward elastic cross sections tend to depend primarily on u, and, hence for small variations in the projectile momentum, also primarily on cos θ. The destruction of the (first) minimum, on the other hand, results from the kinematic fact that phenomena occurring at a fixed t, and which are

nominally independent of the projectile energy necessarily appear at variable u values. Consequently, the (first) minimum falls at different abscissa values for different momentum sets, thus smearing away any evidence of the minimum.

Forward peak. As usual the forward diffraction peak dominates the other features of the differential cross section. According to the results of other experiments (Chapter 1) this peak widens with increasing projectile momentum--in contrast, for example, to the shrinking observed in P-P elastic scattering. However, because our statistics are meager, and momentum bite narrow, no attempt was made to measure the slope, or antishrinking of the forward peak.

The first minimum. The first minimum, first observed by Lynch, et al. (1962), appears unusually pronounced in our data owing to the linearity of our ordinates. The position of these minima in t--the appropriate variable if the minima, like the forward peak, interpret as diffraction effects--was determined by fitting the bottom half of each valley (as measured with respect to the top of the secondary maximum) with the parabolic form $A + B(t-t(min))^2$, where A specifies the height of the minimum, B its relative width, and t(min) its position

along the abscissa. The results of this fit are given in Table 11.1-1, and indicate that the minima, like the widths of the diffraction peak, work toward the larger $|t|$ values with increasing projectile momentum. The energy dependence of t(min) was estimated quantitatively by fitting the six t(min) values with the linear form $|t(min)| = C + Dp^*$, where p^* denotes the CM momentum. The resulting fit produced the values $C = .21 \pm 0.1$ $(GeV/c)^2$, $D = .30 \pm 0.1$ GeV/c at a least-square error of 9.1, thus confirming the tendency of t(min) to increase with beam momentum.

The secondary maximum. Like the first minimum, the secondary maximum was first observed at 1.61 GeV/c by G. Lynch et al. (1962). Actually, this enhancement appears more a reaction to the first minimum than some independent fluctuation, with the intensity lost through the destructive interference at the minimum appearing redisplayed as constructive interference at the secondary maximum. Presumably, also, the angular variable t also describes the secondary maximum, if the two phenomena are in fact related. To determine the height, width, and position of the maxima the top half of each was fitted with an inverted parabola of the form $A + B(t-t(max))^2$. The results of this fit, which are

TABLE 11.1-1

Parabolic Fits to the First Minima

PLAB	PCM	A	B	|t(min)|
1.63	.663	0.73	110.5	.408±.076
1.77	.704	0.73	88.9	.425±.060
1.83	.722	1.04	41.0	.415±.092
1.88	.739	0.63	70.4	.438±.036
1.95	.756	0.86	43.3	.448±.045
2.20	.822	0.64	32.3	.473±.051

TABLE 11.1-2

Parabolic Fits to the Secondary Maxima

PLAB	PCM	A	B	|t(max)|
1.63	.663	2.35	-30.54	.640±.060
1.77	.704	2.23	-27.50	.681±.032
1.83	.722	1.90	-11.40	.625±.051
1.88	.739	2.05	-21.80	.700±.019
1.95	.756	1.74	- 8.90	.718±.046
2.20	.822	1.71	-15.70	.764±.024

presented in Table 11.1-2, indicate that the maxima, like the forward peaks, and first minima, move toward the larger $|t|$ values with increasing p^*. A quantitative estimate of this shift was undertaken by fitting the six t(max) values of Table 11.1-2 with the linear form $|t(max)| = C + Dp^*$. The results of this fit gave $C = .28 \pm 0.1$ $(GeV/c)^2$, $D = .56 \pm 0.2$ GeV/c at a least-square error of 16.6, also indicating a mild growth of $|t(max)|$ with increasing p^*.

Appearance of the plateau. The gently sloping plateau following the secondary maximum appears distinctly at the five lowest momentum sets, and presumably results from Rayleigh-like scattering between the projectile and target. The plateau appears to initiate at the point where the secondary maximum drops below this s-wave like background. Since no particular interference is observed near the cross-over point, the two waves appear more or less incoherently generated. According to this interpretation the data points forward of the plateau likely depend primarily on t, while those backward of the break more probably depend on cos θ. To determine the location of the cross-over point, data forward of the break was fitted with the linear form $A - Bt$, while the data backward of this point was fitted

with the analogous form A' - B't. The position of the break was then defined by the intersection of these lines. The results of these fits, and the break point, t(break), are shown in Table 11.1-3, and indicate, consistent with our other observations, that the diffraction field moves outward in $|t|$ with increasing p^*. A quantitative estimate of this movement was then made by fitting t(break) with the linear form $|t(\text{break})| = C + Dp^*$. The resulting fit led to the values $C = .46 \pm .12$ $(\text{GeV/c})^2$, $D = 2.16 \pm .24$ GeV/c at a least-square error of 3.4, the sign of D indicating outward movement with p^*.

Fluctuations in the plateau. The event distributions in PLAB and cos θ backward of the secondary maximum are shown in the plots of Figure 10.6-10. Generally speaking, the distributions remain fairly flat in both s and cos θ, thus suggesting the presence of a general s-wave background in this region. In the very backward direction a backward peak appears to rise from the background at the lowest three momentum sets near cos $\theta = -0.9$. Since our scanning efficiency dropped to zero backward of $|u| = .01$ $(\text{GeV/c})^2$, the enhancement could actually be a good deal larger than indicated.

TABLE 11.1-3

Linear Fits to Break

PLAB	PCM	A	B	C'	D'	|t(break)|
1.63	.663	9.38	-9.52	+0.48	-0.18	0.95±0.20
1.77	.704	7.89	-7.17	-0.23	+0.38	1.08±0.20
1.83	.722	8.21	-7.22	+0.59	-0.21	1.09±0.20
1.88	.739	4.40	-3.44	+0.47	-0.17	1.20±0.20
1.95	.756	5.65	-4.53	+0.28	-0.02	1.19±0.20
2.20	.822	3.37	-2.41	-0.59	-0.19	1.25±0.20

11.2 Comparison with Scattering Theory

The angular distributions presented in Chapter 10 above apparently neither support nor invalidate the optical, eikonal, exchange, or Regge models discussed earlier. On the other hand, the experimental findings indicate (to varying degrees) how these models should be interpreted and parameterized for PBAR-P elastic scattering.

Optical model: Basically independent of energy, the optical model provides a surprisingly accurate description of elastic scattering. The gaussian nature of the forward peak (in momentum transfer) suggests, for example, that the interaction potential is also gaussian, and, assuming the validity of the Chou-Yang hypothesis, that the projectile and target also have gaussian probability densities. Off the forward peak the measured PBAR-P differential cross section drops much more slowly than predicted by a simple gaussian potential, and indicates that a more sophisticated parameterization is required. In addition, the pronounced first minimum observed near $|t| = 0.4$ $(GeV/c)^2$ suggests that a sharper edged potential--perhaps a square-well--dominates the scattering in this region. On the other hand, the square-well potential leads to a differential cross

section that 1) has several distinct zeros, and 2) drops inversely as the cube of the momentum transfer. Since the observed data possesses neither of these characteristics, the square-well also represents an inadequate description of the collision process.

The above observations suggest, however, that a hybrid potential might accurately describe the data. In particular, it might be conjectured that the interaction potential contains enough gaussian structure to match the sharp drop in the differential cross section, and enough square-well character to obtain the various maxima and minima present in the experimental data. The convolution operation provides one method for mixing the effects of two such potentials. In fact, by convolving a square-well with a gaussian one obtains an interaction potential that looks like a square-well, but has rounded corners. The scattering amplitude generated in this case will have the maxima and minima characteristic of the square well, and the exponential drop produced by its gaussian structure. Consequently, the hybrid potential leads 1) a smoother looking interaction potential, 2) a scattering amplitude more consistent with the observed cross section, and 3) an optical model with three parameters, namely,

the well depth, the well diameter, and gaussian's radius.

The hybrid model, as outlined above, still predicts zeros in the differential cross section, an effect clearly not present in the experimental data. On the other hand, the plateau observed beyond the secondary maximum suggests that a second amplitude might be contributing, and that this amplitude might also be filling in the first-minimum created by the square well. Owing to the flatness of the plateau, one suspects (in the spirit of the optical model) that the amplitude in question arises from a second potential having a highly localized spatial structure. This potential, combined with the hybrid form conjectured above, leads to a four-parameter optical model capable of describing the essential features of the forward PBAR-P scattering cross section.

Eikonal picture: The eikonal picture differs from the optical model in that the former attempts to account for the distortion and/or depletion suffered by the incident beam. In the limit of small phase shifts, however, the eikonal formulas all degenerate to the ones arising from the optical model, so that comparisons with experiment become the same with either picture. Conversely, when phase shifts are large, the two scattering amplitudes

become quite distinct, and thus allow different interpretations of the data. In particular, the need for a hybrid potential disappears, since the first-minimum secondary-maximum sequence can be attributed to interference between a high-energy and difference amplitude, as explained below.

Using an eikonal picture, the observed PBAR-P differential cross section may be attributed in part to absorption by a gaussian cloud, and in part to scattering from a spatially localized core. The forward peak is then credited to the gaussian cloud, and the flat plateau to the inner core. As in the optical model, a gaussian interaction potential leads to a gaussian shaped differential cross section, since, when expanded in powers of the phase shift, the eikonal amplitude approximates the one for the optical model to first order. Mathematically speaking,

$$f(k,\Delta) = f_1(k,\Delta) + f_2(k,\Delta)$$

$$\simeq k \int \chi(b)\ J_o(\Delta b)\ b\ db$$

$$+ ik \int \chi^2(b)\ J_o(\Delta b)\ b\ db$$

The first-order term $f_1(k,\Delta)$, being linear in the eikonal $\chi(b)$, and hence also the interaction potential, indicates

optical-type scattering. Consequently, a gaussian potential will produce a gaussian cross section characterized by an rms momentum transfer that varies inversely as the radius of the potential.

The second-order term $f_2(k,\Delta)$ appears quadratic in the eikonal, and thus indicates some higher-order scattering process. Squaring the eikonal, of course, narrows its rms radius, and hence widens the diffraction field described by $f_2(k,\Delta)$. The same result obtains if the projectile suffers two successive small-angle scatters off the interaction potential. In this case the angular distribution still looks gaussian, except that the diffraction field widens owing to the larger momentum transfers possible with two collisions. It is thus convenient to interpret $f_2(k,\Delta)$ as arising from double scattering on the potential. This point of view allows simple explanation of the dip-bump sequence seen in the PBAR-P differential cross section.

At large enough momentum transfers $f_2(k,\Delta)$, having the shallower slope, dominates the single-scattering amplitude $f_1(k,\Delta)$. At the cross-over point substantial interference may be expected between the two amplitudes. In the present experiment such interference appears destructive owing to the pronounced minimum observed near

$|t| = 0.4$ $(GeV/c)^2$. At larger momentum transfers the interference term becomes small (that is, $f_1(k,\Delta)$ falls exponentially relative to $f_2(k,\Delta)$), and $f_2(k,\Delta)$ alone dominates the amplitude. As the interference term diminishes, the cross section rises again to form the secondary maximum at $|t| = 0.7$ $(GeV/c)^2$, and at still larger momentum transfers the cross section drops (with the shallower slope) toward the flat plateau, below which it plunges around $|t| = 1.1$ $(GeV/c)^2$.

Exchange model: The exchange model, as developed here, presumes that at high energies the forward elastic scattering amplitude reflects the absorption occurring into the production and annihilation channels, and that at lower energies the various exchange mechanisms modify this basic amplitude according to a prescription provided by the eikonal picture. As discussed earlier, the peripheral P-P and PBAR-P amplitudes are linked by charge conjugation and crossing symmetry to the direct-channel PBAR-P amplitude. Thus, at high energies both processes should have the same forward scattering amplitude:

$$i(k\sigma_t/4\pi)\ \exp(-R_o^2\Delta^2)$$

or, equivalently, the same eikonal:

$$ik \{1 - \exp i\chi_o(k,b)\}$$

$$= [i(k\sigma_t/4\pi)/2R_o^2] \exp(-b^2/4R_o^2)$$

At energies attainable with present accelerators, the forward P-P cross section tends to shrink (as predicted by the Regge-pole picture), while the PBAR-P cross section definitely antishrinks, thus indicating a contribution from some strong secondary process. In this connection, R. Arnold (1967) observes that in PBAR-P scattering "the annihilation cross sections ... are equal in importance to those of production without annihilation, and the latter are comparable to the corresponding P-P reactions." Thus, one expects that the PBAR-P amplitude differs from the P-P one because of the extra absorption introduced by the annihilation channels.

In a Feynman picture, the first-order PBAR-P annihilation amplitude results from the exchange of a nucleon between the target and projectile. If spin can be neglected, the (covariant) annihilation potential takes the usual Yukawa form

$$U_a(b,z) = -iU_1 \exp(-mr)/mr$$

where m denotes the mass of the exchanged nucleon. As shown above, this potential leads to an eikonal of the form:

$$\chi_a(k,b) = (iU_1/kMm)\ K_o(mb) \qquad (M = \sqrt{s})$$

where K_o denotes the zero-order modified Bessel function. Thus, according to the eikonal perturbation formula, the P-P and PBAR-P amplitudes differ by

$$f_a(k,\Delta) = k \int_0^\infty \chi_a \exp(i\chi_o)\ J_o(\Delta b)\ b\ db$$

Rather than evaluate this (difficult) integral directly, we note that within the spirit of the approximation

$$K_o(mb) \leftrightarrow 1/(\Delta^2 + m^2)$$

$$\simeq \exp(-\Delta^2/m^2)/m^2 \leftrightarrow 1/2\ \exp(-m^2b^2/4)$$

where the double-headed arrow denotes Fourier-Bessel transform correspondance. Hence, upon substitution we obtain the pair of formulas:

$$f_o = i(k\sigma_t/4\pi)\ \exp(-R_o^2\Delta^2)$$

$$f_a = (iU_1/Mm^3)\ \exp(-\Delta^2/m^2)$$

$$- [iU_1\sigma_t/8\pi MmR_o^2(m^2 + 1/R_o^2)]$$

$$\cdot \exp[-\Delta^2/(m^2 + 1/R_o^2)]$$

Note that f_a vanishes at high energies, so that f_o dominates the scattering amplitude.

At lower energies f_a may be expected to modify f_o

in an experimentally detectable way. Since $m^2 \simeq 1$ $(GeV/c)^{+2}$, and $R_o^2 \simeq 5$ $(GeV/c)^{-2}$, the diffraction field associated with f_a looks much wider than that for f_o. Consequently, at sufficiently large scattering angles, f_a will dominate f_o, and the differential cross section will appear to change slope. At the cross-over point destructive interference presumably occurs, giving rise to the familiar minimum at $|t| = 0.4$ $(GeV/c)^2$. At still larger scattering angles a secondary maximum appears, followed by an exponential drop to the flat plateau observed in this study. Strong antishrinking may also occur, as noted below.

Regge theory: In a Regge picture the difference between the P-P and PBAR-P scattering amplitudes may be credited to the exchange of nucleon-isobar trajectories between the target and projectile. At high energies the PBAR-P scattering amplitude is, of course, dominated by diffraction scattering, so that

$$f_o(k,\Delta) = i(k\sigma_t/4\pi)\ \exp(-R_o^2\Delta^2)$$

where $\sigma_t \simeq 40$ mb, and $R_o^2 \simeq 5$ $(GeV/c)^{-2}$. The high-energy eikonal to be associated with this amplitude obtains as a solution to

$$f_o(k,\Delta) = ik \int_0^\infty \{1 - \exp i\chi_o(k,b)\}\ J_o(\Delta b)\ b\ db$$

Inverting the Fourier-Bessel transform, and then substituting for $f_o(k,b)$ yields:

$$ik \{1 - \exp i\chi_o(k,b)\}$$

$$= [i(k\sigma_t/4\pi)/2R_o^2] \exp(-b^2/4R_o^2)$$

This easily solved formula defines $\chi_o(k,b)$ implicitly.

At lower energies the amplitude deviates from $f_o(k,b)$ owing to trajectory exchange between the target and projectile. The (covariant) Regge-pole amplitude for such a process takes the usual form:

$$Mf_1(k,\Delta) = iA_1(\Delta)(s/s_o)^{\alpha_1(\Delta)}$$

where $M = \sqrt{s}$. Studies (Barger and Cline [1967]) of backward pion-nucleon scattering--presumably also dominated by nucleon-isobar exchange--indicate that

$$A_1(\Delta) = \text{constant}$$

$$\alpha_1(\Delta) = \alpha_o - R_o^2\Delta^2$$

with $\alpha_o = .15$, and $R_o^2 = 5\ (\text{GeV/c})^{-2}$. Thus, the Regge pole scattering amplitude takes the simplified form:

$$f_1(k,\Delta) = i(A_1/M)(s/s_o)^{\alpha_o} \exp(-R_o^2\Delta^2 \ln(s/s_o))$$

The eikonal to be associated with this amplitude obtains

as a solution to

$$f_1(k,\Delta) = k \int_0^\infty \chi_1(k,b)\ J_o(\Delta b)\ b\ db$$

In other words,

$$k\chi_1(k,b) = i[A_1(s/s_o)^{\alpha_o}/2MR_o^2\ \ln(s/s_o)]$$

$$\cdot\ \exp(-b^2/4R_o^2\ \ln(s/s_o))$$

As expected, $\chi_1(k,b)$, and hence also the exchange amplitude vanish at high energies.

The net scattering amplitude--valid at both high and moderate energies--is given by the Fourier-Bessel transform:

$$f(k,b) = ik \int_0^\infty \{1 - \exp i\chi(k,b)\}\ J_o(\Delta b)\ b\ db$$

$$\chi(k,b) = \chi_o(k,b) + \chi_1(k,b)$$

The above formula contains just one free parameter, namely, A_1, and suggests that an unambiguous fit to the PBAR-P differential cross section is possible. To determine a best value for A_1 fits were made to the forward PBAR-P cross section over a wide range of momenta (.15 to 1.98 GeV/c). A best fit obtained with A_1 = 10.8 ±0.6 GeV-F, and resulted in the curves shown in Figure 11.2-1. Although not part of the fitted data

sample, all curves evidence distinct dip-bump structure, as well as substantial antishrinking. The dip-bump structure arises for reasons cited under the exchange-model described above; the antishrinking follows from an argument given by Arnold (1967), and is discussed in Section 6.4 above.

Strong antishrinking also occurs in the exchange model, as shown in Figure 11.2-2. These curves were obtained as above, except that $\chi_1(k,b)$ was replaced with $\chi_a(k,b)$, where

$$\chi_a(k,b) = i(U_1/kMm)\ K_o(mb)$$

and a value instead obtained for U_1, namely, 13180 ± 690 GeV^2/F. These curves evidence both antishrinking and dip-bump structure, so that the Regge and exchange picture yield similar qualitative cross-section behavior. To determine which model best matches the experimental data, the forward slope, first minimum, and secondary maximum have been compared with the values measured experimentally, as shown respectively in Figures 11.2-3,4,5. Both theories follow the observed data remarkably well, especially considering the high-energy character of the approximation. Detailed inspection of these curves indicates, however, that the Regge picture is more consistent with the measured structure than the absorption-

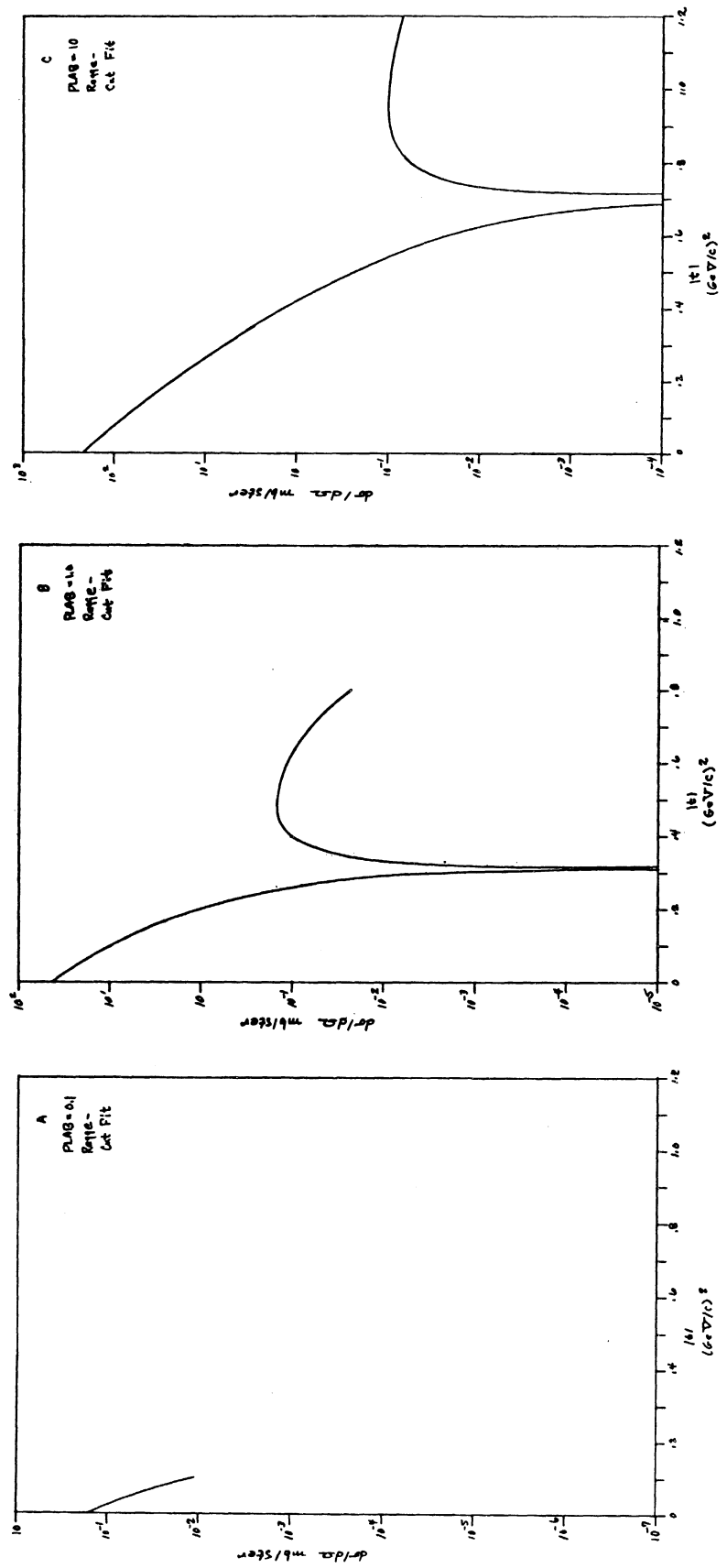

Figure 11.2-1. Regge-Model Fit to PBAR-P Elastic. Predicted elastic scattering cross sections shown at (A) 0.1 GeV/c, (B) 1.0 GeV/c, and (C) 10.0 GeV/c.

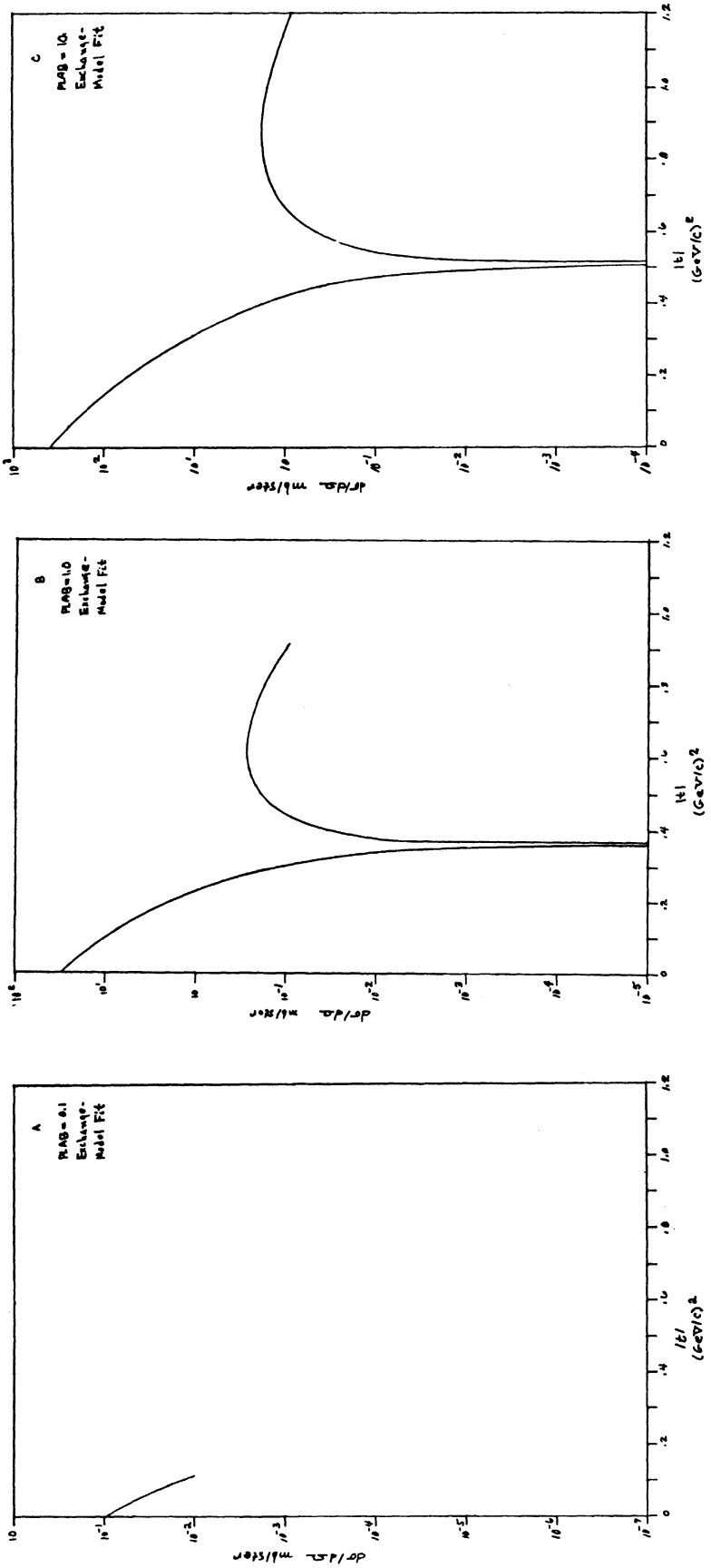

Figure 11.2-2. Exchange-Model Fit to PBAR-P Elastic. Predicted elastic scattering cross sections shown at (A) 0.1 GeV/c, (B) 1.0 GeV/c, and (C) 10.0 GeV/c.

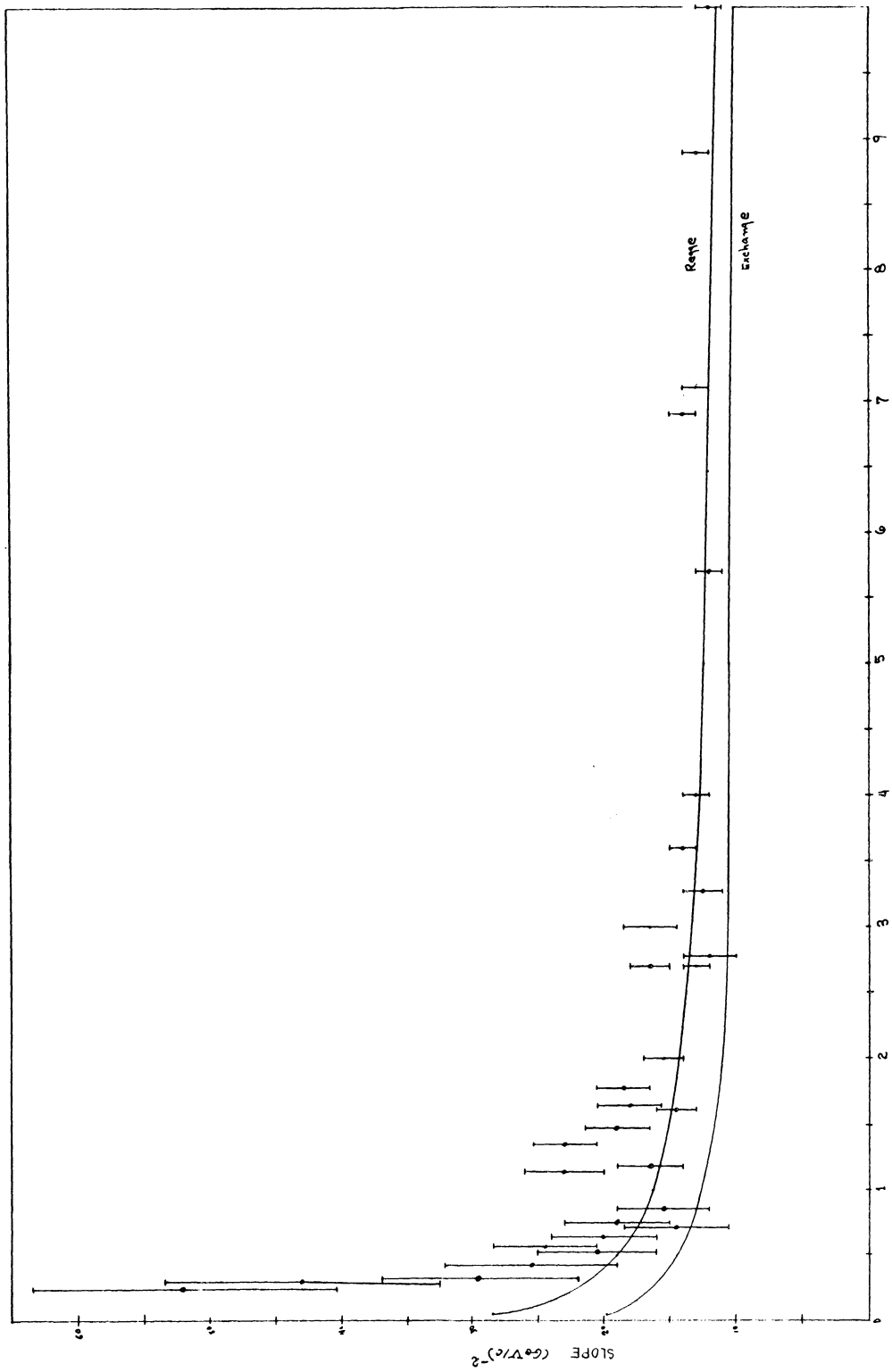

Figure 11.2-3. Exchange- and Regge-Model Predictions for Forward Peak. The experimental data has been taken from the sources quoted in the Appendix.

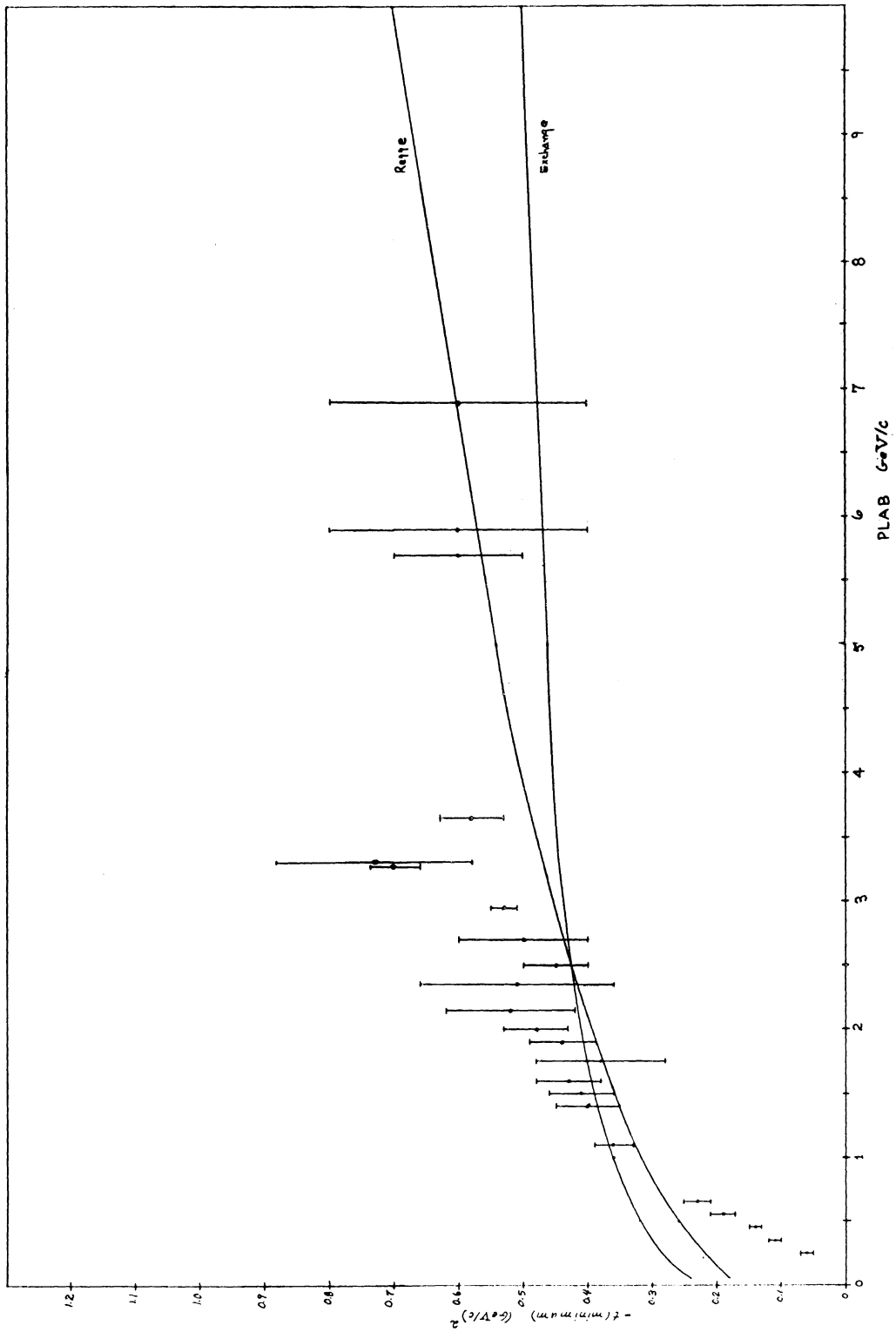

Figure 11.2-4. Exchange- and Regge-Model Predictions for First Minimum. The experimental data has been taken from the sources quoted in the Appendix.

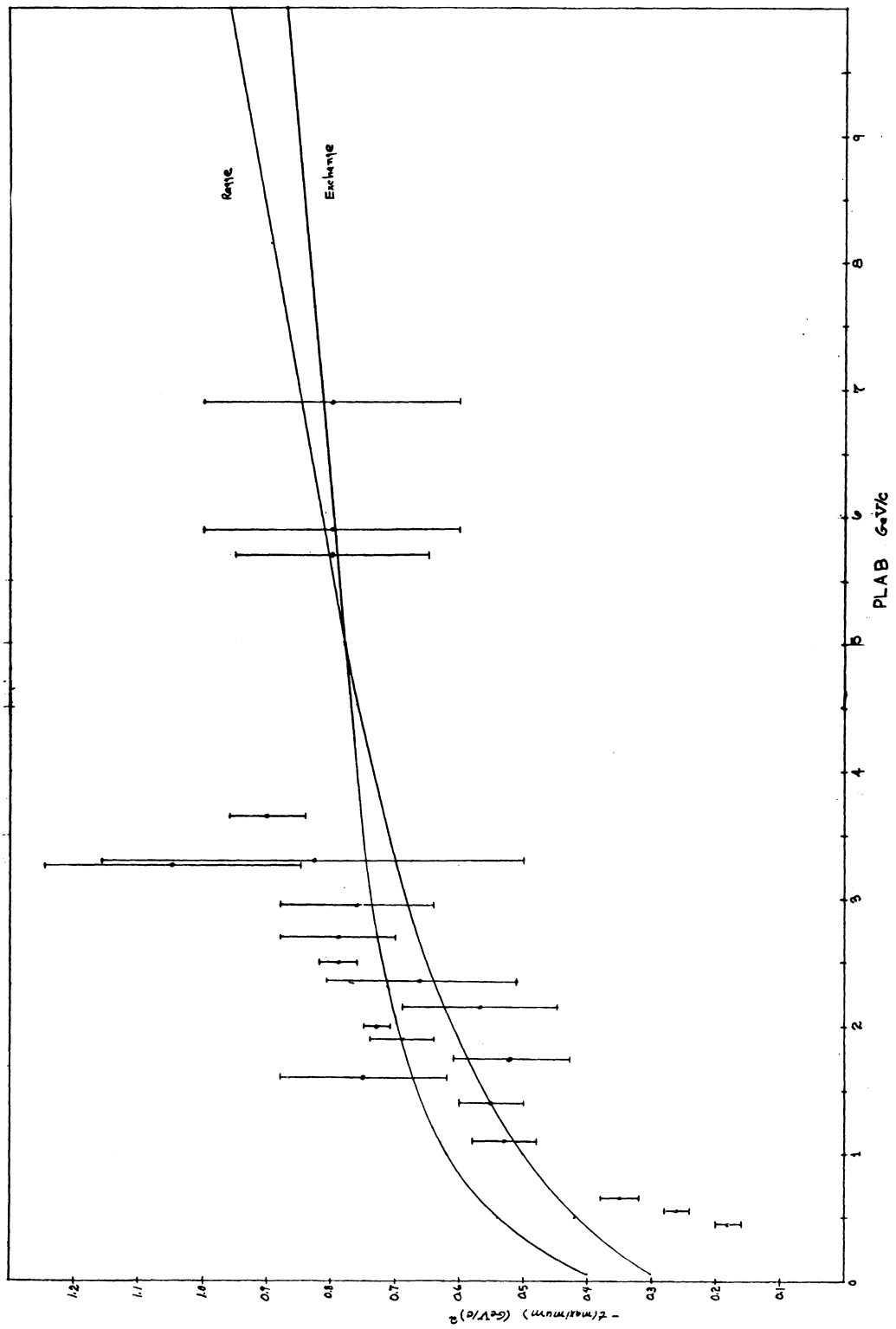

Figure 11.2-5. Exchange- and Regge-Model Predictions for Secondary Maximum. The experimental data has been taken from the sources quoted in the Appendix.

corrected exchange model.

11.3 Backward Cross Section

According to Figure 10.7-10 the backward elastic cross section rises sharply below 1.95 GeV/c lab momentum, or 2400 MeV CM emergy. The effect becomes especially noticeable at the largest scattering angles ($-0.9 > \cos\theta > -1.0$), where the cross section drops more than a factor of three between 1.70 GeV/c, and 1.95 GeV/c. Structure at these momenta has also been observed by R. J. Abrams, et al. (1967) in both the PBAR-P and PBAR-D total cross sections. Using the two cross sections to untangle isospin states, this group also determined that such structure could be attributed to a pair of I=1 resonances at 2345 MeV (width=140), and 2190 MeV (width =140), and an I=0 resonance at 2380 MeV (width=85). (These bumps may also be credited to nucleon-isobar production, as discussed below.) To compare these findings with our own, the points given in Figure 10.6-10A have been replotted with an energy abscissa in Figure 11.3-1, and the resonances hypothesized by R. J. Abrams, et al. (1967) shown as horizontal bars above the data. Inspection of this figure indicates that the rapid cross-section rise appearing in our data more likely results from resonance structure at 2345 MeV, than 2380 MeV.

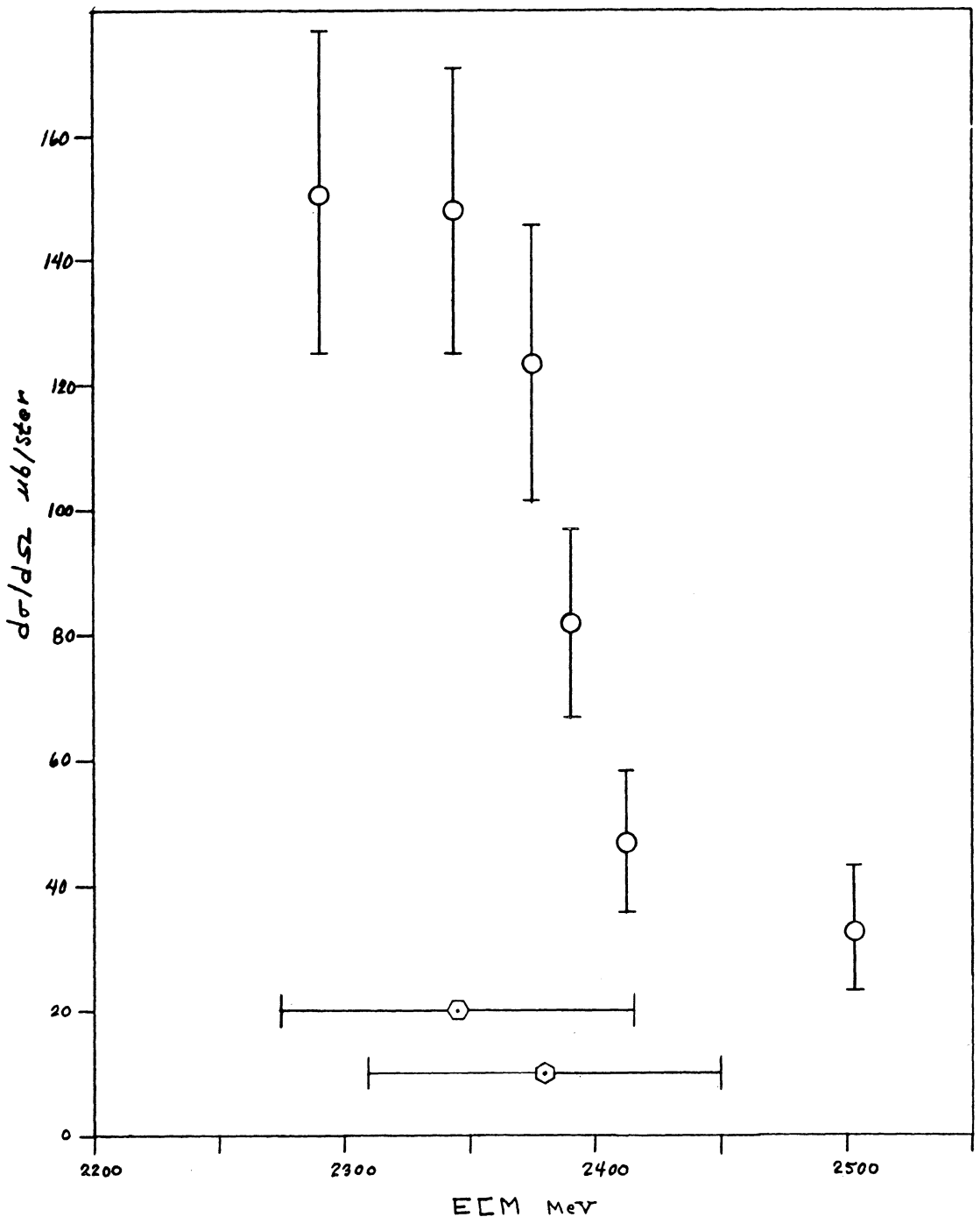

Figure 11.3-1. Backward Energy Cross Section. Histogrammed events have $-0.9 > \cos\theta > -1.0$. The horizontal bars indicate the position, and width of the resonances hypothesized by R.J. Abrams, et al. (1967).

As noted in Section 2.4 above, the minimum expected total cross section for a resonance with (2J+1)K = 1.0--approximately the value quoted for the structures observed by R. J. Abrams, et al. (1967)--decreases from .120 mb at J=2 to .046 mb at J=6. On the other hand, the absence of any three standard-deviation peak in the backward hemisphere cross sections of Figure 10.6-10D indicates that a boson resonance communicating with the backward hemisphere must do so with less than .100 mb of cross section. Consequently, the total cross-section enhancements observed at 2345 and 2380 by R. Abrams cannot be credited to the formation of a single boson resonance with spin less than three, and one-half its elastic scattering amplitudes decaying into the backward hemisphere.

Other nearby cross-section measurements indicate that additional structure exists in the backward cross section. However, owing to smaller data samples these experimenters cite results only for the wider angular interval $-0.80 > \cos\theta > -1.0$, thus possibly diluting evidence for high-spin boson resonances. In addition, corrections for square-hit scanning efficiency--known to be important from the present study--were not apparently undertaken in these experiments. Thus, to compare our

results with those of others, our data has been recompiled using the wider angular interval, and with corrections for square-hit scanning efficiency removed. The new backward cross sections, along with those reported by G. Lynch, et al. (1962), W. Cooper, et al. (1968), Z. Ma, et al. (1968), are shown in Figure 11.3-2. For comparison the resonances conjectured by R. J. Abrams, et al. (1967) have been indicated with the three upper horizontal bars. Similarly, the two lower bars show the boson structures detected by M. Focacci, et al.(1966) with a missing-mass spectrometer at 2382 MeV (width < 30), and at 2195 MeV (width < 13).

Inspection of the data collected together in Figure 11.3-2 shows that another (or perhaps the same) bump appears in the backward cross section below our energies. As noted by W. Cooper, et al. (1968), this structure may be credited to resonance formation at 2190 MeV, as originally proposed by R. J. Abrams et al. (1967). The activity at 2290 MeV, on the other hand, suggests a sharp dip in the backward cross section near 1.60 GeV/c. Evidence supporting this interpretation, though weak, amounts to the following: 1) The last two points taken by Cooper, et al. (1968) indicate a rapid drop in the backward cross section which cannot be attrib-

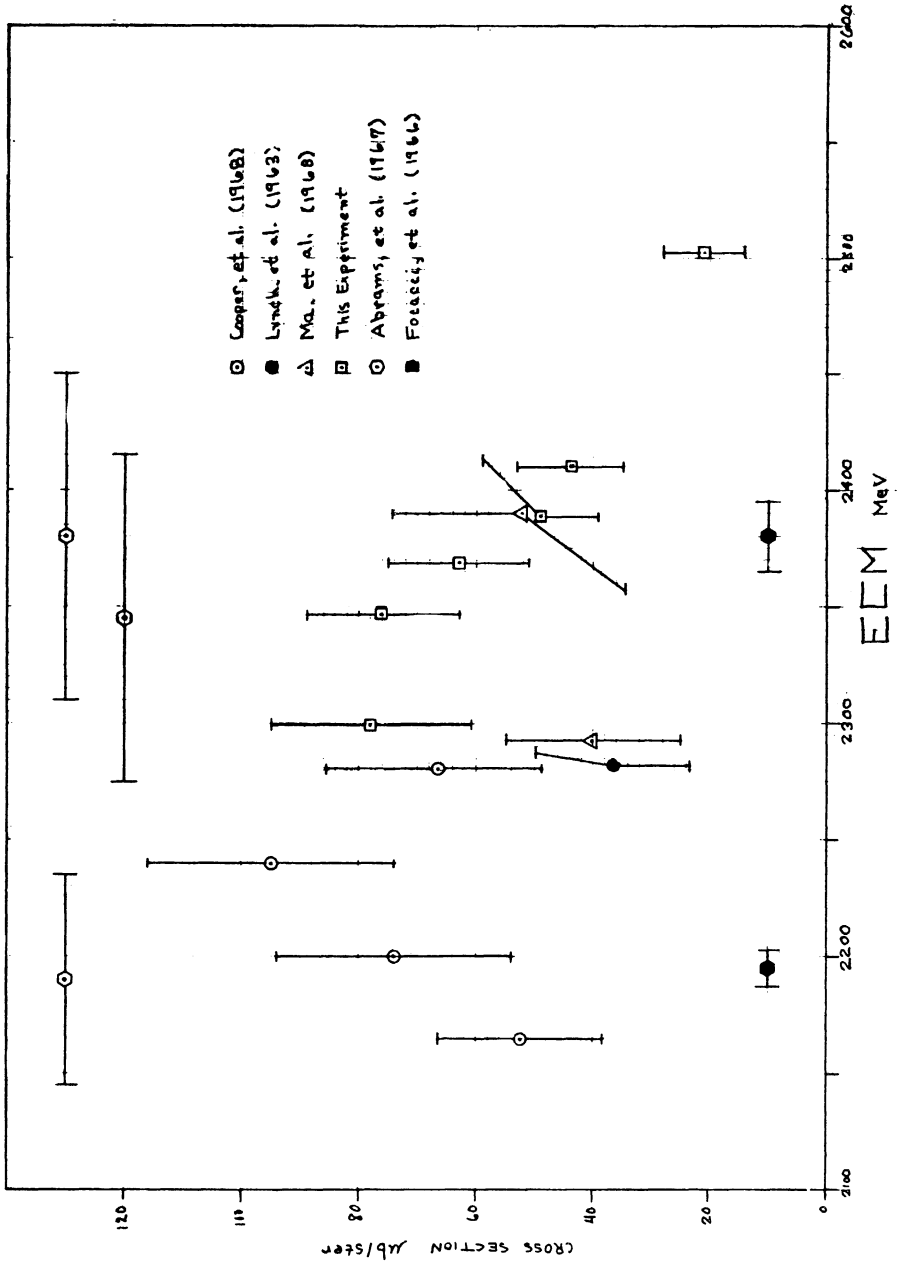

Figure 11.3-2. Combined Backward Energy Cross Section. The histogrammed events have $-0.8 > \cos\theta > -1.0$. See text for an interpretation of the structure near 2290 MeV.

uted to inter-experiment normalization error. 2) The point reported by Z. Ma, et al. (1968) at 1.58 GeV/c appears much lower than our 1.63 GeV/c measurement, the two experiments appearing consistently normalized owing to the proximity of the two data points at 1.88 GeV/c. 3) The point taken by G. Lynch, et al. (1962) at 1.61 GeV/c appears consistent with Z. Ma, et al. (1968), lending support to the conjecture that neither point is anomalously low.

Rapid activity in the backward PBAR-P cross section has also been observed at lower energies by D. Cline, et al. (1968), and such structure has been credited in part to Ericson fluctuations. Ericson fluctuations occur when two or more resonant states couple to the same system, and the spacing between these states is small compared to their average width. The amplitudes associated with these resonances may then interfere, thereby producing cross-section structure over-and-above that expected from the resonances alone. Such fluctuations have been observed in nuclear physics, as noted by T. Ericson (1965). Assuming, as conjectured above, that direct channel resonances form and decay at both 2190 and 2345 MeV--with the widths quoted by R. J. Abrams, et al. (1967)--one may speculate that the activity

observed at 2290 MeV amounts to an Ericson fluctuation. Such fluctuations, however, resist analysis, as a minimum of three amplitudes (two resonances, plus the background) mix to form the observed structure.

Both the elastic and inelastic cross sections may vary rapidly near the energy threshold for the reaction

PBAR + P → QBAR + Q

where Q and QBAR denote a pair of (perhaps unrelated) baryon states. The inelastic cross section fluctuates because it depends linearly on k' (where k' represents the CM momentum of the QBAR), since k' increases rapidly above its threshold value of k'=0. The elastic cross section, on the other hand, fluctuates because the double-exchange diagram shown in Figure 11.3-3 becomes energetically possible, and contributes to the measured cross section. Below threshold the inelastic process cannot, of course, be observed, while the elastic one may still occur with a finite probability, since energy-momentum conservation need only hold within the constraints imposed by the uncertainty principle.

As noted by R. J. Abrams, et al. (1967), the bumps observed in the PBAR-P and PBAR-D may be attributed

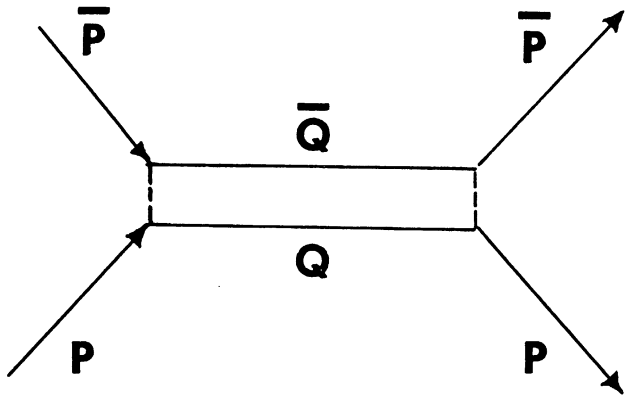

Figure 11.3-3. Elastic Threshold Reaction. The exchanged particles are mesons.

to nucleon-isobar production near threshold, instead of boson resonance formation at the energies quoted above. In this case the energy fluctuations in the elastic cross section depend on the Feynman propagators for the hyperons Q and QBAR, while changes in the angular distribution arise from the meson exchanges. Since the Q and QBAR may take any energies E' and E" such that their sum equals the invariant mass M, the energy dependence of the threshold reaction will depend on a factor

$$\iint \frac{\delta(M-E'-E")}{(E'^2-m'^2)(E"^2-m"^2)}\, dE'\, dE"$$

where m'(m") denotes the (perhaps complex) mass of the Q(QBAR). The delta function, of course, kills one of the integrals, turning the remaining one into a convolution integral. Application of the convolution theorem then yields a term proportional to

$$1/[\, M^2 - (m' + m")^2]$$

This factor, being formally identical to the one describing a direct channel resonance of mass (m' + m"), indicates that the elastic cross section looks resonant at the threshold for a (well-coupled) inelastic process. However, the angular distributions observed in the present experiment look too structured to be attributed to the

production of baryons at threshold, as explained below.

11.4 Angular Character of Backward Peak

The backward peak appearing at our lowest three momentum sets may be credited to a direct-channel boson resonance with mass 2345 MeV, and width 140 MeV. To ascertain the angular nature of this enhancement, events from these momentum sets have been combined, and histogrammed against cos θ in Figure 11.4-1. According to this plot, the backward peak emerges from the plateau around cos θ = -0.9, and then rises approximately four standard deviations above the plateau in the last angular interval. When the various background amplitudes are small, the observed structure results entirely from resonance amplitudes, and the remarks of Chapter 2 apply directly. On the other hand, if the background amplitudes compare with those of the resonance--as suggested in Chapter 6--the situation becomes more complicated. In either case, however, upper and lower limits may be placed on the spin of the resonance, according to the arguments presented below.

Weak background. When all the background amplitudes are weak relative to those of the resonance, and thus contribute only negligibly to the differential cross section,

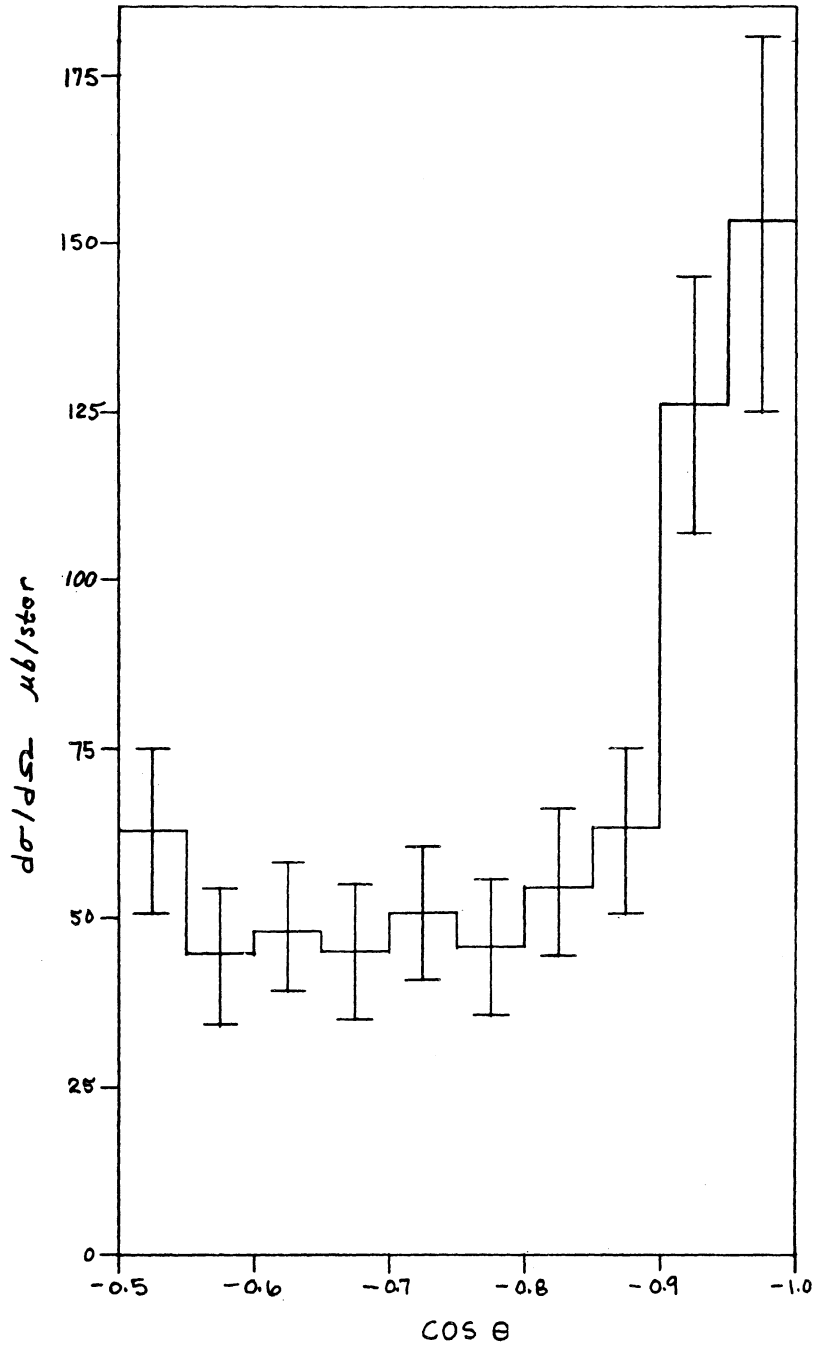

Figure 11.4-1. Backward Angular Cross Section. The histogram contains all events from the 1.63, 1.77, and 1.83 GeV/c momentum sets.

the angular distributions shown in Figures 2.5-1,2,3 represent those expected from the decay of the resonance. Owing to the existence of a plateau forward of cos θ = -0.9, the observed enhancement appears consistent only with the distributions shown in Figure 2.5-3, since the other curves contain oscillatory structure not present in the measured cross section. In addition, spin assignments J=1,2,3 all lead to angular distributions (Figure 2.5-3A) too smooth to match the sharp change in cross section seen at cos θ = -0.9. On the other hand, spin assignments larger than J=5 produce plateau-to-peak cross-section ratios larger than the factor of three characterizing the measured data. Thus in the presence of a weak background a good lower limit for J is 4, and good upper limit is 5, as entered in column one of Table 11.4-1.

Incoherent background. When the background is strong, but incoherent in the sense that interference terms formed with the resonance remain small, the observed angular distribution represents a superposition of background and resonance effects. The background in this case presumably fluctuates slowly, and thus generates part of the plateau seen forward of cos θ = -0.9. This implies that the singlet, or either triplet state could produce the observed enhancement, with the background smoothing, or

TABLE 11.4-1

Resonance Spin Assignments

	Weak Background	Incoherent Background	Coherent Background
J(upper)	5	5	8
J(lower)	4	3	3

otherwise masking the oscillatory structure present in Figures 2.5-1 and 2.5-2. Inspection of the latter two figures indicates that even with such background, spin assignments lower than J=3 lead to backward enhancements too flat to be consistent with the observed data. On the other hand, Figure 2.5-3 suggests for similar reasons that J be at least four. As to an upper limit, Figures 2.5-1,2 indicate that spins greater than four lead to backward enhancements too sharply peaked to match with the measured cross sections. Figure 2.5-3 shows, on the other hand, that J=5 represents an upper limit for this triplet-state possibility. Thus, with a wholly incoherent background a good lower limit for J appears to be three, and safe upper one five.

Coherent background. When the background is both strong and coherent, so that interference effects dominate the amplitude, the observed angular distribution represents a nonlinear combination of background and resonance structure. The various interference terms, being a mixture of partial waves, look like products of associated Legendre polynomials,

$$P_{L'}^{LZ'}(\cos\theta) \quad P_{L''}^{LZ''}(\cos\theta)$$

where L" denotes the orbital angular momentum of the

background wave, and L' that for the resonance. For a resonance of spin J the orbital angular momentum L' may take any of the three values J-1, J, J+1, while for background waves like those necessary to form a forward diffraction peak, values for L" considerably in excess of thirty may be expected. Consequently, though the Legendre products quoted above form substantially less than a (mathematically) complete set, they may still simulate very complicated structure when the magnitudes and phases of the background are correct. In particular, for any given J these products may readily simulate--within statistical error--the crude angular-distribution measurement shown in Figure 11.4-1. For this reason it is difficult to place a theoretical upper limit on the resonance spin, although as a practical matter spins in excess of seven or eight appear unreasonable. As to a lower limit, owing to the absence of any three standard-deviation structure in the backward hemisphere cross section of Figure 10.6-10D, spins less than three for the 2345 MeV resonance may be ruled out, as noted in Section 11.3 above.

The sharp backward peak shown in Figure 11.4 might also be interpreted as a threshold effect associated with the production of baryons . The angular

dependence expected at threshold can, in principle, be determined using the Feynman diagram shown in Figure 11.3-3. In practice, however, substantial absorption occurs, and the observed cross section appears more wider than predicted by an unadorned exchange model. On the other hand, the low kinetic energy of the Q and QBAR near threshold, and the requirement of CP invariance in the strong interaction place severe restrictions on the participating partial waves. In particular, near threshold the QBAR-Q system resides mostly in an S-wave state, so that the total spin J must obtain from the intrinsic spins of the Q and QBAR. For a pair of spin 3/2 particles, like the $N^*(1238;3/2,3/2^+)$ and its anti-particle, this can be as high as J=3. However, CP invariance requires that

$$S(\text{initial}) = S(\text{intermediate}) = S(\text{final})$$

so that L=0 implies J=0,1. The J=0 possibility leads to a bump in the total cross section with a flat angular distribution, while J=1 case leads to a term quadratic in the first-degree Legendre polynomial. Neither of these, however, is consistent with the sharp backward peak shown in Figure 11.4-1. Experiments tend to confirm these conclusions. For example, W. Cooper, et al. (1968) found no smooth excitation function that both reproduced

their cross sections for single pion production, and the bumps observed in the total cross section by R. J. Abrams, et al. (1967). In a similar effort, but at energies overlapping our own, Z. Ma, et al. (1968) found no structure in their single-pion production cross sections that could be associated with the 2345 and 2380 MeV resonances hypothesized by R. J. Abrams, et al. (1967).

If, as conjectured, the observed enhancement results from the decay of a legitimate boson resonance, its effects ought also to be observed in other reaction channels. According to Figure 10.6-10 the enhancement cross section drops rapidly between 1.63 and 1.88 GeV/c, a result paralleling a similarly rapid drop in the di-pion annihilation cross section measured by J. Chapman, et al. (1968). The angular distribution associated with this reaction evidences no forward or backward peak--as would be expected if the annihilation were proceeding via nucleon or dibaryon exchange--thus suggesting that the di-pion final state obtains mostly via the decay of one or more intermediate states. The angular distribution observed by J. Chapman, et al. (1968) follows a fourth-degree Legendre polynomial remarkably well, lending strong support to a J=4 spin assignment for the intermediate state. This value is, of course, consistent with the estimates quoted in Table 11.4-1 above.

APPENDIX A

PROJECTIVE GEOMETRY OF MURA CHAMBER

A.1 Introduction

The angles, curvature, and bubble density of the projected track are determined by examining the differential geometry of the viewing-screen image. Since the projection formulas are space variant, the viewing-screen azimuth obtains from the slope of bound, rather than free vectors. Curvature, on the other hand, follows from the usual two-dimensional curvature formula applied to the projection of a bound cylindrical helix. Finally, the bubble density is determined by examining the contraction, or dilation of vertex-zone spatial length on projection of a track through the camera lenses.

The geometry assumed for the formulas presented below is shown in Figure A.1-1. Call p the distance from the camera lens to the nominal plane of the beam tracks, and q the distance from the back of the camera lens to the plane containing the film. With the co-ordinates shown, the image (u,v) of a vector (x,y,z) bound to the point (x',y',0) has the form:

$$u = q[px + zx']/p(p - z)$$

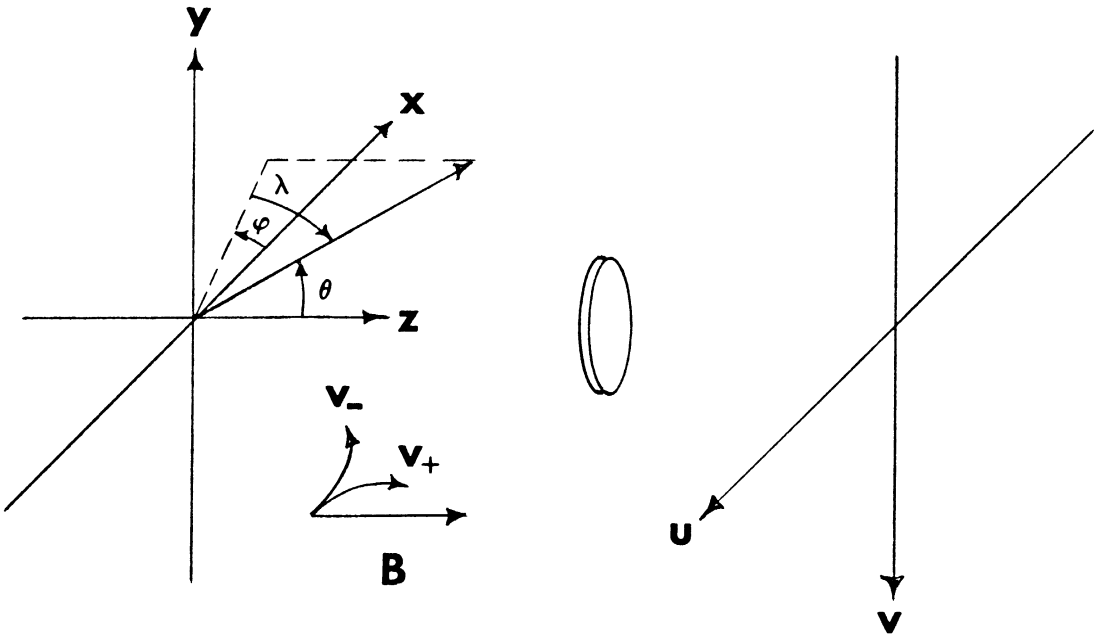

Figure A.1-1. Camera and Chamber Geometry. Here v_+ and v_- denote positive and negative particle tracks, and the curved vectors the directions they tend to orbit. (The beam enters in the xy-plane.)

$$v = q[py + zy']/p(p - z)$$

Note that the projection (u,v) depends explicitly on the coordinates to which the vector (x,y,z) is bound.

From the geometrical point of view it is more convenient to deal with spherical coordinates (r,θ,ϕ) centered on the vector (x',y',0) than the rectangular coordinates (x,y,z). In this case

$$x = r \sin\theta \cos\phi = r \cos\lambda \cos\phi$$
$$y = r \sin\theta \sin\phi = r \cos\lambda \sin\phi$$
$$z = r \cos\theta \qquad = r \sin\lambda$$

where $\lambda = \pi/2 - \theta$ denotes the track's dip angle. Similarly, it sometimes proves convenient to work with the cylindrical coordinates (ρ,ψ) in the plane of the film:

$$u = \rho \cos\psi$$
$$v = \rho \sin\psi$$

A.2 Projection of Azimuth

The angle ψ that the projected track makes with the u-axis obtains by parameterizing x with the parameter t = r, and then looking at the derivative:

$$\tan\psi = dv/du = (dv/dt)/(du/dt)$$
$$= \frac{p \sin\phi + y' \tan\lambda}{p \cos\phi + x' \tan\lambda}$$

Note that the projected azimuth depends on the collision vertex (x',y',0), but not the lens-to-film distance q.

A.3 Projection of Bubble Density

The viewing screen bubble density obtains from the ratio of spatial distance on film to spatial distance in the chamber. Thus, we consider

$$du^2 + dv^2 = [(\partial u/\partial t)^2 + (\partial v/\partial t)^2]\, dt^2$$

Consequently, the viewing screen bubble density follows from the ratio:

$$\text{ionization(film)} \;/\; \text{ionization(chamber)} = q[(p\cos\lambda\cos\phi + x'\sin\lambda)^2 + (p\cos\lambda\sin\phi + y'\sin\lambda)^2]^{1/2}/p^2$$

where the right-hand formula is just the bracketed expression above, evaluated at collision vertex (x',y',0).

A.4 Projection of Curvature

Viewing-screen track curvature obtains by parameterizing the space curve as a cylindrical helix, and then using the well-known curvature formula:

$$K = (u'v'' - u''v')/(u'^2 + v'^2)^{3/2}$$

on the projected image. (Here the primes denote

derivatives with respect to t.) The magnetic field generating the helix is presumed parallel to the camera axis, so that the particles orbit in helices with radius of curvature

$$a = P \cos \lambda / .3B$$

and pitch

$$b = P \sin \lambda / .3B$$

where P denotes the momentum of the particle in MeV/c, and B the magnetic field in kilogauss.

The derivatives u', u", v', v" follow after some algebra:

$$u' = q[pa \cos \phi + bx']/p^2$$

$$v' = q[pa \sin \phi + by']/p^2$$

$$u" = q[\pm pa \sin \phi]/p^2 + 2qb[pa \cos \phi + bx']/p^3$$

$$v" = q[\mp pa \sin \phi]/p^2 + 2qb[pa \sin \phi + by']/p^3$$

where the upper (lower) signs refer to positive (negative) particles. (The magnetic field B points in the positive z-direction, that is, toward the cameras.)

A.5 Rotation of Event Geometry

In simulating two-prong events one normally begins with a beam track running parallel to the x-axis, and suffering an interaction at the point (x',y',0) with the outgoing tracks in the xy-plane. In this case the track geometries must be rotated about the x-axis by various angles α to account for the various azimuthal possibilities for the interaction, and about the z-axis by some angle β to obtain the correct pitch of the beam with respect to the x-axis. If an outgoing track originally makes angle ϕ_o with the x-axis, then after these two rotations its dip λ and azimuth ϕ are given by

$$\sin \lambda = \sin \alpha \sin \phi_o$$

$$\tan \phi = \frac{\cos \alpha \cos \beta \sin \phi_o + \sin \beta \cos \phi_o}{\cos \beta \cos \phi_o - \cos \alpha \sin \beta \sin \phi_o}$$

These complicated-looking formulas are readily evaluated with a digital computer.

APPENDIX B

SCANNING EFFICIENCY THEORY

B.1 Introduction

In this appendix we discuss the random-miss, correlated-miss, and two-scanner models for scanning efficiency. The random-miss model, which is more or less conventional in bubble-chamber work, is based on the hypothesis that all events are of equal difficulty, and hence that events missed by one scanner are independent of those missed by the other. The correlated-miss model on the other hand, incorporates the hypothesis that some events are more difficult than others, and thus that some correlation exists between the events missed by the first scanner, and those missed by the second.

B.2 Random-Miss Model[†]

The random-miss model for scanning efficiency is based on the hypothesis that all events are equally difficult for the scanners, and that no tendency exists for the scanners to miss one event rather than another. Such a hypothesis is tenable only if all events,

---

[†]Most of the material in this section was brought to the author's attention by his colleague M. Church.

regardless of their exact topology, stand out equally prominently against the beam-track background. Mathematically speaking, the random-miss assumption implies that the events missed by the scanners are statistically independent, and that no correlation exists, for example, between event topology and scanning efficiency. In this case probabilities are given as simple sums and products, and no calculus is required to specify scanning efficiency, as in the correlated-miss model introduced below.

A second tenet of the random-miss model holds that the concept of an average scanner with an average scanning efficiency is meaningful for the experiment. The average scan efficiency is determined by making a histogram of the scan efficiencies obtained for each scanner on each roll, and then calculating the mean e, and rms width Δe of the resulting distribution. The average scan efficiency may then be considered well defined if the uncertainty δe in e is small compared to the other statistical errors of the experiment. The uncertainty δe in e is given by the usual formula

$$\delta e = \Delta e/\sqrt{N}$$

where N is the number of entries in the histogram. For example, if N=625, e = 80%, Δe = 5%, then δe = 1/5%.

Errors of this order are considered negligible in most bubble-chamber experiments.

When the film is double scanned the overall efficiency on each roll improves materially, since, under the random-miss hypothesis, the events missed by the first scanner stand a good chance of being picked up by the second, and conversely. To calculate the efficiency for the double-scan, let N_1 be the number of events seen by just one scanner, N_2 the number seen by two scanners, and $N_o = N_1 + N_2$ the number observed by either or both scanners. Then, if the film contains N_t events that pass the scan rules, the above numbers are related to the single-scan efficiency e by

$$N_1 = 2N_t(1 - e)e$$
$$N_2 = N_t e^2$$
$$N_o = N_t[1 - (1 - e)^2] = N_t(2e - e^2)$$

Since $N_o = N_1 + N_2$, we have two independent equations in the two unknowns e and N_t. To determine e we divide N_1 by N_2, and solve directly for e obtaining

$$e = 2N_2/(N_1 + 2N_2) = 2N_2/(N_o + N_2)$$

The double-scan efficiency is, of course, given by

N_o/N_t, so that

$$E = N_o/N_t = 2e - e^2 = 4N_oN_2/(N_o + N_2)^2$$

The above formulas may be applied to the experiment as a whole, or, if it is suspected that e depends on some parameter like the center-of-mass scattering angle, to some restricted portion of the data.

If some of the film has been triple scanned, the validity of the random-miss hypothesis can be checked by counting the number N_1 of events seen by just one scanner, the number N_2 seen by two scanners, and the number N_3 seen by all three scanners. In this case the numbers are related to e by

$$N_1 = 3N_t(1 - e)^2e$$
$$N_2 = 3N_t(1 - e)e^2$$
$$N_3 = N_te^3$$

We now have three equations in two unknowns, and the system is overdetermined. However, if the random-miss hypothesis holds, any pair will yield the same value for e as any other pair. On the other hand, if the hypothesis fails, e will depend on the pair chosen.

B.3 Correlated-Miss Model[†]

In many experiments, and in particular for the present one, some events prove more difficult for the scanners than others. The variance in difficulty can arise for a manifold of reasons: for example, the topology of some events may stand out distinctly on the scanning screen, while for others it may be obfuscated by other events, as well as the beam-track background. Similarly, in some cases the event topology may be wholly unique, while in others it may closely resemble that of an unstudied channel. Such effects are generally quite subtle, and virtually impossible to treat analytically. However, when the variance is small one can hope to account for such effects by making first order corrections to the scan-efficiency formulas for the random-miss model; this, in fact, is the objective of the correlated-miss model introduced below.

To set the foundations for the correlated-miss model, we consider a hypothetical experiment wherein the greatest share of events are of the random-miss variety, while only a small fraction tend to be missed by the second scanner if already missed by the first. In

---

[†]The author is indebted to statistician R. Todd for many of the ideas contained in this section.

particular, we postulate that the events follow a linearly biased gaussian-distribution law in a difficulty variable D:

$$\rho(D) = 2D \exp(- D^2) \qquad (D > 0)$$

From the scanner's point of view events in the range $0 < D < 1$ are relatively easy to find, while those with $D > 1$ present a serious challenge to his scanning ability--although he may still have a high efficiency for finding them. The distribution has been given a linearly biased gaussian form, since 1) events tend to be distributed this way in practice,† 2) the exact form of the distribution plays little role in determining the first order corrections to the random-miss model, and 3) the mathematics resulting from this distribution are particularly simple (contain no radicals).

The average scanner generally displays a better efficiency for the easy events than for the more difficult ones. To account for this tendency we postulate that the average scan efficiency e has a gaussian dependence on D:

$$e(D) = e_o \exp(- D^2/D_o^2)$$

---

†In most bubble-chamber experiments, the greater share of events tend to be of intermediate difficulty, with only a few being extremely easy or extremely difficult to find.

where e_o is the average scanner's efficiency for zero difficulty events, and D_o the difficulty at which his efficiency drops to 1/e of its best value. According to this formula, and the one preceding it, the average scanner will find a total of N_o events on a roll containing N_t good events, where

$$N_o = N_t \int_0^\infty \rho(D)\ e(D)\ dD = N_t e_o D_o^2/(D_o^2 + 1)$$

Note that if the scanners have no trouble with the difficult events, the number found is

$$N_o = N_t e_o \qquad (D_o >> 1),$$

a formula identical to that for the random-miss model. On the other hand, if the difficult events represent a severe problem for the scanners, the number found will be

$$N_o = N_t e_o D_o^2 \qquad (D_o << 1).$$

Finally, if the scanners have no trouble at all with the easy events, but tend to miss the difficult ones, the number found is given by

$$N_o = N_t D_o^2/(D_o^2 + 1) \qquad (e_o = 1),$$

a formula useful, for example, in the present experiment.

DOUBLE SCANNING: When the film is double scanned we expect a marked improvement in the overall scan efficiency, since, even under the correlated-miss hypothesis, the events missed by the first scanner stand a good chance of being observed by the second, and conversely. To calculate the efficiency for the double scan, let N_1 be the number of events found by just one scanner, N_2 the number found by two scanners, and $N_o=N_1+N_2$ the number found by either or both scanners. Then,

$$N_1 = 2N_t \int_0^\infty \rho(1-e)e \, dD$$

$$= 2N_t e_o D_o^2/(D_o^2 + 1) - 2N_t e_o^2 D_o^2/(D_o^2 + 2)$$

$$N_2 = N_t \int_0^\infty \rho e^2 \, dD = N_t e_o^2 D_o^2/(D_o^2 + 2)$$

We have two equations in the three unknowns N_t, e_o, D_o, so that the system is indeterminate. However, we can eliminate N_t and write e_o in terms of D_o:

$$e_o = 2N_2(D_o^2 + 2)/[(2N_2 + N_1)(D_o^2 + 1)]$$

a formula that will prove useful in the sequel.

In certain cases one of the two parameters e_o or D_o can be suppressed, thus allowing solution for the other in terms of N_1 and N_2.† If, for example, the

†Most of the arguments presented in this paragraph were worked out in collaboration with M. Church.

scanners have about the same problem with both the easy and difficult events, the parameter D_o will be large, and

$$e_o = 2N_2/(2N_2 + N_1) \qquad (D_o >> 1)$$

as in the random-miss model. On the other hand, if they have little trouble with the easy events, but tend to miss the more difficult ones, the parameter e_o will approach unity, and D_o will be specified by

$$(D_o^2 + 1)/(D_o^2 + 2) = 2N_2/(2N_2 + N_1)$$

from which we conclude that $D_o^2 = 2N_2/N_1 - 1$. Under the latter hypotheses the scanning efficiency for the individual scanners is given by

$$\begin{aligned} e &= D_o^2/(D_o^2 + 1) \\ &= [2N_2/(2N_2 + N_1)][1 - (N_1/2N_2)^2] \end{aligned}$$

Similarly, the overall scanning efficiency is given by

$$E = [4N_oN_2/(N_o + N_2^2)][1 - (N_1/2N_2)^2]$$

Note that in both expressions the bracketed quantity specifies the difference between the random-miss and correlated-miss efficiencies. When the average scanning efficiency is high, $N_2 >> N_1$, and the two theories give the same results. Otherwise, the correlated-miss hypothesis adds a small correction to the usual formulas.

TRIPLE SCANNING: If some of the film has been triple scanned, the parameters, e_o and D_o may be determined explicitly. Let N_1 be the number of events found by just one scanner, N_2 the number found by two scanners, and N_3 the number found by all three scanners. Then,

$$N_1 = 3N_t \int \rho(1 - e)^2 e \, dD$$

$$N_2 = 3N_t \int \rho(1 - e)e^2 \, dD$$

$$N_3 = N_t \int \rho e^3 \, dD$$

The three integrals are simple functions of e_o and D_o. Thus, we have three equations in the three unknowns N_t, e_o, D_o, and the system is solvable. Since N_t is the least interesting of the three variables, we eliminate it by dividing N_1 and N_2 by N_3, obtaining upon evaluation of the integrals

$$\frac{N_1}{N_3} = \frac{3(D_o^2 + 3)}{e_o^2(D_o^2 + 1)} - \frac{6(D_o^2 + 3)}{e\,(D_o^2 + 2)} + 3$$

$$\frac{N_2}{N_3} = \frac{3(D_o^2 + 3)}{e_o(D_o^2 + 2)} - 3$$

This pair of equations is readily solved for the unknowns e_o and D_o. We omit, however, the explicit solution, since

the algebra is fairly involved and not particularly illuminating.

REMARKS: The equations of the correlated-miss model should, and in fact do go over to those for the random-miss model in the limit D_o approaches infinity. In this sense, the random-miss model represents a special case of the correlated miss-model, and should be used whenever its hypotheses are observed to hold. In doubtful cases the validity of the random-miss hypothesis may be checked by using the triple scans to determine e_o and D_o. If D_o turns out to be large, say greater than five, the random-miss hypothesis is probably valid. If, on the other hand, D_o takes on an intermediate value, say, in the range $1 < D_o < 5$, the correlated-miss model will give the more accurate scan efficiencies. Finally, if D_o is small, that is, less than unity, neither model can be considered reliable, and a revision of the scan rules should be considered.

The internal consistency of the correlated-miss model may be tested by checking that the values for e_o and D_o obtained from the triple scans satisfy the formula in e_o and D_o obtained from the double scans. Discrepancies between the two may arise either because the

exponential parameterizations are unsound, or because the double and triple scanners were of different scanning ability. When the discrepancy is not too large, the former problem may be resolved by reformulating the difficulty distribution $\rho(D)$, and/or the scanning efficiency dependence $e(D)$. On the other hand, if the scanners were of different capability, one can use separate efficiency formulas $\rho(D)$ for the double and triple scans.

APPENDIX C

ISOSPIN COMPOSITION OF NUCLEON-ANTINUCLEON SYSTEM

C.1 Isospin States of Nucleon

The antinucleon-nucleon system consists of two I=1/2 baryons, whose charge Q is related to their baryon number B, and z-component of isospin IZ by the well-known formula:

$$Q = IZ + B/2$$

As usual in quantum mechanics, the joint probability amplitude obtains as the product of the individual amplitudes. Thus, for example, the isospin part of the joint probability amplitude for a PBAR-P system is just

$$|1/2,+1/2\rangle|1/2,-1/2\rangle = \sqrt{1/2}\ |1,0\rangle + \sqrt{1/2}\ |0,0\rangle,$$

The bracketed quantity $|I,IZ\rangle$, defined explicitly in Table C.1-1, is Dirac's short-hand notation for the isospin eigenfunction. The right-hand expression represents the decomposition of the PBAR-P isospin amplitude into its I=0 and I=1 components; the radicals are the well-known Clebsch-Gordon coefficients, and given in Table C.1-2 below. If this table is used oppositely it instead decomposes the I=1, and I=0 nucleon-antinucleon

TABLE C.1-1

Isospin States of Nucleon

Particle	B	I	IZ	Q	|I,IZ>	Symbol
Proton	+1	1/2	+1/2	1	|1/2,+1/2>	|P>
Neutron	+1	1/2	-1/2	0	|1/2,-1/2>	|N>
Antineutron	-1	1/2	+1/2	0	|1/2,+1/2>	|NBAR>
Antiproton	-1	1/2	-1/2	-1	|1/2,-1/2>	|PBAR>

TABLE C.1-2

Clebsch-Gordon Coefficients

Joint Amplitude	|1,+1>	|1,0>	|0,0>	|1,-1>
|1/2,+1/2>|1/2,+1/2>	1	0	0	0
|1/2,+1/2>|1/2,-1/2>	0	$+1/\sqrt{2}$	$+1/\sqrt{2}$	0
|1/2,-1/2>|1/2,+1/2>	0	$+1/\sqrt{2}$	$-1/\sqrt{2}$	0
|1/2,-1/2>|1/2,-1/2>	0	0	0	1

states, as shown in Table C.1-3.

C.2 Charge Conjugation and Charge Symmetry

The operation of charge conjugation, C, converts a particle to its antiparticle without changing its spatial position, momentum, or spin. Specifically, charge conjugation changes the sign of a particle's baryon number, parity, strangeness, charge, and other additive quantum numbers, and thus converts the non-spatial portion of the particle's eigenfunction to (plus or minus) its antiparticle's. For a nucleon-antinucleon system the sign of the conjugated eigenfunction obtains via the generalized Pauli principle, which states that

$$E(\text{space})\ E(\text{spin})\ C\ |J,JZ;I,IZ\rangle = -|J,JZ;I,IZ\rangle,$$

where the E operators exchange the denoted coordinates. Owing to the well-known properties of the spherical harmonics, and the necessity for Fermi-Dirac statistics among fermions, the exchange of the space coordinates yields a factor $(-1)^{L}$, while that of the spin a factor $(-1)^{S+1}$. Thus, for the nucleon-antinucleon system

$$C = (-1)^{L+S}$$

Moreover, since the parity operation applied to the system yields

TABLE C.1-3

Eigenstates of Isospin

|I,IZ>	Unnormalized Eigenstates#
|1,+1>	+|P,PBAR>
|1,0>	+|P,BAR> +|N,NBAR>
|1,-1>	+|N,PBAR>
|0,0>	+|P,PBAR>-|N,NBAR>

#To normalize these states divide by the square root of the number of Dirac kets.

TABLE C.3-1

Charge Symmetry on Nucleon-Antinucleon Systems

Original State	Unnormalized Decomposition	Charge Symmetry	Resulting State
|P,NBAR>	|1,+1>	-|1,-1>	-|N,PBAR>
|P,PBAR>	|1,0>+|0,0>	-|1,0>+|0,0>	-|N,NBAR>
|N,NBAR>	|1,0>-|0,0>	-|1,0>-|0,0>	-|P,PBAR>
|N,PBAR>	|1,-1>	-|1,+1>	-|P,NBAR>

$$P(\text{system}) = P(\text{orbital})\ P(\text{particle})\ P(\text{antiparticle})$$
$$= (-1)^{L+1},$$

it is also true that

$$CP = (-1)^{S+1}.$$

Happily, C, P, CP are all conserved by the strong interaction.

The operation of charge symmetry, S, on the other hand, converts a given system to one with opposite z-component of isospin. Specifically, charge symmetry rotates the isospin vector 180 degrees about the y-axis. For integer isospin systems this operation implies that the polar and azimuthal angles suffer the following transformations:

$$S = (\theta \to \pi - \theta,\ \phi \to \pi - \phi)$$

It will be noted that this operation is wholly equivalent to a coordinate inversion, I,

$$I = (\theta \to \pi - \theta,\ \phi \to \phi - \pi)$$

followed by a reflection, R,

$$R = (\theta \to \theta,\ \phi \to -\phi)$$

The spherical harmonics, understood as eigenfunctions of

isospin space, undergo the following changes under these operators:

$$S\ Y_L^M = RI\ Y_L^M = R\ (-1)^L\ Y_L^M = (-1)^L\ Y_L^{-M}$$

In other words, in Dirac notation

$$S|I,IZ\rangle = (-1)^I\ |I,-IZ\rangle$$

for integer I.

C.3 G-Parity

G-parity, defined as charge symmetry followed by charge conjugation, is useful as it is conserved in the strong interaction. For a system of N pions the G-parity is given by the analog of Furry's theorem for photons:

$$G = (-1)^N$$

This relation follows from the observation that the positive, negative, and neutral pions all belong to the same isospin triplet, and hence when S is applied to the joint isospin amplitude

$$|I1,IZ1\rangle\ |I2,IZ2\rangle\ |I3,IZ3\rangle\ \ldots$$

it generates a factor (-1) for each Dirac ket, as well as changes the sign of all the z-components is isospin.

Since the negative pion is the antiparticle of the positive one, and the neutral member its own antiparticle, charge conjugation changes the sign of the z-components back to their original values, and multiplies the resulting expression by N times the C-eigenvalue of the neutral pion. Since the neutral pion is its own antiparticle, it is necessarily an eigenstate of C, and its eigenvalue must be the same as the two photon state it prefers to decay into, which--regardless of the photon's particular C-eigenvalue--must be plus one.

Unlike the multiple pion system, the PBAR-P system cannot be assigned a definite G-parity; that is, for the nucleon-antinucleon system

$$G = (-1)^{L+S+I},$$

and L+S+I may be even or odd in general. Nevertheless, the PBAR-P system may communicate with a system of definite G-parity, especially when forming a resonance where the intermediate state consists of a system of pions. In the latter case, only that portion of the PBAR-P amplitude having the right G-parity will enter the resonant state. Thus, it is useful to construct nucleon-antinucleon isospin amplitudes that are eigenstates of both I and G. This is accomplished in the usual way by

TABLE C.3-2

Eigenstates of Isospin and G-Parity †

$\|I,IZ;G\rangle$	$(-1)^{L+S}$	Unnormalized Eigenstates#
$\|1,+1;+1\rangle$	-1	$+\|P,NBAR\rangle-\|NBAR,P\rangle$
$\|1,+1;-1\rangle$	+1	$+\|P,NBAR\rangle+\|NBAR,P\rangle$
$\|1,0;+1\rangle$	-1	$-\|P,PBAR\rangle+\|N,NBAR\rangle-\|NBAR,N\rangle+\|PBAR,P\rangle$
$\|1,0;-1\rangle$	+1	$-\|P,PBAR\rangle+\|N,NBAR\rangle+\|NBAR,N\rangle-\|PBAR,P\rangle$
$\|1,-1;+1\rangle$	-1	$+\|N,PBAR\rangle-\|PBAR,N\rangle$
$\|1,-1;-1\rangle$	+1	$+\|N,PBAR\rangle+\|PBAR,N\rangle$
$\|0,0;+1\rangle$	+1	$-\|P,PBAR\rangle-\|N,NBAR\rangle-\|NBAR,N\rangle-\|PBAR,P\rangle$
$\|0,0;-1\rangle$	-1	$-\|P,PBAR\rangle-\|N,NBAR\rangle+\|NBAR,N\rangle+\|PBAR,P\rangle$

#To normalize these states divide by the square root of the number of Dirac kets.

†J. Vander Velde, private communication.

forming linear combinations of the amplitudes listed in Table C.3-1. One such construction is shown in Table C.3-2. Note that all states satisfy

$$G = C(-1)^I,$$

as well as yield G upon successive application of the operators S and C.

APPENDIX D

PREVIOUS EXPERIMENTAL RESULTS

TABLE D.1-1

Experimental Measurements of Diffraction Peak[@]

Experimenter	PLAB	Slope	Cross Sec.
A. Hossian, et al. (1965)	.15	"flat"	8.1 ±1.3
A. Hossian, et al. (1965)	.24	-53.5 ±7.3	21.5 ±2.3
B. Cork, et al. (1957)	.29	-44.7 ±7.8	23.7 +4.2
A. Hossian, et al. (1965)	.31	-33.5 ±4.0	24.4 ±2.5
B. Cork, et al. (1957)	.42	-25.5 ±6.7	27.2 ±4.7
C. Coombes, et al. (1958)	.52	-20.8 ±4.3	29.4 ±2.8
B. Cork, et al. (1957)	.54	-24.7 ±3.7	28.5 ±4.8
C. Coombes, et al. (1958)	.64	-20.3 ±3.9	37.2 ±2.9
B. Cork, et al. (1957)	.72	-16.2 ±3.9	27.1 ±7.2
C. Coombes, et al. (1958)	.75	-19.2 ±4.1	32.1 ±2.8
C. Coombes, et al. (1958)	.86	-15.3 ±3.8	36.1 ±4.0
T. Elioff, et al. (1959)	1.14	-22.9 ±2.8	57.2 ±3.4
L. Dobrzynski, et al. (1966)	1.18	-16.5 ±1.7	52.7 ±14.8
T. Elioff, et al. (1959)	1.34	-22.8 ±2.4	72.9 ±4.8
T. Elioff, et al. (1959)	1.48	-19.0 ±2.6	70.5 ±6.2
N. Xuong, et al. (1961)	1.61	-14.5 ±1.6	67.1 ±7.9
T. Elioff, et al. (1959)	1.64	-18.0 ±2.3	64.9 ±5.9
R. Armenteros, et al. (1960)	1.70	-15.7 ±1.7	74.2 ±3.9

[@]Slope in $(GeV/c)^{-2}$; forward cross section in mb/ster.

TABLE D.1-1 (Cont.)

Experimental Measurements of Diffraction Peak[@]

Experimenter	PLAB	Slope	Cross Sec.
C. Daum, et al. (1968)	1.73	-19.3 ±2.7	221.2 ±96.6
T. Elioff, et al. (1959)	1.77	-18.4 ±1.8	74.8 ±3.9
R. Armenteros, et al. (1960)	1.98	-15.7 ±1.7	76.1 ±5.6
C. Daum, et al. (1968)	2.13	-8.7 ±3.6	53.7 ±28.4
C. Daum, et al. (1968)	2.37	-12.1 ±2.4	110.2 ±47.7
V. Domingo, et al. (1967)	2.70	-13.3 ±0.2	93.1 ±1.7
R. Armenteros, et al. (1960)	2.78	-11.9 ±2.0	107.5 ±12.2
C. Daum, et al. (1968)	2.97	-7.3 ±0.5	40.6 ±9.6
B. Escoubes, et al. (1963)	3.00	-16.3 ±2.2	107.4 ±4.6
T. Ferbel, et al. (1965)	3.28	-12.8 ±0.8	104.8 ±3.7
B. Escoubes, et al. (1963)	3.60	-14.1 ±0.6	105.1 ±5.0
O. Czyzewski, et al. (1965)	4.00	-13.0 ±0.6	---
K. Bockann, et al. (1966)	5.70	-12.0 ±0.4	140.1 ±7.2
T. Kitagaki, et al. (1968)	6.90	-14.3 ±1.5	198.3 ±29.8
K. Foley, et al. (1963)	7.20	-13.2 ±0.5	---
K. Foley, et al. (1963)	8.90	-12.8 ±0.2	---
K. Foley, et al. (1963)	10.00	-11.8 ±2.9	---
K. Foley, et al. (1965)	11.80	-12.3 ±0.8	---
K. Foley, et al. (1963)	12.00	-12.7 ±0.3	---
K. Foley, et al. (1965)	15.91	-8.8 ±1.0	---

[@]Slope in $(GeV/c)^{-2}$; forward cross section in mb/ster.

TABLE D.2-1

Experimental Measurements of First Minimum[@]

Experimenter	PLAB	t(min)	Cross Sec.
J. Berryhill, et al. (1968B)	.25#	.06 ±.01	30.00 ±30.00
J. Berryhill, et al. (1968B)	.35#	.11 ±.01	10.60 ±9.50
J. Berryhill, et al. (1968B)	.45#	.14 ±.01	7.90 ±2.60
J. Berryhill, et al. (1968B)	.55#	.19 ±.02	6.70 ±2.20
J. Berryhill, et al. (1968B)	.65#	.23 ±.02	4.00 ±1.50
L. Dobrzynski, et al. (1966)	1.18	.36 ±.03	.60 ±0.60
J. Berryhill, et al. (1968A)	1.40#	.40 ±.05	2.00 ±0.50
B. Barish, et al. (1966)	1.50	.41 ±.05	3.00 ±.50
G. Lynch, et al. (1963)	1.61	.43 ±.05	.95 ±.75
C. Daum, et al. (1968)	1.73	.38 ±.10	.90 ±.65
This Experiment	1.88	.44 ±.05	.72 ±.20
B. Barish, et al. (1966)	2.00	.48 ±.05	1.20 ±.20
C. Daum, et al. (1968)	2.13	.52 ±.10	2.55 ±.50
C. Daum, et al. (1968)	2.37	.51 ±.15	2.86 ±.45
B. Barish, et al. (1968)	2.50	.45 ±.05	1.30 ±.20
V. Domingo, et al. (1967)	2.70	.50 ±.10	.60 ±.50
C. Daum, et al. (1968)	2.97	.53 ±.20	2.45 ±.45
T. Ferbel, et al. (1965)	3.28	.70 ±.20	.55 ±.55
B. Escoubes, et al. (1963)	3.30#	.73 ±.15	.56 ±.10
W. Katz, et al. (1967)	3.66	.58 ±.05	.35 ±.10
K. Bockann, et al. (1966)	5.70	.60 ±.10	.10 ±.10
A. Ashmore, et a. (1968)	5.90	.60 ±.20	.10 ±.10
T. Kitagaki, et al. (1968	6.90	.60 ±.20	.02 ±.05

[@]t(min) in $(GeV/c)^2$; cross section at t(min) in $mb/(GeV/c)^2$.

[#]Indicates a nominal value.

TABLE D.3-1

Experimental Measurements of Secondary Maximum[@]

Experimenter	PLAB	t(max)	Cross Sec.
D. Cline, et al. (1968)	.45#	.18 ±.02	16.30 ±3.30
D. Cline, et al. (1968)	.55#	.26 ±.02	23.80 ±2.30
D. Cline, et al. (1968)	.65#	.35 ±.03	16.50 ±1.70
L. Dobrzynski, et al. (1966)	1.18	.53 ±.05	3.50 ±1.20
J. Berryhill, et al. (1968A)	1.40#	.55 ±.05	3.50 ±1.00
G. Lynch, et al. (1963)	1.61	.74 ±.13	2.20 ±0.70
C. Daum, et al. (1968)	1.73	.52 ±.09	2.60 ±0.65
This Experiment	1.88	.69 ±.05	2.00 ±0.20
B. Barish, et al. (1966)	2.00	.73 ±.02	3.00 ±0.20
C. Daum, et al. (1968)	2.13	.57 ±.12	2.89 ±0.48
C. Daum, et al. (1968)	2.37	.66 ±.15	3.10 ±0.42
B. Barish, et al. (1966)	2.50	.79 ±.03	2.50 ±0.20
V. Domingo, et al. (1967)	2.70	.79 ±.09	1.20 ±0.17
C. Daum, et al. (1968)	2.97	.76 ±.12	2.80 ±0.30
T. Ferbel, et al. (1965)	3.28	1.05 ±.20	1.08 ±0.54
B. Escoubes, et al. (1963)	3.30#	.83 ±.33	.69 ±0.09
W. Katz, et al. (1967)	3.66	.90 ±.06	.66 ±0.18
K. Bockmann, et al. (1966)	5.70	.80 ±.15	.30 ±.10
A. Ashmore, et al. (1968)	5.90	.80 ±.20	.30 ±.10
T. Kitagaki, et al. (1968)	6.90	.80 ±.20	.10 ±.10

[@]t(max) in $(GeV/c)^2$; cross section at t(max) in $mb/(GeV/c)^2$.

#Indicates a nominal value.

TABLE D.4-1

Backward Cross Section Measurements[@]

Experimenter	PLAB	Cross[$]	Cross[$]
D. Cline, et al. (1968)	.25	.250 ±.075	51.00 ±15.00
D. Cline, et al. (1968)	.35	.150 ±.050	16.00 ±5.30
D. Cline, et al. (1968)	.45#	.200 ±.050	13.00 ±3.30
D. Cline, et al. (1968)	.55#	.450 ±.050	20.00 ±2.30
D. Cline, et al. (1968)	.65#	.375 ±.050	1.20 ±0.16
W. Cooper, et al. (1968)	1.25	.055 ±.020	.59 ±.22
W. Cooper, et al. (1968)	1.35	.075 ±.025	.71 ±.24
W. Cooper, et al. (1968)	1.46	.090 ±.020	.76 ±.17
Z. Ma, et al. (1968)	1.58#	.037 ±.015	.28 ±.11
W. Cooper, et al. (1968)	1.59	.065 ±.015	.48 ±.11
G. Lynch, et al. (1963)	1.61	.050 ±.020	.36 ±.15
This Experiment	1.63	.078 ±.017	.56 ±.12
This Experiment	1.77	.076 ±.013	.47 ±.08
This Experiment	1.83	.063 ±.012	.40 ±.07
This Experiment	1.88	.049 ±.010	.28 ±.06
Z. Ma, et al. (1968)	1.89#	.049 ±.009	.28 ±.06
This Experiment	1.95	.044 ±.009	.24 ±.05
This Experiment	2.20	.021 ±.007	.11 ±.03
V. Domingo, et al. (1967)	2.70	.003 ±.003	.01 ±.01
W. Katz, et al. (1967)	3.66	.002 ±.001	.01 ±.01

[@]For events in the range $-0.8 > \cos\theta > -1.0$.

#Indicates a nominal value.

[$]Left column in mb/steradians, right in mb/$(\text{GeV/c})^2$.

REFERENCES

R. Abrams, R. Cool, G. Giacomelli, T. Kycia, B. Leontic, K. Li, and D. Michael, Phisical Review Letters, Vol. 18, p. 1209 (1967).

L. Agnew, T. Elioff, W. Fowler, R. Lander, W. Powell, E. Segre, H. Steiner, H. White, C. Wiegand, and T. Ypsilantis, Physical Review, Vol. 118, p. 1371 (1959).

C. Akerlof, R. Hieber, A. Krisch, K. Edwards, L. Ratner, and K. Ruddick, Physical Review Letters, Vol. 17, p. 1105 (1966).

C. Akerlof, R. Hieber, A. Krisch, K. Edwards, L. Ratner, and K. Ruddick, Physical Review, Vol. 159, p. 1138 (1967).

G. Alexander, A. Dar, and U. Karshon, Physical Review Letters, Vol. 14, p. 918 (1965).

V. Amaldi, T. Fazzini, G. Fidecaro, C. Ghesquiere, M. Legros, and H. Steiner, Nuovo Cimento, Vol. XXXIV, p. 826 (1964).

D. Amati, M. Fierz, and V. Glaser, Physical Review Letters, Vol. 4, p. 89 (1960).

D. Amati, S. Fubini, and A. Stanghellini, Nuovo Cimento, Vol. 26, p. 896 (1926).

D. Amati, S. Fubini, and A. Stanghellini, Physics Letters, Vol. 1, p. 29 (1962).

R. Armenteros, C. Coombes, B. Cork, G. Lambertson, and W. Wenzel, Physical Review, Vol. 119, p. 2068 (1960).

R. Arnold, Physical Review, Vol. 136, p. B1388 (1964).

R. Arnold, Physical Review, Vol. 140, p. 131022 (1965).

R. Arnold, Physical Review Letters, Vol. 14, p. 657 (1965).

R. Arnold, Argonne National Laboratory Report No. ANL-7173 (1966).

R. Arnold, Physical Review, Vol. 153, p. 1523 (1967).

REFERENCES (Cont.)

R. Arnold, Argonne National Laboratory Report No. ANL/HEP 6804 (1968).

R. Arnold, and T. Blackmon, Argonne National Laboratory Report ANL/HEP 6814 (1968).

A. Ashmore, C. Damerell, W. Frisken, R. Rubinstein, J. Orear, D. Owen, R. Peterson, A. Read, D. Ryan, and D. White, Physical Review Letters, Vol. 21, p. 387 (1968).

D. Avison, Physical Review, Vol. 154, p. 1570 (1967).

D. Avison, Physical Review, Vol. 154, p. 1583 (1967).

J. Ball, and G. Chew, Physical Review, Vol. 109, p. 1385 (1958).

V. Barger, and M. Olsson, Physical Review Letters, Vol. 16, p. 545 (1966).

V. Barger, Reviews of Modern Physics, Vol. 40, p. 129 (1968).

B. Barish, D. Fong, R. Gomez, D. Hartill, J. Pine, A. Tollestrup, A. Maschke, and T. Zipf, Physical Review Letters, Vol. 17, p. 720 (1966).

H. Benson, Mesons and Spectator Protons in $\pi^+ d \rightarrow \pi^+\pi^-\pi^o pp$ at 3.65 BeV/c, University Microfilms, Ann Arbor, Michigan (1966).

J. Berryhill, and D. Cline, Physical Review Letters, Vol. 21, p. 770 (1968).

J. Berryhill, D. Cline, and J. English, Physics Letters 27B, 573 (1968).

J. Blatt and L. Biedenham, Reviews of Modern Physics, Vol. 24, p. 258 (1952).

J. Blatt and V. Weiskopf, Theoretical Nuclear Physics, Wiley, New York (1952).

K. Bockmann, B. Nellen, E. Paul, B. Wagini, I. Borecka, J. Diaz, U. Heeren, V. Liebermeister, E. Lohrmann, E. Raubold, P. Soding, S. Wolff, J. Kidd, L. Mandelli, L. Mosca, V. Pelosi, S. Ratti, and L. Tallone, Nuovo Cimento, Vol. XLII, p. 954 (1966).

REFERENCES (Cont.)

D. Bugg, D. Salter, G. Stafford, R. George, K. Riley, and R. Tapper, Physical Review, Vol. 146, p. 980 (1966).

G. Burbidge, and F. Hoyle, Scientific American, Vol. 198, No. 4 (1958).

J. Button, and B. Maglic, Physical Review, Vol. 127, p. 1297 (1952).

N. Byers, and C. Yang, Physical Review, Vol. 142, p. 976 (1966).

O. Chamberlain, E. Segre, C. Wiegand, and T. Ypsilantis, Physical Review, Vol. 100, p. 947 (1955).

O. Chamberlain, D. Keller, R. Mermod, E. Segre, H. Steiner, and T. Ypsilantis, Physical Review, Vol. 108, p. 1553 (1957).

E. Chambers, and R. Hofstadter, Physical Review, Vol. 103, p. 1454 (1956).

L. Champomier, Lawrence Radiation Laboratory Report UCRL 11222 (1963).

J. Chapman, Three-Pion Production by 1.95 BeV/c π^+ Mesons on Hydrogen, University Microfilms, Ann Arbor (1965).

J. Chapman, F. Hess, J. Lys, C. Murphy and J. Vander Velde, Physical Review Letters, Vol. 21, p. 1718 (1968).

G. Chew, and F. Low, Physical Review, Vol. 113, p. 1640 (1959).

G. Chew, and S. Mandelstam, Physical Review, Vol. 119, p. 467 (1960).

G. Chew, and S. Frautschi, Physical Review, Vol. 124, p. 264 (1961).

G. Chew, and S. Frautschi, Physical Review Letters, Vol. 7, p. 394 (1961).

G. Chew, Reviews Modern Physics, Vol. 34, p. 394 (1962).

REFERENCES (Cont.)

G. Chew, and S. Frautschi, Physical Review Letters, Vol. 8, p. 41 (1962).

G. Chew, Physical Review Letters, Vol. 9, p. 233 (1962).

G. Chikovani, L. Dubal, M. Focacci, W. Kienzle, B. Levrat, B. Maglic, M. Martin, C. Nef, P. Schubelin, and J. Sequinot, Physics Letters, Vol. 22, p. 233 (1966).

C. Chiu, S. Chu, and L. Wang, Physical Review, Vol. 161, p. 1563 (1967).

T. Chou, and C. Yang, Physical Review, Vol. 170, p. 1591 (1968).

T. Chou, and C. Yang, Physical Review Letters, Vol. 20, p. 1213 (1968).

D. Cline, J. English, D. Reeder, R. Terrell, J. Twitty, Physical Review Letters, Vol. 21, p. 1268 (1968).

C. Coffin, N. Dikmen, L. Ettlinger, D. Meyer, A. Saulys, K. Terwilliger, and D. Williams, Physical Review Letters, Vol. 15, p. 838 (1965).

G. Cohen-Tannoudji, A. Morel, and N. Navelet, Nuovo Cimento, Vol. 48A, p. 1075 (1967).

E. Condon, and G. Shortley, Theory of Atomic Spectra, Cambridge University Press, Cambridge, England (1935).

C. Coombes, B. Cork, W. Galbraith, G. Lambertson, and W. Wenzel, Physical Review, Vol. 112, p. 1303 (1958).

W. Cooper, L. Hyman, W. Manner, B. Musgrave, and L. Voyvodic, Physical Review Letters, Vol. 20, p. 1059 (1968).

B. Cork, G. Lambertson, O. Piccioni, and W. Wenzel, Physical Review, Vol. 107, p. 248 (1957).

B. Cork, O. Dahl, D. Miller, A. Tenner, and C. Wang, Nuovo Cimento, Vol. XXV, p. 497 (1962).

L. Cutrona, "Recent Developments in Coherent Optics," in Symposium on Modern Optics, ed. J. Tippet, M.I.T. Press, Boston (1965).

REFERENCES (Cont.)

O. Czyzewski, B. Escoubes, Y. Goldschmidt-Clermont, M. Guinea-Moorhead, D. Morrison, S. De Unamuno-Escoubes, Physics Letters, Vol. 15, p. 188 (1965).

C. Daum, F. Erne, J. Lagnaux, J. Sens, M. Steuer, and F. Udo, Nuclear Physics, Vol. B6, p. 617 (1968).

T. Day, transcribed seminar on TVGP-SQUAW, Argonne National Laboratory (1967).

L. Dobrzynski, C. Ghesquiere, N. Xuong, and H. Tofte, Physics Letters, Vol. 23, p. 614 (1966).

V. Domingo, G. Fisher, L. Marshall-Libby, R. Sears, Physics Letters, Vol. 24B, p. 642 (1967).

S. Drell, Physical Review Letters, Vol. 5, p. 342 (1960).

S. Drell, Reviews of Modern Physics, Vol. 33, p. 458.

R. Eisberg, Fundamentals of Modern Physics, John Wiley and Sons, Inc., New York (1961).

T. Elioff, L. Agnew, O. Chamberlain, H. Steiner, C. Wiegand, and T. Ypsilantis, Physical Review Letters, Vol. 3, p. 285 (1959).

T. Elioff, L. Agnew, O. Chamberlain, H. Steiner, C. Wiegand, and T. Ypsilantis, Physical Review, Vol. 128, p. 869 (1962).

B. Escoubes, A. Fedrighini, Y. Goldschmidt-Clermont, M. Guinea-Moorhead, T. Hofmokl, R. Lewisch, D. Morrison, M. Schneeberger, S. De Unamuno, H. Dehne, E. Lohrmann, E. Raubold, P. Soding, M. Teucher, and G. Wolf, Physics Letters, Vol. 5, p. 132 (1963).

L. Ettlinger, The Secondary Maximum In Pion-Proton Elastic Scattering from 2.5 GeV/c to 6.0 GeV/c, University Microfilms, Ann Arbor, Michigan (1966).

T. Ferbel, A. Firestone, J. Sandweiss, H. Taft, M. Gailloud, T. Morris, A. Bachman, P. Baumel, R. Lea, Physical Review, Vol. 137, p. B1250 (1965).

E. Fermi, Nuovo Cimento, Vol. 11, p. 407 (1954).

REFERENCES (Cont.)

S. Fernbach, R. Serber, and T. Taylor, Physical Review, Vol. 75, p. 1352 (1949).

S. Fernbach, W. Heckrotte, and J. Lapore, Physical Review, Vol. 97, p. 1059 (1955).

H. Feshbach, and V. Weiskopf, Physical Review, Vol. 76, p. 1550 (1949).

R. Feynman, Physical Review, Vol. 76, p. 749 (1949).

R. Feynman, Physical Review, Vol. 76, p. 769 (1949).

R. Feynman, Quantum Electrodynamics, W. A. Benjamin, Inc., New York (1962).

M. Focacci, W. Kienzle, B. Levrat, B. Maglic, and M. Martin, Physical Review Letters, Vol. 17, p. 890 (1966).

K. Foley, S. Lindenbaum, W. Love, S. Ozaki, J. Russell, and L. Yuan, Physical Review Letters, Vol. 11, p. 503 (1963).

K. Foley, R. Gilmore, S. Lindenbaum, W. Love, S. Ozaki, E. Willen, R. Yamada, and L. Yuan, Physical Review Letters, Vol. 15, p. 45 (1965).

W. Frahn, and R. Venter, Annals of Physics (N.Y.), Vol. 27, p. 135 (1964).

N. Francis, and K. Watson, Physical Review, Vol. 92, p. 291 (1953).

S. Frautschi, M. Gell-Mann, and F. Zachariasen, Physical Review, Vol. 126, p. 2204 (1962).

S. Frautschi, Physical Review Letters, Vol. 17, p. 722 (1966).

J. Froehlich, Argonne National Laboratory Report No. JAF-1 (1965).

M. Froissart, Physical Review, Vol. 123, p. 1053 (1961).

W. Galbraith, E. Jenkins, T. Kycia, B. Leontic, R. Phillips, A. Read, R. Rubinstein, Physical Review, Vol. 138, p. B913 (1965).

REFERENCES (Cont.)

R. Glauber, "High-Energy Collision Theory," in Lectures in Theoretical Physics, ed. W. Brittin, et al. (Interscience Publishers, Inc., New York, 1959), Vol. 1.

A. Goldhaber, Physical Review, Vol. 134, p. B600 (1964).

K. Gottfried, and J. Jackson, Nuovo Cimento, Vol. 34, p. 735 (1964).

P. Grannis, J. Arens, F. Betz, O. Chamberlain, B. Dieterle, C. Schultz, G. Shapire, H. Steiner, L. Van Rossum, and D. Weldon, Physical Review, Vol. 148, p. 1297 (1966).

F. Henyey, G. Kane, J. Pumplin, and M. Ross, Physical Review Letters, Vol. 21, p. 946 (1968).

F. Henyey, K. Kajantie, and G. Kane, Physical Review Letters, Vol. 21, p. 1788 (1968).

M. Kreisler, F. Martin, M. Perl, M. Longo, and S. Powell, Physical Review Letters, Vol. 16, p. 1217 (1966).

A. Hossian, and M. Shaukat, Nuovo Cimento, Vol. XXXVIII, p. 737 (1965).

J. Hufner, and A. De Shalit, Physics Letters, Vol. 15, p. 52 (1965).

J. Jackson, J. Donohue, K. Gottfried, R. Keyser, and B. Svensson, Reviews of Modern Physics, Vol. 139, p. B428 (1965).

J. Jackson, Reviews Modern Physics, Vol. 37, p. 484 (1965).

G. Kane, private communication (1967).

W. Katz, B. Forman, and T. Ferbel, Physical Review Letters, Vol. 19, p. 265 (1967).

T. Kitagaki, K. Takahashi, S. Tanaka, T. Sato, A. Yamaguchi, K. Hasegawa, R. Sugawara, and K. Tamat, Physical Review Letters, Vol. 21, p. 175 (1968).

Z. Koba, and G. Takeda, Progress Theoretical Physics Japan, Vol. 19, p. 269 (1958).

REFERENCES (Cont.)

A. Krisch, "Diffraction Model for Strong Interactions and Shrinkage of the Forward Diffraction Peak," in Lectures in Theoretical Physics, ed. W. E. Brittin, et al. (University of Colorado Press, Boulder, Colorado, 1966), Vol. IX.

A. Krisch, and J. Krisch, 1967 Heidelberg Conference on High-Energy Physics.

A. Krisch, Physical Review Letters, Vol. 19, p. 1149 (1967).

S. Lindenbaum, W. Love, J. Niederer, S. Ozaki, J. Russell, L. Yuan, Physical Review Letters, Vol. 7, p. 185 (1961).

G. Lynch, R. Foulks, G. Kalbfleisch, S. Limentani, J. Shafer, M. Stevenson, and N. Xoung, Physical Review, Vol. 131, p. 1276 (1963).

J. Lys, "Direct-Channel Resonances in Antiproton-Proton Elastic Scattering," University of Michigan Bubble-Chamber Group Research Note No. 91/68, Ann Arbor, Michigan (1968).

Z. Ma, D. Parker, G. Smith, R. Sprafka, M. Abolins, and A. Rittenberg, XIV International Conference on High-Energy Physics (1968).

B. Maglic, Nuovo Cimento, Vol. XLV, p. 949 (1966).

G. Moliere, Z. Fur Naturforschung, Vol. 2A, p. 133 (1947).

J. Nicholson, Messenger math., Vol. 37, p. 84 (1907).

J. Nicholson, Philosophical Magazine, Vol. 19, p. 516 (1910).

J. Nicholson, Philosophical Magazine, Vol. 20, p. 157 (1910).

J. Orear, D. Owen, F. Peterson, A. Read, D. Ryan, D. White, A. Ashmore, C. Damerell, W. Frisken, R. Rubinstein, Physics Letters, Vol. 28B, p. 61 (1968).

R. N. Phillips, "Regge Poles in High-Energy Scattering," Harwell Research Note No. HL 66/3798 (1966).

REFERENCES (Cont.)

H. Poincare, Rendiconti Circolo Mat. Palermo, Vol. 29, p. 169 (1910).

I. Pomeranchuk, Soviet Physics--JETP, Vol. 34, p. 499 (1958).

T. Regge, Nuovo Cimento, Vol. 14, p. 951 (1959).

T. Regge, Nuovo Cimento, Vol. 15, p. 1947 (1960).

L. Rodberg, Nuclear Physics, Vol. 15, p. 72 (1959).

M. Ross, and G. Shaw, Physical Review Letters, Vol. 12, p. 627 (1964).

F. Salzman, and G. Salzman, Physical Review, Vol. 120, p. 599 (1960).

F. Salzman, and G. Salzman, Physical Review, Vol. 121, p. 1541 (1961).

R. Serber, Physical Review Letters, Vol. 10, p. 357 (1963).

R. Serber, Reviews of Modern Physics, Vol. 36, p. 649 (1964).

R. Serber, Reviews of Modern Physics, Vol. 36, p. 649 (1965).

R. Setti, Elementary Particles, University of Chicago Press, p. 69ff (1963).

A. Sommerfeld, Partial Differential Equations in Physics, Academic Press, Inc., New York, p. 282 (1949).

N. Sopkovich, Nuovo Cimento, Vol. 26, p. 186 (1962).

A. Stirling, P. Sonderegger, J. Kirz, P. Falk-Varant, O. Guisan, C. Bruneton, P. Borgeaud, M. Yvert, J. Guilland, C. Caverzavsio, and B. Amblard, Physical Review Letters, Vol. 20, p. 75 (1966).

E. Squires, Nuovo Cimento, Vol. 25, p. 242 (1962).

S. Suwa, A. Yokosawa, N. Booth, R. Esterling, and R. Hill, Physical Review Letters, Vol. 15, p. 560 (1965).

REFERENCES (Cont.)

S. Suwa, A. Yokosawa, N. Booth, R. Esterling, and R. Hill, Physical Review Letters, Vol. 16, p. 714 (1966).

G. Von Dardel, D. Frisch, R. Mermod, R. Milburn, and P. Piroue, Physical Review Letters, Vol. 5, p. 333 (1960).

G. Watson, Proc. Roy. Society (London), Vol. 95, p. 83 (1918).

J. White, Physics Letters, Vol. 26B, p. 461 (1968).

N. Xuong, G. Lynch, and C. Hinrichs, Physical Review, Vol. 124, p. 575 (1961).

ACKNOWLEDGEMENTS

It is a pleasure to acknowledge the assistance of the following people, all of whom contributed materially to the success of the research effort:

Professor Daniel Sinclair for kindly serving as chairman of the author's doctoral committee, and providing careful professional and scientific guidance during the course of the work.

Professors L. Cutrona, G. Kane, A. Krisch, and B. Roe for serving as members of the author's doctoral committee.

Professor J. Vander Velde for proposing the experiment and aiding in its analysis.

Professors J. Chapman and T. Murphy for setting up the programs CAST-TVGP-SQUAW and contributing generously to the experimental effort.

Professors G. Kane and M. Ross for their continued interest and generous theoretical assistance.

Professor A. Krisch for several illuminating discussions in connection with the optical model.

Dr. J. Lys for contributing invaluably to both the experimental and programming efforts.

Dr. F. Henyey for several stimulating discussions in connection with the Regge model.

Dr. W. Gibbs for his enthusiastic experimental, theoretical, and spiritual assistance.

Dr. L. Lovell for suggesting numerous methods to better expedite the research and thesis efforts.

Mr. M. Church for numerous penetrating theoretical discussions and several excellent computer programs.

Mr. H. Ring for his continued interest and generous programming assistance.

Mr. I. Khaduri for managing the (gross) beam count and tabulating its results.

Messrs. C. Arnold, K. Bartley, J. Davidson, A. Fisher, H. Husing, R. Kiang, J. Koschik, and J. Morfin for their support and consideration as friends and fellow graduate students.

Mr. C. Dwyer for managing the (profile) beam counts and analyzing the optics of the MURA chamber.

Miss L. Peterson for writing an extensive book-

keeping program and kindly helping with other programming problems.

Mr. A. Loceff for setting up the program SUMX and aiding with other programming problems.

Misses B. Bell and B. Stitt for helpful programming assistance.

Messeurs B. Hoppe, P. Radatz, K. K. Rao, I. Russo, A. Vander Mollen, and Misses M. Breuckner, J. Drapkin, V. French, M. Rauer for their invaluable technical support.

Mrs. A. Falconer, the author's wife, for her continuous encouragement and unfailing support, including the key-punching of this manuscript onto data cards.